



**1 A search for flavour changing neutral currents
2 involving a top quark and a Z boson, using the
3 data collected by the CMS collaboration at a
4 centre-of-mass energy of 13 TeV**

5 Isis Van Parijs

**6 Proefschrift ingediend met het oog op het behalen van de academische graad
7 Doctor in de Wetenschappen.**

Published in Faculteit Wetenschappen & Bio-ingenieurswetenschappen
 Vrije Universiteit Brussel
At 10 November 2017.

8

Responsible Contact: Isis Van Parijs
 Intitute for High Energy Physics
Promotor: Prof. Jorgen D'Hondt

9 First Referee: Prof. Dr. J. D'Hondt
 Date of Hand-in: 10 November 2017
 Date of Defense: 10 December 2017

Contents

11	1 Theoretical basis	1
12	1.1 Elementary particles and forces	1
13	1.2 Standard Model Lagrangian, connecting fields with particles	3
14	1.3 Flavours in the SM	5
15	1.4 The top quark in the SM	6
16	1.5 Effective field theories	11
17	1.6 Motivation for new physics	14
18	1.7 An effective approach beyond the SM: FCNC involving a top quark	15
19	1.8 Experimental constraints on top-FCNC	18
20	2 Experimental set-up	23
21	2.1 The Large Hadron Collider	23
22	2.2 The Compact Muon Solenoid	27
23	2.2.1 CMS coordinate system	27
24	2.2.2 Towards the heart of CMS	28
25	2.2.3 Data acquisition	37
26	2.2.4 Phase 1 upgrades	37
27	2.2.5 CMS computing model	39
28	3 Analysis techniques	41
29	3.1 Hadron collisions at high energies	41
30	3.2 Event generation	44
31	3.2.1 Fundamentals of simulating a proton collision	44
32	3.2.2 Programs for event generation	44
33	3.2.3 Generating FCNC top-Z interactions	46
34	3.2.4 Generating SM background events	48
35	3.3 Multivariate analysis techniques: Boosted Decision Trees	50
36	3.4 Statistical methodology	52
37	4 Event reconstruction and identification	55
38	4.1 Object Reconstruction	55
39	4.1.1 Charged particle tracks	57
40	4.1.2 Following the Muon's Footsteps	57
41	4.1.3 The path of the Electron	57

42	4.1.4 Primary Vertex Reconstruction	58
43	4.1.5 Calorimeter clusters	58
44	4.2 Particle flow identification	59
45	4.3 Pileup mitigation and luminosity measurement	59
46	4.4 Physics object reconstruction and identification	60
47	4.4.1 Muons	60
48	4.4.2 Electrons	62
49	4.4.3 Jets	63
50	4.4.4 Jets from b fragmentation	66
51	4.4.5 Missing transverse energy	69
52	4.5 Summary of corrections	69
53	5 Event selection and categorisation	71
54	5.1 Baseline event selection and filters	71
55	5.1.1 Event cleaning	74
56	5.1.2 Estimation of the trigger efficiency	76
57	5.1.3 Corrections	77
58	5.1.4 Reconstruction of kinematic variables	81
59	5.2 Analysis Strategy	82
60	5.3 Data driven NPL background simulation	83
61	5.4 Regions and channels	85
62	5.4.1 WZCR	86
63	5.4.2 TTCR and STCR	87
64	5.4.3 TTSR and STSR	87
65	6 The search for FCNC involving a top quark and a Z boson	89
66	6.1 Construction of template distributions	89
67	6.1.1 Distributions of the BDT variables	90
68	6.1.2 BDTs	90
69	6.1.3 Transverse mass in WZCR	90
70	6.2 Systematic uncertainties	91
71	6.3 Limit setting procedure validation	92
72	6.4 Result and discussion	94
73	6.4.1 One dimensional limits	105■
74	6.4.2 Two-dimensional limits	107■
75	7 Denouement of the top-Z FCNC hunt at 13 TeV	111■
76	Appendices	111■
77	A Trigger scale factors	113■
78	B Dilepton controlplots	125■
79	C Statistical independent regions	127■
80	Bibliography	129■

Theoretical basis

1

82 The Standard Model (SM) [1] is a name given in the 1970s to a theory describing the fun-
 83 damental particles and their interactions. This quantum field theory describes the particles
 84 and their interactions as fields and has successfully incorporated three of the four fundamental
 85 forces in the universe. In [Section 1.1](#), the particle content of the SM is summarised, while
 86 [Section 1.2](#) describes the SM Lagrangian and its symmetries. In [Section 1.3](#), the flavour content
 87 of the SM is highlighted, and [Section 1.4](#) focusses on the top quark in the SM.

88 The successful theory of the SM has some shortcomings which are discussed in [Section 1.6](#)
 89 and lead to searches for a more general theory. One of such is using an effective field theory
 90 (EFT) approach [2] to search for new physics in a model independent way. In [Section 1.7](#) an
 91 EFT model focussing on flavour changing neutral currents (FCNC) involving a top quark is
 92 presented. Its current experimental constraints are given in [Section 1.8](#).

93 **1.1 Elementary particles and forces**

94 The interactions in nature can be described by four forces, the strong force, the electromagnetic
 95 (EM) force, the weak force and the gravitational force. These interactions happen via particles
 96 with an integer spin known as bosons. The strong interaction is mediated by eight gluons g ,
 97 while the electromagnetic force is mediated by photons γ , and the weak force by Z and W^\pm
 98 bosons. In [Table 1.1](#), the forces and their characteristics are shown. The gravitational force is
 99 the only force not included in the SM and can be neglected for energies lower than the Planck
 scale (1.22×10^{19} GeV).

Table 1.1: The four forces of nature and their characteristics.

	Range	Mediator
Strong force	10^{-15} m	8 gluons
Electromagnetic force	∞	photon
Weak force	10^{-18} m	W^\pm , Zbosons
Gravitational force	∞	unknown

101 The fermions are the particles that make up the visible matter in the universe. They carry
 102 half integer spin and can be subdivided into leptons and quarks, where leptons do not interact
 103 strongly. Each fermion has a corresponding anti-fermion which has the same mass and is
 104 oppositely charged. The electron e is the first elementary particle discovered [3] and belongs
 105 to the first generation of leptons together with the electron neutrino ν_e . The second generation
 106 comprises the muon μ and muon neutrino ν_μ , whereas the third generation consists of the tau
 107 τ and tau neutrino ν_τ . The neutrinos are neutral particles, while the other leptons have charge
 108 $\pm q_e$ with q_e representing the elementary charge of 1.602×10^{-19} C. The masses of charged
 109 leptons differ by four orders of magnitude between the first and third generations. In the SM
 110 the neutrinos are assumed to be massless, nonetheless it is experimentally established that
 111 neutrinos do have a tiny non-zero mass [4, 5]. In Table 1.2, the leptons and their properties in
 the SM are summarised.

Table 1.2: The properties of the leptons in the three generations of the SM [6], where q_e represents the elementary charge.

	Generation	Particle	Mass	Charge
First		e^-	0.511 MeV	$-q_e$
		ν_e	≈ 0	0
Second		μ^-	106 MeV	$-q_e$
		ν_μ	≈ 0	0
Third		τ^-	1 777 MeV	$-q_e$
		ν_τ	≈ 0	0

112

113 The quarks can also be divided into three generations. Unlike the leptons, they carry
 114 colour charge and can interact via the strong interaction. The top quark, discovered in 1995
 115 at the Tevatron [7, 8], is the heaviest SM particle with a mass¹ measured to be $173.34 \pm$
 116 $0.27(\text{stat}) \pm 0.71(\text{syst})$ GeV [9]. The quarks and their properties are summarised in Table 1.3.
 117 In nature, only colour neutral objects can exist. This has as consequence that quarks are bound
 118 through gluons into mesons (quark+anti-quark) and baryons (three quarks). These mesons
 119 and baryons are mostly short-lived and unstable particles that rapidly decay through W^\pm and Z
 120 bosons. The only known stable baryon is the proton, made up of two up quarks and one down
 121 quark.

122 The scalar boson, commonly known as the Higgs boson, is the last piece of the SM discovered
 123 in 2012 [10, 11]. It is responsible for the masses of the W^\pm and Zboson, and that of the fermions.

¹In this thesis all masses and energies are expressed in natural units, where the speed of light and \hbar are taken to be equal to one.

Table 1.3: The properties of the quarks in the three generations of the SM [6], where q_e represents the elementary charge.

	Generation	Particle	Mass	Charge
First	up u	$2.2^{+0.6}_{-0.4}$ MeV	$\frac{2}{3} q_e$	
	down d	$4.7^{+0.5}_{-0.4}$ MeV	$\frac{-1}{3} q_e$	
Second	charm c	1.28 ± 0.03 GeV	$\frac{2}{3} q_e$	
	strange s	96^{+8}_{-4} MeV	$\frac{-1}{3} q_e$	
Third	top t	173.1 ± 0.6 GeV	$\frac{2}{3} q_e$	
	bottom b	$4.18^{+0.04}_{-0.03}$ GeV	$\frac{-1}{3} q_e$	

124 1.2 Standard Model Lagrangian, connecting fields with particles

125 The SM is a quantum field theory and thus describes the dynamics and kinematics of particles
 126 and forces by a Lagrangian \mathcal{L} . The theory is based on the $SU(3)_C \times SU(2)_L \times U(1)_Y$ gauge
 127 symmetry, where $SU(2)_L \times U(1)_Y$ describes the electroweak interaction and $SU(3)_C$ the strong
 128 interaction. The indices refer to colour C, the left chiral nature of the $SU(2)_L$ coupling L, and the
 129 weak hypercharge Y. Its Lagrangian is constructed such that symmetries representing physics
 130 conservation laws such as conservation of energy, momentum and angular momentum are
 131 contained. The symmetries under local gauge transformations are sustained by demanding
 132 gauge invariance².

The $U(1)_Y$ group has one generator Y with an associated gauge field B_μ . The three gauge fields W_μ^1 , W_μ^2 , and W_μ^3 , are associated to $SU(2)_L$ with three generators that can be written as half of the Pauli matrices:

$$T_1 = \frac{1}{2} \begin{pmatrix} 0 & 1 \\ 1 & 0 \end{pmatrix}, \quad T_2 = \frac{1}{2} \begin{pmatrix} 0 & -i \\ i & 0 \end{pmatrix}, \quad \text{and} \quad T_3 = \frac{1}{2} \begin{pmatrix} 1 & 0 \\ 0 & -1 \end{pmatrix}. \quad (1.1)$$

The generators T^a satisfy the Lie algebra:

$$[T_a, T_b] = i\epsilon_{abc} T^c \text{ and } [T_a, Y] = 0, \quad (1.2)$$

133 where ϵ_{abc} is an antisymmetric tensor. The gauge fields of $SU(2)_L$ only couple to left-handed
 134 fermions as required by the observed parity violating nature of the weak force. The $SU(3)_C$
 135 group represents quantum chromodynamics (QCD). It has eight generators corresponding to
 136 eight gluon fields $G_\mu^{1\dots 8}$. Unlike $SU(2)_L \times U(1)_Y$, $SU(3)_C$ is not chiral.

Under $SU(3)_C$ quarks are colour triplets while leptons are colour singlets. This implies that the quarks carry a colour index ranging between one and three, whereas leptons do not take part in strong interactions. Based on the chirality, the quarks and leptons are organized in doublets or singlets. Each generation i of fermions consists of left-handed doublets and right-handed

²Different field configurations of unobservable fields can result in identical quantities. Transformations between such configurations are called gauge transformation and the absence of change in the measurable quantities is a characteristic called gauge invariance.

singlets:

$$l_{L,i} = \begin{pmatrix} e_{L,i} \\ v_{L,i} \end{pmatrix}, \quad e_{R,i}, \quad q_{L,i} = \begin{pmatrix} u_{L,i} \\ d_{L,i} \end{pmatrix}, \quad u_{R,i}, \text{ and } d_{R,i} \quad (1.3)$$

The SM Lagrangian can be decomposed as a sum of four terms

$$\mathcal{L}_{SM} = \mathcal{L}_{gauge} + \mathcal{L}_f + \mathcal{L}_{Yuk} + \mathcal{L}_\phi, \quad (1.4)$$

137 that are related to the gauge, fermion, Yukawa and scalar sectors. The gauge Lagrangian
 138 regroups the gauge fields of all three symmetry groups, and the fermionic part consists of kinetic
 139 energy terms for quarks and leptons. The interaction between fermions and the scalar doublet
 140 ϕ gives rise to fermion masses and is described by the Yukawa Lagrangian. The scalar part of
 141 the Lagrangian is composed of a kinematic and potential component related to the scalar boson.

For the electroweak theory, two coupling constants are introduced, namely g' for $U(1)_Y$ and g for $SU(2)_L$. The physically observable gauge bosons of this theory are the photon field A_μ , the Z boson field Z_μ^0 , and the W boson fields W_μ^\pm . These are a superposition of the four gauge fields of $SU(2)_L \times U(1)_Y$:

$$\begin{aligned} A_\mu &= \sin \theta_W W_\mu^3 + \cos \theta_W B_\mu, \\ Z_\mu^0 &= \cos \theta_W W_\mu^3 - \sin \theta_W B_\mu, \text{ and} \\ W_\mu^\pm &= \sqrt{\frac{1}{2}} (W_\mu^1 \mp i W_\mu^2), \end{aligned} \quad (1.5)$$

142 where θ_W represents the weak mixing angle defined as $\tan \theta_W = \frac{g'}{g}$.

143 The coupling constant representing the strength of the QCD interactions is denoted as g_s . In
 144 QCD there is asymptotic freedom whereby the strong coupling constant becomes weaker as the
 145 energy with which the interaction between strongly interacting particles is probed increases,
 146 and stronger as the distance between the particles increases. A consequence of this is known as
 147 colour confinement, the quarks and gluons can not exist on their own and are not observed
 148 individually. They are bound in colour neutral states called hadrons, this process is known as
 149 hadronisation.

150 Electroweak symmetry breaking

151 In \mathcal{L}_{gauge} and \mathcal{L}_f are no mass terms for fermions present because only singlets under $SU(3)_C \times$
 152 $SU(2)_L \times U(1)_Y$ can acquire a mass with an interaction of the type $m^2 \phi^\dagger \phi$ without breaking
 153 the gauge invariance. In order to accommodate mass terms for fermions and gauge fields,
 154 electroweak symmetry breaking, leading to \mathcal{L}_ϕ is introduced.

The scalar doublet is introduced in the SM as

$$\phi = \frac{1}{\sqrt{2}} \begin{pmatrix} \varphi_1 + i\varphi_2 \\ \varphi_3 + i\varphi_4 \end{pmatrix}. \quad (1.6)$$

Its field potential is of the form

$$V(\phi) = \mu^2 \phi^\dagger \phi + \lambda (\phi^\dagger \phi)^2, \quad (1.7)$$

with $\mu^2 < 0$ and λ a positive integer. This choice of parameters gives the potential a "Mexican hat" shape. It has an infinite set of minima (ground states) and by expanding the field around an arbitrary choice of ground state, the electroweak symmetry is broken (EW):

$$\phi = \begin{pmatrix} 0 \\ \frac{v}{\sqrt{2}} \end{pmatrix} + \hat{\phi}, \quad (1.8)$$

where v is the vacuum expectation value (vev), measured to be around 245 GeV and corresponds to $\sqrt{\frac{-\mu}{\lambda}}$. The scalar doublet's four degrees of freedom are reduced to three degrees of freedom that couple to the gauge fields and fix the W^+ , W^- and Zbosons. The remaining fourth degree of freedom has given rise to a physically observable particle, called the Brout-Englert-Higgs (BEH) boson. This spontaneous symmetry breaking leaves the gauge invariance intact and gives masses to the W^\pm and Zbosons as:

$$m_W = \frac{1}{2} v |g| \quad \text{and} \quad m_Z = \frac{1}{2} v \sqrt{g'^2 + g^2}. \quad (1.9)$$

¹⁵⁵ The Brout-Englert-Higgs field couples universally to fermions with a strength proportional to their masses, and to gauge bosons with a strength proportional to the square of their masses.

1.3 Flavours in the SM

Flavour changing charged currents are introduced in 1963 by Nicola Cabibbo [12]. Via interactions with a W boson the flavour of the quarks is changed. At the time of the postulation only up, down, and strange quarks were known and the charged weak current was described as a coupling between the up quark and d_{weak} , where d_{weak} is a linear combination of the down and strange quarks, $d_{\text{weak}} = \cos\theta_c d + \sin\theta_c s$. This linear combination is a direct consequence of the chosen rotation

$$\begin{pmatrix} d_{\text{weak}} \\ s_{\text{weak}} \end{pmatrix} = \begin{pmatrix} \cos\theta_c & \sin\theta_c \\ -\sin\theta_c & \cos\theta_c \end{pmatrix} \begin{pmatrix} d \\ s \end{pmatrix} = \mathcal{R} \begin{pmatrix} d \\ s \end{pmatrix}, \quad (1.10)$$

where the rotation angle θ_c is known as the Cabibbo angle. This provides a definition for the charged weak current between u and d quarks,

$$J_\mu = \bar{u} \gamma_\mu (1 + \gamma_5) d_{\text{weak}}. \quad (1.11)$$

A consequence of Cabibbo's approach is that the s_{weak} is left uncoupled, leading to Glashow, Iliopoulos and Maiani (GIM) [13–15] to require the existence of a fourth quark with charge $\frac{2}{3}q_e$. This quark, known as the charm quark, couples to s_{weak} and a new definition of the charged weak current is modified to

$$J_\mu = (\bar{u} \quad \bar{c}) \gamma_\mu (1 + \gamma_5) \mathcal{R} \begin{pmatrix} d \\ s \end{pmatrix} = \bar{U} \gamma_\mu (1 + \gamma_5) \mathcal{R} D. \quad (1.12)$$

The neutral weak current is defined as

$$J_3 = \bar{U} \gamma_\mu (1 + \gamma_5) [\mathcal{R}, \mathcal{R}^\dagger] D, \quad (1.13)$$

and is diagonal in flavour space. This has as consequence that no flavour changing neutral currents occur at tree-level interactions [1].

Kobayashi and Maskawa generalised the Cabibbo rotation matrix to accommodate a third generation of quarks. The result is a 3×3 unitary matrix known as the CKM matrix, responsible for the mixing of weak interaction states of down-type quarks:

$$\begin{pmatrix} d_{\text{weak}} \\ s_{\text{weak}} \\ b_{\text{weak}} \end{pmatrix} = \begin{pmatrix} V_{ud} & V_{us} & V_{ub} \\ V_{cd} & V_{cs} & V_{cb} \\ V_{td} & V_{ts} & V_{tb} \end{pmatrix} \begin{pmatrix} d \\ s \\ b \end{pmatrix} = \mathcal{V}_{\text{CKM}} \begin{pmatrix} d \\ s \\ b \end{pmatrix}, \quad (1.14)$$

where \mathcal{V}_{CKM} is unitary ($\mathcal{V}_{\text{CKM}}^\dagger \mathcal{V}_{\text{CKM}} = \mathbb{1}$). A general 3×3 unitary matrix depends on three real angles and six phases. For the CKM matrix, the freedom to redefine the phases of the quark eigenstates can remove five of the phases, leaving a single physical phase known as the Kobayashi-Maskawa phase. This phase is responsible for the charge parity violation in the SM [16]. Each element V_{ij} of \mathcal{V}_{CKM} represents the transition probability of a quark i going to a quark j , and is experimentally determined to be [6]

$$\mathcal{V}_{\text{CKM}} = \begin{pmatrix} 0.97425 \pm 0.00022 & 0.2253 \pm 0.0008 & (4.13 \pm 0.49) \times 10^{-3} \\ 0.225 \pm 0.008 & 0.986 \pm 0.016 & (41.1 \pm 1.3) \times 10^{-3} \\ (8.4 \pm 0.6) \times 10^{-3} & (40.0 \pm 2.7) 10^{-3} & 1.021 \pm 0.032 \end{pmatrix}. \quad (1.15)$$

From Equation 1.15 follows that top quarks predominantly decay via charged weak currents to bottom quarks, with a probability consistent with unity. In the SM, FCNC can only occur via higher loop interactions which are highly suppressed. The expected transition probabilities for a top quark decaying via a FCNC interaction in the SM are given in Table 1.4, where it is clear that the FCNC top quark interactions of the SM is still beyond the reach of the sensitivity of current experiments.

Table 1.4: The predicted branching fractions \mathcal{B} for FCNC decays involving the top quark in the SM [17].

Process	\mathcal{B} in the SM	Process	\mathcal{B} in the SM
$t \rightarrow uZ$	8×10^{-17}	$t \rightarrow cZ$	1×10^{-14}
$t \rightarrow u\gamma$	4×10^{-16}	$t \rightarrow c\gamma$	5×10^{-14}
$t \rightarrow ug$	4×10^{-14}	$t \rightarrow cg$	5×10^{-12}
$t \rightarrow uH$	2×10^{-17}	$t \rightarrow cH$	3×10^{-15}

165

1.4 The top quark in the SM

Discovered in 1995 by the CDF and D0 collaborations at the Tevatron with proton-antiproton data [18, 19], the top quark plays an important role in studying high energy physics. Its Yukawa

interaction is given by

$$\mathcal{L}_{\text{top-Yukawa}} = -\frac{\lambda_t \nu}{\sqrt{2}} \bar{t}_L t_R - \frac{\lambda_t}{\sqrt{2}} H \bar{t}_L t_R + \text{h.c.}, \quad (1.16)$$

yielding a Yukawa coupling of [6]

$$\lambda_t = \frac{\sqrt{2} m_t}{\nu} = 0.991 \pm 0.003. \quad (1.17)$$

167 This Yukawa coupling is very large compared to the other Yukawa couplings in the SM ($\mathcal{O}(10^{-2})$),
 168 leading to the belief that the top quark may have an important role in understanding the
 169 mechanism of electroweak symmetry breaking. On top of this, the very short lifetime of the top
 170 quark makes it an excellent candidate to study the properties of a bare quark. Its high mass,
 171 almost 40 times higher than the mass of the closest fermion in mass, leads to a large coupling
 172 with the Higgs boson and makes the top quark an interesting candidate to investigate how
 173 particles acquire mass.

174 The CKM matrix element V_{tb} , given in [Equation 1.15](#), is experimentally found to be much
 175 larger than V_{ts} , V_{td} , and close to unity. The top quark decays through electroweak interactions
 176 since the W boson mass is smaller than the top quark mass and the W boson can be on shell. A
 177 consequence of this is that the top quark has a very short lifetime of only $1/\Gamma_t \approx 5 \cdot 10^{-25}$ s [6]
 178 leading to the fact that the formation of bound states involving top quarks are not allowed.
 179 This lifetime is even shorter than the typical hadronisation timescale of $1/\Lambda_{\text{QCD}} \approx 10^{-23}$ s,
 180 prohibiting gluons to radiate from the top quark and keeping its spin coherent. Since the
 181 electroweak interactions have a vector-axial vector (V-A) coupling structure³, the top quark
 182 spin orientation can be derived from the angular distributions of its decay products. This makes
 183 it possible to study the polarisation of top quarks from the angular distributions in various
 184 processes.

185 The massiveness of the top quark leads to the fact that a large amount of energy is needed to
 186 create one. This is only the case for high energy collisions such as those happening in the Earth's
 187 upper atmosphere when cosmic rays collide with particles in air, or by particle accelerators.
 188 The production of top quarks happens in two ways: single via the electroweak interaction or in
 189 pairs via the strong interaction. At hadron colliders, the dominant production mechanism is top
 190 quark production via gluon ($gg \rightarrow t\bar{t}$) or quark fusion ($q\bar{q} \rightarrow t\bar{t}$). In [Figure 1.1](#), the different top
 191 quark pair production mechanisms are shown. The production channel of gluon fusion is the
 192 main contributor to the top quark pair cross section at the LHC compared to quark fusion at the
 193 Tevatron. The $gg \rightarrow t\bar{t}$ process contributes 80-90% to the total top quark pair cross section in
 194 the LHC centre-of-mass energy regime of 7-14 TeV [6]. In [Table 1.5](#) the predicted top quark
 195 pair production cross sections are given for the LHC and the Tevatron, while in [Figure 1.2](#), a
 196 summary plot of the LHC and Tevatron top quark pair cross section measurements as a function
 197 of the centre-of-mass energy can be found.

198 The singly produced top quarks are produced via the electroweak interaction. These production
 199 mechanisms are subdivided at leading order into three main channels based on the virtuality

³In the SM a vector - axial vector coupling structure $(\gamma^\mu - \gamma^\mu \gamma^5)$ is predicted that only permits left-handed fermions or right-handed anti fermions to interact with a spin-1 particle.

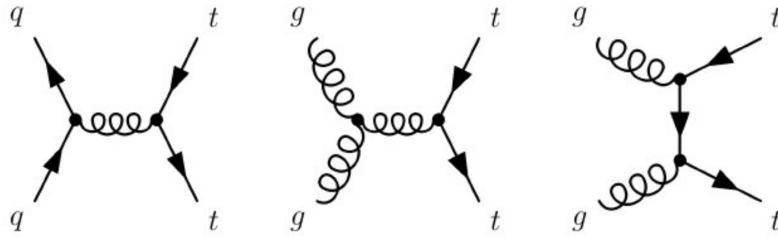


Figure 1.1: Leading order diagrams of the top quark pair production. Gluon fusion (right and middle) are the dominant processes at the LHC, while quark fusion (left) is the dominant one at the Tevatron.

Table 1.5: Predictions on the top quark pair production cross sections at next-to-next-to-leading order with next-to-next-to-leading log soft gluon resummation per centre-of-mass energy [6]. The first uncertainty is from scale dependence, while the second uncertainty originates from parton density functions.

Experiment	Top quark mass	Centre-of-mass energy	Cross section (pb)
Tevatron	$m_t = 173.3$ GeV	$\sqrt{s} = 1.96$ TeV	$\sigma_{\bar{t}t} = 7.16^{+0.11+0.17}_{-0.20-0.12}$
LHC	$m_t = 173.2$ GeV	$\sqrt{s} = 7$ TeV	$\sigma_{\bar{t}t} = 173.6^{+4.5+8.9}_{-5.9-8.9}$
LHC	$m_t = 173.2$ GeV	$\sqrt{s} = 8$ TeV	$\sigma_{\bar{t}t} = 247.7^{+6.3+11.5}_{-8.5-11.5}$
LHC	$m_t = 173.2$ GeV	$\sqrt{s} = 13$ TeV	$\sigma_{\bar{t}t} = 816.0^{+19.4+34.4}_{-28.6-34.4}$

200 ($Q^2 = -p_\mu p^\mu$) of the exchanged W boson. In Figure 1.3, the corresponding Feynman diagrams
 201 are shown. The single top quark production cross sections, given in Table 1.6, are smaller than
 202 the top quark pair production cross sections since the electroweak coupling strength is smaller
 203 than the strong coupling strength. In addition, for the single top quark production, there is the
 204 need of sea quarks (b, \bar{q}) in the initial states for which the parton density functions increase
 205 less steeply at low momentum fractions compared to the gluon parton density functions.

206 The production via the t -channel has a virtuality of the W boson $Q^2 > 0$, making it space-like.
 207 It is produced via the scattering of the W boson of a bottom quark coming from a proton
 208 or from gluon splitting ($g \rightarrow b\bar{b}$). It has the highest single top quark cross section in proton
 209 collisions and the top quark production is roughly twice as large than the antitop quark. This is
 210 a consequence of the up-down valence quark composition of the proton. This feature makes the
 211 t -channel sensitive to the parton density functions of the proton. The s -channel is the production
 212 mechanism with the smallest cross section. Here the W boson is time-like ($Q^2 < 0$) which
 213 requires the W boson to have a large virtuality to produce the heavier top quark. It is produced
 214 from two quarks belonging to the same isodoublet (e.g. $u\bar{d}$) and subsequently decays to $t\bar{b}$.
 215 This process gets enhanced by many beyond the Standard Model scenarios via the addition of
 216 new heavy particles such as W' . The tW -channel has a top quark produced in association with a
 217 W boson produced on shell $Q^2 = -m_W^2$. This mode is negligible at the Tevatron, but of relevant
 218 size at the LHC. The tW -channel is sensitive to new physics affecting the Wtb vertex. The single
 219 top quark production cross section measurements by the CMS collaboration can be found in
 220 Figure 1.4.

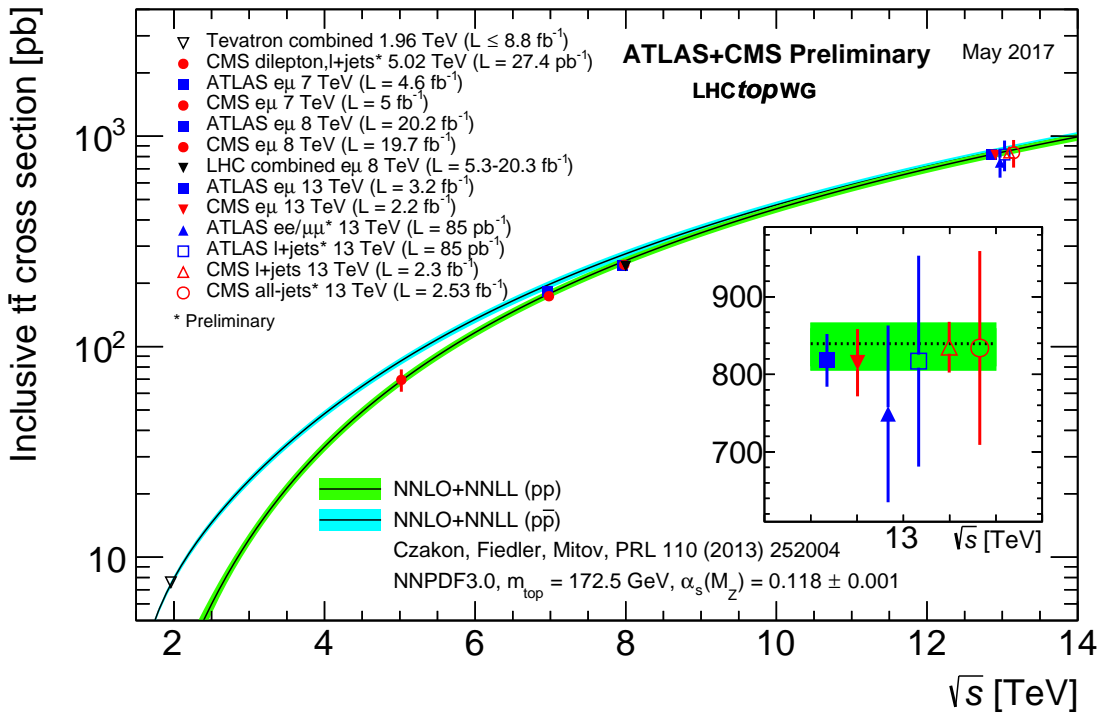


Figure 1.2: Summary of the LHC and the Tevatron measurements of the top quark pair production cross section as function of the centre-of-mass energy compared with the next-to-next-to-leading order QCD calculation. The theory bands are the uncertainties due to renormalization and factorisation scales, parton density functions and the strong coupling. The mass of the top quark is assumed to be 172.5 GeV. Measurements for the same centre-of-mass energy are slightly off-set for clarity. Figure taken from [20].

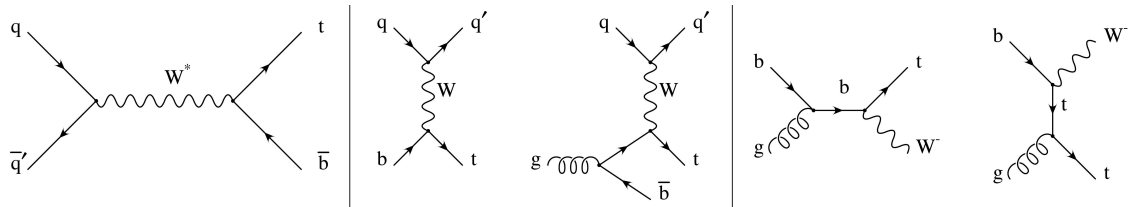


Figure 1.3: Leading order Feynman diagrams of the electroweak production of single top quarks in the s -channel (left), t -channel (middle), and for the tW associated production. Figure taken from [21].

Table 1.6: Predictions on the single top quark production cross sections at next-to-leading order per centre-of-mass energy [6]. The uncertainties from scale dependence and from parton density functions are combined in quadrature or given separately (scale + PDF). For the t -channel the relative proportions to t and \bar{t} are 65% and 35%. For the s -channel this is respectively 69% and 31%. The tW -channel has an equal proportion of top and antitop quarks. For Tevatron, the top quark mass is assumed to be 173.3 GeV, while the LHC predictions use $m_t = 172.5$ GeV [6, 22].

Collider	Centre-of-mass energy	Cross section $\sigma_{t+\bar{t}}$ (pb)		
		t -channel	s -channel	tW -channel
Tevatron	$\sqrt{s} = 1.96$ TeV	$2.06^{+0.13}_{-0.13}$	$1.03^{+0.05}_{-0.05}$	-
LHC	$\sqrt{s} = 7$ TeV	$63.89^{+2.91}_{-2.52}$	$4.29^{+0.19}_{-0.17}$	$15.74^{+0.40+1.10}_{-0.40-1.14}$
LHC	$\sqrt{s} = 8$ TeV	$84.69^{+3.76}_{-3.23}$	$5.24^{+0.22}_{-0.20}$	$22.37^{+0.60+1.40}_{-0.60-1.40}$
LHC	$\sqrt{s} = 13$ TeV	$216.99^{+9.04}_{-7.71}$	$10.32^{+0.40}_{-0.36}$	$71.7^{+1.80+3.40}_{-1.80-3.40}$

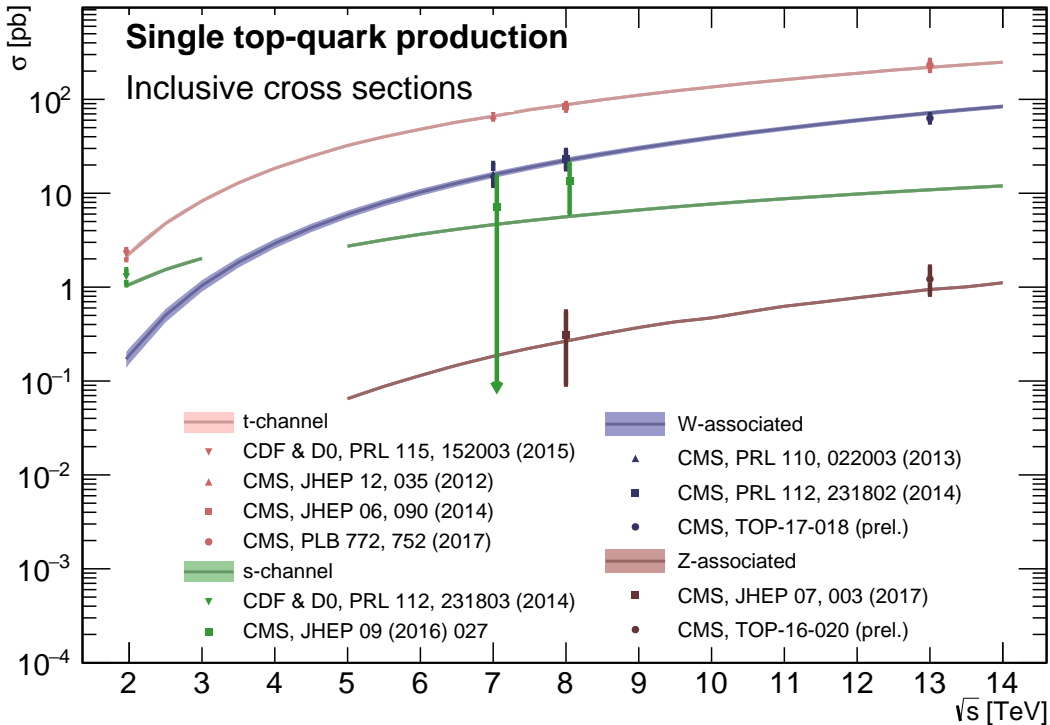


Figure 1.4: Summary of the measurements of the single top quark production cross section as function of the centre-of-mass energy. Figure taken from [23].

221 1.5 Effective field theories

222 Problems can be simplified if one looks at the relevant scale of the process that one want to
 223 investigate, for example the chemical properties of an hydrogen atom can be described without
 224 any knowledge of quark interactions inside the proton. In this case, the proton can be considered
 225 the elementary object (indivisible) due to the fact that the binding energy of the constituents is
 226 much bigger than the energy of the electron in orbit around the proton. Effective field theories
 227 are based on this kind of separation of different energy scales in a system [24]. Effective field
 228 theories can be used for theories where the perturbative expansion cannot be trusted, e.g. QCD
 229 at low energy, or as bottom up approach to look for new physics in a model independent way.
 230 The latter is the way effective field theory will be used throughout this thesis.

The main idea behind effective field theory is easily explained via the example of the Fermi theory. Fermi explained in 1933 [25] the β -decay as a product of currents:

$$\mathcal{L}_{\text{EFT}}^{\text{Fermi}} = -\frac{G_F}{\sqrt{2}} J^\mu J_\mu^\dagger, \quad (1.18)$$

where G_F is the Fermi coupling constant, measured to be $G_F \approx 1.17 \times 10^{-5} \text{ GeV}^{-2}$. The current J_μ can written as the sum of an hadronic J_μ^h and leptonic J_μ^l current, where for simplicity only the leptonic current discussed.

$$J_\mu^l = \sum_i \bar{\nu}_i \gamma_\mu (1 - \gamma_5) l. \quad (1.19)$$

231 Historically, charged currents were flavour universal and the later discovered parity violation of
 232 the weak interaction led to the V-A structure. After this, the $SU(2)_L$ symmetry was postulated
 233 and the existence of neutral currents was predicted. The effective Lagrangian used then (given
 234 in Equation 1.18), could nowadays be build starting from $SU(2)_L$ symmetries only.

The muon decay can be computed from two different starting points. The effective Fermi Lagrangian provides the decay width of the muon into an electron and two neutrinos

$$\Gamma(\mu \rightarrow e \bar{\nu}_e \nu_\mu) \approx \frac{1}{96\pi^3} \frac{m_\mu^2}{\Lambda_F^4}, \quad (1.20)$$

where Λ_F is the energy scale defined as

$$\frac{G_F}{\sqrt{2}} = \frac{1}{\Lambda_F^2}. \quad (1.21)$$

From muon decay measurements, the value of Λ_F is determined to be $\Lambda_F \approx 348 \text{ GeV}$ [24]. From the SM Lagrangian, one could also calculate the muon decay. Considering that the momenta involved are small compared to the W boson mass, the propagator's denominator can be expanded as [1]

$$\frac{1}{p^2 - m_W^2} = -\frac{1}{m_W^2} - \frac{p^2}{m_W^4} + \dots \quad (1.22)$$

Looking at the first term, and identifying

$$\frac{g^2}{8m_W} = \frac{1^2}{\Lambda_F}, \quad (1.23)$$

one sees that this corresponds with [Equation 1.20](#), thus the effective Lagrangian in [Equation 1.18](#) is the first term of the expansion in $\frac{1}{m_W^2}$ applied on the full Lagrangian.

An effective theory is thus a Taylor expansion in the ratio of two scales and the only remnants of the full theory at low energies are the symmetries and the values of the coupling constants. If the expansion parameter is small, one can truncate the series leading to the Lagrangian containing a finite number of free coefficients, making predictions possible. The error on these predictions is then of the order as the truncated piece.

The SM can be seen as an effective theory applicable up to energies not exceeding a scale Λ . Therefore, remnants should still be valid and the theory above that scale should have a gauge group containing $SU(3)_C \times SU(2)_L \times U(1)_Y$ and all the SM degrees of freedom, as well as reduce to the SM at lower energies. The general SM Lagrangian becomes then

$$\mathcal{L}_{SM+EFT} = \mathcal{L}_{SM}^{(4)} + \frac{1}{\Lambda} \sum_k C_k^{(5)} Q_k^{(5)} + \frac{1}{\Lambda^2} \sum_k C_k^{(6)} Q_k^{(6)} + \mathcal{O}\left(\frac{1}{\Lambda^3}\right), \quad (1.24)$$

where $Q_k^{(n)}$ are dimension- n operators (currents) and $C_k^{(n)}$ the corresponding dimensionless coupling constants, so-called Wilson coefficients. The Wilson coefficients are determined by the underlying high energy theory.

In the Warsaw basis [\[26\]](#), a set of independent operators of dimension 5 and 6 are built out of the SM fields and are consistent with the SM gauge symmetries and is fully derived in Ref. [\[26\]](#). In general the various measurements show a good agreement with the SM predictions and by lack of deviations from the SM, limits on the anomalous couplings can be derived. The estimated coupling strengths per operator contributing to single top quark production obtained from various measurements at the LHC and Tevatron are shown in [Figure 1.5](#) for which the conventions are discussed in Ref. [\[27\]](#). These results are consistent with the SM expectation for which those operators vanish.

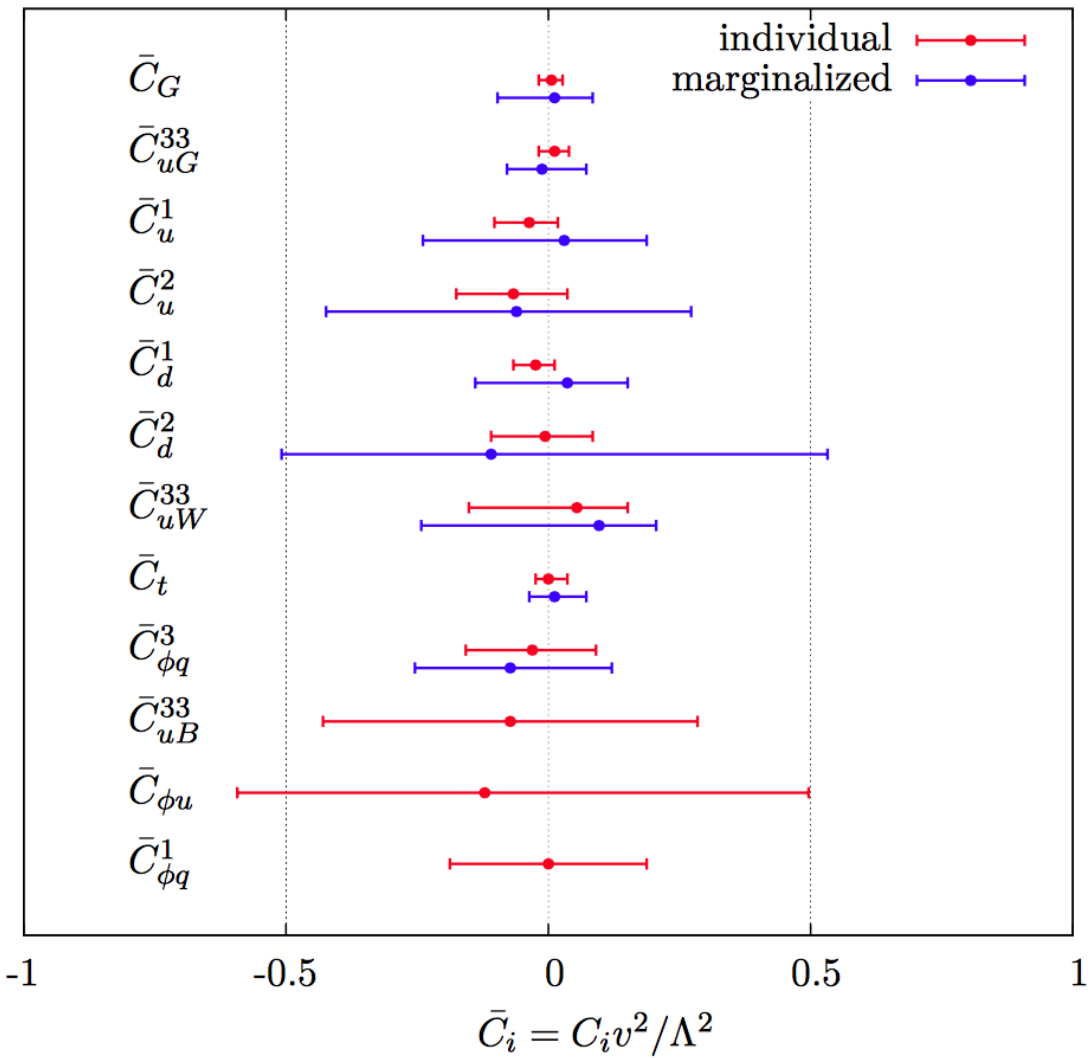


Figure 1.5: Global fit results of top quark effective field theory to experimental data including all constrained operators at dimension six. For the operators, the Warsaw basis of [26] is used. The bounds are set on the Wilson coefficients of various operators contributing to top quark production and decay in two cases (red) all other coefficients set to zero, or (blue) all other coefficients marginalized over. Figure taken from [28].

253 **1.6 Motivation for new physics**

254 Many high energy experiments confirm the success of the SM. In particular the scalar boson,
 255 the cornerstone of the SM, has consecrated the theory. Unfortunately there are also strong
 256 indications that the SM ought to be a lower energy expression of a more global theory. The
 257 existence of physics beyond the SM (BSM) [29] is strongly motivated. These motivations are
 258 based on direct evidence from observation such as the existence of neutrino masses, the existence
 259 of dark matter and dark energy, or the matter-antimatter asymmetry, and also from theoretical
 260 problems such as the hierarchy problem, the coupling unification or the large numbers of free
 261 parameters in the SM.

262 In the SM, the neutrinos are assumed to be massless, while experiments with solar, atmospheric,
 263 reactor and accelerator neutrinos have established that neutrinos can oscillate and change flavour
 264 during flight [4, 5]. These oscillations are only possible when neutrinos have masses. The
 265 flavour neutrinos (ν_e , ν_μ , ν_τ) are then linear expressions of the fields of at least three mass
 266 eigenstate neutrinos ν_1 , ν_2 , and ν_3 .

267 The ordinary or baryonic matter described by the SM describes only 5% of the mass (energy)
 268 content of the universe. Astrophysical evidence indicated that dark matter is contributing
 269 to approximately 27% and dark energy to 68% of the content of the universe. From the
 270 measurements of the temperature and polarizations anisotropies of the cosmic microwave
 271 background by the Planck experiment [30], the density of cold non baryonic matter is determined.
 272 Cold dark matter is assumed to be only sensitive to the weak and gravitational force, leading
 273 to only one possible SM candidate: the neutrino. However, these are too light to account for
 274 the vast amount of dark matter and other models are needed. Dark energy is assumed to be
 275 responsible for the acceleration in the expansion of the universe [31].

276 At the Big Bang, matter and antimatter are assumed to be produced in equal quantities.
 277 However, it is clear that we are surrounded by matter. So where did all the antimatter go?
 278 In 1967, Sakharov identified three mechanisms that are necessary to obtain a global matter
 279 antimatter asymmetry [32]. These mechanisms are those of baryon and lepton number violation,
 280 that at a given moment in time there was a thermal imbalance for the interactions in the universe,
 281 and there is charge C and charge parity CP violation⁴.

282 The large number of free parameters in the SM comes from the nine fermion masses, three
 283 CKM mixing angles and one CP violating phase, one EM coupling constant g' , one weak coupling
 284 constant g , one strong coupling constant g_s , one QCD vacuum angle, one vacuum expectation
 285 value, and one mass of the scalar boson. This large number of free parameters leads to the
 286 expectation of a more elegant and profound theory beyond the SM.

287 The hierarchy problem [33] is related to the huge difference in energy between the weak
 288 scale and the Planck scale. The vev of the Brout-Englert-Higgs field determines the weak scale
 289 that is approximately 246 GeV. The radiative corrections to the scalar boson squared mass m_H^2 ,
 290 coming from its self couplings and couplings to fermions and gauge bosons, are quadratically

⁴The rate of a process $i \rightarrow f$ can be different from the CP-conjugate process: $\tilde{i} \rightarrow \tilde{f}$. The SM includes sources of CP-violation through the residual phase of the CKM matrix. However, these could not account for the magnitude of the asymmetry observed.

291 proportional to the ultraviolet momentum cut-off Λ_{UV} . This cut-off is at least equal to the energy
 292 to which the SM is valid without the need of new physics. For the SM to be valid up to the
 293 Planck mass, the correction to m_H^2 becomes thirty orders of magnitude larger than m_H^2 . This
 294 implies that an extraordinary cancellation of terms should happen. This is also known as the
 295 naturalness problem of the H boson mass.

The correction to the squared mass of the scalar boson coming from a fermion f , coupling to the scalar field ϕ with a coupling λ_f is given by

$$\Delta m_H^2 = -\frac{|\lambda_f|^2}{8\pi^2} \Lambda_{\text{UV}}^2, \quad (1.25)$$

while the correction to the mass from a scalar particle S with a mass m_S , coupling to the scalar field with a Lagrangian term $-\lambda_S |\phi|^2 |S|^2$ is

$$\Delta m_H^2 = \frac{|\lambda_S|^2}{16\pi^2} \left(\Lambda_{\text{UV}}^2 - 2m_S^2 \ln \left(\frac{\Lambda_{\text{UV}}}{m_S} \right) + \dots \right). \quad (1.26)$$

296 As one can see the correction term to m_H^2 is much larger than m_H^2 itself. By introducing BSM
 297 physics models that introduce new scalar particles at the TeV scale that couple to the scalar
 298 boson one can cancel the Λ_{UV}^2 divergence and avoid this fine-tuning.

299 The choice of the $SU(3)_C \times SU(2)_L \times U(1)_Y$ symmetry group itself as well as the separate
 300 treatment of the three forces included in the SM raises concern. The intensity of the forces
 301 show a large disparity around the electroweak scale, but have comparable strengths at higher
 302 energies. The electromagnetic and weak forces are unified in a electroweak interaction, but the
 303 strong coupling constant does not encounter the other coupling constants at high energies. In
 304 order to reach a grand unification, the running of couplings can be modified by the addition of
 305 new particles in BSM models.

306 1.7 An effective approach beyond the SM: FCNC involving a top 307 quark

308 The closeness of the top quark mass to the electroweak scale led physicists to believe that it is a
 309 sensitive probe for new physics. Studying its properties is therefore an important topic of the
 310 experimental program at the LHC. Several extensions of the SM enhance the FCNC branching
 311 fractions and can be probed at the LHC [17], from which some of them are shown in Table
 312 1.7. Previous searches have been performed at the Tevatron by the CDF [34] and D0 [35]
 313 collaborations, and at the LHC by the ATLAS [36–40] and CMS [41–45] collaborations.

314 The impact of BSM models can be written in a model independent way by means of an
 315 effective field theory valid up to an energy scale Λ . The leading effects are parametrized by a
 316 set of fully gauge symmetric operators that are added to the SM Lagrangian and can be reduced
 317 to a minimal set of operators as seen in Equation 1.24. For simplicity, the assumption is made
 318 that new physics effects are exclusively described by dimension-6 operators, thus neglecting

Table 1.7: The predicted branching fractions \mathcal{B} for FCNC interactions involving the top quark in some BSM models [17]: quark singlet (QS), generic two Higgs doublet model (2HDM) and the minimal supersymmetric extensions to the SM (MSSM);

Process	QS	2HDM	MSSM	Process	QS	2HDM	MSSM
$t \rightarrow uZ$	$\leq 1.1 \times 10^{-4}$	—	$\leq 2 \times 10^{-6}$	$t \rightarrow cZ$	$\leq 1.1 \times 10^{-4}$	$\leq 10^{-7}$	$\leq 2 \times 10^{-6}$
$t \rightarrow u\gamma$	$\leq 7.5 \times 10^{-9}$	—	$\leq 2 \times 10^{-6}$	$t \rightarrow c\gamma$	$\leq 7.5 \times 10^{-9}$	$\leq 10^{-6}$	$\leq 2 \times 10^{-6}$
$t \rightarrow ug$	$\leq 1.5 \times 10^{-7}$	—	$\leq 8 \times 10^{-5}$	$t \rightarrow cg$	$\leq 1.5 \times 10^{-7}$	$\leq 10^{-4}$	$\leq 8 \times 10^{-5}$
$t \rightarrow uH$	$\leq 4.1 \times 10^{-5}$	$\leq 5.5 \times 10^{-6}$	$\leq 10^{-5}$	$t \rightarrow cH$	$\leq 4.1 \times 10^{-5}$	$\leq 10^{-3}$	$\leq 10^{-5}$

319 neutrino physics. In the fully gauge symmetric case, the EFT Lagrangian is then given by

$$\mathcal{L}_{\text{SM+EFT}} = \mathcal{L}_{\text{SM}} + \sum_i \frac{\bar{c}_i}{\Lambda^2} O_i + \mathcal{O}\left(\frac{1}{\Lambda^3}\right), \quad (1.27)$$

where the Wilson coefficients \bar{c}_i depend on the considered theory and on the way that new physics couples to the SM particles. Taking into account that Λ is large, contributions suppressed by powers of Λ greater than two are neglected. Additionally, all four fermion operators are omitted for the rest of this thesis. The Warsaw basis is adopted for the independent effective operators [26], parametrising the new physics effects relevant for the flavour changing neutral current interactions of the top quark as, all flavour indices understood,

$$\begin{aligned} \mathcal{L}_{\text{EFT}}^t = & \frac{\bar{c}_{uG}}{\Lambda^2} \Phi^\dagger \cdot [\bar{Q}_L \sigma^{\mu\nu} \mathcal{T}_a u_R] G_{\mu\nu}^a + \frac{\bar{c}_{uB}}{\Lambda^2} \Phi^\dagger \cdot [\bar{Q}_L \sigma^{\mu\nu} u_R] B_{\mu\nu} + \frac{2\bar{c}_{uW}}{\Lambda^2} \Phi^\dagger T_i \cdot [\bar{Q}_L \sigma^{\mu\nu} u_R] W_{\mu\nu}^i \\ & + i \frac{\bar{c}_{hu}}{\Lambda^2} \left[\Phi^\dagger \overleftrightarrow{D}_\mu \Phi \right] [\bar{u}_R \gamma^\mu u_R] + i \frac{\bar{c}_{hq}^{(1)}}{\Lambda^2} \left[\Phi^\dagger \overleftrightarrow{D}_\mu \Phi \right] [\bar{Q}_L \gamma^\mu Q_L] \\ & + i \frac{4\bar{c}_{HQ}^{(3)}}{\Lambda^2} \left[\Phi^\dagger T_i \overleftrightarrow{D}_\mu \Phi \right] [\bar{Q}_L \gamma^\mu T^i Q_L] + \frac{\bar{c}_{uh}}{\Lambda^2} \Phi^\dagger \Phi \Phi^\dagger \cdot [\bar{Q}_L u_R] + \text{h.c.}, \end{aligned} \quad (1.28)$$

where the left handed $SU(2)_L$ doublet of the quark fields is denoted by Q_L , the up-type right handed fields by u_R , the down-type right handed fields by d_R , the $SU(2)_L$ doublet of the Higgs field by Φ , the field strength tensors as

$$\begin{aligned} B_{\mu\nu} &= \partial_\mu B_\nu - \partial_\nu B_\mu, \\ W_{\mu\nu}^k &= \partial_\mu W_\nu^k - \partial_\nu W_\mu^k - g \epsilon_{ij}^k W_\mu^i W_\nu^j, \\ G_{\mu\nu} &= \partial_\mu G_\nu^a - \partial_\nu G_\mu^a + g_s f_{bc}^a G_\mu^b G_\nu^c, \end{aligned} \quad (1.29)$$

denoting the structure constant of the $SU(3)_C$ group as f_{bc}^a and the structure constant of the $SU(2)_L$ group as ϵ_{ij}^k . The gauge covariant derivatives are also standard defined as

$$D_\mu \Phi = \partial_\mu \Phi - \frac{1}{2} i g' B_\mu \Phi - i g T_k W_\mu^k \Phi \quad (1.30)$$

with the conventions of Section 1.2. The representation matrices T of $SU(2)_L$ are defined in Equation 1.1, while the representation matrices \mathcal{T} of $SU(3)_C$ are the Gell-Mann matrices [1].

The hermitian derivative operator is defined as

$$\Phi^\dagger \overleftrightarrow{D} \Phi = \Phi^\dagger D^\mu \Phi - D_\mu \Phi^\dagger \Phi. \quad (1.31)$$

After electroweak symmetry breaking, the operators induce [17, 46] both corrections to the SM couplings and new interactions at tree level such as FCNC interactions. The FCNC interactions of the top quark that are not present in the SM are given by

$$\mathcal{L}_{\text{EFT}}^t = \frac{\sqrt{2}}{2} \sum_{q=u,c} \left[g' \frac{\kappa_{t\gamma q}}{\Lambda} A_{\mu\nu} \bar{t} \sigma^{\mu\nu} (f_{\gamma q}^L P_L + f_{\gamma q}^R P_R) q \right. \quad (1.32)$$

$$+ \frac{g}{2\cos\theta_W} \frac{\kappa_{tZq}}{\Lambda} Z_{\mu\nu} \bar{t} \sigma^{\mu\nu} (f_{Zq}^L P_L + f_{Zq}^R P_R) q \quad (1.33)$$

$$+ \frac{\sqrt{2}g}{4\cos\theta_W} \zeta_{tZq} \bar{t} \gamma^\mu (f_q^L P_L + f_q^R P_R) q Z_\mu \quad (1.34)$$

$$+ g_s \frac{\kappa_{tgq}}{\Lambda} Z_{\mu\nu} \bar{t} \sigma^{\mu\nu} (f_{gq}^L P_L + f_{gq}^R P_R) q G_\mu^a \quad (1.35)$$

$$+ \eta_{Hqt} \bar{t} (\hat{f}_q^L P_L + \hat{f}_q^R P_R) q H + \text{h.c.} \Big], \quad (1.36)$$

where the value of the FCNC couplings at scale Λ are represented by $\kappa_{tZq}, \kappa_{tgq}, \kappa_{t\gamma q}, \zeta_{tZq}$, and η_{Hqt} . These are assumed to be real and positive, with the unit of GeV^{-1} for κ_{txq}/Λ and no unit for ζ_{xqt} and η_{xqt} . In the equation $\sigma^{\mu\nu}$ equals to $\frac{i}{2} [\gamma^\mu, \gamma^\nu]$, and the left- and right-handed chirality projector operators are denoted by P_L and P_R . The electromagnetic coupling constant is denoted by g' , the strong interaction coupling is denoted as g_s , while the electroweak interaction is parametrised by the coupling constant g and the electroweak mixing angle θ_W . The complex chiral parameters are normalized according to $|f_{xq}^L|^2 + |f_{xq}^R|^2 = 1$, $|\tilde{f}_q^L|^2 + |\tilde{f}_q^R|^2 = 1$, and $|\hat{f}_q^L|^2 + |\hat{f}_q^R|^2 = 1$. In the expression for $\mathcal{L}_{\text{EFT}}^t$, the unitary gauge is adopted and the scalar field is expanded around its vacuum expectation value v with H being the SM scalar boson. The field strength tensors of the photon A_μ , the gluon field $G_\mu^{a..8}$, and the Z boson Z_μ^0 are defined as

$$\begin{aligned} A_{\mu\nu} &= \partial_\mu A_\nu - \partial_\nu A_\mu, \\ Z_{\mu\nu} &= \partial_\mu Z_\nu - \partial_\nu Z_\mu, \text{ and} \\ G_{\mu\nu} &= \partial_\mu G_\nu^a - \partial_\nu G_\mu^a + g_s f_{bc}^a G_\mu^b G_\nu^c. \end{aligned} \quad (1.37)$$

320 Note that there are two coupling constants arising in $\mathcal{L}_{\text{EFT}}^t$, which is a residue of electroweak
 321 symmetry breaking. The massive Z boson will appear in both the Z_μ^0 field as well as the covariant
 322 derivative, leading to an extra Z-vertex.

323 The relations between the Wilson coefficients in (1.28) and the coupling strengths of the
 324 interactions in Equation 1.36 can be derived. The 14 effective operators are mapped onto 10
 325 free parameters providing a more minimal parametrisation of the anomalous interactions of the
 326 top quark.

$$\begin{aligned}
 \kappa_{tgq} f_{gq}^L &= \frac{\nu}{g_s \Lambda} [\bar{c}_{uG}]_{i3}^*, & \kappa_{tgq} f_{gq}^R &= \frac{\nu}{g_s \Lambda} [\bar{c}_{uG}]_{3i}, \\
 \kappa_{t\gamma q} f_{\gamma q}^L &= \frac{\nu}{g' \Lambda} [\cos \theta_W \bar{c}_{uB} - \sin \theta_W \bar{c}_{uW}]_{i3}^*, & \kappa_{t\gamma q} f_{\gamma q}^R &= \frac{\nu}{g' \Lambda} [\sin \theta_W \bar{c}_{uB} - \cos \theta_W \bar{c}_{uW}]_{3i}, \\
 \kappa_{tZq} f_{Zq}^L &= -\frac{2\cos \theta_W \nu}{g \Lambda} [\sin \theta_W \bar{c}_{uB} + \cos \theta_W \bar{c}_{uW}]_{i3}^*, & \kappa_{tZq} f_{Zq}^R &= -\frac{2\cos \theta_W \nu}{g \Lambda} [\cos \theta_W \bar{c}_{uB} + \sin \theta_W \bar{c}_{uW}]_{3i}, \\
 \zeta_{tZq} \tilde{f}_{Zq}^L &= -\frac{2\nu^2}{\Lambda^2} [(\bar{c}_{hq}^{(1)} - \bar{c}_{hq}^{(3)})_{i3} + (\bar{c}_{hq}^{(1)} - \bar{c}_{hq}^{(3)})_{3i}^*], & \zeta_{tZq} \tilde{f}_{Zq}^R &= -\frac{2\nu^2}{\Lambda^2} [(\bar{c}_{hu})_{i3} + (\bar{c}_{hu})_{3i}^*], \\
 \eta_{tHq} \hat{f}_{Hq}^L &= \frac{3\nu^2}{2\Lambda^2} [\bar{c}_{uh}]_{i3}^*, & \eta_{tHq} \hat{f}_{Hq}^R &= \frac{3\nu^2}{2\Lambda^2} [\bar{c}_{uh}]_{3i}.
 \end{aligned} \tag{1.38}$$

327 1.8 Experimental constraints on top-FCNC

Experiments commonly put limits on the branching fractions which allow an easier interpretation across different EFT models by use of the branching fraction

$$\mathcal{B}(t \rightarrow qX) = \frac{\delta_{txq}^2 \Gamma_{t \rightarrow qX}}{\Gamma_t}, \tag{1.39}$$

328 where $\Gamma_{t \rightarrow qX}$ represents the FCNC decay width⁵ for a coupling strength $\delta_{txq}^2 = 1$, and Γ_t the full
 329 decay width of the top quark. In the SM, supposing a top quark mass of 172.5 GeV, the full
 330 width becomes $\Gamma_t^{\text{SM}} = 1.32$ GeV [47].

331 Searches for top-FCNC usually adopt a search strategy depending on the experimental set-up
 332 and the FCNC interaction of interest, looking either for FCNC interactions in the production of a
 333 single top quark or in its decay for top quark pair interactions. In Figure 1.6, these two cases
 334 are shown for the tZq vertex.

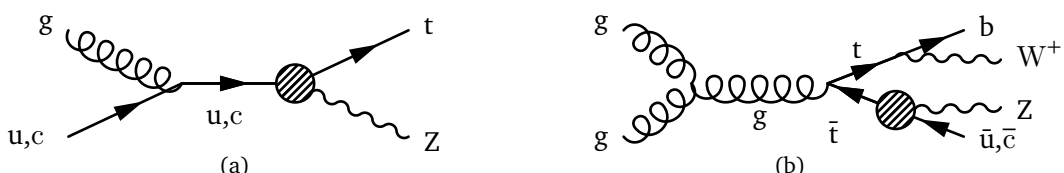


Figure 1.6: Feynman diagrams for the processes with a tZq FCNC interaction, where the FCNC interaction is indicated with the shaded dot. (a) Single top quark production through an FCNC interaction. (b) Top quark pair production with an FCNC induced decay.

⁵The decay width of a certain process represents the probability per unit time that a particle will decay. The total decay width, defined as the sum of all possible decay widths of a particle, is inversely proportional to its lifetime.

336 The observation of top-FCNC interactions has yet to come and experiments have so far only
 337 been able to put upper bounds on the branching fractions. An overview of the best current limits
 338 is given in [Table 1.8](#). In [Figure 1.7](#) a comparison is shown between the current best limits set by
 339 ATLAS and CMS with respect to several BSM model benchmark predictions. From there one can
 340 see that FCNC searches involving a Z or H boson are close to excluding or confirming several
 341 BSM theories. In [Figure 1.9](#), the searches performed by CMS are summarised. For the tZq
 342 vertex, the best limit from CMS comes from Ref. [41] where both single top quark and top quark
 343 pair are studied. The observed (expected) limits 95% CL at 8 TeV for the FCNC tZq interaction
 344 by CMS are $\mathcal{B}(t \rightarrow uZ) < 2.2 \times 10^{-4}$ (2.7×10^{-4}) and $\mathcal{B}(t \rightarrow cZ) < 4.9 \times 10^{-4}$ (12×10^{-4}). In
 345 [Figure 1.8](#), the summary of the 95% confidence level observed limits on the branching fractions
 346 of the top quark decays to a charm or up quark and a neutral boson is given, considering the
 results from the HERA, the LEP, the Tevatron, and the LHC.

Table 1.8: Overview of the most stringent observed and expected experimental limits on top-FCNC branching fractions \mathcal{B} at 95% confidence level.

Process	Search mode	Observed \mathcal{B}	Expected \mathcal{B}	Experiment	
$t \rightarrow uZ$	top quark pair decay	1.7×10^{-4}	2.4×10^{-4}	ATLAS	[40]
$t \rightarrow u\gamma$	single top quark production	1.3×10^{-4}	1.9×10^{-4}	CMS	[43]
$t \rightarrow ug$	single top quark production	4.0×10^{-5}	3.5×10^{-5}	ATLAS	[37]
$t \rightarrow uH$	top quark pair decay	2.4×10^{-3}	1.7×10^{-3}	ATLAS	[39]
$t \rightarrow cZ$	top quark pair decay	2.3×10^{-4}	3.2×10^{-4}	ATLAS	[40]
$t \rightarrow c\gamma$	single top quark production	2.0×10^{-3}	1.7×10^{-3}	CMS	[43]
$t \rightarrow cg$	single top quark production	2.0×10^{-4}	1.8×10^{-4}	ATLAS	[37]
$t \rightarrow cH$	top quark pair decay	2.2×10^{-3}	1.6×10^{-3}	CMS	[39]

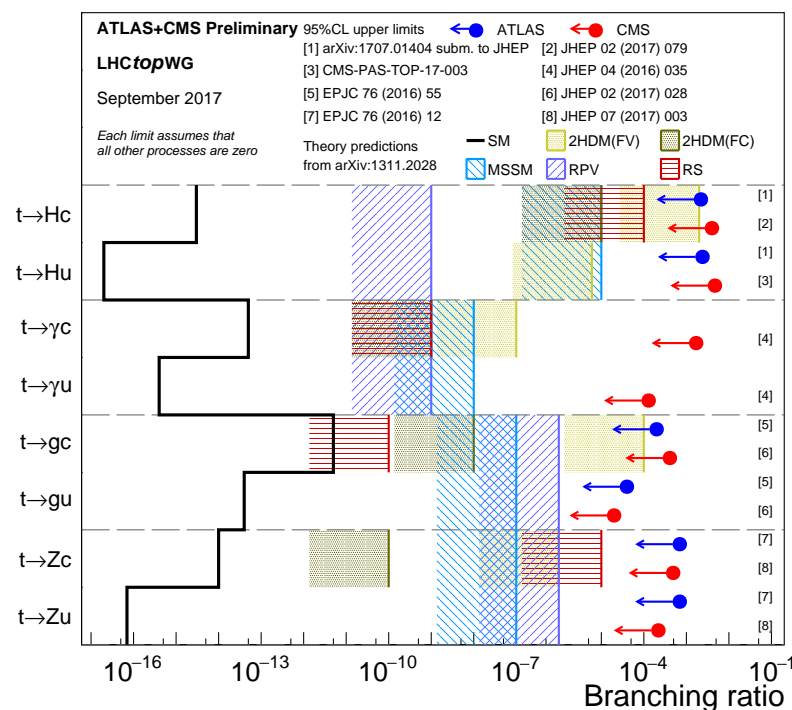


Figure 1.7: Current best limits set by CMS and ATLAS for top-FCNC interactions. Figure taken from [23]. (TO DO Remake with new atlas results)

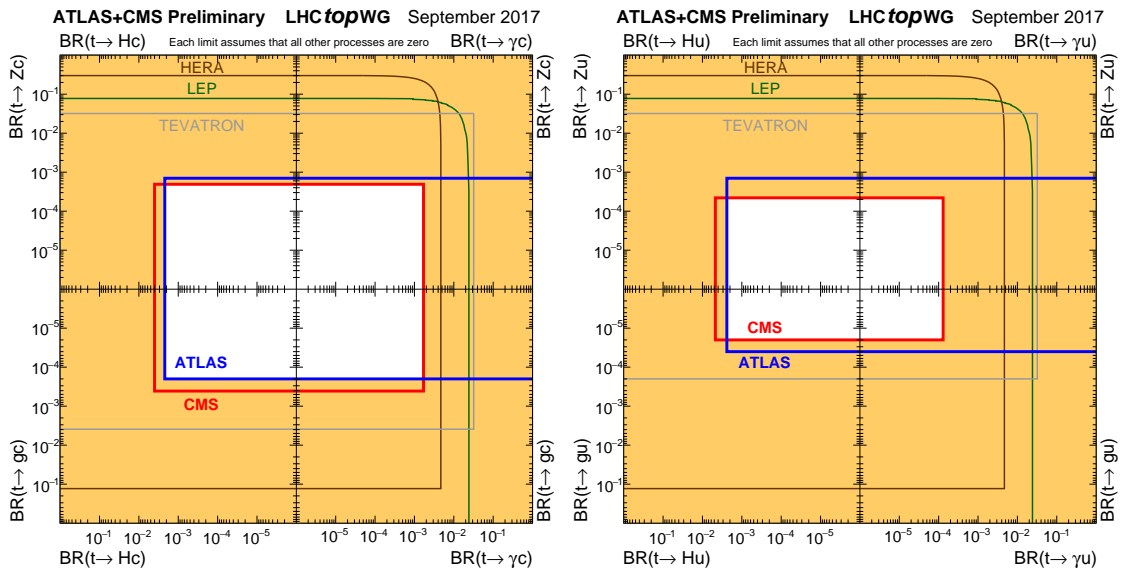


Figure 1.8: Summary of the current 95% confidence level observed limits on the branching fractions of the top quark decays via flavour changing neutral currents to a charm (left) or up (right) quark and a neutral boson. The coloured lines represent the results from HERA (the most stringent limits between the ones obtained by the H1 and ZEUS collaborations, in brown), LEP (combined ALEPH, DELPHI, L3 and OPAL collaborations result, in green), TEVATRON (the most stringent limits between the ones obtained by the CDF and D0 collaborations, in grey). The yellow area represents the region excluded by the ATLAS and the CMS Collaborations. Figure taken from [20].

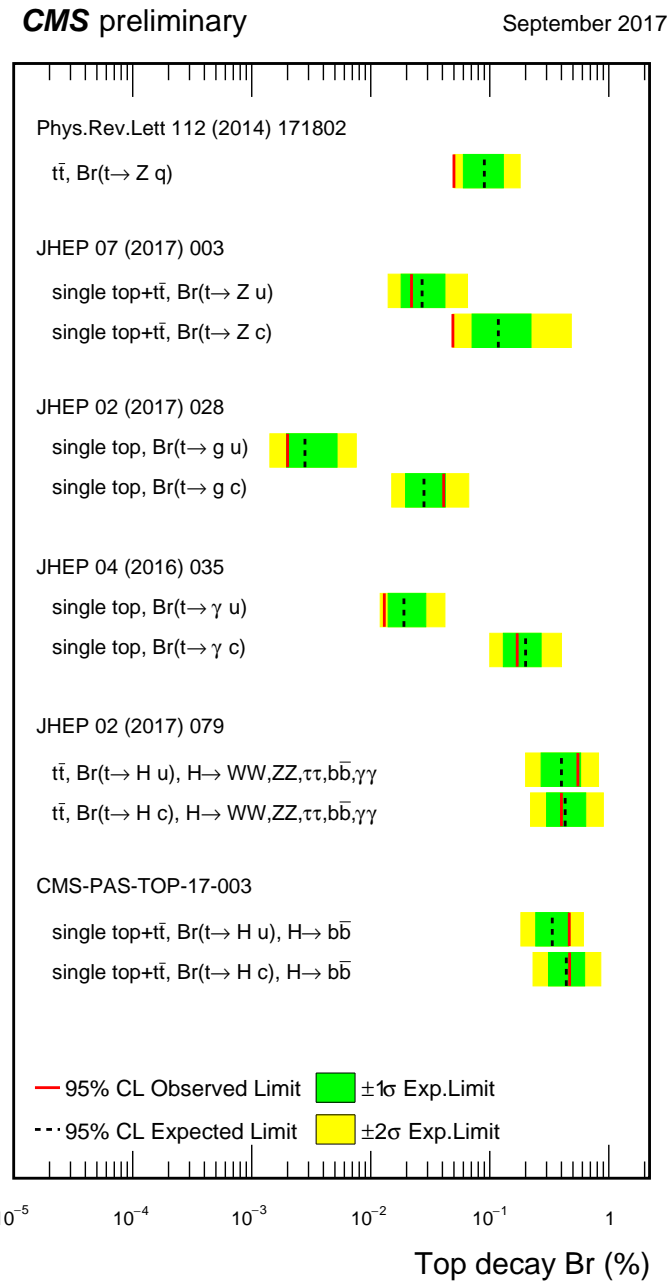


Figure 1.9: Summary of the FCNC branching fractions from CMS searches at 8 TeV. Figure taken from [23].

Experimental set-up

2

349 A key objective of the Large Hadron Collider (LHC) was the search for the Brout-Englert-Higgs
 350 boson. The Large Electron Positron (LEP) [48] and Tevatron [49] experiments established
 351 that the mass of the scalar boson has to be larger than 114 GeV [50, 51], and smaller than
 352 approximate 1 TeV due to unitarity and perturbativity constraints [52]. On top of this, the
 353 search for new physics such as supersymmetry or the understanding of dark matter were part
 354 of the motivation for building the LHC. Since the start of its operation, the LHC is pushing the
 355 boundaries of the Standard Model, putting the most stringent limits on physics beyond the
 356 Standard Model as well as precision measurements of the parameters of the Standard Model. A
 357 milestone of the LHC is the discovery of the scalar boson in 2012 by the two largest experiments
 358 at the LHC [10, 11].

359 This chapter is dedicated to the experimental set-up of the LHC and the Compact Muon
 360 Solenoid (CMS) experiment. Section 2.1 describes the LHC and its acceleration process for
 361 protons to reach their design energies. The CMS experiment and its components are presented
 362 in Section 2.2. The upgrades performed during the long shutdown in 2013 are discussed
 363 in Section 2.2.4. The data acquisition of CMS is presented in Section 2.2.3, while the CMS
 364 computing model is shown in Section 2.2.5.

365 **2.1 The Large Hadron Collider**

366 The LHC has started its era of cutting edge science on 10 September 2008 [53] after approval by
 367 the European Organisation of Nuclear Research (CERN) in 1995 [54]. Installed in the previous
 368 LEP tunnel, the LHC consists of a 26.7 km quasi ring, that is installed between 45 and 170 m
 369 under the French-Swiss border amidst Cessy (France) and Meyrin (Switzerland). Built to study
 370 rare physics phenomena at high energies, the LHC can accelerate mainly two types of particles,
 371 protons and lead ions Pb^{45+} , and provides collisions at four interaction points, where the particle
 372 bunches are crossing. Experiments for studying the collisions are installed at each interaction
 373 point.

374 As can be seen in Figure 2.1, the LHC is the last element in a chain that creates, injects and
 375 accelerates protons. The starting point is the ionisation of hydrogen, creating protons that are
 376 injected in a linear accelerator (LINAC 2). Here, the protons obtain an energy of 50 MeV. They

377 continue to the Proton Synchrotron Booster (PSB or Booster), where the packs of protons are
 378 accelerated to 1.4 GeV and each pack is split up in twelve bunches with 25 or 50 ns spacing.
 379 The Proton Synchrotron (PS) then increases their energy to 25 GeV before the Super Proton
 380 Synchrotron (SPS) increases the proton energy up to 450 GeV. Each accelerator ring expands in
 381 radius in order to reduce the energy loss of the protons by synchrotron radiation¹. Furthermore,
 382 the magnets responsible for the bending of the proton trajectories have to be strong enough
 383 to sustain the higher proton energy. Ultimately, the proton bunches are injected into opposite
 384 directions into the LHC, where they are accelerated to 3.5 TeV (in 2010 and 2011), 4 TeV (in
 2012 and 2013) or 6.5 TeV (in 2015 and 2016) [55].

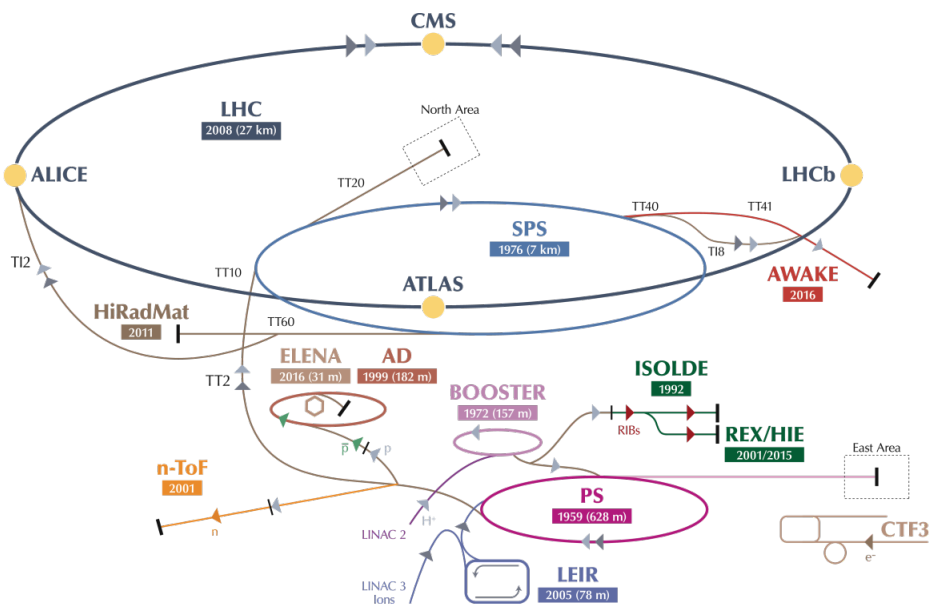


Figure 2.1: Schematic representation of the accelerator complex at CERN [56]. The LHC (dark blue) is the last element in chain of accelerators. Protons are successively accelerated by LINAC 2, the Booster, the Proton Synchrotron (PS) and the Super Proton Synchrotron (SPS) before entering the LHC.

385

386 In Figure 2.2 the LHC programme is shown. the first data collisions, so-called Run 1 period,
 387 lasted from 2008 until 16 February 2013 after which the CERN accelerator complex shut down
 388 for two years of planned maintenance and consolidation during so-called long shutdown 1
 389 (LS1). On 23 March 2015, the new data taking period known as Run 2 started. With a brief end
 390 of the year extended technical stop (EYETS). The main activities carried out during the EYETS
 391 were the maintenance of systems such as the cryogenics, the cooling, electrical systems, etc.;
 392 the replacement of the magnet, as well as a de-cabling and cabling campaign on the SPS. Run 2
 393 will last until July 2018 when the long shutdown 2 (LS2) will begin for 2 years. The main goal
 394 of this shutdown is the LHC injectors upgrade (LUI), but also maintenance and consolidation
 395 will be performed. Furthermore, preparations for the High Luminosity LHC, which will start in

¹This energy loss is proportional to the fourth power of the proton energy and inversely proportional to the bending radius.

396 2024, will be done. More information about phase 1 upgrades during LS1 and EYETS is given
 397 in [Section 2.2.4](#).

398 Before the start of the LHC in 2010, the previous energy record was held by the Tevatron collider
 399 at Fermilab, colliding protons with antiprotons at $\sqrt{s} = 1.96$ TeV. When completely filled, the
 LHC nominally contains 2220 bunches in Run 2, compared to 1380 in Run 1 (design: 2200).

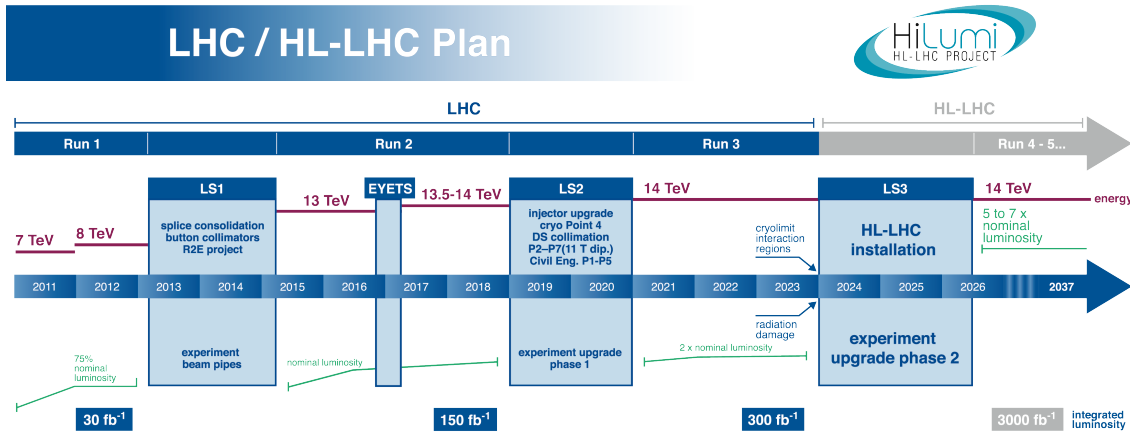


Figure 2.2: The HL-LHC timeline. Figure taken from [57].

400

401 Inside the LHC ring [58], the protons are accelerated by the means of radio frequency cavities,
 402 while 1232 dipole magnets of approximately 15 m long, each weighing 35 t ensure the deflection
 403 of the beams. The two proton beams circulate in opposite direction in separate pipes inside of
 404 the magnet. Through the use of a strong electric current in the coils of the magnet, magnetic
 405 fields are generated and cause the protons to bend in the required orbits. In order for the coil
 406 to become superconducting and able to produce a strong magnetic field of 8.3 T, the magnet
 407 structure is surrounded by a vessel. This vessel is filled with liquid Helium making it possible
 408 to cool down the magnet to 1.9 K. In order to get more focussed and stabilised proton beams,
 409 additional higher-order multipole and corrector magnets are placed along the LHC beam line.

410 The LHC is home to seven experiments, each located at an interaction point:

- 411 • A Toroidal LHC ApparatuS (ATLAS) [59] and the Compact Muon Solenoid (CMS) [60]
 412 experiments are the two general purpose detectors at the LHC. They both have a hermetic,
 413 cylindrical structure and were designed to search for new physics phenomena along with
 414 precision measurements of the Standard Model. The existence of two distinct experiments
 415 allows cross-confirmation of any discovery.
- 416 • A Large Ion Collider Experiment (ALICE) [61] and the LHC Beauty (LHCb) [62] experi-
 417 ments are focusing on specific phenomena. ALICE studies strongly interacting matter
 418 at extreme energy densities where a quark-gluon plasma forms in heavy ion collisions
 419 (Pb-Pb or p-Pb). LHCb searches for differences between matter and antimatter with the
 420 focus on b physics.

- The forward LHC (LHCf) [63] and the TOTal cross section, Elastic scattering and diffraction dissociation Measurement (TOTEM) [64] experiments are two smaller experiments that focus on head-on collisions. LHCf consists of two parts placed before and after ATLAS and studies particles created at very small angles. TOTEM is placed in the same cavern as CMS and measures the total proton-proton cross section and studies elastic and diffractive scattering.
- The Monopoles and Exotics Detector At the LHC (MoEDAL) [65] experiment is situated near LHCb and tries to find magnetic monopoles.

For the enhancement of the exploration of rare events and thus enhancing the number of collisions, high beam energies as well as high beam intensities are required. The luminosity [66] is a measurement of the number of collisions that can be produced in a detector per square meter and per second and is the key role player in this enhancement. The LHC collisions create a number of events per second given by

$$N_{\text{event}} = L\sigma_{\text{event}}, \quad (2.1)$$

where σ_{event} is the cross section of the process of interest and L the machine instantaneous luminosity. This luminosity depends only on the beam parameters and is for a Gaussian beam expressed as

$$L = \frac{1}{4\pi} N_b n_b f_{\text{rev}} \frac{N_b}{\epsilon_n} \left(1 + \left(\frac{\theta_c \sigma_z}{2\sigma^*} \right)^2 \right)^{-\frac{1}{2}} \frac{\gamma_r}{\beta^*}. \quad (2.2)$$

The number of particles per bunch is expressed by N_b , while n_b is the number of bunches per beam, f_{rev} the revolution frequency, γ_r the relativistic gamma factor, ϵ_n the normalized transverse beam emittance - a quality for the confinement of the beam, β^* the beta function at the collision point - a measurement for the width of the beam, θ_c the angle between two beams at the interaction point, σ_z the mean length of one bunch, and σ^* the mean height of one bunch. In Equation 2.2, the blue part represents the stream of particles, the red part the brilliance, and the green part the geometric reduction factor due to the crossing angle at the interaction point.

The peak design luminosity for the LHC is $10^{34} \text{ cm}^{-2}\text{s}^{-1}$, which leads to about 1 billion proton interactions per second. In 2016, the LHC was around 10% above this design luminosity [67]. The luminosity is not a constant in time since it diminishes due to collisions between the beams, and the interaction of the protons and the particle gas that is trapped in the centre of the vacuum tubes due to the magnetic field. The diffusion of the beam degrades the emittance and therefore also the luminosity. For this reason, the mean lifetime of a beam inside the LHC is around 15 h. The integrated luminosity - the luminosity provided in a certain time range - recorded by CMS and ATLAS over the year 2016 is given in Figure 2.3. In Run 2, the peak luminosity is $13\text{-}17 \times 10^{33} \text{ cm}^{-2}\text{s}^{-1}$ compared to $7.7 \times 10^{33} \text{ cm}^{-2}\text{s}^{-1}$ in Run 1. The recorded luminosity is validated for physics analysis keeping 35.9 fb^{-1} during 2016 data taking.

Multiple proton-proton interactions can occur during one bunch crossing, referred to as pileup. On average, the number of pileup events is proportional to the luminosity times the total inelastic proton-proton cross section. In 2016, an average of about 27 of pileup interactions has been observed in 13 TeV proton collisions at the interaction point of CMS. For 2012, this number was about 21 pileup interactions for 8 TeV collisions.

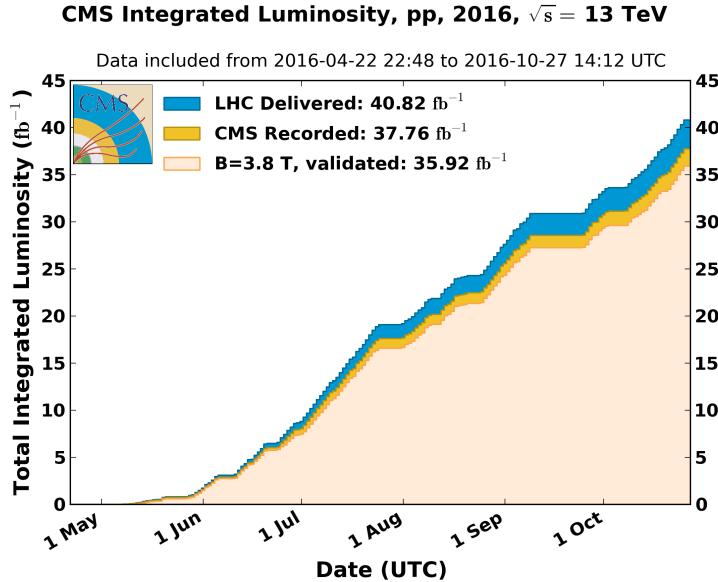


Figure 2.3: Cumulative off-line luminosity measured versus day delivered by the LHC (blue), and recorded by CMS (orange), and certified as good physics analysis during stable beams (light orange) during stable beams and for proton collisions at 13 TeV centre-of-mass energy in 2016. [68].

451 2.2 The Compact Muon Solenoid

452 At one of the collision points of the LHC, the CMS detector [69–71] is placed. Weighing 14 000 t,
453 this cylindrical detector is about 28.7 m long and 15 m in diameter. It has an onion like structure
454 of several specialised detectors and contains a superconducting solenoid with a magnetic field of
455 3.8 T. Living in a hadronic environment, multi-jet processes produced by the strong interaction
456 are the main source of background for rare physics processes. Therefore, good identification,
457 momentum resolution, and charge determination of muons, electrons and photons are one of
458 the main goals of the CMS detector. Additionally, a good charged particle momentum resolution
459 and reconstruction efficiency in the inner tracker provides identification for jets coming from b
460 quarks or tau particles. Also the electromagnetic resolution for an efficient photon and lepton
461 isolation as well as a good hadronic calorimeter for the missing transverse energy² were kept
462 into account while designing CMS. In Figure 2.4, an overview of the CMS detector is shown.

463 2.2.1 CMS coordinate system

The coordinate system used by CMS can be found in Figure 2.5. The origin of the right handed orthogonal coordinate system is chosen to be the point of collisions. The x-axis points towards the centre of the LHC ring such that the y-axis points towards the sky, and the z-axis lies tangent to the beam axis. Since the experiment has a cylindrical shape, customary coordinates are used to describe the momentum \vec{p} : the distance $p = |\vec{p}|$, the azimuthal angle³ $\phi \in [-\pi, \pi]$, the

²The missing transverse energy comes from an imbalance in the transverse plane. This will be discussed in Chapter 4.

³The azimuthal angle is the angle between the x-axis and the projection in the transverse plane of the momentum \vec{p} , denoted as \vec{p}_T .

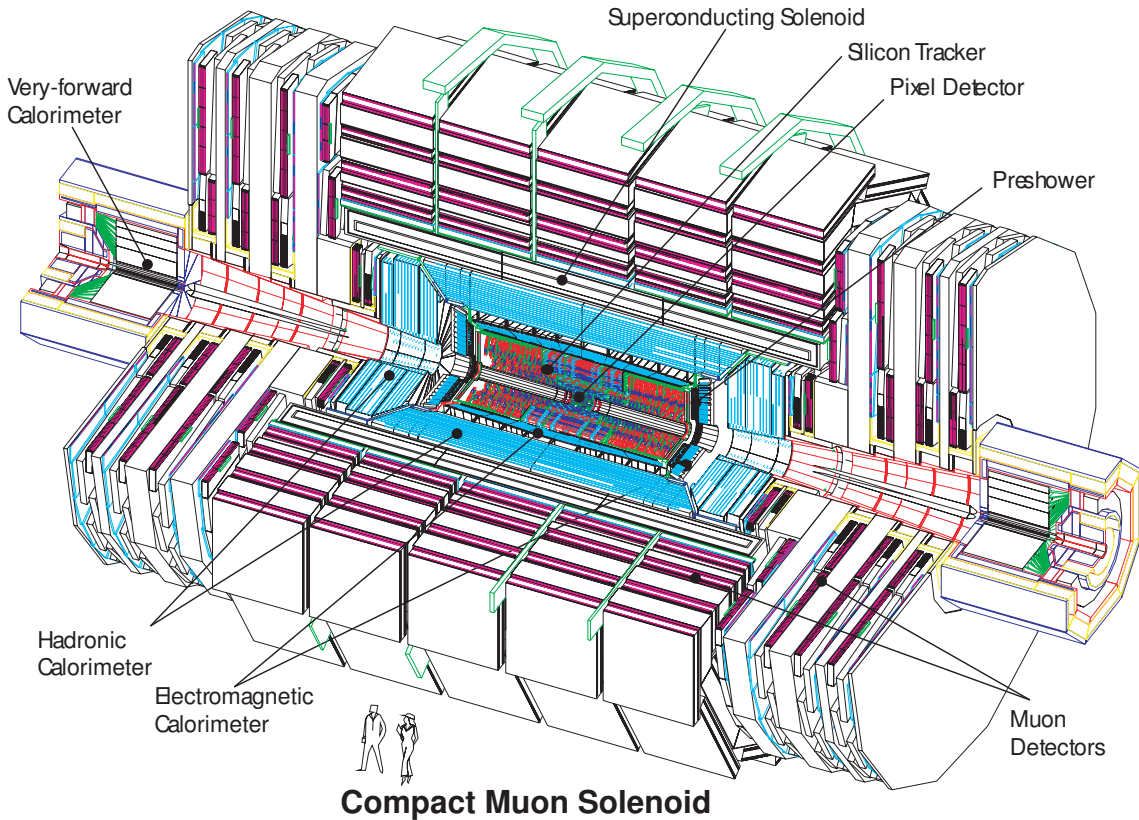


Figure 2.4: Mechanical layout of the CMS detector. Figure taken from [72].

pseudo-rapidity⁴ η :

$$\eta = -\ln \left(\tan \left(\frac{\theta}{2} \right) \right). \quad (2.3)$$

For the energies considered at the LHC, where $E \gg m$, the pseudo-rapidity is a good approximation of the rapidity y

$$y = \frac{1}{2} \ln \left(\frac{E + p_z}{E - p_z} \right), \quad (2.4)$$

⁴⁶⁴ where the difference of rapidities of two particles is invariant under a Lorentz boost in the
⁴⁶⁵ z-direction.

466 2.2.2 Towards the heart of CMS

⁴⁶⁷ The CMS detector can be divided into two parts. A central barrel is placed around the beam
⁴⁶⁸ pipe ($|\eta| < 1.4$), and two plugs (endcaps) ensure the hermeticity of the detector. In [Figure 2.4](#)
⁴⁶⁹ and [Figure 2.6](#) the onion like structure of the CMS detector is visible. The choice of a solenoid
⁴⁷⁰ of 12.9 m long and 5.9 m diameter gives the advantage of bending the particle trajectories in the

⁴The pseudo rapidity is expressed by the polar angle θ between the direction of \vec{p} and the beam.

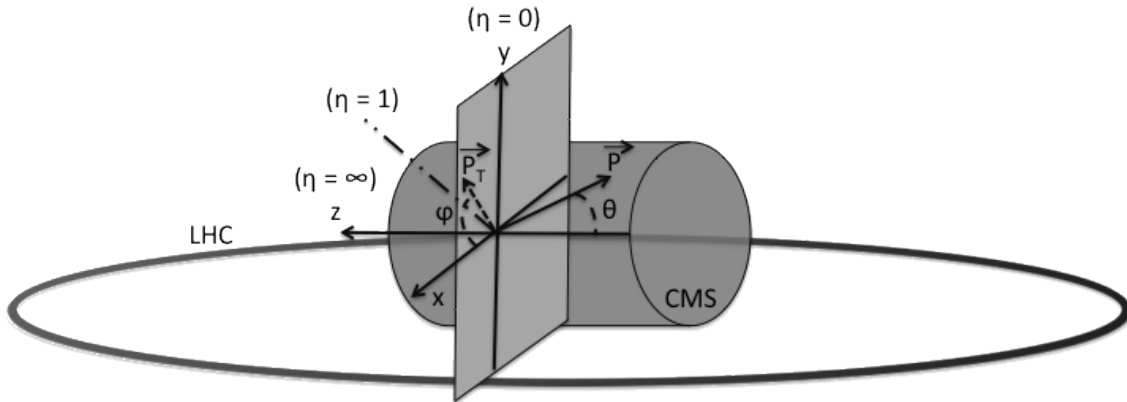


Figure 2.5: Representation of the coordinate system used by CMS. The point of origin is put at the collision point. The x-axis points towards the centre of the LHC ring such that the z-axis lies tangent to the beam axis.

471 transverse plane. The hadronic calorimeter (Section 2.2.2.3), the electromagnetic calorimeter
 472 (Section 2.2.2.4) and the tracker (Section 2.2.2.5) are within the solenoid (Section 2.2.2.2),
 473 while the muon chambers (Section 2.2.2.1) are placed outside the solenoid. The data used for
 474 the search presented in this thesis is collected after the long shutdown 1. After discussing each
 475 part of CMS in their Run 1 configuration, Section 2.2.4 elaborates on their different upgrades
 476 for the data collected in Run 2.

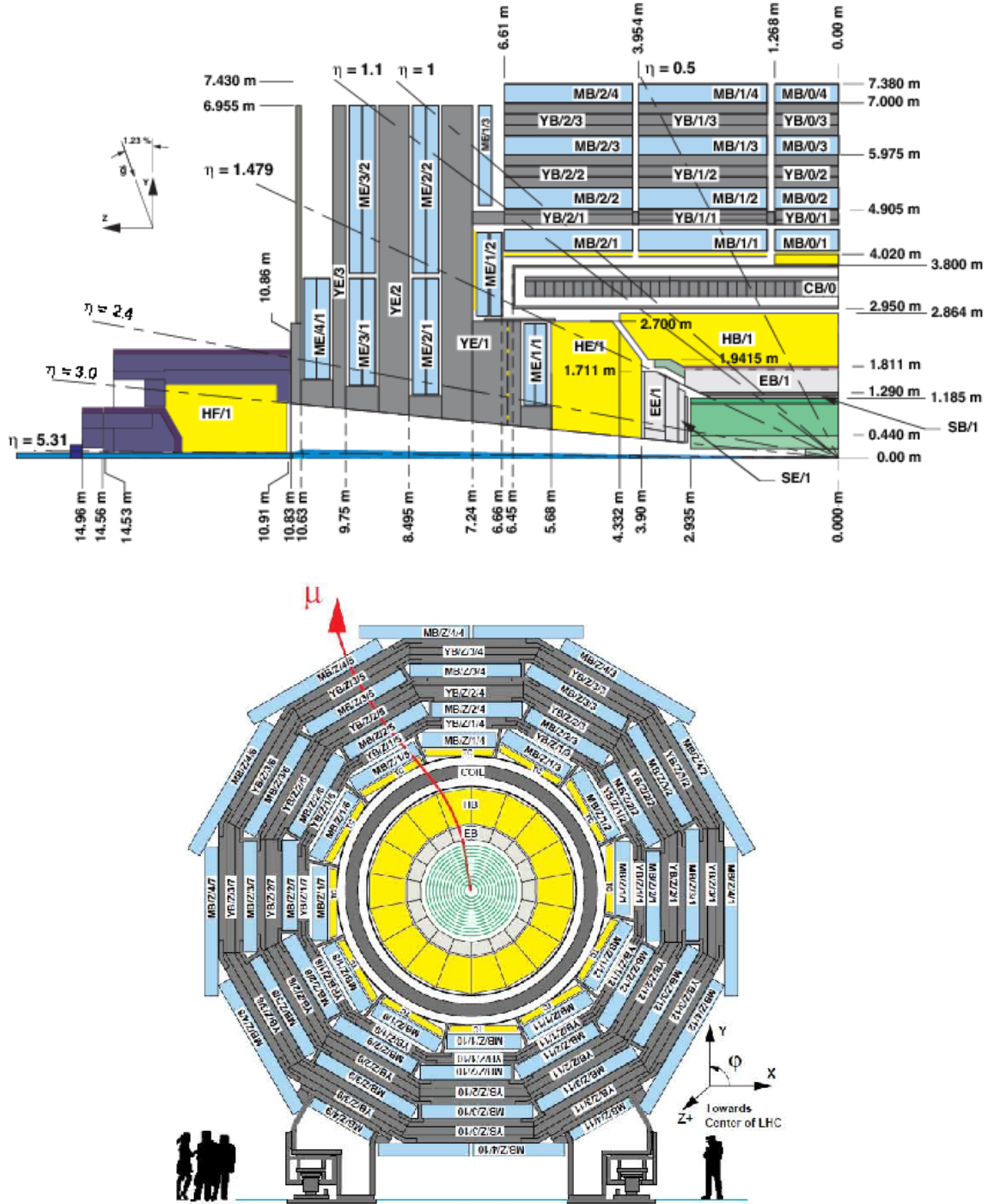


Figure 2.6: Schematic view of the CMS detector in the Run 1 configuration. The longitudinal view of one quarter of the detector is given at the top, while the transversal view is shown at the bottom. The muon system barrel elements are denoted as $MBZ/N/S$, where $Z = -2 \dots +2$ is the barrel wheel number, $N = 1 \dots 4$ the station number and $S = 1 \dots 12$ the sector number. Similarly, the steel return yokes are denoted as $YBZ/N/S$. The solenoid is denoted as $CB0$, while the hadronic calorimeter is denoted as HE (endcap)/ HB (barrel)/ HF (forward) and the electromagnetic calorimeter as EE (endcap)/ EB (barrel). The green part represents the tracking system (tracker + pixel). Figure taken from [73].

477 **2.2.2.1 Muon system**

478 The outermost part of CMS consists of the muon system. The magnet return yoke is interleaved
 479 with gaseous detector chambers for muon identification and momentum measurement. The
 480 barrel contains muon stations arranged in five separate iron wheels, while in the endcap four
 481 muon stations are mounted onto three independent iron discs on each side. Each barrel wheel
 482 has 12 sectors in the azimuthal angle.

483 The muon system is divided into three parts, shown in [Figure 2.7](#). The muon rate and neutron
 484 induced backgrounds are small and the magnetic field is very low for the barrel, thus CMS can
 485 use drift tube (DT) chambers. For the endcaps however, the muon and background flux is much
 486 higher and there is a need to use cathode strip chambers (CSC) which are able to provide a
 487 faster response, higher granularity and have a better resistance against radiation. In order to
 488 form a redundant trigger system, resistive plate chambers (RPC) are added. This makes a total
 of 250 DT, 540 CSC and 610 RPC chambers. In [Figure 2.6](#) the arrangement is shown.

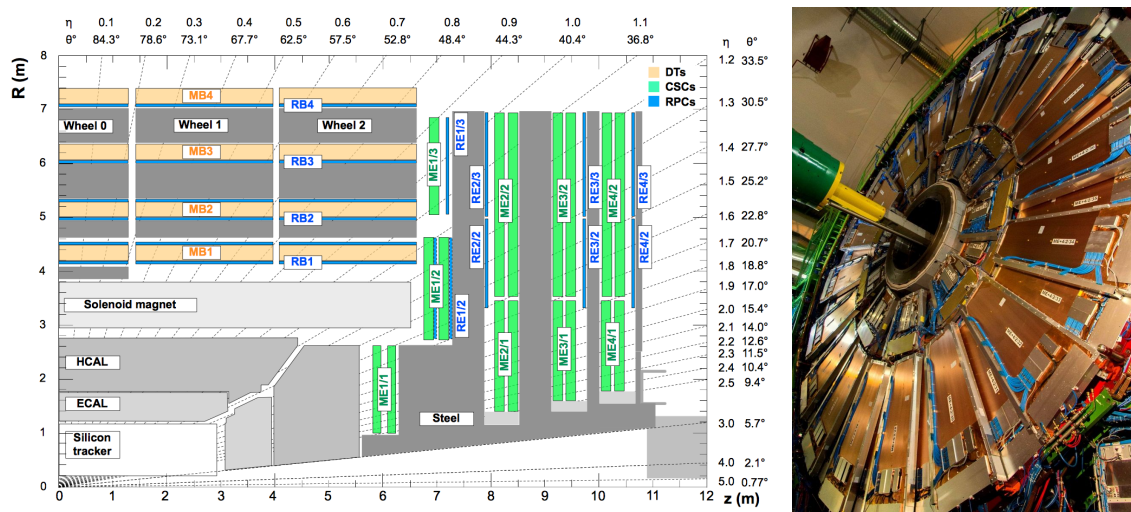


Figure 2.7: (Left) Schematic view of one quarter of the CMS muon system in the Run 1 configuration. The cathode strip chambers (CSC) are shown in green, the drift tubes (DT) are shown in yellow, while the resistive plate chambers (RPC) are shown in blue. Figure taken from [73]. (Right) Cathode strip chambers (ME+4/2 chambers on YE+3). Photo taken from [74].

489

490 Providing a measurement for $|\eta| < 1.2$, the DT chambers in the barrel are on average $2 \times 2.5\text{m}^2$
 491 in size and consist of 12 layers of DT cells⁵ arranged in three groups of four. The $r\phi$ coordinate is
 492 provided by the two outside groups, while the middle group measures the z coordinate. For the
 493 outer muon station, the DT chambers contain only 8 layers of DT cells, providing a muon position
 494 in the $r\phi$ plane. There are four CSC stations in each endcap, providing muon measurements for
 495 $0.9 < |\eta| < 2.4$ (Run 1 configuration). These CSCs are multi-wired proportional chambers that
 496 consist of 6 anode wire planes crossed by 7 copper strips cathode panels in a gas volume. The
 497 r coordinate is provided by the copper strips, while the ϕ coordinate comes from the anode
 498 wires, giving a two dimensional position measurement. There are six layers of RPCs in the

⁵The DT cells are 4 cm wide gas tubes with positively charged stretched wires inside.

499 barrel muon system and one layer into each of the first three stations of the endcap. They are
 500 made from two high resistive plastic plates with an applied voltage and separated by a gas
 501 volume. Read-out strips mounted on top of the plastic plates detect the signal generated by a
 502 muon passing through the gas volume. The RPCs provide a fast response with a time resolution
 503 of 1 ns and cover a range of $|\eta| < 1.8$ for the Run 1 configuration.

504 The muon system provides triggering on muons, identifying muons and improves the momen-
 505 tum measurement and charge determination of high p_T muons. On top of the muon system,
 506 a fraction of the muon energy is deposited in the electromagnetic calorimeter, the hadronic
 507 calorimeter, and outer calorimeter. The high magnetic field enables an efficient first level trigger
 508 and allows a good momentum resolution of $\Delta p/p \approx 1\%$ for a p_T of 100 GeV and $\approx 10\%$ for a
 509 p_T of 1 TeV. There is an efficient muon measurement up to $|\eta| < 2.4$.

510 2.2.2.2 Solenoid

511 Making use of the knowledge of previous experiments like ALEPH and DELPHI at LEP and H1
 512 at HERA, CMS chose for a large super conducting solenoid with a length of 12.9 m and a
 513 inner bore of 5.9 m [71]. With 2168 turns, a current of 18.5 kA resulting in a magnetic field of
 514 3.8 T, and a total energy of 2.7 GJ, a large bending power can be obtained for a modestly-sized
 515 solenoid. In order to ensure a good momentum resolution in the forward regions, a favourable
 516 length/radius was necessary. In [Figure 2.8](#), a photo of the CMS solenoid is shown.

517 The solenoid uses a high-purity aluminium stabilised conductor with indirect cooling from
 518 liquid helium, together with full epoxy impregnation. A four-layer winding is implemented that
 519 can withstand an outward pressure of 64 atm. The NbTi cable is co-extruded by pure aluminium
 520 that acts as a thermal stabilizer and has an aluminium alloy for mechanical reinforcement. The
 521 return of the magnetic field is done by five wheels, noted by YB in [Figure 2.6](#).

522 2.2.2.3 Hadronic calorimeter

523 The hadronic calorimeter (HCAL) is dedicated to precisely measure the energy of charged and
 524 neutral hadrons via a succession of absorbers and scintillators. This makes it crucial for physics
 525 analyses with hadronic jets or missing transverse energy. The HCAL barrel extends between
 526 $1.77 < r < 2.95$ m, where r is the radius in the transverse plane with respect to the beam. Due
 527 to space limitations, the HCAL needs to be as small as possible and is made from materials
 528 with short interaction lengths⁶. On top of this, the HCAL should be as hermetic as possible and
 529 extend to large absolute pseudo rapidities such that it can provide a good measurement of the
 530 missing transverse energy.

531 The quality of the energy measurements is dependent on the fraction of the hadronic shower
 532 that can be detected. Therefore, the HCAL barrel (HB) inside the solenoid is reinforced by an
 533 outer hadronic calorimeter between the solenoid and muon detectors (HO, see [Figure 2.9](#)), using
 534 the solenoid as extra absorber. This increases the thickness to 12 interaction lengths. The HB

⁶Here the interaction length is the nuclear interaction length and this is the length needed for absorbing 36.7% of the relativistic charged particles. For the electromagnetic calorimeter this is defined in radiation length X_0 . The radiation length is the mean distance over which a high energy electron loses all but $1/e$ of its energy by bremsstrahlung.

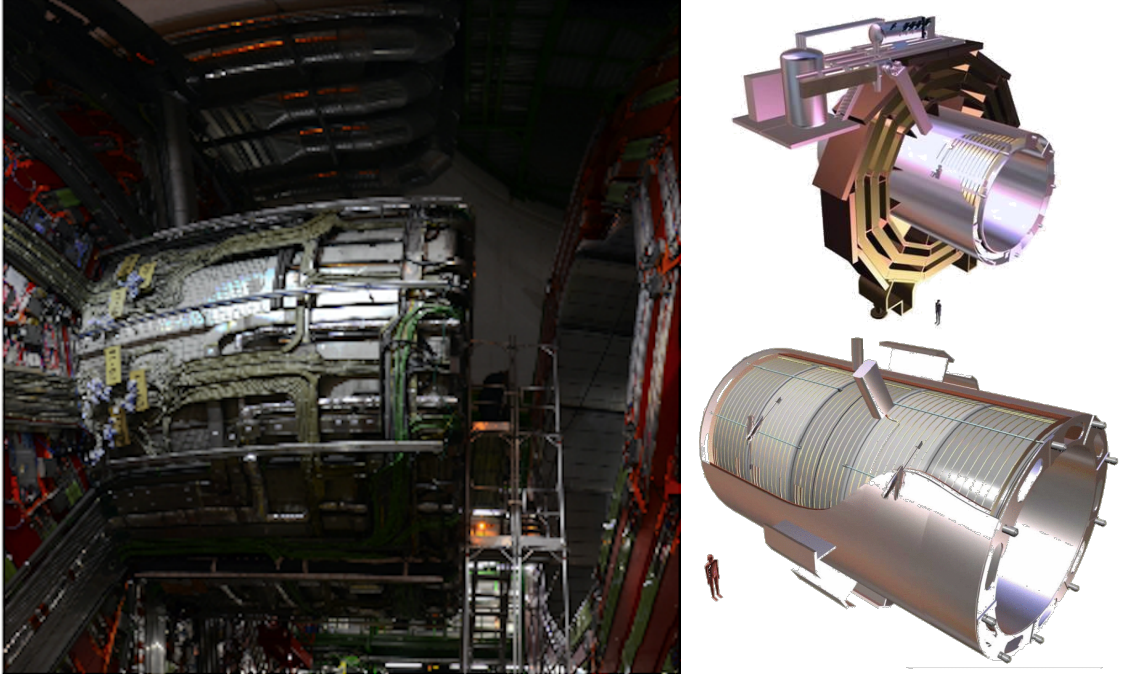


Figure 2.8: (Left) CMS solenoid during the long shutdown in 2013. (Right) An impression of the solenoid magnet taken from [75].

535 and HO provide measurements for $|\eta| < 1.3$, while an endcap on each side (HE, $1.3 < |\eta| < 3$)
 536 and a forward calorimeter (HF, $3.0 < |\eta| < 5.2$) extend the pseudo rapidity range.

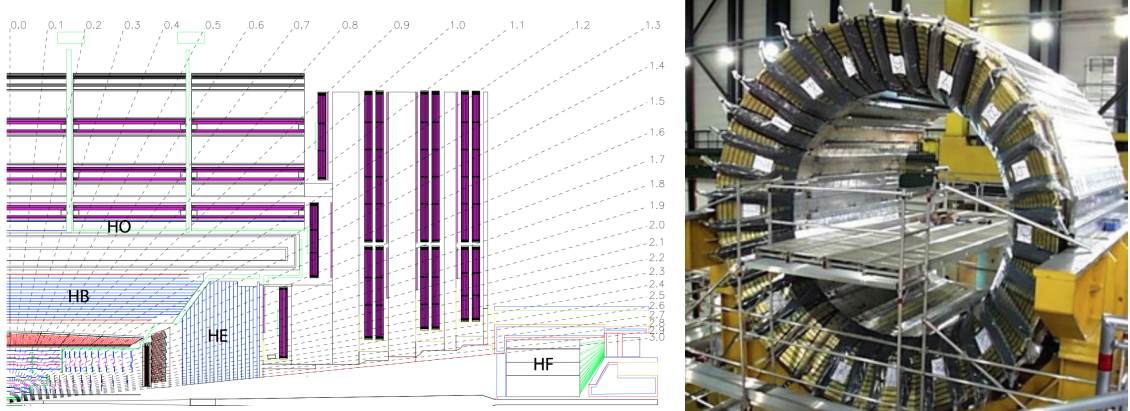


Figure 2.9: (Left) Longitudinal view of the CMS detector showing the locations of the HB, HE, HO, and HF calorimeters. Figure taken from [60]. (Right) CMS barrel calorimeter. Photo taken from [76].

537 The HB is made of 16 absorber plates where most of them are built from brass and others are
 538 made from stainless steel and is about five to ten interaction lengths thick. It is divided in $\eta \times \phi$
 539 towers and contains 2592 read-out channels. The HO complements the HB and extends the
 540 reach up to twelve interaction lengths. This subsystem contains 2160 read-out channels. The
 541 HE is also composed of brass absorber plates and has a thickness corresponding to approximately

ten interaction lengths, with 2592 read-out channels. The HF experiences intense particle fluxes with an expected energy of 760 GeV deposited on average in a proton interaction at a centre-of-mass of 14 TeV, compared to 100 GeV in the rest of the detector. Therefore, these are Cherenkov light detectors made of radiation hard quartz fibres. The main causes of such large energy events are high energy muons and charged particles from late showering hadrons. During Run 1, it became clear that the glass windows of the photon multiplier tubes (PMTs) had to be replaced, which was done during LS1 [77]. The HF represents 1728 read-out channels.

The HCAL and electromagnetic calorimeter combined, can measure the hadron energy with a resolution $\Delta E/E \approx 100\% \sqrt{E[\text{GeV}]} + 5\%$.

2.2.2.4 Electromagnetic calorimeter

The electromagnetic calorimeter (ECAL) is designed to measure the energy of photons and electrons and covers $|\eta| < 3$. It is an hermetic, homogeneous detector and consists of 75 848 lead tungstate (PbWO_4) crystals. These crystals have a fast response time - 80% of the light is emitted within 25 ns- and are radiation hard. The electromagnetic showers produced by passing electrons or photons, ionize the crystal atoms which emit a blue-green scintillation light, that is collected by silicon avalanche photodiodes (APDs) in the barrel and vacuum phototriodes (VPTs) in the endcaps. The crystals and the APD response are sensitive to temperature changes and require a stable temperature.

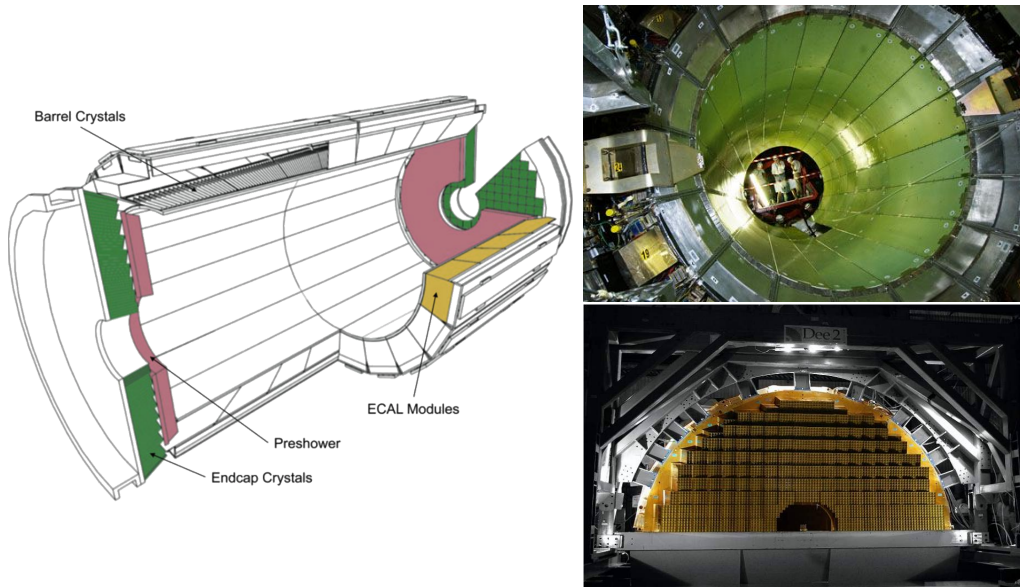


Figure 2.10: (Left) Schematic cross section of the electromagnetic calorimeter taken from [60]. (Right top) The ECAL barrel during construction [78]. (Right bottom) One half of an EE [79].

There are three parts: a central barrel (EB), an endcap region (EE) and a preshower (ES) (Figure 2.10). The EB has an inner radius of 129 cm and corresponds to a pseudo rapidity of $0 < |\eta| < 1.479$. At a distance of 314 cm from the vertex and covering a pseudo rapidity of $1.479 < |\eta| < 3.0$, are the EE. They consist of semi-circular aluminium plates from which structural units of 5×5 crystals (super crystals) are supported. The ES is placed in front of

565 the crystal calorimeter over the endcap pseudo rapidity range with two planes of silicon strip
 566 detectors as active elements.

The electromagnetic shower will typically involve more than one channel. More than 90% of the energy of a 35 GeV electron or photon is contained in a 5×5 matrix of crystals. Therefore, a clustering algorithm is performed in order to associate the energy deposits to the particles impinging the calorimeter. The achieved precision [80] for the barrel is 2×10^{-3} rad in ϕ and 10^{-3} in η . For the endcaps this is 5×10^{-3} rad in ϕ and 2×10^{-3} in η . The energy is reconstructed by a supercluster algorithm, taking into account energy radiated via bremsstrahlung or conversion [60]. The energy resolution is given by

$$\frac{\sigma(E)}{E} = \frac{2.8\%}{\sqrt{E}} \oplus \frac{0.128}{E(\text{GeV})} \oplus 0.3\%, \quad (2.5)$$

567 in the absence of a magnetic field, where the contributions come from the stochastic, noise and
 568 constant terms respectively. The dominating term is the constant term ($E_{\text{shower}} \approx 100$ GeV)
 569 and thus the performance is highly dependent on the quality of calibration and monitoring.

570 2.2.2.5 Inner tracking system and operations

571 The tracking system (tracker) [81] is the detecting unit closest to the point of interaction.
 572 Responsible for the reconstruction of trajectories from charged particles with $|\eta| < 2.5$ that
 573 are bent by the magnetic field, it provides a measurement of the momentum. The tracker is
 574 also responsible for the determination of the interaction point or vertex. It should be able to
 575 provide high granularity as well as fast read-out, and be able to endure high radiation. For
 576 these reasons, the CMS collaboration chose silicon detector technology.

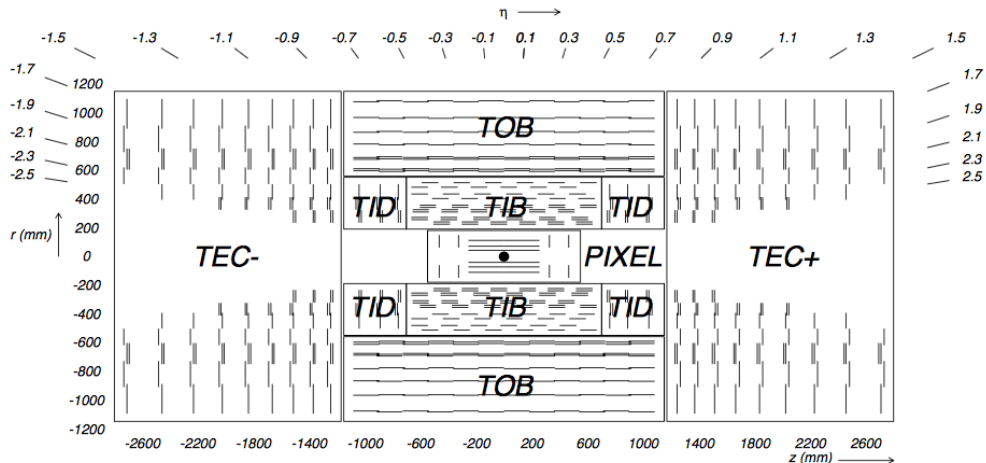


Figure 2.11: Schematic cross section through the CMS tracker. Each line represents a detector module. Double lines indicate back-to-back modules that deliver stereo hits. Figure taken from [60].

577 The tracking system consists of a cylinder of 5.8 m long and 2.5 m in diameter. It is immersed
 578 in a co-axial magnetic field of 3.8 T provided by the solenoid. As shown in Figure 2.11, the
 579 tracker is built up from a large silicon strip tracker with a small silicon pixel tracker inside. The

580 inner pixel region ($4.4 < r < 10.2$ cm), gets the highest flux of particles. Therefore, pixel silicon
 581 sensors of $100 \times 150 \mu\text{m}^2$ are used. It consists of three cylindrical barrels that are complemented
 582 by two discs of pixel modules at each side. The silicon strip tracker ($20 < r < 116$ cm) has three
 583 subdivisions. The Tracker Inner Barrel and Discs (TIB, TID, see [Figure 2.13](#)) are composed
 584 of four barrel layers accompanied by three discs at each end. The outer part of the tracker -
 585 Tracker Outer Barrel (TOB) - consists of 6 barrel layers. In the outer discs, there are nine discs
 586 of silicon sensors, referred to as Tracker End Caps (TEC).



Figure 2.12: The pixel barrel being re-installed after the Long Shutdown in 2015, around the beam pipe at CMS [82].



Figure 2.13: First half of the inner tracker barrel, consisting of three layers of silicon modules [83].

587 The pixel detector, shown in [Figure 2.12](#), has 1440 modules that cover an area of about 1 m^2
 588 and have 66 million pixels. It provides a three-dimensional position measurement of the hits
 589 arising from the interaction from charged particles with the sensors. In transverse coordinate
 590 ($r\phi$), the hit position resolution is about $10 \mu\text{m}$, while $20\text{-}40 \mu\text{m}$ is obtained in the longitudinal
 591 coordinate (z). The sensor plane position provides the third coordinate. The TIB/TID, shown in
 592 [Figure 2.13](#), delivers up to four $r\phi$ -measurements using $320 \mu\text{m}$ thick silicon micro-strip sensors.
 593 These sensors are placed with their strips parallel to the beam axis in the barrel and radial
 594 in the discs. In the TIB, the first two layers have a strip pitch of $80 \mu\text{m}$, while the remaining
 595 two have a strip pitch of $120 \mu\text{m}$. This leads to a respective single point resolution of $23 \mu\text{m}$
 596 and $35 \mu\text{m}$. For the TID, the pitch varies between $100 \mu\text{m}$ and $141 \mu\text{m}$. The TOB provides six
 597 $r\phi$ -measurements with a single point resolution of $53 \mu\text{m}$ in the first four layers, and $35 \mu\text{m}$ in
 598 the last two layers. It consists of $500 \mu\text{m}$ thick microstrip sensors with strip pitches of $183 \mu\text{m}$
 599 (first 4 layers) or $122 \mu\text{m}$ (last two layers). The TEC provides up to 9 ϕ -measurements via 9
 600 discs consisting of up to 7 rings of silicon microstrip sensors of $97 \mu\text{m}$ to $184 \mu\text{m}$ average pitch.

601 A second co-ordinate measurement (z in the barrel, r on the discs) is provided through the
 602 use of a second micro strip detector module mounted back-to-back with a stereo angle of 100
 603 mrad. This is done on the modules in the first two layers and rings of the TIB, TID, and TOB, as
 604 well as rings 1,2, and 5 of the TECs (blue line in [Figure 2.11](#)). The resolution in the z direction
 605 is approximately $230 \mu\text{m}$ in the TIB and $530 \mu\text{m}$ in the TOB, and is varying with pitch in the
 606 TID and TEC. To allow overlay and avoid gaps in acceptance, each module is shifted slightly
 607 in r or z with respect to its neighbouring modules within a layer. With this detector lay-out,
 608 at least nine points per charged particle trajectory can be measured in an $|\eta|$ range up to 2.4,
 609 where at least four of them being two dimensional. The CMS silicon tracker provides 9.3 million
 610 read-out channels and covers an active area of about 198 m^2 .

611 **2.2.3 Data acquisition**

612 At a design luminosity of $10^{34} \text{ cm}^{-2}\text{s}^{-1}$, the proton interaction rate exceeds 1 GHz. Given the
 613 large size of an event (about 1 MB), the high crossing rate, and that typically tens of collisions
 614 happen at the same time, it is impossible for the CMS experiment to store all the data generated.
 615 In order to deal with the large amount of data, a two level trigger system has been put in place.
 616 The first level (Level-1) is a custom hardware system, while a second high level trigger (HLT) is
 617 software based, running on a large farm of computers.

618 **CMS Level-1 Trigger**

619 The Level-1 Trigger has to be a flexible, maintainable system, capable of adapting to the
 620 evolving physics programme of CMS [84]. Its output rate is restricted to 100 kHz imposed
 621 by the CMS read-out electronics. It is implemented by custom hardware and selects events
 622 containing candidate objects - e.g. ionization deposits consistent with a muon, or energy clusters
 623 corresponding to an electron / photon / tau lepton / missing transverse energy / jet. Collisions
 624 with large momenta can be selected with the use of the scalar sum of the transverse momenta
 625 of the jets.

626 By buffering the raw data from the CMS subdetectors in front-end drivers, the Level-1 Trigger
 627 has a pipeline memory of 3.2 μs to decide whether to keep an event or reject it. The trigger
 628 primitives (TP) from the calorimeters and muon detectors are processed in several steps and
 629 combined into a global trigger. This information is then combined with the input from the other
 630 subsystems for the HLT. The separate inputs are synchronized to each other and the LHC orbit
 631 clock and sent to the global trigger module. Here, Level-1 Trigger algorithms are performed
 632 within 1 μs to decide whether to keep the event.

633 **CMS HLT Trigger**

634 The HLT is an array of commercially available computers with a programmable menu that has
 635 an output rate of on average 400 Hz for off-line event storage. The data processing is based on
 636 an HLT path. This is a set of algorithmic steps to reconstruct objects to define selection criteria.
 637 Here, the information of all subdetectors can be used to perform algorithms on higher level
 638 reconstructed objects.

639 **2.2.4 Phase 1 upgrades**

640 Before the start of taking collision data for 13 TeV operations on 3 June 2015, CMS had a
 641 long shutdown (LS1) [85]. During this shutdown, the section of the beryllium beam pipe
 642 within CMS was replaced by a narrower one. This operation required the pixel detector to be
 643 removed and reinserted into CMS. During Run 2, higher particle fluxes with respect to Run
 644 1 are expected. To avoid longterm damage caused by the intense particle flux at the heart of
 645 CMS, the tracker has been made ready to operate at much lower temperature than during Run
 646 1. The electromagnetic calorimeter preshower system was damaged during Run 1, therefore the
 647 preshower discs were removed, repaired and reinstalled successfully inside CMS in 2014. To
 648 help the discrimination between interesting low momentum muons coming from collisions and
 649 muons caused by backgrounds, a fourth triggering and measurement station for muons was

added in each of the endcaps. Several new detectors were installed into CMS for measuring the collision rate within the detector and to monitor beam related backgrounds.

During the LS1, the muon system underwent major upgrades [86, 87]. In the fourth station of each endcap, the outermost rings of CSC and RPC chambers were completed, providing an angular coverage of $1.2 < |\eta| < 1.8$ for Run 2, increasing the system redundancy, and allowing tighter cuts on the trigger quality. In order to reduce the environmental noise, outer yoke discs have been placed on both sides for the endcaps. At the innermost rings of the first station, the CSCs have been upgraded by refurbishing the read-out electronics to make use of the full detector granularity instead of groups of three as was the case for Run 1. In Figure 2.7 (right), the refurbishing of the CSCs is shown.

Since the HF experiences intense particle fluxes, it became clear during Run 1 that the glass windows of the PMTs need replacing. For the ECAL in Run 1, the energy reconstruction happened via a weighted sum of the digitized samples [88]. For Run 2 however, the reconstruction had to be made more resistant for out-of-time pileup and a multi-fit approach has been set into place. In this approach, the pulse shape is modelled as a sum of one in-time pulse plus the out-of-time pulses [80]. The energy resolution is better than 2% in the central barrel region and 2-5 % elsewhere.

During the first data taking period of the LHC (2010 to 2013), the tracker operated at $+4^{\circ}\text{C}$. With the higher LHC beam intensities from 2015 onwards, the tracker needs to be operated at much lower temperatures. The reason for this is that with intense irradiation, the doping concentration changes, the leakage current increases proportional to the fluence and the charge collection efficiency decreases due to charge trapping. Mostly the leakage current (I) is affected by the temperature change:

$$I \propto T^2 e^{-\frac{E_g}{2kT}}, \quad (2.6)$$

where T is the operating temperature, E_g the band gap and k the Boltzmann constant. There is approximately a factor 15 between the leakage currents at room temperatures and at -10°C .

During the LS1, the CMS cooling plant was refurbished [89] and the fluorocarbon cooling system overhauled. To help suppressing the humidity inside the tracker, new methods for vapour sealing and insulation were applied. Furthermore, several hundred high-precision sensors are used to monitor the humidity and temperature. In order to get as dry air as possible, a new dry-gas plant provides eight times more dry gas (air or nitrogen) than during the first run, and allows regulation of the flow. As a final addition, the cooling bundles outside the tracker are equipped with heater wires and temperature sensors in order to maintain safe operations above the cavern dew point. For the data taking in 2015-2016, the tracker operated at -15°C .

In Run 2, with the increase in centre-of-mass energy and a higher luminosity, a larger number of simultaneous inelastic collisions per crossing is expected with respect to Run 1. For this, the CMS Level-1 has been upgraded [90]. All hardware, software, databases and the timing control system have been replaced for Run 2, where the main changes are that the muon system now uses the redundancy of the muon detector system earlier to make a high resolution muon trigger.

682 Other upgrades are also performed, including providing the global trigger with more Level-1
683 Trigger algorithms.

684 After the first half of Run 2, the innermost part of detection in CMS (pixel detector) was
685 replaced, enhancing the particle tracking capabilities of CMS. The data used in the framework
686 of this thesis however is from before this upgrade. More information on the Pixel upgrade can
687 be found in Refs. [91, 92].

688 **2.2.5 CMS computing model**

689 The selected data is stored, processed and dispersed via the Worldwide Large Hadron Collider
690 Computing Grid (WLCG) [93, 94]. This has a tiered structure that functions as a single, coherent
691 system.

692 At CERN and the Wigner Research Centre for physics, a single Tier-0 is located. The raw data
693 collected by the experiments is archived here, and a first reconstruction of the data is done.
694 This data is then already in a file format usable for physics analysis. Furthermore, it is able to
695 reprocess data when new calibrations become available. The Tier-0 site distributes this data
696 to a total of 14 Tier-1 centres. They carry out data reprocessing and store real data as well as
697 simulated data. The Tier-1 further distributes the data to over 150 Tier-2 centres. These make
698 the data accessible for physics analysis and are also being used for the production of simulated
699 data. The data is made accessible for physicists around the world. For CMS, the Tier-0 site at
700 CERN reconstructs the full collision events and the backup of the data is sent to seven Tier-1
701 computer centres in France, Germany, Italy, Spain, Taiwan, UK, and the US. At the Tier-1 sites
702 the events are again reconstructed using refined calibration constants. The patterns are created
703 and the more complex events are sent to forty Tier-2 centres for specific analysis tasks.

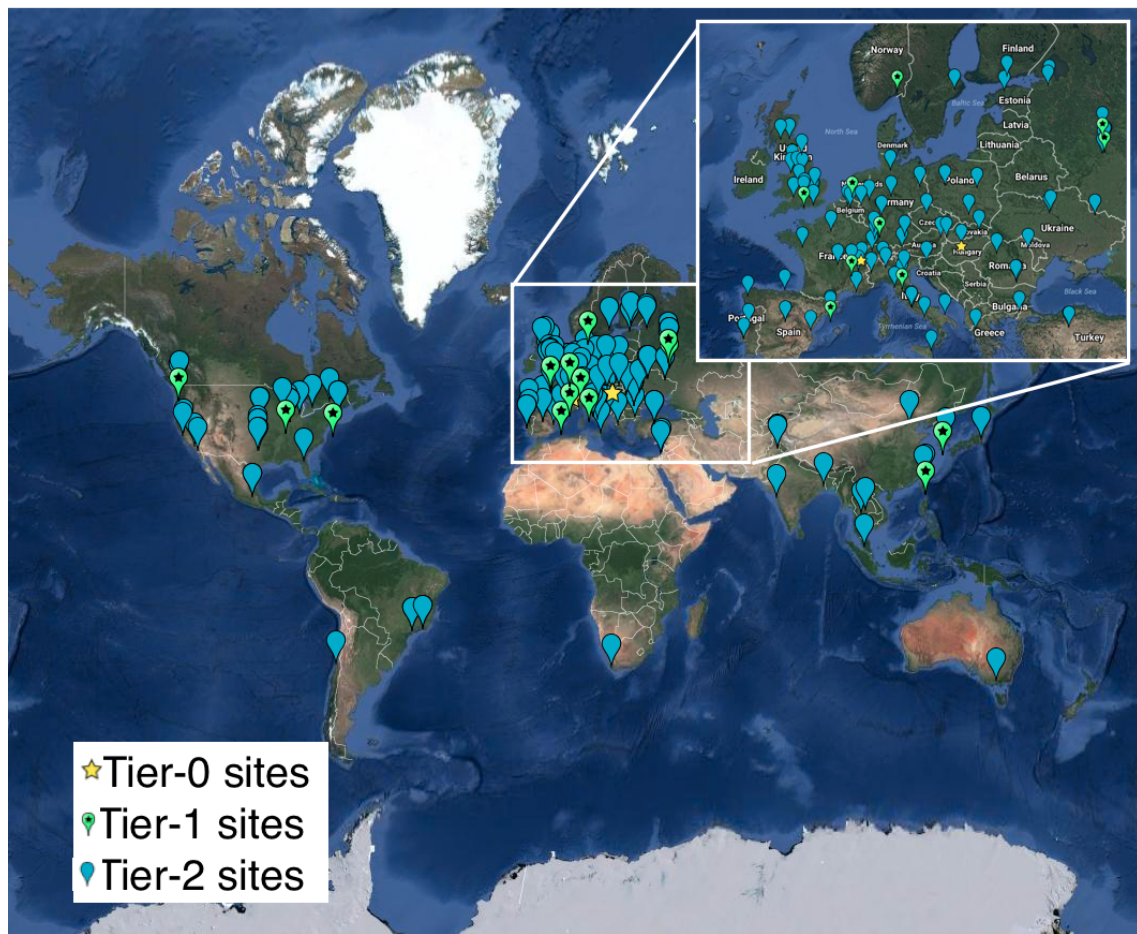


Figure 2.14: Worldwide LHC Computing Grid in 2017 [95].

Analysis techniques

3

705 In order to study the collisions coming from high energy experiments, many tools have been
 706 developed. In [Section 3.1](#), the physics of hadron collision at high energies are presented. These
 707 insights are used to generate events via Monte Carlo event generators, explained in [Section](#)
 708 [3.2](#). Machine learning helps to differentiate between signal- and background like events. In
 709 [Section 3.3](#), the multivariate technique of boosted decision trees is explained. This yields
 710 powerful discriminants for separating signal and background events and provides distributions
 711 for template-based maximum likelihood fits. The fitting method used in the search presented
 712 in this thesis is discussed in [Section 3.4](#).

713 3.1 Hadron collisions at high energies

All partons can be approximated as free when there is sufficiently high momentum transfer in hadron collisions. This makes it possible to treat a hadron-hadron scattering as a single parton-parton interaction. The momentum of the parton can then be expressed as a fraction of the hadron momentum

$$\vec{p}_{\text{parton}} = x \vec{p}_{\text{hadron}}, \quad (3.1)$$

where x is referred to as the Björken scaling variable. The interaction $p_A p_B \rightarrow X$ can then be factorised in terms of partonic cross sections $\hat{\sigma}_{ij \rightarrow X}$ [96]

$$\sigma_{p_A p_B \rightarrow X} = \sum_{ij} \iint dx_1 dx_2 f_i^A(x_1, Q^2) f_j^B(x_2, Q^2) d\hat{\sigma}_{ij \rightarrow X}, \quad (3.2)$$

714 where i and j are the partons resolved from protons A and B. The parton density functions
 715 (PDF) are denoted as $f_i(x_j, Q^2)$, and Q^2 is the factorisation scale more commonly denoted as
 716 μ_F . This factorisation scale represents the energy at which the hadronic interaction can be
 717 expressed as a product of the partonic cross section and the process independent PDF. In [Figure](#)
 718 [3.1](#), the kinematic regions in x and μ_F are shown for fixed target and collider experiments.

719 The parton density functions (PDF) [97–99] represent the momentum distribution of the
 720 proton amongst its partons at an energy scale μ_F . These functions are obtained from global fits
 721 to data since they can not be determined from first principles. From measurements on deep

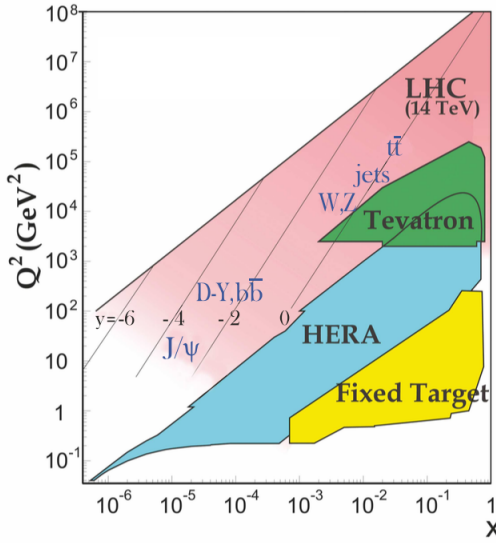


Figure 3.1: Kinematic regions in momentum fraction x and factorisation scale Q^2 probed by fixed-target and collider experiments. Some of the final states accessible at the LHC are indicated in the appropriate regions, where y is the rapidity. In this figure, the incoming partons have $x_{1,2} = (M/14 \text{ TeV})e^{\pm y}$ with $Q = M$ where M is the mass of the state shown in blue in the figure. For example, exclusive J/ψ and Υ production at high $|y|$ at the LHC may probe the gluon PDF down to $x \sim 10^{-5}$. Figure taken from [6].

722 inelastic scattering using lepton-proton collision by the HERA collider [100], supplemented
 723 with proton-antiproton collisions from the Tevatron [101], and proton collision data from the
 724 ATLAS, CMS and LHCb collaborations at the LHC (Run 1) [102] the PDFs are determined and
 725 included in global PDF sets known as the PDF4LHC recommendation [99]. Their measurement
 726 at scale μ_F is extrapolated to higher energies by use of the DGLAP equations [103]. Once
 727 these PDFs are known, the cross section of a certain process can be calculated and used as
 728 input for the Monte Carlo generators used to make the simulated data samples at the LHC. In
 729 the framework of this thesis, the NLO PDF4LHC15_100 set is used. This set is an envelope of
 730 three sets: CT14, MMHT2014 and NNPDF3.0 [99]. As illustration, the dependency of the PDFs
 731 on the momentum fraction x is shown for the NNPDF3.0 set on hadronic scale $\mu_F^2 = 10 \text{ GeV}^2$
 732 and LHC scale $\mu_F^2 = 10^4 \text{ GeV}^2$ in Figure 3.2. The gluon density dominated for most values of
 733 the momentum fraction, implying that it is easier to probe gluons than the quarks. When the
 734 Björken scale is to one, the parton densities of the valence quarks of the proton, up and down
 735 quarks, dominate over the gluon density. The sea quarks originating from gluon splitting, the
 736 charm, anti-up, and anti-down quarks, have lower densities in general for the proton. The
 737 resolution scale Q^2 is typically taken to be the energy scale of the collision. For the top quark pair
 738 production a scale of $Q^2 = (350 \text{ GeV})^2$ is chosen, meaning that the centre-of-mass energy of the
 739 hard interaction is about twice the top quark mass. The uncertainty on the parton distributions
 740 is evaluated using the Hessian technique [104], where a matrix with a dimension identical to
 741 the number of free parameters needs to be diagonalised. In the case of PDF4LHC15_100 set, this
 742 translates into 100 orthonormal eigenvectors and 200 variations of the PDF parameters in the
 743 plus and minus direction.

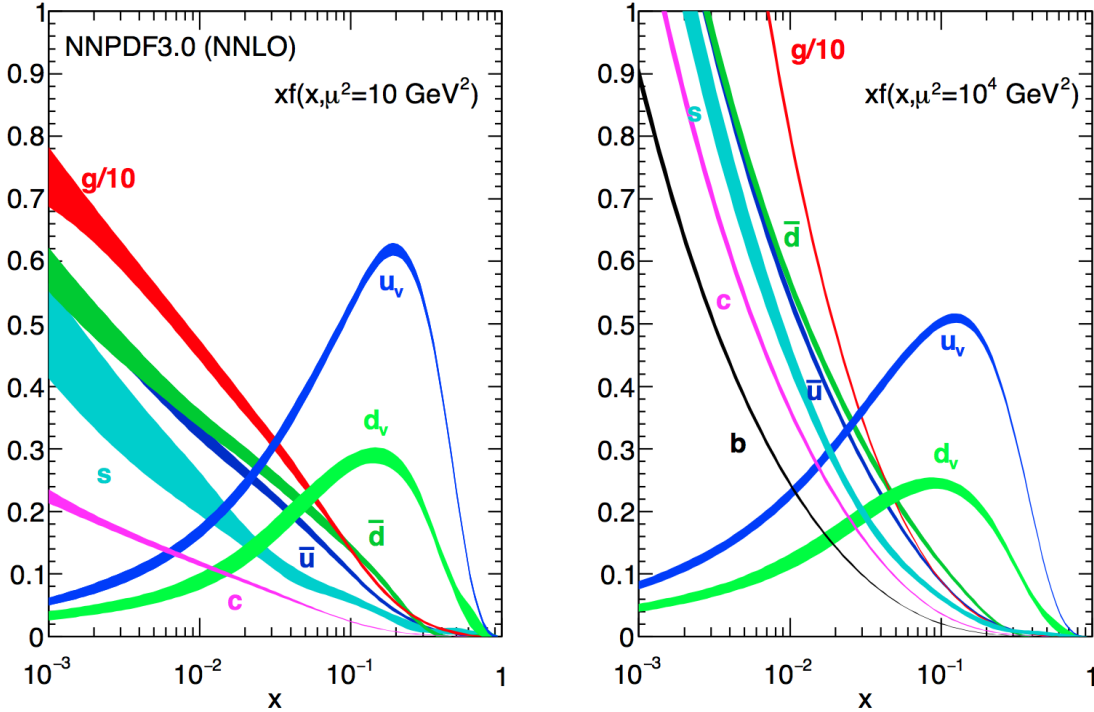


Figure 3.2: The momentum fraction x times the parton distribution functions $f(x)$, where $f = u_v, d_v, \bar{u}, \bar{d}, s, c$, or g as a function of the momentum fraction obtained in the NNLO NNPDF3.0 global analysis at factorisation scales $\mu^2 = 10 \text{ GeV}^2$ (left) and $\mu^2 = 10^4 \text{ GeV}^2$ (right), with $\alpha_s(M_Z^2) = 0.118$. The gluon PDF has been scaled down by a factor of 0.1. Figure taken from [6].

Quantum fluctuations can cause divergences at high energies. This is solved by introducing a renormalization scale μ_R to redefine physical quantities, making the theory still able to describe the experimental regime. A consequence of this method is that the coupling constants will run as a function of μ_R . Beyond the renormalization scale, the high energy effects such as the loop corrections to propagators (self energy) are absorbed in the physical quantities through a renormalization of the fields. In particular, the running behaviour of the strong coupling constant¹ α_S is found to be

$$\alpha_S = \frac{\alpha_S(\mu_0^2)}{1 + \alpha_S(\mu_0^2) \frac{33-2n_f}{12\pi} \ln\left(\frac{|\mu_R^2|}{\mu_0^2}\right)}, \quad (3.3)$$

744 with n_f the number of quarks and μ_0 the reference scale at which the coupling is known. The
 745 current world average of the strong coupling constant at the Z boson mass is $\alpha_S(\mu_R = m_Z) =$
 746 0.1181 ± 0.0011 [6]. From Equation 3.3 one can see easily that the coupling strength decreases
 747 with increasing renormalization scale, this is known as asymptotic freedom. Additionally,
 748 following the behaviour of $\alpha_S(\mu_R^2)$, a limit $\Lambda_{\text{QCD}} \approx 200 \text{ MeV}$ is found for which α_S becomes
 749 larger than one. Under this limit, the perturbative calculations of observables can no longer be
 750 done.

¹The strong coupling constant is defined as $\alpha_S = \frac{g_S^2}{4\pi}$.

Cross sections can be written in terms of interacting vertices contributing to the matrix element (ME) originating from elements of a perturbative series [105], allowing them to be expanded as a power series of the coupling constant α

$$\sigma = \sigma_{\text{LO}} \left(1 + \left(\frac{\alpha}{2\pi} \right) \sigma_1 + \left(\frac{\alpha}{2\pi} \right)^2 \sigma_2 + \dots \right). \quad (3.4)$$

751 Leading order (LO) accuracy contains the minimal amount of vertices in the process, then
 752 depending on where the series is cut-off one speaks of next-to-leading order (NLO), or next-to-
 753 next-to-leading order (NNLO) accuracy in α . Predictions including higher order corrections
 754 tend to be less affected by theoretical uncertainties originating from a variation of the chosen
 755 renormalization and factorisation scales.

756 3.2 Event generation

757 In order to compare reconstructed data with theoretical predictions, collision events are gener-
 758 ated and passed through a simulation of the CMS detector and an emulation of its read-out. For
 759 the detector simulation, a so-called Full Simulation package [106, 107] based on the Geant4
 760 toolkit [108] is employed. This allows detailed simulations of the interactions of the particles
 761 with the detector material.

762 3.2.1 Fundamentals of simulating a proton collision

763 The generation of $\text{pp} \rightarrow \text{X}$ events is subdivided into sequential steps [109–111], as shown in
 764 Figure 3.3.

765 The interaction of two incoming protons is often soft and elastic leading to events that are not
 766 interesting in the framework of this thesis. More intriguing are the hard interactions between
 767 two partons from the incoming protons. The event generation starts from the matrix elements of
 768 a hard scattering process of interest. The corresponding cross section integral is sampled using
 769 Monte Carlo techniques and the resulting sample of events reflects the probability distribution
 770 of a process over its final state phase space. A parton shower (PS) program is then used to
 771 simulate the hadronisation of final state partons, coming from the sample of events of the hard
 772 interaction, into hadrons which then decay further. On top of this, radiation of soft gluons or
 773 quarks from initial or final state partons is simulated. These are respectively referred to as
 774 initial state radiation (ISR) or final state radiation (FSR). The contributions from soft secondary
 775 interactions, the so-called underlying event (UE), and colour reconnection effects are also taken
 776 into account. A brief overview of the programs used for the event generation of the signal and
 777 main background processes used in the search presented in this thesis, is given in Section 3.2.2.

778 3.2.2 Programs for event generation

779 The FEYNRULES package [112] allows for the calculation of the Feynman rules in momentum
 780 space for any quantum field theory model. By use of a Lagrangian, the set of Feynman rules asso-
 781 ciated with this Lagrangian is calculated. Via the Universal FeynRules Output (UFO) [113]
 782 the results are then passed to matrix element generators.

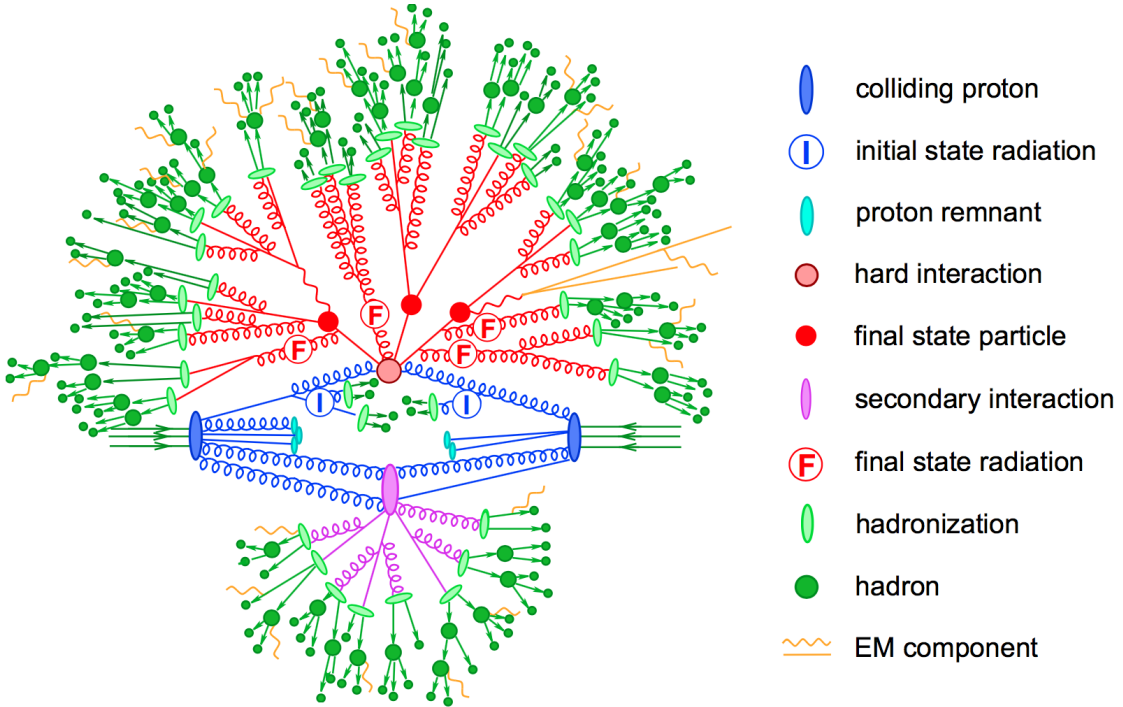


Figure 3.3: Sketch of a hadron collision as simulated by a Monte-Carlo event generator. The red blob in the centre represents the hard collision, surrounded by a tree-like structure representing Bremsstrahlung as simulated by parton showers. The purple blob indicates a secondary hard scattering event. Parton-to-hadron transitions are represented by light green blobs, dark green blobs indicate hadron decays, while yellow lines signal soft photon radiation. Figure taken from [111].

783 The MadGraph program [114] is used to interpret the physics model and calculate the cor-
 784 responding Feynman diagrams and matrix elements. After this, MadEvent [115] is used to
 785 calculate the corresponding partons. These generated parton configurations are then merged
 786 with Pythia [116–118] parton showers using the MLM merging scheme [119].

787 The MadGraph5_aMC@NLO program [120] combines the LO MadGraph [114] and the aMC@NLO
 788 program into a common framework. This combination supports the generation of samples at
 789 LO or NLO together with a dedicated matching to parton showers using the MC@NLO [121]
 790 or FxFx [122] schemes respectively. The FxFx scheme produces a certain fraction of events
 791 with negative weights originating from the subtraction of amplitudes that contain additional
 792 emissions from the NLO matrix element to prevent double-counting.

793 The POWHEG box (versions 1 and 2) [123–128] contains predefined implementations of various
 794 processes at NLO. It applies the POWHEG method for ME- to PS- matching, where the hardest
 795 radiation generated from the ME has priority over subsequent PS emission to remove the overlap
 796 with the PS simulation.

797 The JHU generator (version 7.02) [129–132] is used to generate the parton level information
 798 including full spin and polarization correlations. It is commonly used for studying the spin and
 799 parity properties of new resonances such as $ab \rightarrow X \rightarrow VV$, where $V = Z, W, \gamma$.

800 The generation of events from processes involving the production and decay of resonances
 801 creates a computational heavy load, especially at NLO. The narrow width approximation assumes
 802 that the resonant particle is on-shell. This factorizes the production and decay amplitude,
 803 allowing to perform the simulation of the production and decay of heavy resonances like top
 804 quarks or Higgs bosons to be performed in separate steps. The MadSpin program [133] extends
 805 this approach and accounts for off-shell effects through a partial reweighting of the events.
 806 Additionally, spin correlation effects between production and decay products are taken into
 807 account.

808 The Pythia program (versions 6 and 8) [116–118] generates events of various processes
 809 at LO. However, more commonly it is only used for its PS simulation and is then used after
 810 other LO and NLO event generators to perform subsequent parton showering, hadronisation,
 811 and simulation of the underlying event. In this thesis the underlying event tunes [134] are the
 812 CUETP8M2T4, CUETP8M1 and CUETP8M2.

813 The detector response is simulated via the Geant4 [108] program. This program tracks the
 814 particles through the detector material via a detailed description of the detector and generates
 815 several hits throughout several sensitive layers. In addition, the response of the detector
 816 electronics to these hits are simulated.

817 3.2.3 Generating FCNC top-Z interactions

818 The FCNC processes are generated by interfacing the Lagrangian in Equation 1.36 with
 819 MadGraph5_aMC@NLO by means of the FeynRules package and its Universal FeynRules
 NOTE: RH⁸²⁰
 and LH⁸²¹
 gave the⁸²²
 same re-⁸²³
 sulting vari-⁸²⁴
 ables and⁸²⁵
 RH is easier⁸²⁶
 to simulate⁸²⁷
 since those⁸²⁸
 are singlets⁸²⁹
 under SU⁸²⁷
 (no doublet⁸²⁸
 with b)⁸²⁹
 output format. The complex chiral parameters are arbitrary chosen to be $f_{Xq}^L = 0$ and $f_{Xq}^R = 1$.
 The processes are generated with the MadGraph5_aMC@NLO (version 2.2.2) and showered with
 Pythia (version 8.22). The signal consists of two components: events describing the top quark
 pair production followed by an FCNC decay of one top quark ($t \rightarrow Zq$), and events with the FCNC
 single top quark production ($Zq \rightarrow t$) for which the top quark decays according to theSM. The
 leading order generation of the single top quark FCNC process $tZ + 0,1$ jet including a merging
 technique can not be done since $tZ + 1$ jet also contains contributions from top quark pair FCNC
 where one quark is decaying in tZ . Therefore, single top quark and top quark pair processes
 are generated independently, where the single top quark process is generated without the extra
 hard jet, and the top quark pair FCNC process is generated with up to two extra jets.

830 The signal rates are estimated by use of the MadGraph5_aMC@NLO program for estimating the
 831 partial widths. The anomalous couplings are left free to float for this estimation, and only one
 832 coupling is allowed to be non-vanishing at a time. The results are presented in Table 3.1.

833 The anomalous single top quark cross sections are calculated by convolution of the hard
 834 scattering matrix elements with the LO order set of NN23L01 [135] partons densities. The NLO
 835 effects are modelled by multiplying each LO cross section by a global k -factor. The LO single top
 836 quark production cross section and the global k -factors for the top-Z production are shown in
 837 Table 3.2. The hard scattering events are then matched to parton showers to Pythia to account
 838 for the simulation of the QCD environment relevant for hadronic collisions.

Table 3.1: Leading order partial widths related to the anomalous decay modes of the top quark, where the new physics scale Λ is given in GeV.

Anomalous coupling	vertex	Partial decay width (GeV)
κ_{tZq}/Λ	tZu	$1.64 \times 10^4 \times (\kappa_{tZu}/\Lambda)^2$
	tZc	$1.64 \times 10^4 \times (\kappa_{tZc}/\Lambda)^2$
ζ_{tZq}	tZu	$1.69 \times 10^{-1} \times (\zeta_{tZu})^2$
	tZc	$1.68 \times 10^{-1} \times (\zeta_{tZc})^2$

Table 3.2: Leading order single top quark production cross section at a centre-of-mass of 13 TeV for $pp \rightarrow tZ$ or $t\bar{Z}$, where the new physics scale is given in GeV. The NLO k -factors [136] are given in the last column.

Anomalous coupling	vertex	Cross section (pb) $pp \rightarrow t + pp \rightarrow \bar{t}$	$\sigma_{pp \rightarrow \bar{t}}/\sigma_{pp \rightarrow t}$	NLO k -factor
κ_{tZq}/Λ	tZu	$1.92 \times 10^7 \times (\kappa_{tZu}/\Lambda)^2$	0.12	1.40
	tZc	$2.65 \times 10^6 \times (\kappa_{tZc}/\Lambda)^2$	0.50	1.40
ζ_{tZq}	tZu	$8.24 \times 10 \times (\zeta_{tZu})^2$	0.14	1.40
	tZc	$1.29 \times 10 \times (\zeta_{tZc})^2$	0.50	1.40

The top quark pair cross sections are derived from the SM $t\bar{t}$ cross section, calculated with MadGraph5_aMC@NLO at NLO at a centre-of-mass of 13 TeV ($\sigma_{t\bar{t}}^{\text{SM,NLO}} = 6.741 \times 10^2 \text{ pb}$), and considering the decay $t\bar{t} \rightarrow (bW^\pm)(X_{qt})$. The branching fraction $\mathcal{B}(t \rightarrow bW^\pm)$ is assumed to be equal to one and the FCNC branching fraction is calculated as

$$\mathcal{B}(t \rightarrow qX) = \frac{\Gamma_{t \rightarrow qX}}{\Gamma_t^{\text{SM}} + \Gamma_t^{\text{FCNC}}} \approx \frac{\Gamma_{t \rightarrow qX}}{\Gamma_t^{\text{SM}}}, \quad (3.5)$$

where $\Gamma_{t \rightarrow qX}$ is given in Table 3.1, $\Gamma_t^{\text{SM}} = 1.32 \text{ GeV}$ [47], and the assumption $\Gamma_t^{\text{FCNC}} \ll \Gamma_t^{\text{SM}}$ is made. In Table 3.3 the resulting NLO cross sections for the top-Z FCNC interactions are given.

Table 3.3: Next to leading order top quark pair cross section for the top-Z FCNC interactions $t\bar{t} \rightarrow (bW^\pm)(X_{qt})$ with a full leptonic decay at a centre-of-mass of 13 TeV, where $\sigma_{pp \rightarrow t\bar{t}}^{\text{SM,NLO}} = 6.741 \times 10^2 \text{ pb}$, $\mathcal{B}(Z \rightarrow \ell\bar{\ell}) = 3.36 \times 3 \times 10^{-2}$, and $\mathcal{B}(W \rightarrow \ell\nu) = 10.80 \times 3 \times 10^{-2}$.

Anomalous coupling	vertex	Process	Cross section (pb)
κ_{tZq}/Λ	tZu	$t\bar{t} \rightarrow (b\ell^+\nu)(\bar{u}\ell^+\ell^-)$	$2.727 \times 10^5 \times (\kappa_{tZu}/\Lambda)^2$
		$t\bar{t} \rightarrow (\bar{b}\ell^-\bar{\nu})(u\ell^+\ell^-)$	$2.727 \times 10^5 \times (\kappa_{tZu}/\Lambda)^2$
	tZc	$t\bar{t} \rightarrow (b\ell^+\nu)(\bar{c}\ell^+\ell^-)$	$2.726 \times 10^5 \times (\kappa_{tZc}/\Lambda)^2$
		$t\bar{t} \rightarrow (\bar{b}\ell^-\bar{\nu})(c\ell^+\ell^-)$	$2.726 \times 10^5 \times (\kappa_{tZc}/\Lambda)^2$
ζ_{tZq}	tZu	$t\bar{t} \rightarrow (b\ell^+\nu)(\bar{u}\ell^+\ell^-)$	$2.807 \times (\zeta_{tZu})^2$
		$t\bar{t} \rightarrow (\bar{b}\ell^-\bar{\nu})(u\ell^+\ell^-)$	$2.807 \times (\zeta_{tZu})^2$
	tZc	$t\bar{t} \rightarrow (b\ell^+\nu)(\bar{c}\ell^+\ell^-)$	$2.807 \times (\zeta_{tZc})^2$
		$t\bar{t} \rightarrow (\bar{b}\ell^-\bar{\nu})(c\ell^+\ell^-)$	$2.807 \times (\zeta_{tZc})^2$

3.2.4 Generating SM background events

The SM tZq sample is generated using the MadGraph5_aMC@NLO generator (version 2.2.2) [137] at leading order accuracy. The t $\bar{t}Z$ and triboson samples were generated using the MadGraph5_aMC@NLO generator (version 2.2.2), interfaced through the dedicated MC@NLO matching scheme [121]. The WZ+jets and t $\bar{t}W$ samples are produced with up to one additional parton at next-to-leading order accuracy using MadGraph5_aMC@NLO (version 2.2.2) and using FxFx approach [138] for matching and merging. The samples of t $\bar{t}H$, WW, ZZ, and single top quark production channels are generated with the POWHEG box (versions 1 and 2) [123–128]. The JHU generator [129–132] is used for the tqH sample, while the tWZ sample is generated using MadGraph5_aMC@NLO at leading order [114]. All events are interfaced to Pythia version 8.22 [118] to simulate parton shower, hadronisation, and underlying event. Additionally, MadSpin is used for the tZq, WZ+jets, t $\bar{t}Z$, t $\bar{t}W$, tWZ, and triboson samples.

The complete list of SM samples is given in Table 3.4, along with their cross sections at a centre-of-mass of 13 TeV. The cross sections without a reference are coming from the generator with which the sample has been made, for some of them the uncertainties are provided by the Generator Group [139]. For each MC sample, the integrated luminosity that the sample represents is estimated as the number of simulated events divided by the cross section of the generated process. This luminosity is then matched to integrated luminosity of 35.9 fb^{-1} represented by the data used for analysis. For processes generated with MadGraph5_aMC@NLO, the effective number of simulated events is used, taking into account positive and negative event weights. In Figure 3.4, a summary is given of the SM cross section measurements performed by the CMS collaboration. These cross sections are all in agreement with their SM predictions.

Table 3.4: SM MC samples used in this analysis with their corresponding cross section at a centre-of-mass of 13 TeV and MadGraph5_aMC@NLO correction C when applicable. The generators used for each sample are indicated and the simulation of the parton shower, hadronisation, and underlying event is done by Pythia version 8.22 [118] for all samples.

Process	Generator	Cross section (pb)	C	Ref.
$WZ \rightarrow 3\ell\nu$	MadGraph5_aMC@NLO+MadSpin	5.26	1.61	[139]
tZq with $Z \rightarrow \ell^+\ell^-$	MadGraph5_aMC@NLO+MadSpin	0.0758	3.77	[139]
tqH with $H \rightarrow ZZ \rightarrow \ell^+\ell^-\ell^+\ell^-$	JHU	$8.80 \cdot 10^{-6}$	-	[139]
$t\bar{t}W + \text{jets}$ with $W \rightarrow \ell\nu$	MadGraph5_aMC@NLO+MadSpin	0.2043 ± 0.0020	1.94	[139]
$t\bar{t}Z \rightarrow 2\ell + 2\nu + \text{other}$, with $m_{\ell\ell} > 10$ GeV	MadGraph5_aMC@NLO+MadSpin	0.2529 ± 0.0004	2.15	[139]
$t\bar{t}H, \text{no } b\bar{b} \text{ decays}$	POWHEG	0.2151	-	[139]
$t\bar{t}H, b\bar{b} \text{ decays}$	POWHEG	0.2934	-	[139]
$WW \rightarrow 2\ell 2\nu$	POWHEG	12.178	-	[140]
$ZZ \rightarrow 4\ell$	POWHEG	0.3366	-	[139]
WZZ	MadGraph5_aMC@NLO+ MadSpin	0.05565	1.14	[139]
ZZZ	MadGraph5_aMC@NLO	0.01398	1.17	[139]
single top quark tWZ , with $Z_\mu \rightarrow \ell^+\ell^-$	MadGraph5_aMC@NLO(LO)+MadSpin	0.001123	-	[139]
single top quark t-channel \bar{t}	POWHEG+MadSpin	$44.33^{+1.76}_{-1.49}$	-	[139]
single top quark t-channel t	POWHEG+MadSpin	$26.38^{+1.32}_{-1.18}$	-	[139]
single top quark $t\bar{W}$	POWHEG	$35.85 \pm 0.90 \text{ (scale)} \pm 1.70 \text{ (PDF)}$	-	[139]
single top quark tW	POWHEG	$35.85 \pm 0.90 \text{ (scale)} \pm 1.70 \text{ (PDF)}$	-	[139]
$t\bar{t}$	POWHEG	$831.76^{+19.77+35.06}_{-29.20-35.06}$	-	[139]
$Z/\gamma^* + \text{jets}$, with $m_{\ell\ell} > 50$ GeV	MadGraph5_aMC@NLO	$3 \times (1921.8 \pm 0.6 \pm 33.2)$	1.49	[139]
$Z/\gamma^* + \text{jets}$, with $10 \text{ GeV} < m_{\ell\ell} < 50 \text{ GeV}$	MadGraph	18610	-	[139]

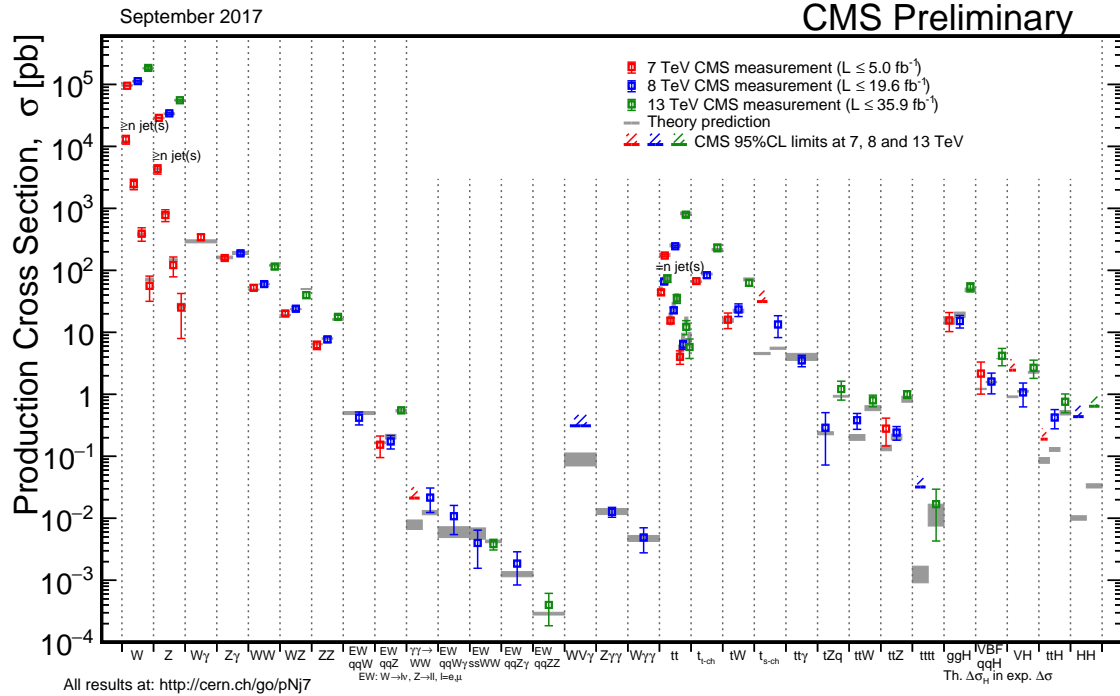


Figure 3.4: Summary of the SM cross section measurements performed by the CMS collaboration. Figure taken from [23]

863 3.3 Multivariate analysis techniques: Boosted Decision Trees

864 The need of processing large quantities of data and discriminating between events with largely
 865 similar experimental signatures makes multivariate analysis (MVA) a largely used method in the
 866 physics community. Multivariate classification methods based on machine learning techniques
 867 are a fundamental ingredient to most analyses. The advantage of using a MVA classifier is
 868 that it can achieve a better discrimination power with respect to a simpler analysis based on
 869 individual selection criteria or poorly discriminating variables. A risk of using MVA classifiers
 870 is overtraining. This happens when there are too many model parameters of an algorithm
 871 adjusted to too few data points. This leads to an increase in the classification performance over
 872 the objectively achievable one.

873 There are many software tools that exist for MVA. In this thesis the Tool for Multivariate
 874 Analysis (TMVA) [141] is used. This software is an open source project included into
 875 ROOT [142]. By training on events for which the classification is known, a mapping function
 876 is determined that describes a classification or an approximation of the underlying behaviour
 877 defining the target value (regression). In this thesis boosted decision trees (BDT) are employed
 878 for the classification of events as implemented in the TMVA framework [141]. This multivariate
 879 technique is based on a set of decision trees where each tree yields a binary output depending
 880 on the fact that an event is signal- or background-like. This has as advantage that several
 881 discriminating variables can be combined into a powerful one-dimensional discriminant D.

882 The decision tree is constructed by training on a dataset for which the outcome is already
 883 provided, such as simulation datasets with signal and background processes (supervised learn-
 884 ing). Different trees can be combined into a forest where the final output is determined by the
 885 majority vote of all trees, so-called boosting. This stabilises the decision trees against statistical
 886 fluctuations and makes it possible to keep the decision trees very shallow, making the method
 887 more robust against overtraining. Examples of such boosting algorithms are Adaptive Boosting
 888 (AdaBoost) and Gradient Boosting [143]. In this thesis Gradient boost is used with a learning
 889 rate of 0.2-0.3 and the depth of the tree is set to three. Additionally, the Gradient boost is
 890 used in combination with bagging, so-called stochastic gradient boosting. Bagging smears the
 891 statistical fluctuations in the training data and therefore stabilises the response of the classifier
 892 and increases the performance by eliminating overtraining. More information about stochastic
 893 gradient boosting can be found in Ref. [144].

894 The discriminating power of a BDT is assessed by analysing the receiver operating characteristic
 895 (ROC) curve. This curve represents the background rejection over the signal efficiency of the
 896 remaining sample. The area under the curve (AUC) is compared to random guessing in order
 897 to identify the best classifier can be identified. When the multivariate discriminator has no
 898 discriminating power, the resulting AUC will be 0%, while 50% means fully separated event
 classes. In Figure 3.5 examples of ROC curves are shown.

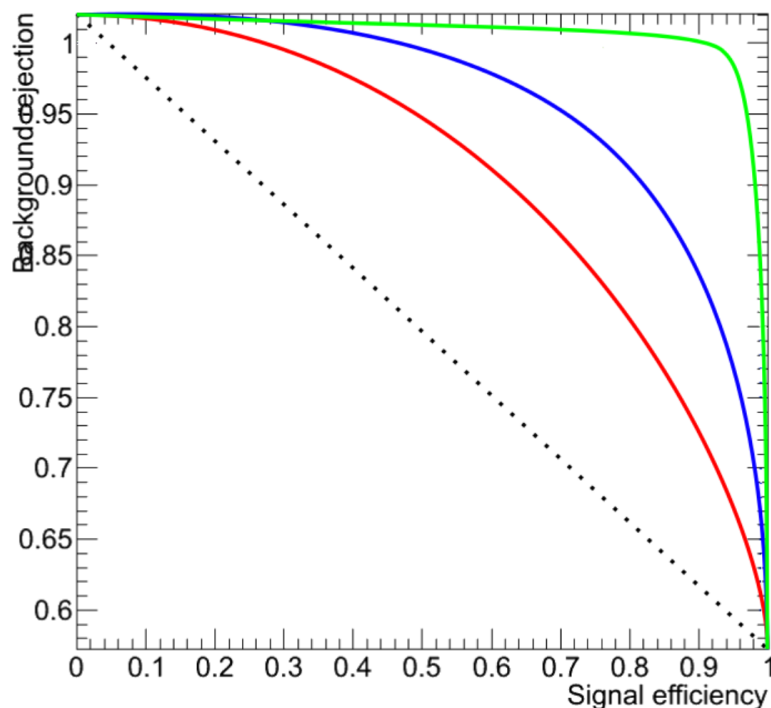


Figure 3.5: Example of ROC curves. In this example, the green method is better than the blue one, which is better than the red one. The dashed line represents a case where there is no separation. Figure taken from [145].

3.4 Statistical methodology

The search performed in the framework of this thesis requires the simultaneous analysis of data from different decay channels. The statistical methodology used for this search is developed by the ATLAS and CMS collaborations in the context of the LHC Higgs Combination group [146–149]. The Higgs Combined Tool [150] is a RooStats [151] framework which runs different statistical methods. In this section, only the statistical tools necessary for the performed search are described [152].

The event yields of signal and background processes are denoted as s and b respectively. These represent event counts in multiple bins or unbinned probability density functions. By use of simulation, predictions on both signal and background yields are made the multiple uncertainties on these predictions are accounted for by introducing nuisance parameters θ such that $s = s(\theta)$ and $b = b(\theta)$.

The Bayesian and modified classical frequentist statistical approaches are used in high energy physics to characterise the absence of a signal. The level of incompatibility of data with a signal hypothesis is quantified in terms of confidence levels (CL). The convention is to require a 95% CL for excluding a signal. In general limits are not set on the signal cross section directly, but are set on the signal strength modifier μ . The signal strength modifier is defined such that it equally changes all the cross sections of all production mechanisms of the signal by the same scale.

In this thesis, the modified frequentist approach [153, 154] for confidence levels that adopts the classical frequentist method to allow nuisance parameters, is used. It constructs a likelihood $\mathcal{L}(\text{data}|\mu, \theta)$ is as

$$\mathcal{L}(\text{data}|\mu, \theta) = \text{Poisson}(\text{data}|\mu s(\theta) + b(\theta)) \text{pdf}(\tilde{\theta}|\theta). \quad (3.6)$$

The probability density function $\text{pdf}(\tilde{\theta}|\theta)$ describes all sources of uncertainty. In this thesis, all sources of uncertainties are assumed to be either 100% correlated or uncorrelated. Partially correlated uncertainties are broken down to subcomponents that fit those requirements, allowing to include all constraints in the likelihoods in a clean factorised form.

A systematic uncertainty pdf $\rho(\theta|\tilde{\theta})$ for the nuisance θ with nominal value $\tilde{\theta}$ is used. It reflects the degree of belief of what the true value of the θ is. In this thesis, the approach from the Higgs Combined Tool is used where the pdfs $\rho(\theta|\tilde{\theta})$ are re-interpret as posteriors of real or imaginary measurements $\tilde{\theta}$

$$\rho(\theta|\tilde{\theta}) \sim \text{pdf}(\tilde{\theta}|\theta) \pi_\theta(\theta), \quad (3.7)$$

where $\pi_\theta(\theta)$ is the hyper prior for the (imaginary) measurements. The the pdfs used by the Higgs Combine Tool are described in Ref. [149].

The data in Equation 3.6 represents either the actual observation or pseudo-data to construct sampling distributions. For a binned likelihood, the Poisson probabilities to observe n_i events in bin i is given as

$$\text{Poisson}(\text{data}|\mu s(\theta) + b(\theta)) = \prod_i \frac{(\mu s_i(\theta) + b_i(\theta))^{n_i}}{n_i!} e^{-\mu s_i(\theta) - b_i(\theta)}. \quad (3.8)$$

At the LHC, the test statistic is defined as

$$q_\mu = -2 \ln \frac{\mathcal{L}(\text{data} | \mu, \hat{\theta}_\mu)}{\mathcal{L}(\text{data} | \hat{\mu}, \hat{\theta}_\mu)}, \quad (3.9)$$

where the likelihood is maximised in the numerator (maximum likelihood estimator, MLE) for a given μ and (pseudo) data at $\hat{\theta}_\mu$, while $\hat{\mu}$ combined with $\hat{\theta}$ defines the point for which the likelihood reaches its global maximum. The estimated signal strength modifier $\hat{\mu}$ can not become negative since a signal rate is positive defined by physics. Furthermore, an upper constraint on the MLE $\hat{\mu} \leq \mu$ is imposed.

The signal is excluded at $1 - \alpha$ confidence level when

$$\text{CLs} = \frac{P(q_\mu \geq q_\mu^{\text{obs}} | \mu s + b)}{P(q_\mu \geq q_\mu^{\text{obs}} | b)} \leq \alpha, \quad (3.10)$$

with $P(q_\mu \geq q_\mu^{\text{obs}} | \mu s + b)$ the probability to observe a value of the test statistic at least as large as the one observed in data q_μ^{obs} , under the signal plus background ($s + b$) hypothesis, and $P(q_\mu \geq q_\mu^{\text{obs}} | b)$ for the background only (b) hypothesis. These probabilities are defined as

$$p_\mu = P(q_\mu \geq q_\mu^{\text{obs}} | \mu s + b) = \int_{q_\mu^{\text{obs}}}^{\infty} f(q_\mu | \mu, \hat{\theta}_\mu^{\text{obs}}) dq_\mu, \\ 1 - p_b = P(q_\mu \geq q_\mu^{\text{obs}} | b) = \int_{q_{\mu=0}^{\text{obs}}}^{\infty} f(q_\mu | \mu = 0, \hat{\theta}_{\mu=0}^{\text{obs}}) dq_\mu, \quad (3.11)$$

where p_μ and p_b are the p-values associated to the two hypothesis, and $f(q_\mu | \mu, \hat{\theta}_\mu^{\text{obs}})$ and $f(q_\mu | \mu = 0, \hat{\theta}_{\mu=0}^{\text{obs}})$ are the probability density functions of the signal plus background and background only hypothesis constructed from toy Monte Carlo pseudo data. These are generated with nuisance parameters fixed to $\hat{\theta}_{\mu=0}^{\text{obs}}$ (background only) and $\hat{\theta}_\mu^{\text{obs}}$ (signal plus background). The 95% CL level upper limit on μ is achieved by adjusting μ until $\text{CL} = 0.05$, this is the so-called observe limit. The expected median upper limit and the $\pm 1\sigma$ and $\pm 2\sigma$ bands for a hypothesis is generated by a large set of pseudo data and calculate the CLs and the value of μ at 95% CL for each of them. A cumulative probability distribution can be build by starting the integration from the side corresponding to low event yields. The median expected value, so-called expected limit at 95% CL, is where the cumulative distribution function crosses the 50% quantile. The $\pm 1\sigma$ (68%) and $\pm 2\sigma$ (95%) bands on the expected limit are defined by the crossings of the 16% and 84%, and 2.5% and 97.5% quantiles.

In order to significantly reduce computing time, the Asymptotic CL method is used. This method avoids an ensemble of toy Monte Carlo samples and instead replaces it by one representative dataset, called Asimov dataset. This dataset is constructed such that all observed quantities are set equal to their MLE values ($\hat{\theta}_{\text{Asimov}} = \theta_0$). More information about this procedure can be found in Refs. [147].

4

Event reconstruction and identification

947

948 The simulated data after the detector simulation described in [Section 3.2](#), has the exact same
949 format as the real collision data recorded at the CMS experiment. Therefore the same software
950 can be used for the reconstruction of both simulation and real data. In [Section 4.1](#), the object
951 reconstruction is explained. After reconstructing the objects, they are connected to physics
952 objects need to be identified ([Section 4.2](#)) and corrected for pileup ([Section 4.3](#)). The objects
953 used for physics analysis have extra requirements as shown in [Section 4.4](#). A summary of all
954 the corrections applied to data and simulation is given in [Section 4.5](#).

955 4.1 Object Reconstruction

956 In [Figure 4.1](#), the particle interaction in a transverse slice of the CMS detector is shown. When
957 a particle enters the detector, it first enters the tracker where charged particle trajectories,
958 so-called tracks, and origins, so-called vertices, are reconstructed from signals or hits in the
959 sensitive layers. The magnetic field bends the charged particles making it able to measure the
960 electric charges and momenta of charged particles. The electron and photons are absorbed in
961 the ECAL and the corresponding electromagnetic showers are detected as clusters of energy
962 in adjacent cells. From this, the energy and the direction of the particles can be determined.
963 The charged and neutral hadrons can also initiate a hadronic shower in the ECAL that is fully
964 absorbed in the HCAL. The clusters from these showers are also used to estimate the energy
965 and direction. Muons and neutrino's pass through the calorimeters without little to no energy
966 loss and the neutrinos even escape the CMS detector undetected while muons produce hits in
967 the muon detectors.

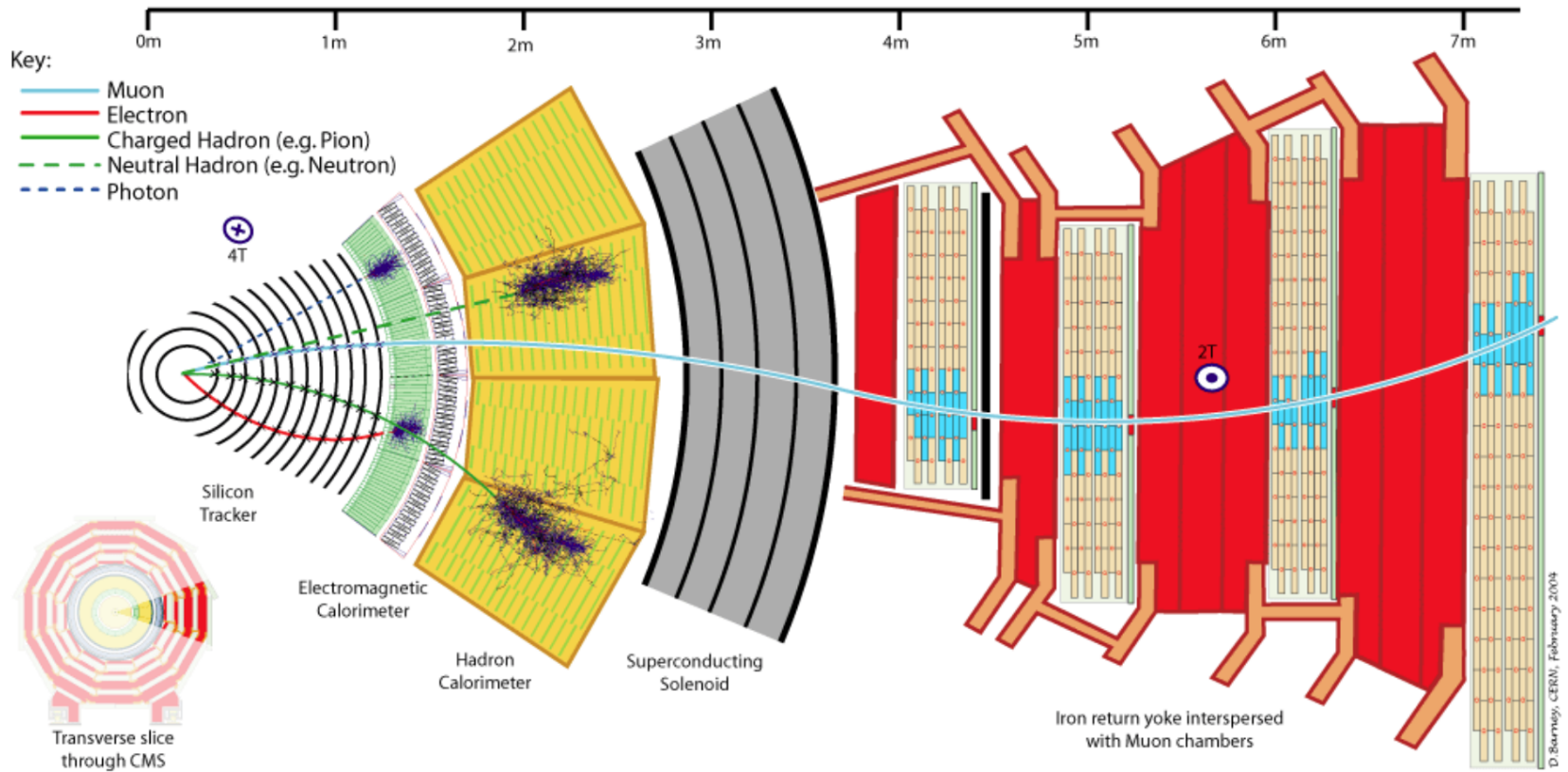


Figure 4.1: Cross-section of the CMS detector with all parts of the detector labelled. This sketch shows the specific particle interactions from a beam interaction point to the muon detector. The muon and charged pion are positively charged, the electron is negatively charged. Figure taken from [155].

968 The particle flow (PF) [155] reconstruction algorithm correlates the tracks and clusters
 969 from all detector layers with the identification of each final state particle, and combines the
 970 corresponding measurements to reconstruct the properties. The muon is identified by a track
 971 in the inner tracker connected to a track in the muon detector as described in Section 4.1.2.
 972 The electrons are identified by a track and an ECAL cluster, not connected to an HCAL cluster
 973 as described in Section 4.1.3. The ECAL and HCAL clusters without a track link identify the
 974 photons and neutral hadrons, while the addition of the tracker determines the energy and
 975 direction of a charged hadron.

976 4.1.1 Charged particle tracks

977 An iterative tracking algorithm is responsible for the reconstruction of the tracks made by
 978 charged particles in the inner tracking system. Each iteration consists of four steps [71]: the
 979 track-seed generation, the pattern recognition algorithm, removal of track-hit ambiguities and
 980 a final track fit. The pattern recognitions done by use a Kalman filter method [156, 157] which
 981 into account the magnetic field and multiple scattering effects. All hits that are unambiguously
 982 associated to the final track are removed from the list of available hits. In order to associate the
 983 remaining hits, the procedure is repeated with looser track reconstruction criteria. The use of
 984 the iterative track reconstruction procedure has a high track finding efficiency, where the fake
 985 track reconstruction rate is negligible.

NOTE: Ik kan hier stoppen en 4.1.1, 4.1.2, 4.1.3.4.1.4 volledig schrappen (dus enkel primary vertex houden)

986 4.1.2 Following the Muon's Footsteps

987 The muon reconstruction [158] has three subdivisions: local reconstruction, regional reconstruction
 988 and global reconstruction. The local reconstruction is performed on individual detector
 989 elements such as strip and pixel hits in the inner tracking system, and muon hits and/or segments
 990 in the muon chambers. Independent tracks are reconstructed in the inner tracker - called tracker
 991 tracks - and in the muon system, called standalone muon tracks. Based on these tracks, two
 992 reconstructions are considered: Global Muon reconstruction and Tracker Muon reconstruction.
 993 The first is an outside in approach starting from a standalone muon track while the second uses
 994 an inside-out approach starting from tracker tracks. For low transverse momenta ($p_T \lesssim 5$ GeV),
 995 the tracker muon reconstruction is more efficient than the global muon approach. This is due
 996 to the fact that tracker muons only require a single muon segment in muon system, while the
 997 global muon approach requires typically segments in at least two muon stations. These tracker
 998 muons are used for identifying muons from the hadronisation of b or c quarks. The global muon
 999 approach typically improves the tracker reconstruction for $p_T \gtrsim 200$ GeV.

1000 4.1.3 The path of the Electron

1001 Standard tracking algorithms are based on Kalman filtering which assume that the energy loss
 1002 is Gaussian distributed. Since the electron tracks are increasingly curved in the magnetic field
 1003 as a function of its flight distance, these standard tracking algorithms are not suitable to fit the
 1004 electron tracks and different filtering algorithm, the Gaussian sum filter (GSF) [159] is used
 1005 instead.

1006 In CMS, the electrons are reconstructed in two ways. The older ECAL based tracking is
 1007 developed to identify high energetic isolated electrons. This tracking algorithm starts from

1008 ECAL clusters with a transverse energy above 4 GeV and extrapolates from these cluster the
 1009 position of the hits in the tracker. Another, tracker based algorithm uses all the tracks with
 1010 a p_T higher than 2 GeV found with iterative tracking as seeds. The electron seeds from the
 1011 ECAL- and tracker-based procedures are merged into a unique collection and are then refitted
 1012 by using the summed Gaussian distributions as uncertainty per hit in the track fit. The electron
 1013 efficiency is measured in 8 TeV proton collision data to be better than 93% for electrons with an
 1014 ECAL supercluster energy of $E_T > 20$ GeV [160]. For electrons with an $E_T > 25$ GeV in 13 TeV
 1015 proton collision data, the efficiency is about 96%[161].

1016 4.1.4 Primary Vertex Reconstruction

1017 The primary vertex (PV) reconstruction is able to measure the location of all proton interaction
 1018 vertices in each event consisting of the signal vertex and all vertices from pileup events. First
 1019 tracks are selected to be consistent with being produced promptly in the primary interaction [81].
 1020 Then the tracks are grouped according to the z coordinate of their closest approach to the beam
 1021 line [162] and a vertex fitting algorithm [163] is performed. The primary vertex is found as the
 1022 vertex corresponding to the highest sum of squared track transverse momenta and is taken to
 1023 be the main interaction point. The resolution on the primary vertex is about 14 μm in $r\phi$ and
 1024 about 19 μm in the z direction for primary vertices with the sum of the track $p_T > 100$ GeV
 1025 for 2016 data taking.

1026 4.1.5 Calorimeter clusters

1027 The energy and direction of stable neutral particles such as photons and neutral hadron are recon-
 1028 structed using a cluster algorithm. This algorithm also separates neutral particles from charged
 1029 hadron energy deposits, and reconstructs and identifies electrons and their bremsstrahlung
 1030 photons. Furthermore, the cluster algorithm is contributing to the energy measurements of
 1031 charged hadrons that don't have accurate tracks parameters, e.g. for low quality and high
 1032 transverse momentum tracks. The clustering is performed separately in each subdetector:
 1033 ECAL barrel and endcaps, HCAL barrel and endcaps, and the two preshower layers. The HF has
 1034 no clustering algorithm since the electromagnetic or hadronic components give rise to an HF
 1035 EM or HF HAD cluster.

1036 The clustering algorithm consist of different steps. First seeds are identified when cells have
 1037 an energy larger than the seeding threshold and larger than their neighbouring cells. Then
 1038 topological clusters are made by accumulating cells that share at least a corner with a cell
 1039 already in the cluster and an energy above a cell threshold set to twice the noise level. The
 1040 third step is an expectation maximization algorithm that reconstructs the cluster [155] and
 1041 assumes that the energy deposits are Gaussian distributed. The calorimeter clusters are used
 1042 for reconstructing photons and neutral hadrons. The clusters that are not in the vicinity of the
 1043 extrapolated charged tracks identified as neutral hadrons or photons. If the energy deposits are
 1044 in vicinity of charged tracks, such is the case for charged hadrons, the neutral particle energy
 1045 deposit is measured as an excess over the charged particle deposit.

1046 **4.2 Particle flow identification**

1047 The several PF elements from the various CMS subdetectors are connected through a link
 1048 algorithm. This algorithm tests any pair of elements in an event, only considering nearest
 1049 neighbours in the $\eta\phi$ -plane. The quality of the link is determined via the distance between the
 1050 two elements and PF blocks of elements are formed from elements with a direct link or indirect
 1051 link through common elements. The identification and reconstruction follows a particular order
 1052 in each PF block. After each identification and reconstruction the corresponding PF elements
 1053 (tracks and clusters) are removed from the PF block.

1054 The muons are the first to be identified and reconstructed. These are reconstructed if their
 1055 momenta are compatible with corresponding track only momenta. Then the electron and its
 1056 corresponding brehmstrahung photons, are identified and reconstructed by using of the GSF
 1057 tracking. At the same time, the energetic and isolated photons are identified as well. The
 1058 remaining elements in the PF block are subjected to a cross identification of charged hadrons,
 1059 neutral hadrons, and photons that arise from parton fragmentation, hadronisation, and decays
 1060 in jets. The charged hadron candidate is made from the remaining candidates that have a
 1061 charged particle track associated with them. Then the charged particle energy fraction is
 1062 subtracted from the calibrated energy of the linked calorimeter clusters and the remaining
 1063 energy is assigned to the neutral energy. Depending on the excess of neutral energy in the ECAL
 1064 and HCAL clusters, a photon or a neutral hadron is assigned respectively. The pseudorapidity
 1065 range of the inner tracker limits the information on the particles charge to $|\eta| < 2.4$. Outside
 1066 this range a simplified identification is done for hadronic and electromagnetic candidates only.

1067 **4.3 Pileup mitigation and luminosity measurement**

For the 8 TeV dataset, an average of about 21 pileup interactions happen per bunch cross section. For the dataset taken at 13 TeV, the number of pileup interactions increases to about 27 interactions per bunch crossing. These interactions are spread around the beam axis around the centre of the CMS coordinate system and follow a normal distribution with a standard deviation of about 5 cm [155]. The number of pileup interactions is estimated from the number of interaction vertices reconstructed from charged particle tracks, or from the instantaneous luminosity of the given bunch crossing with dedicated detectors and the inelastic proton-proton crossing. The luminosity of the CMS interaction point is estimated from measuring certain process rates with luminometers such as the pixel detector, HF calorimeter, and the pixel luminosity telescope [164]. The instantaneous luminosity from recorded process rate R is then determined as

$$\text{Ldt} = \frac{Rdt}{\sigma_{\text{fid}}}, \quad (4.1)$$

1068 where $\sigma_{\text{fid}} = \sigma \times A$ corresponds to the fiducial cross section recorded in the luminometer
 1069 acceptance A which is determined using van der Meer scans [165]. The overall uncertainty on
 1070 the luminosity measurement is estimated to be 2.5%.

1071 The luminosity is used to infer to number of pileup interactions in data, which can be used
 1072 to corrected the predefined pileup interactions in simulation. Then an event weight can be

1073 derived from the ratio of the distributions of pileup interactions in data and simulation. For 13
 1074 TeV collisions, the inelastic cross section is measured to be 71.3 ± 3.5 mb [166]. However a
 1075 better agreement in data and simulation for the pileup sensitive variables, such as the number
 1076 of primary vertices, is found with a lower cross section of 69.2 mb with an uncertainty of 4.6%.

1077 4.4 Physics object reconstruction and identification

1078 The particle flow objects are used for building physics objects that are used for analysis. Analyses
 1079 use jets, muons, electrons, photons, taus and missing transverse momentum \vec{p}_T with extra,
 1080 analysis dependent requirements. In the following section, only the physics objects used
 1081 throughout this thesis are discussed.

1082 4.4.1 Muons

1083 The muon candidates used for analysis in this thesis correspond to the tight and loose working
 1084 point. Detailed reports on the performance can be found in [167].

1085 The tight working point rejects objects wrongly reconstructed as muons from hadron showers
 1086 that reach the muon system (punch-throughs), by requiring that the global muon fit includes
 1087 at least one valid hit in the muon chambers for which at least two muon segments in two
 1088 muon stations are present. Furthermore, the muon tracks should have a global fit yielding a
 1089 goodness-of-fit of $\chi^2/\text{ndof} < 10$. Requiring at least one pixel hit in the muon track suppresses
 1090 the decay of muons in flight. Also a minimum of five hits in the tracker is required. Cosmic
 1091 muons and muons originating from pileup interactions are rejected by constricting the distance
 1092 of the muon with respect to the primary vertex by putting limits on $d_{x,y} < 2$ mm and $d_z < 5$
 1093 mm. Also muons according to the loose muon working point will be used in the thesis. These
 1094 are either global muons or tracker muons reconstructed from the particle flow muon object. In
 1095 Table 4.1, the muon requirements for the muons used throughout this thesis are summarised.
 1096 In Figure 4.2, the muon efficiencies for data and simulation is presented. These efficiencies are
 1097 estimated from tag-and-probe methods [167]. Overall, the efficiency is about 95-100%, with
 1098 two drops due to the crack between the wheels of the DT system. The differences between
 1099 data and simulation are corrected by applying p_T - and η -dependent scale factors ($\epsilon_{\text{data}}/\epsilon_{\text{MC}}$)
 1100 to simulated events.

In addition to the identification criteria, the muons are required to be spatially isolated from electromagnetic and hadronic activity. The relative lepton isolation is defined as estimating the total transverse energy of the particles emitted around the direction of the lepton by defining a cone of radius ΔR in $\eta\phi$ plane around the lepton direction. Then a summed energy is calculated from the charged hadrons (CH), neutral hadrons (NH), photons (γ), excluding the lepton itself. This sum is then corrected to remove the energy coming from pileup interactions. The relative isolation for muons \mathcal{I}_μ is defined as [155]:

$$\mathcal{I}_\mu = \frac{\sum p_T(\text{CH}) + \max(0., \sum E_T(\text{NH}), \sum E_T(\gamma) - 0.5 \times \sum E_T(\text{CH}))}{p_T(\mu)}, \quad (4.2)$$

1101 where a cone of $\Delta R = 0.4$ is adopted and the pileup mitigation is based on the $\Delta\beta$ correction.
 1102 The $\Delta\beta$ correction estimates the pileup energy as half of the contribution coming from charged

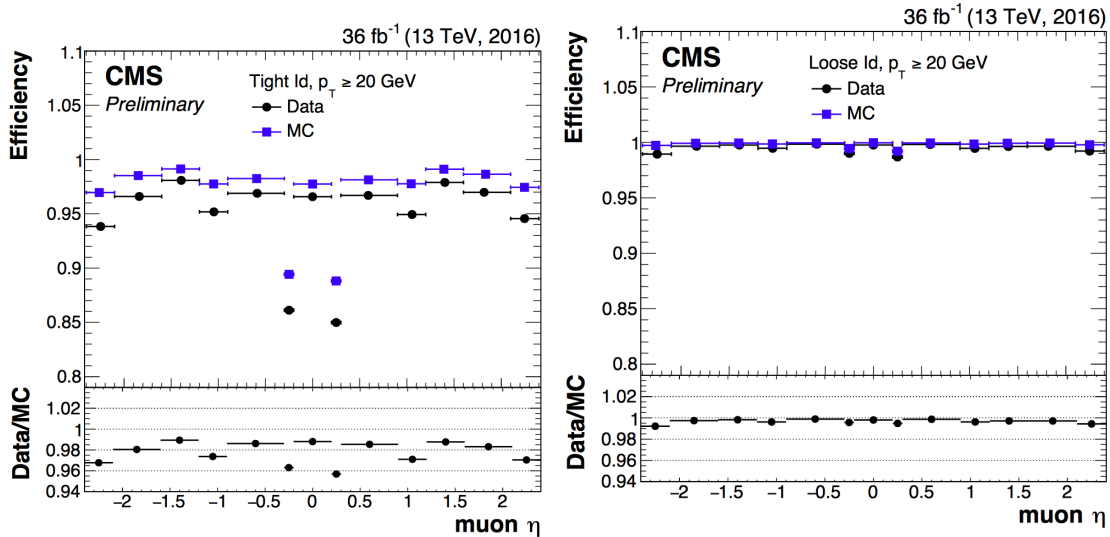


Figure 4.2: Comparison of the muon tight ID (left) and loose ID (right) efficiencies in data and simulation as a function of the pseudorapidity of the muon using the full 2016 dataset. Figure taken from [167].

hadrons. For tight ID muons, this relative isolation should $\mathcal{I}_\mu < 0.15$, while for loose muons this should be $\mathcal{I}_\mu < 0.25$. In Figure 4.3, the isolation efficiencies as a function of the pseudo rapidities using the tag and probe method are shown for the tight muon working point. The efficiencies are 85-100% and have a decline for low- p_T muons. The differences between data and simulation are accounted for by applying η - and p_T -dependent scale factors on the simulation.

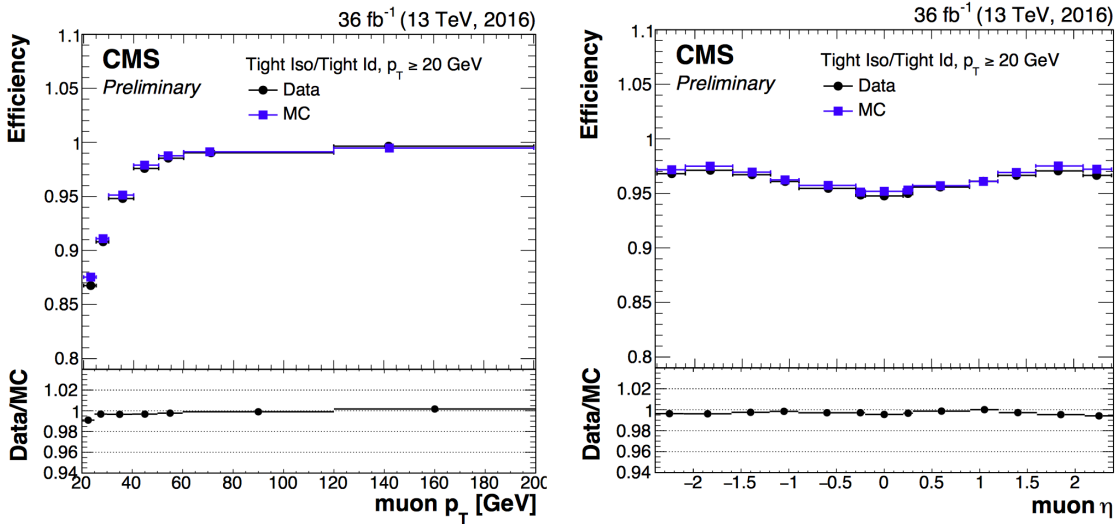


Figure 4.3: Comparison of the muon tight isolation requirement with the muon tight ID efficiencies in data and simulation as a function of the transverse momentum (left) or pseudorapidity (right) of the muon using the full 2016 dataset. Figure taken from [167].

Table 4.1: Muon requirements for the tight and loose working points, used throughout this thesis.

Properties	Loose Muons	Tight Muons
Global muon or Tracker Muon	One or the other	Both
Particle Flow muon	Y	Y
$\chi^2/ndof$ of global muon track fit	N/A	< 10
Nb. of hit muon chambers	N/A	> 0
Nb. of muon stations contained in the segment	N/A	> 1
Size of the transverse impact parameter of the track wrt. to the PV	N/A	$d_{xy} < 2 \text{ mm}$
Longitudinal distance wrt. the PV	N/A	$d_z < 5 \text{ mm}$
Nb. of pixel hits	N/A	> 0
Nb. of tracker layers with hits	N/A	> 5
Relative Isolation	<0.25	<0.15

1108 4.4.2 Electrons

1109 The electrons candidates used correspond to the tight and veto working points. The study of
 1110 the electron reconstruction and identification performance can be found in [161].

1111 Starting from an electron PF candidate with a GSF track that is outside the barrel-endcap
 1112 transition region ($1.4443 < |\eta| < 1.5660$), several requirements are set. The electron track
 1113 should not have more than one (two or three) missing hit in the innermost layer for the tight (veto)
 1114 working point. This dismisses electrons from photon conversions are dismissed. Additionally, a
 1115 photon conversion veto is applied by testing if a pair of electron tracks is originating from a
 1116 common displaced vertex. Furthermore, refined cuts are applied on the shower shape variables
 1117 such as the difference in η or ϕ between the energy weighted supercluster position in the
 1118 ECAL and the track direction in at the innermost tracker position ($\Delta\eta_{\text{in}}$, $\Delta\phi_{\text{in}}$), and the ECAL
 1119 crystal based shower covariance in the η direction ($\sigma_{\eta\eta}$). These cuts also include energy related
 1120 variables such as the absolute difference between the inverse electron energy measured in the
 1121 ECAL and the inverse momentum measured in the tracker ($|1/E - 1/p|$), and the ratio of the
 1122 energy measured in the HCAL and ECAL (H/E). Unlike the muon case, the identification criteria
 1123 also contain requirements on the isolation of the electrons.

Similar to the muons, the electron relative isolation is determined from the sum of the particles in a cone around the electron itself. The cone radius used for electrons is $\Delta R = 0.3$ and a ρ correction for pileup mitigation is applied. For this correction, the expected pileup energy inside the isolation cone is estimated from the median density energy per area of pileup contamination (ρ), computed event by event, and the effective area ($A_{\text{eff.}}$) [155]. This effective area is estimated from simulation and denotes the expected amount of neutral energy from

pileup interactions per ρ within the isolation cone as a function of the pseudo rapidity of the associated ECAL superclusters. Table 4.2 shows the values used for 13 TeV data. The relative electron isolation \mathcal{I}_e is calculated as

$$\mathcal{I}_e = \frac{\sum p_T(\text{CH}) + \max(0., \sum E_T(\text{NH}), \sum E_T(\gamma) - \rho \times A_{\text{eff}})}{p_T(e)}. \quad (4.3)$$

Table 4.2: The effective areas A_{eff} used for the electron relative isolation [168].

η region	$A_{\text{eff.}}$
$0 < \eta < 0.1752$	0.1703
$1.0 < \eta < 0.1479$	0.1715
$1.479 < \eta < 2.0$	0.1213
$2.0 < \eta < 2.2$	0.1230
$2.2 < \eta < 2.3$	0.1635
$2.3 < \eta < 2.4$	0.1937
$2.4 < \eta < 2.5$	0.2393

1124

1125 The efficiency of electron identification is estimated from $Z \rightarrow e^- e^+$ events via the tag-and-
 1126 probe method and is shown in Figure 4.4 for the tight working point. The efficiencies reach
 1127 95 – 100%. The difference between data and simulation are corrected by dedicated p_T - and η
 1128 dependent scale factors as well.

1129 **4.4.3 Jets**

1130 Jets are reconstructed from all reconstructed particles without the charged hadrons associated to
 1131 pileup vertices. The clustering is done via the anti – k_T algorithm [169] with a radius parameter
 1132 for the cone size of the resulting jet of $R = 0.4$. More information about the jet algorithm
 1133 performance can be found in Ref. [170].

1134 The jets used for the analysis discussed in this thesis uses the loose identification working
 1135 point summarised in Table 4.4. The requirements on the jet constituents are based on the
 1136 assumption that a proper jet originating from the hadronisation of a quark or gluon consists of
 1137 multiple PF particles and types. Therefore, the jet should consist of more than one constituent
 1138 and the neutral hadron fraction and neutral EM energy fractions should be less than 99%. For
 1139 the jets within the tracker acceptance ($|\eta| < 2.4$), at least one constituent has to be a charged
 1140 hadron resulting in a charged hadron energy fraction above 0%. Additionally the charged
 1141 EM energy fraction should be less than 99%. On top of these requirements, objects that are
 1142 labelled as jets and found in vicinity of any isolated lepton, $\Delta R < 0.3$, are removed from the jet
 1143 collection in that event to avoid duplications of objects.

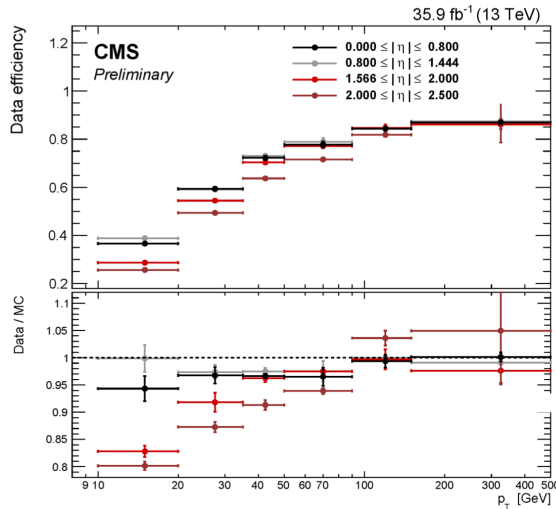


Figure 4.4: Electron identification efficiency as function of the electron transverse momentum from the full 2016 dataset. Figure taken from [161].

Table 4.3: Electron requirements used in this analysis. The requirements are set in the barrel ($|\eta_{supercluster}| \leq 1.479$) and the endcaps ($|\eta_{supercluster}| > 1.479$).

Properties	$ \eta_{supercluster} \leq 1.479$		$ \eta_{supercluster} > 1.479$	
	Veto electron	Tight electron	Veto electron	Tight electron
$\sigma_{\eta\eta}$	< 0.0115	< 0.00998	< 0.037	< 0.0292
$ \Delta\eta_{in} $	< 0.00749	< 0.00308	< 0.00895	< 0.00605
$ \Delta\phi_{in} $	< 0.228	< 0.0816	< 0.213	< 0.0394
H/E	< 0.356	< 0.0414	< 0.211	< 0.0641
relative isolation	< 0.175	< 0.0588	< 0.159	< 0.0571
$ 1/E - 1/p $	$< 0.299 \text{ GeV}^{-1}$	$< 0.0129 \text{ GeV}^{-1}$	$< 0.15 \text{ GeV}^{-1}$	$< 0.0129 \text{ GeV}^{-1}$
expected missing inner hits	≤ 2	≤ 1	≤ 3	≤ 1
pass conversion veto	Y	Y	Y	Y

Table 4.4: Jet criteria used throughout the thesis. The last three requirements are only for jets within the tracker acceptance.

Properties	Loose Jet ID
Neutral hadron fraction	< 0.99
Neutral EM fraction	< 0.99
Number of constituents	> 1
Charged hadron fraction	> 0
Charged multiplicity	> 0
Charged EM fraction	< 0.99

1144 The energy of the reconstructed jets deviates from the energies of the corresponding jets
 1145 clustered from the hadronisation products of true partons from simulations due to non linear
 1146 subdetector response and efficiencies. The jet energy corrections (JEC) calibrate the jets
 1147 in order to have the correct energy scale and resolution. Jet energy scale corrections (JES)
 1148 are determined as a function of pseudorapidity and the transverse momentum from data and
 1149 simulated events by combining several channels and methods. This is extensively described
 1150 in [171]. These corrections account for the effects of pileup, the uniformity of the detector
 1151 response, and residual data-simulation jet energy scale differences. Furthermore, the jet energy
 1152 resolution (JER) is measured in data and simulation as function of pileup, jet size and jet flavour.
 1153 The performance of the jet energy corrections for the 13 TeV dataset can be found in [172].

1154 The JEC are factorised and subsequently correct for the offset energy due to pileup, the detector
 1155 response to hadrons, and residual differences between data and simulation as a function of the
 1156 jet pseudorapidity and transverse momentum. The consecutive steps of JEC are shown in Figure
 4.5. The off set corrections remove the dependence of the jet energy response of additional pileup

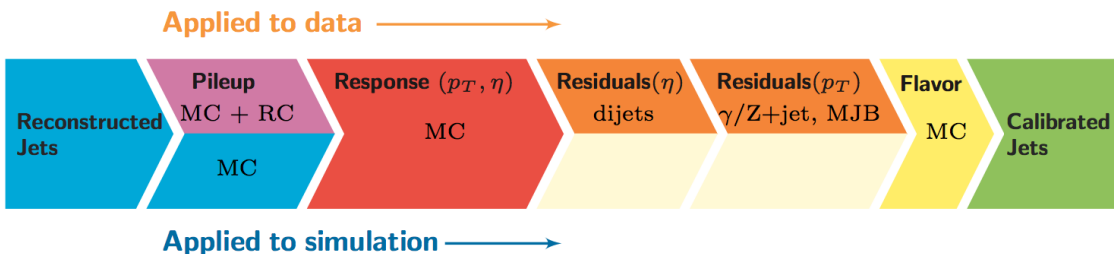


Figure 4.5: The sequence of the JEC for data and simulations. The corrections marked with MC are derived from simulation studies, while RC stands for random cone, and MJB for the analysis of multi-jet events. Figure taken from [171].

1157 activity. It is based on the jet area method, which uses the effective area of the jets multiplied
 1158 by the average density in the event to calculate the offset energy to be subtracted of the
 1159 jets. The correction factors are derived by comparing the jet response with and without pileup

1161 events overlaid. The residual differences between data and detector simulation are determined
 1162 using the random cone method (RC). For this method, many jets are reconstructed in each
 1163 event by clustering particles through placing random cones. This provides a mapping of the
 $\eta\phi$ -space and the average p_T of those jets gives the average energy offset due to pileup [171].
 1165 The next level of corrections have as goal to have an uniform energy response independent
 1166 of the transverse momentum or pseudorapidity of the jet. These corrections are determined
 1167 from simulated events by matching the reconstructed to true particle jets and comparing there
 1168 momenta. The residual corrections between data and simulation are determined by comparing
 1169 the transverse momentum balance in various types of events (multi-jet, Z + jets, and γ + jets),
 1170 using a reference jet in the barrel region. The jet flavour corrections are optional and not used
 1171 for this thesis. More information on the jet flavour corrections can be found in [171]. For jets
 1172 with a transverse momentum above 30 GeV, the uncertainties from the various corrections are
 1173 3-5% for the 13 TeV dataset [172].

After applying JEC, the transverse momentum resolution of the jet is extracted from data and simulated events. There are two methods used to rescale the reconstructed four momentum chosen based on whether or not the simulated jet can be matched to a true jet in simulation. The factors are defined as

$$c_{\text{matched}} = 1 + \frac{p_T^{\text{reco.}} - p_T^{\text{true}}}{p_T^{\text{reco.}}} (s_{\text{JER}} - 1), \\ c_{\text{unmatched}} = 1 + N(0, \sigma_{\text{JER}}) \sqrt{\max(s_{\text{JER}}^2 - 1, 0)}, \quad (4.4)$$

1174 where $N(0, \sigma_{\text{JER}})$ denotes a sample value from a normal distribution centred at zero with
 1175 as standard deviation the relative resolution in simulation σ_{JER} , and s_{JER} the η -dependent
 1176 resolution scale factors. These scale factors are derived from data from di-jet or γ + jets events
 1177 and analysing the p_T balance. The resolution scale factors (data/simulation) are found to be
 1178 1.1-1.2 except for the transition regions around $|\eta| = 3$ and $|\eta| = 1.4$ [172] and given in Table
 1179 4.5.

1180 4.4.4 Jets from b fragmentation

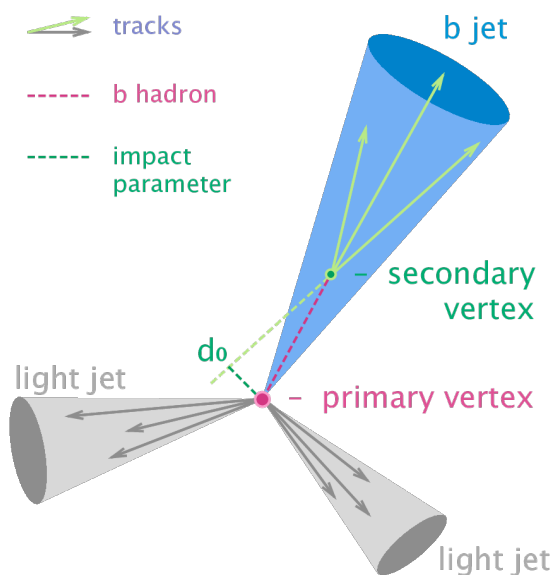
1181 Jets originating from the hadronisation of bottom quarks can be discriminated from jets from
 1182 gluons and light-flavour quarks as well as charm quark fragmentation through the use of b-
 1183 tagging. There are several algorithms developed within CMS to perform b-tagging [173, 174]
 1184 on jets that fall within the pseudorapidity acceptance of the trackers. These algorithms exploit
 1185 the properties of the b quark to identify the jets formed by its fragmentation. These hadrons
 1186 have relative large masses, long lifetimes and daughter particles with hard momentum spectra.
 1187 Additionally, their semi-leptonic decays can be exploited as well. To use b-jet identification
 1188 in an analysis, one needs to know its efficiency and misidentification probability. In general
 1189 these are function of the pseudorapidity and transverse momentum of the considered jet. Their
 1190 performances are directly measured from data by use of b-jet enriched jet samples (multi-jet or
 1191 top-quark decays).

1192 This thesis uses b-jets identified by the Combined Secondary Vertex version 2 (CSVv2)
 1193 algorithm [173]. This algorithm combines secondary vertices together with track based lifetime

Table 4.5: Jet energy scale factors in bins of η with uncertainty

$ \eta $	SF	Uncertainty (\pm)
0-0.5	1.109	0.008
0.5-0.8	1.138	0.013
0.8-1.1	1.114	0.013
1.1-1.3	1.123	0.024
1.3-1.7	1.084	0.011
1.7-1.9	1.082	0.035
1.9-2.1	1.140	0.047
2.1-2.3	1.067	0.053
2.3-2.5	1.177	0.041

information by use of a multivariate technique. The secondary vertex is reconstructed from displaced tracks within a jet, as illustrated in Figure 4.6. The final state b quark is encapsulated in a B meson (e.g. B^\pm , B_0 , B_S) after the hadronisation. This B meson has relatively long lifetime and can travel a measurable distance from the primary vertex before decaying. After reconstruction, the secondary vertices are required to be in accordance with the B meson hypothesis bases on the amount of shared tracks with the primary vertex, the invariant vertex mass to reject kaon decays, and the direction of the tracks compared to the jet axis.

**Figure 4.6:** Sketch showing the common principle of the identification of b-jets. Figure taken from [175]

1201 The b-tagging algorithm performances are evaluated taking into account two cases: discrim-
 1202 ination of b-tagged jets originating from charm quarks, and discrimination of b-tagged jets
 1203 against jets coming from gluons or light (u, d, s) quarks. In Figure 4.7, the misidentification
 1204 probabilities for different b-tagging algorithms within CMS are shown. Based on the misidentifi-
 1205 cation probabilities for a certain threshold on the CSVv2 discriminator, different working points
 1206 are defined. These are shown in Table 4.6. The analysis presented in this thesis uses the loose
 working point which has an average efficiency of 81% and a misidentification rate of 10%.

NOTE: Find reason why I am not using cMVA, omdat CSVv2 op ttbar events is gemeten en cMVA op multijet?

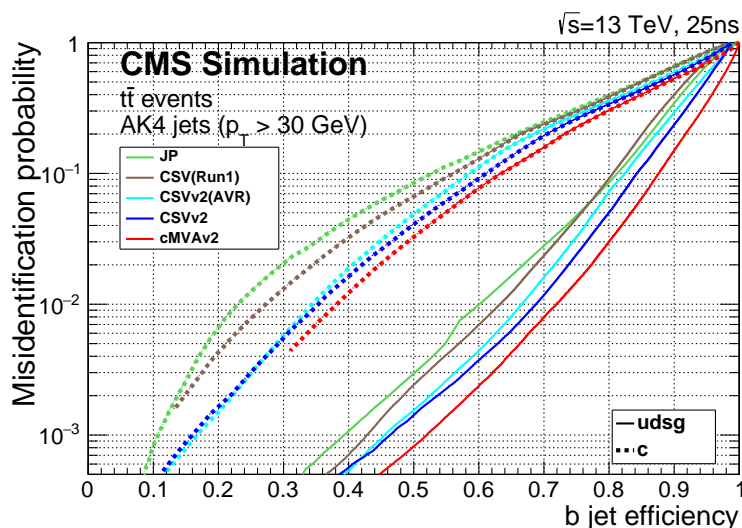


Figure 4.7: Misidentification probabilities of various b-tagging algorithm in simulation. Figure taken from [174].

Table 4.6: Working points used for tagging jets as coming from b quarks for the CSVv2 discriminant.

WP	CSVv2 discr cut	b-tag eff.	misid. prob.
Loose (L)	> 0.5426	≈ 81%	≈ 10%
Medium (M)	> 0.8484	≈ 66%	≈ 1%
Tight (T)	> 0.9535	≈ 46%	≈ 0.1%

1207

1208 The efficiency of tagging a jet as coming from a bottom quark in simulation typically deviates
 1209 somewhat from data. Efficiency scale factors $\epsilon_b^{\text{data}}/\epsilon_b^{\text{MC}}$ are derived from data to account for
 1210 those differences. These scale factors are η -, p_T -, and flavour dependent, where the flavour
 1211 of the jet is determined from matched generated hadrons. For cut based analyses these scale
 1212 factors are applied to the b-tagging efficiencies and mistag rates according to the chosen working
 1213 point [174]. For shape based analysis however, such as the one presented in this thesis, the
 1214 scale factors are applied on the distribution of the b-tagging discriminator. This is the so-called
 1215 IterativeFit method [176].

1216 The uncertainties related to the IterativeFit method cover possible shape discrepancies between
 1217 data and simulation. The uncertainty coming from the purity of the sample is subdivided into
 1218 two uncorrelated uncertainties based on the purity of the light flavoured (lf) and heavy flavoured
 1219 (hf) jet contributions in the sample. Furthermore, the jet energy scale results in jets migrating
 1220 from one p_T bin to an other, having an influence on bin dependent scale factors. The statistical
 1221 fluctuations of the limited amount of entries in each bin are also accounted for and have an
 1222 influence on the scale factor uncertainties. These have four uncorrelated sources: two for heavy
 1223 flavour and two for light flavour jets. Since the uncertainty on the scale factors for the jets
 1224 originating from a charm quark (cf) is determined from the uncertainty on the b scale factors
 1225 resulting in two independent uncertainties [176].

1226 4.4.5 Missing transverse energy

The missing transverse momentum \vec{p}_T and energy E_T^{miss} resulting from particles that do not interact with the detector material, are calculated by balancing the vectorial sum of the transverse momenta of all particles:

$$E_T = |\vec{p}_T|, \quad (4.5)$$

$$\vec{p}_T = - \sum_{i=1}^{N_{\text{particles}}} \vec{p}_{T,i}.$$

1227 The missing transverse energy is influenced by the minimum thresholds in calorimeters, the
 1228 inefficiencies in the tracker, and the non-linear response of the calorimeter to hadronic particles.
 1229 The bias is reduced by correcting the transverse momentum of the jets to particle jet p_T via the
 1230 JEC and propagating it to the missing transverse momentum. The performance of the missing
 1231 transverse energy reconstruction can be found in [177].

1232 4.5 Summary of corrections

1233 Throughout the chapter several corrections are introduced to improve the agreement between
 1234 data and simulation. These corrections are sources of systematic uncertainties for the anal-
 1235 ysis presented in this thesis. Therefore a summary of the corrections and their associated
 1236 uncertainties is provided.

1237 **Lepton scale factors** The systematic uncertainty on the lepton scale factors consist of three
 1238 sources: identification, isolation and tracking. The applied scale factors are varied
 1239 independently within one standard deviation of their measured uncertainties to account
 1240 for their systematic impact on the measurements.

1241 **Jet energy corrections** The momenta of the reconstructed jets are corrected to match the
 1242 expected true energy derived from the hadronisation products of partons in simulation.
 1243 Furthermore, residual corrections and smearing is applied to match the overall energy
 1244 scale and resolution for simulation and data. These corrections are also propagated to
 1245 the missing transverse energy. The systematic uncertainties due to these scale factors are
 1246 estimated by varying them within their uncertainties and repeating the measurements
 1247 with recalibrated jets and missing transverse energy.

1248 **CSVv2 discriminant shape reweighting** There are three sources of uncertainty contributing
1249 to the measurement of the scale factors: statistical uncertainties, jet energy scale and
1250 the purity of the sample. The jet energy scale uncertainty is 100% correlated to the jet
1251 energy uncertainties and is evaluated simultaneously. The uncertainty coming from the
1252 purity of the sample is subdivided into two uncorrelated uncertainties based on the purity
1253 of the light flavoured (lf) and heavy flavoured (hf) jet contributions in the sample. A
1254 one sigma shift in each of the two purity contributions corresponds to a higher/lower
1255 contribution in the purity of the considered flavours. The statistical uncertainties has
1256 four uncorrelated sources, two for heavy flavour and two for light flavour jets. One of
1257 the uncertainties correspond to the shift consistent with the statistical uncertainties of
1258 the sample, while the other is propagated in a way that the upper and lower ends of the
1259 distribution are affected with respect to the centre of the distribution. The uncertainty
1260 on the charm jet scale factors (cf) is obtained from the uncertainty on the heavy flavour
1261 scale factors, doubling it in size and constructing two nuisance parameters to control the
1262 charm flavour scale factors and treating them as independent uncertainties.

1263 **Pileup** Varying the minimum bias cross section, used to calculate the pileup distribution by
1264 $\pm 4.6\%$, results in a systematic shift in the pileup distribution. The uncertainty is estimated
1265 by recalculating the pileup weights to the distributions associated to the minimum bias
1266 cross sections.

1267 **Luminosity** The luminosity is measured with a global uncertainty of 2.5%, affecting the ex-
1268 pected number of events.

Event selection and categorisation

5

1269

1270 A basic event selection is made for selecting signal like events and is discussed in [Section 5.1](#).
1271 Also the effect corrections applied to simulation and data, summarised in [Section 4.5](#) is shown.
1272 The analysis strategy is presented in [Section 5.2](#), defining the signal and background regions
1273 to constrain the huge SM background compared to the expected signal. [Section 5.4](#) discusses
1274 each region that is entering the analysis. On top of the use of background estimation from
1275 control regions, backgrounds that have prompt leptons contaminated by real leptons either from
1276 decays of tau leptons or from hadronized mesons or baryons (collectively commonly referred as
1277 “non-prompt leptons”) as well as by hadrons or jets misidentified as leptons¹ are evaluated with
1278 a data-driven method discussed in [Section 5.3](#).

1279 5.1 Baseline event selection and filters

1280 In this analysis a search is performed in a final state made up of a Z boson and a top quark,
1281 associated or not with a jet, in the leptonic decay of the Z boson and the top quark. The leading
1282 order Feynman diagrams can be seen in [Figure 5.1](#) and [Figure 5.2](#). The signal considers both the
1283 single top quark FCNC (tZ in the final state) and the top quark pair FCNC (tZq with $q = c, u$ in
1284 the final state) events. Their final state signatures consist of three leptons, considering electrons
1285 or muons, and a jet originating from a b quark. For FCNC tZq , there is an additional up or charm
1286 jet. Leptons from tau decays are not vetoed and are entering the analysis via their leptonic
1287 decays. Four different lepton channels based on lepton flavour are considered: 3e, 2e1 μ , 1e2 μ ,
1288 and 3 μ .

1289 The CMS collaboration recorded in the course of 2016 proton at 13 TeV collisions data with
1290 a total recorded integrated luminosity of 35.9 fb^{-1} . The baseline event selection has a goal to
1291 substantially reject SM background events, whilst maintaining a high signal efficiency. The
1292 CMS trigger system, described in [Section 2.2.3](#), filters out the main of the collision events from
1293 uninteresting processes and dedicated trigger paths are defined to single out the events with our
1294 required detector signature. The trigger paths are chosen based on on-line triggering objects
1295 with at least one muon (M), at least one electron (E), at least two muons (MM), at least two

¹These two classes of contamination will be referred to as not prompt-lepton (NPL) samples.

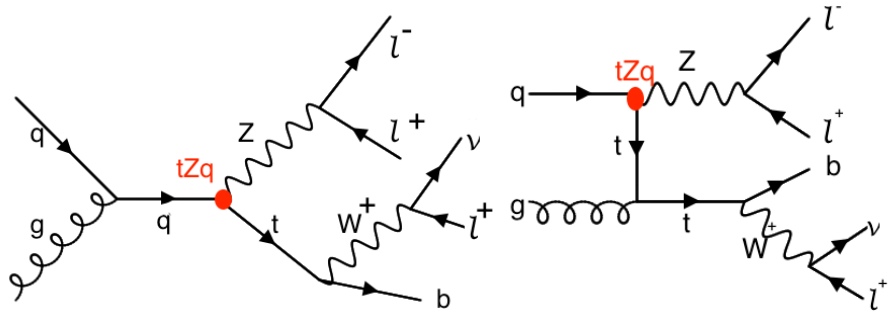


Figure 5.1: Single top quark Feynman diagrams at leading order. The vertex labelled tZq is the sought-for FCNC interaction.

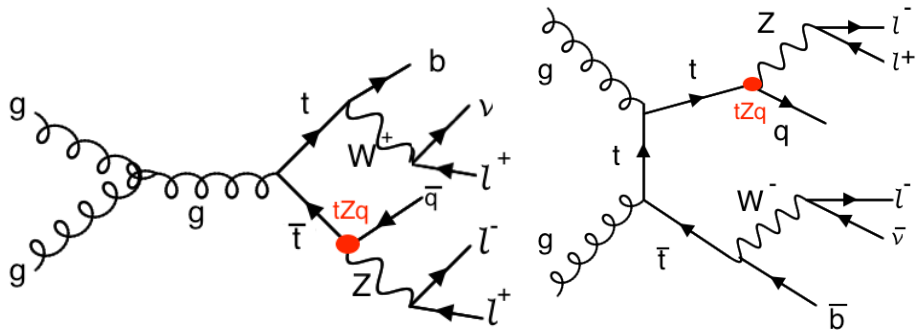


Figure 5.2: Top quark pair Feynman diagram at leading order. The vertex labelled tZq is the sought-for FCNC interaction.

1296 electrons (EE), at least one muon and an electron (ME), at least three muons (MMM), at least
 1297 three electrons (EEE), at least two muons and one electron (MME), or at least two electrons
 1298 and one muon (EEM). For the MC simulation a simple *or* of all triggers is taken and the event
 1299 is considered when it passes one of the trigger paths. For data however, double counting of the
 1300 same event has to be taken into account and a procedure to avoid double counting has been
 1301 put into place. It consists of vetoing in a given dataset the events that are already selected in
 1302 another, as given in Table 5.1.

1303 For the single lepton triggers, at least one electron (muon) with a transverse momentum
 1304 p_T higher than 32 (24) GeV is required. The dilepton triggers require an electron (muon)
 1305 with $p_T > 23$ GeV and a muon (electron) with $p_T > 8$ GeV, or an electron (muon) with
 1306 $p_T > 23$ (17) GeV and an electron (muon) with $p_T > 12$ (8) GeV. Events collected by the
 1307 trilepton triggers require an electron (muon) with $p_T > 16$ (12) GeV, a second electron (muon)
 1308 of $p_T > 12$ (10) GeV, and a third electron (muon) with $p_T > 8$ (5) GeV. The mixed trilepton
 1309 trigger events require two electrons (muons) with $p_T > 12$ (9) GeV and a third muon (electron)
 1310 with $p_T > 8$ (9) GeV. The HLT trigger paths used in data and simulation are summarised in
 1311 Table 5.2.

1312 In order to ensure a full trigger efficiency, the off-line p_T thresholds are set higher than the on-

Table 5.1: Trigger logic used to select data events in order to avoid double counting.

Dataset	Trigger Logic
1e1μ	EM EEM MME
2μ	(MM MMM) && !(EM EEM MME)
2e	(EE EEE) && !(MM MMM) && !(EM EEM MME)
single μ	M && !(EE EEE) && !(MM MMM) && !(EM EEM MME)
single e	E && !M && !(EE EEE) && !(MM MMM) && !(EM EEM MME)

line trigger thresholds. Selected electrons (muons) are required to have $p_T > 35$ (30) GeV and $|\eta| < 2.1(2.4)$. The electrons and muons corresponding to a tight working point, as discussed in Section 4.4.1 (Table 4.1) and Section 4.4.2 (Table 4.3), are used for analysis. Only events with exactly three leptons are being considered. Events with extra leptons according to looser working points are vetoed. The trigger efficiency estimation is described in Section 5.1.2 and is approximately 100%. To ensure that all reconstructed particles considered for the analysis are corresponding to a proton interaction and to remove signals from beam halo particles as well as detector noise,, several filters are used. These are described in Section 5.1.1.

In addition to three leptons, jets and missing transverse energy are expected from the signal signature. The jets are reconstructed using the anti – k_T algorithm with a distance parameter of 0.4 using the particle flow particles that are not identified as isolated leptons as input. The jet momentum is determined as the vectorial sum of the particles contained in the jet. Additional selection criteria are applied to each event to remove spurious jet-like features originating from isolated noise patterns in certain hadron calorimeter regions. The jet requirements are discussed Section 4.4.3. The jets are calibrated in simulation and in data separately, accounting for deposits from pileup and the non-linear detector response. Calibrated jets with $p_T > 30$ GeV and $|\eta| < 2.4$ are selected for the analysis. A selected jet may still overlap with the selected leptons leading to a double-counting of reconstructed objects. To prevent such cases, jets that are found within a cone of $R = 0.3$ around any of the signal electrons (muons) are removed from the collection of selected jets. The jets originating from b quarks are tagged using the CSVv2 algorithm, which combines the information of displaced tracks with information of secondary vertices associated with the jet using a multivariate technique. The jets are tagged as a jet coming from a b quark (b-tagged) if the CSVv2 discriminator is above a certain threshold. This analysis uses a threshold that results in an average b-tagging efficiency of 81% and a misidentification rate of 10%. More information about b-tagging can be found in Section 4.4.4.

The missing transverse momentum vector \vec{p}_T is defined as the projection on the plane perpendicular to the beams of the negative vector sum of the momenta of all reconstructed particles in an event. Its magnitude is denoted by E_T^{miss} as shown in Section 4.4.5. Its longitudinal component is calculated by limiting the lepton + neutrino to the W boson mass. In case two solutions arise, the mass closest to the known top quark mass is used.

Table 5.2: HLT trigger paths used to select data and simulation events.

Trigger path name	Trigger type
HLT_Mu23_TrkIsoVVL_Ele8_CaloIdL_TrackIdL_IsoVL_v	ME
HLT_Mu23_TrkIsoVVL_Ele8_CaloIdL_TrackIdL_IsoVL_DZ_v	ME
HLT_Mu8_TrkIsoVVL_Ele23_CaloIdL_TrackIdL_IsoVL_v	ME
HLT_Mu8_TrkIsoVVL_Ele23_CaloIdL_TrackIdL_IsoVL_DZ_v	ME
HLT_DiMu9_Ele9_CaloIdL_TrackIdL_v	MME
HLT_Mu8_DiEle12_CaloIdL_TrackIdL_v	EEM
HLT_IsoMu24_v	M
HLT_IsoTkMu24_v	M
HLT_Ele32_eta2p1_WPTight_Gsf_v	E
HLT_Mu17_TrkIsoVVL_Mu8_TrkIsoVVL_v	MM
HLT_Mu17_TrkIsoVVL_TkMu8_TrkIsoVVL_v	MM
HLT_Mu17_TrkIsoVVL_Mu8_TrkIsoVVL_DZ_v	MM
HLT_Mu17_TrkIsoVVL_TkMu8_TrkIsoVVL_DZ_v	MM
HLT_TripleMu_12_10_5_v	MMM
HLT_Ele23_Ele12_CaloIdL_TrackIdL_IsoVL_DZ_v	EE
HLT_Ele16_Ele12_Ele8_CaloIdL_TrackIdL_v	EEE

1343 5.1.1 Event cleaning

1344 Some events arising from instrumental noise and beam backgrounds might end up in the
 1345 data [177, 178]. Spurious deposits may appear in the ECAL from non collision origins such as
 1346 beam halo particles, or from particles hitting the sensors in the ECAL photodetectors. Conjointly,
 1347 dead ECAL cells can cause artificial missing transverse energy. Also the HCAL can cause spurious
 1348 energy from particle interactions with the light guides and the photomultiplier tubes of the
 1349 HF, as well as noisy hybrid photo diodes. In CMS, different algorithms, so-called filters, are
 1350 developed to identify and suppress these events.

1351 The ECAL electronics noise and spurious signals from particle interactions with photo detectors
 1352 are mostly removed via topological and timings based selection using ECAL information only.
 1353 The remaining effects such as anomalously high energy crystals and the lack of information
 1354 for channels due to inefficiencies in the read out are removed through dedicated events filters.
 1355 Five ECAL endcap supercrystal have been identified for giving anomalously high energies due
 1356 to high amplitude pulses in several channels at once, and are masked. Furthermore, the crystal
 1357 read out from a small amount of ECAL towers is not available. However, their trigger primitive

information is still available making it possible to estimate the magnitude of unmeasured energy and when the value is too large, the event is filtered out.

The machine induced particles, via beam-gas / beam-pipe/... interactions, that are flying with the beam affect the physics analysis. They leave a calorimeter deposit along a line at constant ϕ in the calorimeter, and interactions in the CSCs will often line up with this deposit. This can be seen in Figure 5.3. Therefore, events containing such beam halo particles are removed from the selection with the CSC Beam Halo Filter. This filter uses information related to the geometric quantities, energy deposits, and timing signatures. For 2016, the filter rejects 85% in a halo-enriched sample, whereas the mistag probability determined from simulation if found to be less than 0.01%.

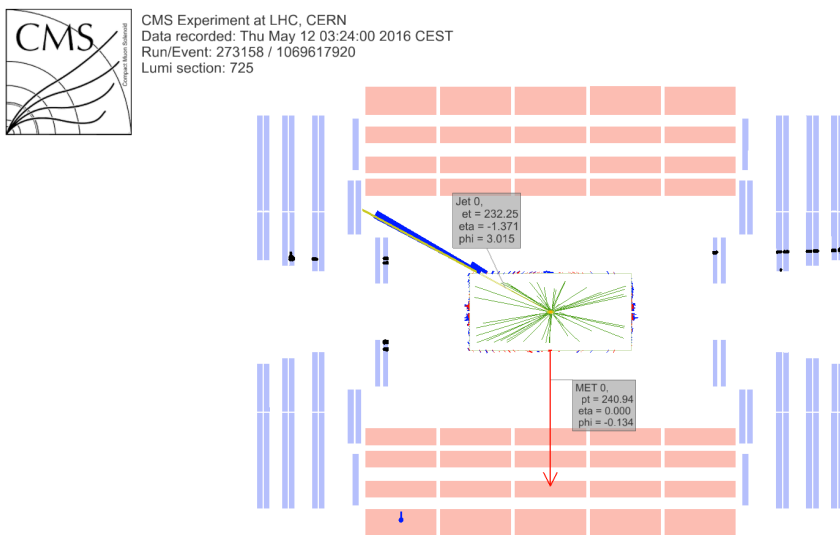


Figure 5.3: Event display of a beam halo event with collinear hits in the CSC (black), missing transverse energy of 250 GeV and a jet of 232 GeV. The hadronic deposit is spread in η , but narrow in ϕ . Figure taken from [177].

Furthermore, there is anomalous high missing transverse energy coming from low quality muons that lead to high- p_T tracks, but are considered not good by the particle flow algorithm. These low quality tracks will be mislabelled as charged hadrons and will therefore be used in the calculation of the missing transverse energy. By investigation the purity of the reconstructed tracks and the relative transverse momentum error of the muons, these events can be filtered out.

Supplementary to previous filters, only events with where the first primary vertex is a well reconstructed primary vertex are selected. The reconstructed primary vertex should have at least five degrees of freedom, the longitudinal distance from the beam spot is maximally 24 cm ($d_z < 24$ cm), and the transversal distance from the beam spot is maximally 2 cm ($d_{xy} < 2$ cm).

1378 **5.1.2 Estimation of the trigger efficiency**

1379 The trigger efficiency in data is estimated using a data sample collected using unprescaled E_T^{miss}
 1380 triggers. These allow events with a missing transverse energy higher than 110 GeV(120 GeV)
 1381 and that the scalar sum of the transverse momenta of the reconstructed PF jets $H_T^{\text{trig.}}$ is at least
 1382 300 GeV (120 GeV), or a calorimeter (PF) E_T^{miss} higher than 200 GeV(300 GeV). For an HB-HE
 1383 cleaned event the PF missing transverse energy threshold is lowered to 170 GeV. These trigger
 1384 paths are summarised in [Table 5.3](#) and chosen to be completely uncorrelated with the lepton
 triggers given in [Table 5.2](#).

Table 5.3: Unprescaled E_T^{miss} HLT trigger paths for estimating the trigger efficiency. An *or* of the triggers
 is used to select events.

Trigger path	Requirement
HLT_PFHT300_PFMET110_v*	PF $E_T^{\text{miss}} > 110$ GeV, PF $H_T^{\text{trig.}} > 300$ GeV
HLT_MET200_v*	calorimeter $E_T^{\text{miss}} > 200$ GeV
HLT_PFMET300_v*	PF $E_T^{\text{miss}} > 300$ GeV
HLT_PFMET120_PFHT120_IDTight_v*	PF $E_T^{\text{miss}} > 120$ GeV, PF $H_T^{\text{trig.,tightWP}} > 120$ GeV
HLT_PFMET170_HBHECleaned_v*	PF $E_T^{\text{miss}} > 170$ GeV, cleaned for HB/HE anomalous signals

1385

The trigger efficiency is studied on the main background, namely WZ+jets, with all corrections applied. For this study, the events passing a three lepton cut and at least one jet are being used. The corresponding efficiencies are then calculated as

$$\epsilon_{\text{data}} = \frac{\text{Nb. of events passing lepton and MET triggers}}{\text{Nb. of events passing MET triggers}} \quad (5.1)$$

$$\epsilon_{\text{MC}} = \frac{\text{Nb. of events passing lepton triggers}}{\text{Nb. of total events}} \quad (5.2)$$

The resulting efficiencies and scale factors can be found in [Table 5.4](#), where the scale factors are defined as

$$SF = \frac{\epsilon_{\text{data}}}{\epsilon_{\text{MC}}} \quad (5.3)$$

1386 More detailed scale factors and efficiencies can be found in [Appendix A](#).

1387 The trigger efficiencies are also measured in function of the p_T of the leptons for which the
 1388 distributions can be found in [Appendix A](#). The resulting scale factors can be found in Figure
 1389 [Figure 5.4](#). The trigger efficiencies are measured to be nearly 100% for both simulation and
 1390 data. The results are dominated by statistics and assigning a large uncertainty to the trigger
 1391 efficiency based on the dataset collected by E_T^{miss} triggers would be over conservative. A one
 1392 percent uncertainty on the trigger selection for the 2e1 μ and 3 μ final states, and 5% for the
 1393 3e and 1e2 μ final states is assigned instead. No scale factors will be applied on simulation as
 1394 they are close to unity. Control plots are made in the dilepton region to validate all corrections
 applied to simulation and can be found in [Appendix B](#).

NOTE: 1395
 Make sure
 this is the
 case

Table 5.4: Trigger scale factors for each channel, after three lepton + jets cut, in the Z mass window, by counting number of events.

	all	3 μ	3e	2e1 μ	1e2 μ
	1.0000	1.0000	0.9541	1.0006	1.0004%

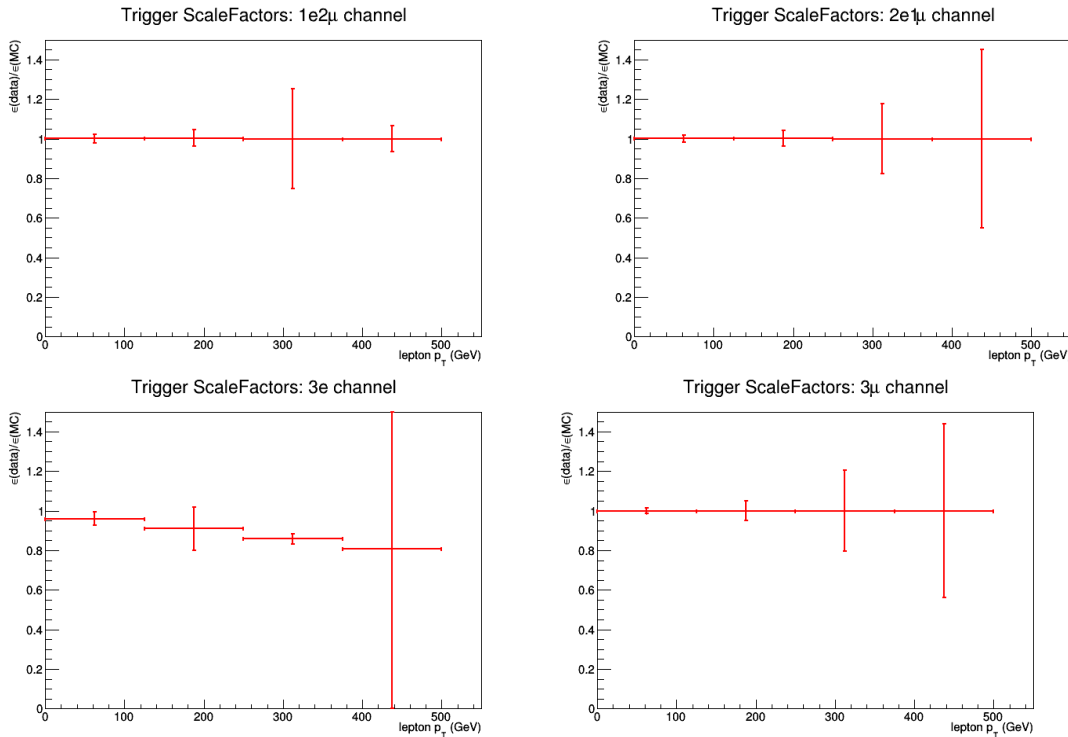


Figure 5.4: The trigger scale factors measured as a function of lepton p_T , using the dataset collected by E_T^{miss} triggers and WZ simulation, after a 3 lepton and jets selection, in the Z mass window. All corrections to simulation are applied. Left, upper: 1e2 μ channel. Right, upper: 2e1 μ channel. Left, lower: 3e channel. Right, lower: 3 μ channel

1396 5.1.3 Corrections

1397 Mismatches between data and simulation are corrected for via the use of scale factors. These are
 1398 elaborately discussed in [Section 4.4](#). In this section a short overview of the applied corrections
 1399 is given and their effect on a dilepton selection is shown.

1400 Pileup reweighting

1401 In data, the number of interactions per bunch crossing (pileup) is calculated with a minimum
 1402 bias cross section of 69.2 mb. The number of simulated pileup events is then reweighed to
 1403 match the expected number of pileup events in data. Pileup reweighting manifests itself as an
 1404 altered shape of the number of reconstructed primary vertices as can be seen in [Figure 5.5](#).

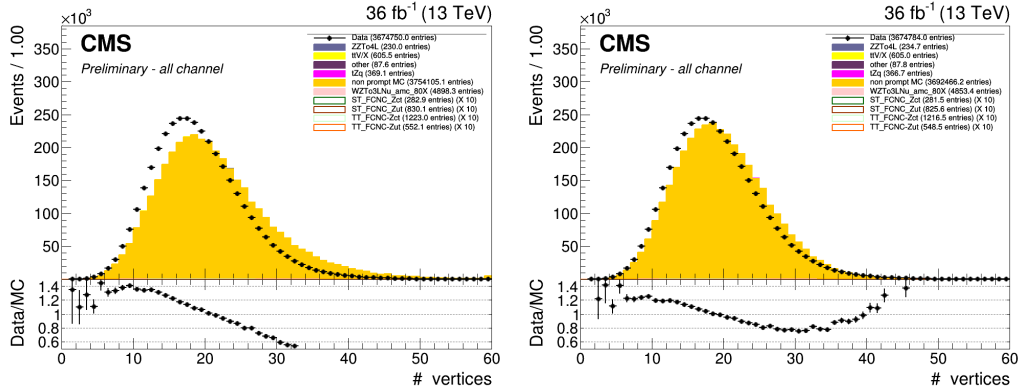


Figure 5.5: The number of primary vertices before (left) and after (right) pileup reweighting. After a dilepton plus jets selection, in the Z mass window.

1405 Note that Figure 5.5 indicates that even after pileup reweighting, the primary vertex multi-
1406 plicity is not well described by simulation. This is a known effect, and using a minimum bias
1407 cross section with a slightly lower value is found to better describe the data. However, the b
1408 tagging scale factors are only provided for the nominal inelastic cross section, and thus this
1409 value is used.

1410 Lepton scale factors

The efficiency to select leptons is different in simulation (ϵ_{MC}) compared to the data (ϵ_{data}). This is corrected for by applying lepton scale factors (SF) to the simulation that are defined as

$$SF = \frac{\epsilon_{\text{data}}}{\epsilon_{\text{MC}}} \quad (5.4)$$

These scale factors are measured for the identification, isolation, tracking and trigger efficiencies of the objects as a function of p_{T} and η (see Section 4.4.1 and Section 4.4.2). Multiplying these scale factors for each lepton provides an overall efficiency:

$$SF_{\text{global}}^{\mu} = \prod_{\text{i}}^{\#\mu} SF_{\text{ID}}^{\mu}(p_{\text{T}}, \eta) SF_{\text{Iso.}}^{\mu}(p_{\text{T}}, \eta) SF_{\text{Trig.}}^{\mu}(p_{\text{T}}, \eta) SF_{\text{track}}^{\mu}(p_{\text{T}}, \eta), \quad (5.5)$$

$$SF_{\text{global}}^e = \prod_{\text{i}}^{\#e} SF_{\text{ID}}^e(p_{\text{T}}, \eta) SF_{\text{Iso.}}^e(p_{\text{T}}, \eta) SF_{\text{Trig.}}^e(p_{\text{T}}, \eta) SF_{\text{track}}^e(p_{\text{T}}, \eta). \quad (5.6)$$

1411 The effect of the scale factors can be found in Figure 5.7 for the electron scaling and Figure 5.6
1412 for the muons. The trigger efficiencies are estimated in Section 5.1.2.

1413 Additionally, corrections are made for the energy resolution of the leptons. For the electrons,
1414 energy smearing and regression is applied [179]. The energy regression uses the detector
1415 information to correct the electron energy in order to have the best energy resolution by
1416 correcting local energy containment, material effects, etc.. The energy scale and smearing

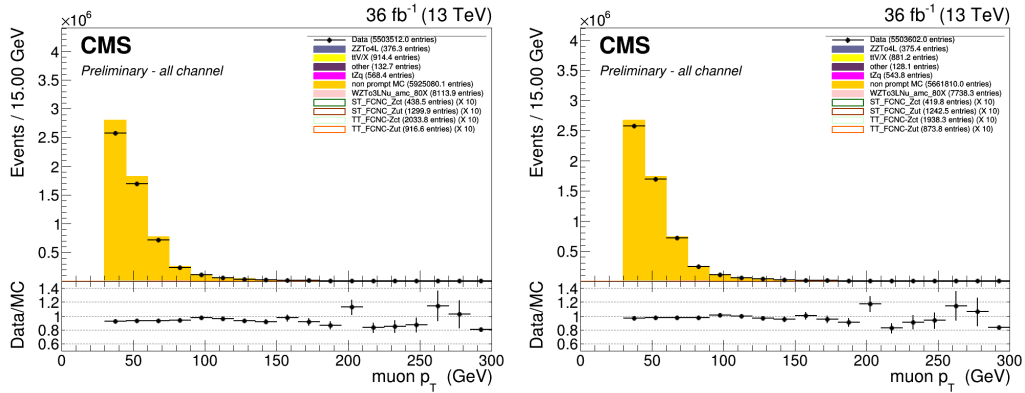


Figure 5.6: The p_T of the muons before (left) and after (right) muon scale factors. After a dilepton plus jets selection, in the Z mass window. Both after the Rochester correction.

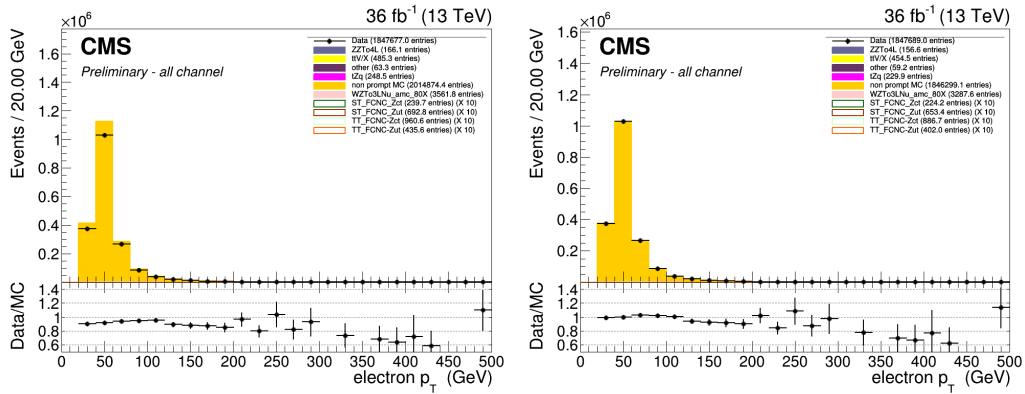


Figure 5.7: The p_T of the electrons before (left) and after (right) electron scale factors. After a dilepton plus jets selection, in the Z mass window. Both after energy scale corrections and smearing.

1417 is done in order to bring the data energy scale to simulation level. It smears the simulation
 1418 energies to have identical energy resolution in simulation and data. For the muons, the p_T is
 1419 corrected using the Rochester method [180, 181]. This correction removes the bias of the muon
 1420 p_T from any detector misalignment or any possible error of the magnetic field. The effect of
 1421 the Rochester correction can be found in Figure 5.8.

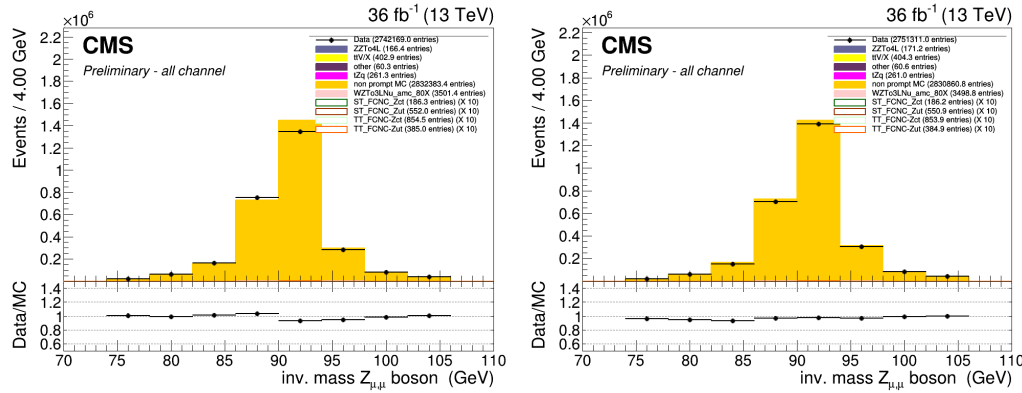


Figure 5.8: The mass of the Z boson consisting of the muons before (left) and after (right) the Rochester correction. After a dilepton plus jets selection, in the Z mass window.

1422 CSVv2 shape correction

1423 In order to make the shape of the CSVv2 b-tagging discriminant in simulation agree with data,
 1424 jet-by-jet based scale factors are applied. These scale factors are a function of the p_T , η and
 1425 CSVv2 value of the jet as discussed in Section 4.4.4. The effect of these scale factors can be
 1426 found in Figure 5.9.

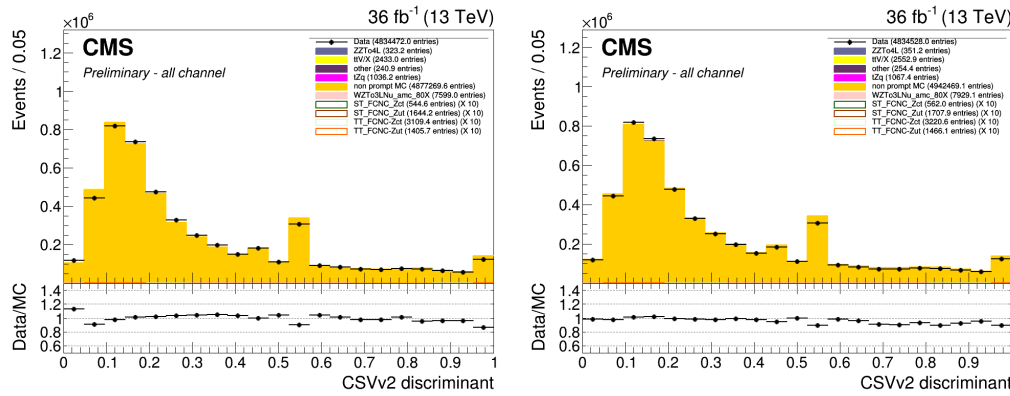


Figure 5.9: The CSVv2 discriminant of the jets before (left) and after (right) b-tag scale factors. After a dilepton plus jets selection, in the Z mass window.

1427 Jet energy

1428 The jet energy in data and simulation is corrected by the measured energy response of the
 1429 detector. This provides p_T - and η dependent scale factors and are directly taken from the
 1430 frontier condition database as discussed in Section 4.4.3. The effect of the jet energy corrections
 1431 can be found in Figure 5.10 and Figure 5.11.

NOTE: Fix31
jer plot

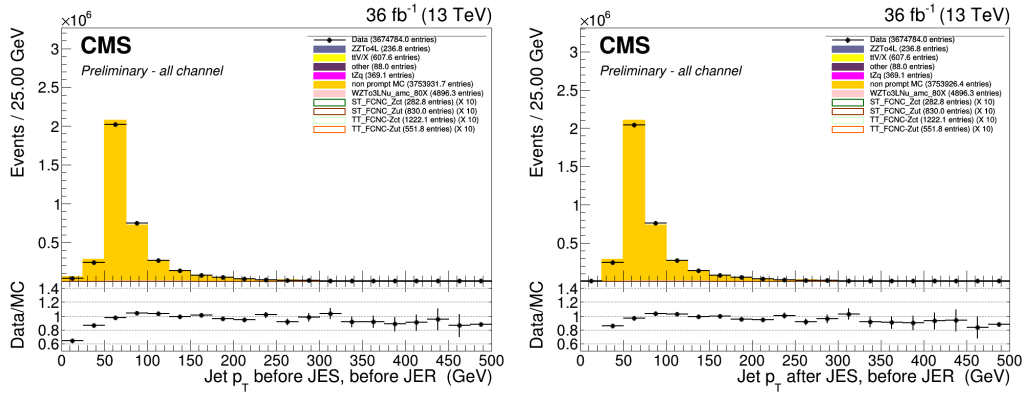


Figure 5.10: The p_T of the jets before (left) and after (right) jet energy scale corrections. After a dilepton plus jets selection, in the Z mass window.

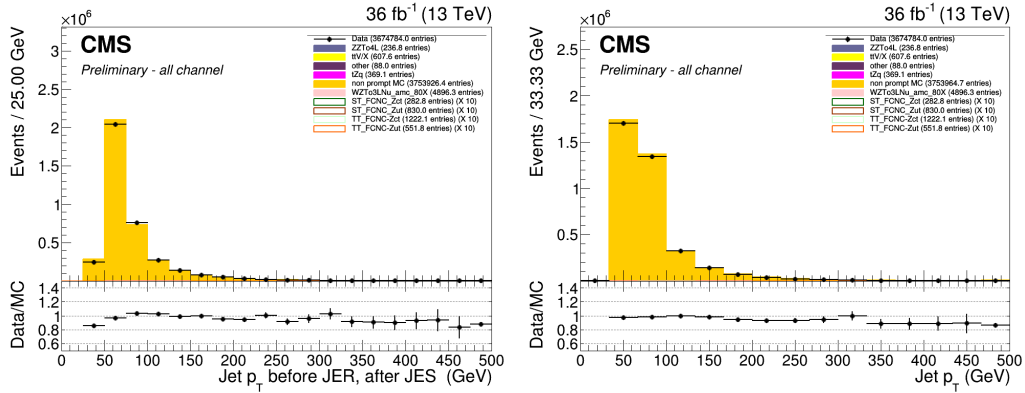


Figure 5.11: The p_T of the jets before (left) and after (right) jet energy resolution smearing. After a dilepton plus jets selection, in the Z mass window.

1432 Missing transverse energy

1433 The energy scale and resolution corrections applied to the jets are propagated back to the
 1434 missing transverse energy (smeared Type I correction) as discussed in [Section 4.4.5](#). This
 1435 rebalances the transverse net momentum of the event and improves the missing transverse
 1436 energy resolution itself.

1437 5.1.4 Reconstruction of kinematic variables

1438 The variables used for the training are related to the reconstructed leptons, jets, Z boson and
 1439 top quark candidates. The Z boson is reconstructed as the sum of the four vectors of the
 1440 two same flavour leptons of opposite sign giving the closest value to the Z mass. The third
 1441 remaining lepton is assigned as the lepton coming from the W boson decay. The reconstruction
 1442 of the SM top quark candidate is more difficult and done by summing the third lepton, the
 1443 SM b-jet and the neutrino (E_T^{miss}). The SM b jet is assigned to the jet with the highest CSVv2
 1444 discriminant. The longitudinal momentum of the neutrino is calculated by putting a constraint

1445 on the lepton+neutrino system with the W mass. In case two solutions are found for the p_z^ν
 1446 component, the one that gives the reconstructed mass (lepton + neutrino + b jet) to the known
 1447 top quark mass is used. The FCNC top quark is reconstructed by summing the reconstructed Z
 1448 boson and the jet giving the mass closest to the top mass, from the jet collection from which the
 1449 SM b jet is removed.

1450 The reconstructed objects are validated using simulation by matching the reconstructed
 1451 objects to their generated counterpart by minimizing ΔR . The efficiencies derived for the
 1452 simulated signal samples and the SM tZq background process can be found in [Table 5.5](#) and
 1453 [Table 5.6](#).

Table 5.5: Efficiencies of assigning the correct leptons in the analysis.

	FCNC tZq	FCNC tZ	SM tZq
W lepton	99%	98%	97%
leptons from the Z boson	99%	98%	97%
all leptons in the decay	99%	98%	97%

Table 5.6: Efficiencies of assigning the correct jets in the analysis.

	FCNC tZq	FCNC tZ	SM tZq
SM b jet	99%	98%	80%
c jet	71%	N/A	50%
u jet	83%	N/A	54%

1454 5.2 Analysis Strategy

1455 The analysis strategy uses five statistically independent regions to extract limits using a likelihood
 1456 fit of various observables. Two signal regions, the tZ (STSR) and tZq (TTSR) signal regions, are
 1457 constructed using the jet multiplicity, focussed on each signal signature (see Tab. 5.9). In order
 1458 to constrain the rate of WZ+jet events as well as that of NPL backgrounds, three control regions
 1459 are defined. The WZ control region (WZCR) focusses on NPLs originating from Z/γ^* + jets
 1460 and simultaneously constrains the WZ+jets background rate. The NPL backgrounds coming
 1461 from a $t\bar{t}$ process are constrained by two control regions, TTCSR and STCSR, one for each signal
 1462 region (TTSR and STSR). In the STSR and TTSR multivariate discriminants based on Boosted
 1463 Decision Trees (BDT) (see [Section 3.3](#)) are used to respectively discriminate FCNC tZ and FCNC
 1464 tZq from backgrounds. In the WZCR a discriminating variable between the two backgrounds,
 1465 WZ+jets and NPLs, is used. In TTCSR and STCSR the dominating process is the $t\bar{t}$ process, and
 1466 its rate is estimated by subtracting all other background predictions from data. A simultaneous
 1467 global fit using the Higgs Combined Tool ([Section 3.4](#)) is performed taking into account each
 1468 region (STSR, TTSR, WZCR, TTCSR and STCSR) for the four different leptonic channels.

5.3 Data driven NPL background simulation

One of the most important background consist of events with not prompt leptons. These are mostly instrumental background and are therefore very difficult to model. The NPL background is estimated from data for both its shape and its normalisation.

The NPL background originates from hadronic objects wrongly reconstructed as leptons, real leptons coming from the semi-leptonic decay of a b or c hadron, or real leptons coming from the conversion of photons that pass the identification and isolation requirements. The dominant source of these NPLs depend on the flavour of the lepton and therefore the events with a not prompt muon ($\text{NP}\mu$) are treated differently than those with a not prompt electron (NPe). For muons, the dominant source is the semi-leptonic decay of heavy flavour hadrons, while for electrons, the dominant sources are hadrons and photon conversions.

The backgrounds causing NPL contributions are mostly $Z/\gamma^* + \text{jets}$ (Drell–Yan) and $t\bar{t} + \text{jets}$ dilepton processes, and in a smaller amount WW processes. All of these backgrounds contain two real leptons and one NPL. Due to the fact that the probability for a lepton to be a NPL is small, backgrounds containing two or more NPL s are neglected in thus search. The assumption is made that for $Z/\gamma^* + \text{jets}$ the two leptons compatible with a Z boson decay are the real leptons, and the additional lepton is coming from a NPL source, while for $t\bar{t} + \text{jets}$ the NPL is associated to the Z boson. This has been validated using Monte Carlo simulation.

The NPL sample is constructed from data by requiring exactly three leptons, from which two are considered real, isolated leptons and the third lepton is identified as a NPL. This NPL is created by loosening its identification and inverting its isolation criteria. The full requirements on the not prompt leptons are given in [Table 5.7](#) and [Table 5.8](#). For NPe, a large fraction is coming from misidentified photons. These are removed by applying a tighter cut on the $1/E - 1/p$ variable, and by limiting the isolation values to be smaller than one.

Table 5.7: Non prompt electron requirements used in this analysis. The requirements are set in the barrel ($|\eta_{supercluster}| \leq 1.479$) and the end caps ($|\eta_{supercluster}| > 1.479$).

Properties	$ \eta_{supercluster} \leq 1.479$	$ \eta_{supercluster} > 1.479$
$\sigma_{\eta\eta}$	< 0.011	< 0.0314
$ \Delta\eta_{in} $	< 0.00477	< 0.00868
$ \Delta\phi_{in} $	< 0.222	< 0.212
H/E	< 0.298	< 0.101
relative isolation	$\geq 0.0588 \ \&\& < 1$	$\geq 0.0571 \ \&\& < 1$
$ 1/E - 1/p $	$< 0.0129 \text{ GeV}^{-1}$	$< 0.0129 \text{ GeV}^{-1}$
expected missing inner hits	≤ 1	≤ 1
pass conversion veto	Y	Y
p_T	$> 35 \text{ GeV}$	$> 35 \text{ GeV}$

Table 5.8: Non prompt muon requirements used in the analysis.

Properties	modified Loose Muon WP
Global muon or Tracker Muon	Both
Particle Flow muon	Y
$\chi^2/ndof$ of global muon track fit	N/A
Nb. of hit muon chambers	N/A
Nb. of muon stations contained in the segment	N/A
Size of the transverse impact parameter of the track wrt. PV	N/A
Longitudinal distance wrt. PV	N/A
Nb. of pixel hits	N/A
Nb. of tracker layers with hits	N/A
Relative Isolation	≥ 0.15
p_T	$> 30 \text{ GeV}$

¹⁴⁹³ **5.4 Regions and channels**

The regions are defined as in Table 5.9 after a common selection of exactly three leptons containing one opposite sign, same flavour pair that is assigned to the Z boson, at least one jet and at the most three jets, the transverse mass of the W boson to be maximal 300 GeV. The transverse mass $m_T(W)$ is reconstructed using

$$m_T(W) = \sqrt{(p_T(l_W) + p_T(v_W))^2 - (p_x(l_W) + p_x(v_W))^2 - (p_y(l_W) + p_y(v_W))^2} \quad (5.7)$$

Table 5.9: The statistically independent regions used in the analysis.

	WZCR	STS R	TTSR	STCR	TTCR
Number of jets	≥ 1	1	≥ 2	1	≥ 2
Number of b jets	0	1	≥ 1	1	≥ 1
$ m_Z^{\text{reco}} - m_Z < 7.5 \text{ GeV}$	Yes	Yes	Yes	No	No
$ m_Z^{\text{reco}} - m_Z < 30 \text{ GeV}$	Yes	Yes	Yes	Yes	Yes
Number of leptons	3	3	3	3	3

¹⁴⁹⁴ Additional leptons with a looser identification are vetoed in order to reduce the contamination
¹⁴⁹⁵ of backgrounds with four or more leptons in the final state, e.g. ZZ, t̄Z, and t̄H. The most
¹⁴⁹⁶ important backgrounds are the ones that contain three prompt leptons in the final state. These
¹⁴⁹⁷ are mainly WZ+jets, t̄Z and SM tZq. For these backgrounds, the three lepton topology is
¹⁴⁹⁸ identical to the FCNC signal: two opposite sign leptons of the same flavour decaying from the Z
¹⁴⁹⁹ boson, and a third additional, high p_T lepton coming from the W boson decay.

¹⁵⁰⁰ For the FCNC tZ final state, one b jet coming from the SM top decay is expected. For the
¹⁵⁰¹ FCNC tZq, an additional light jet is expected. In the t̄Z final state, two b jets are present in the
¹⁵⁰² final state. However, due to inefficiencies of the b-tagging algorithm, one of the two b jets may
¹⁵⁰³ be identified as a light quark jet, giving the same final state as the FCNC tZq final state. For
¹⁵⁰⁴ the WZ+jets final states, one of the b jets produced by gluon splitting can be b-tagged or light
¹⁵⁰⁵ flavour jets coming from the WZ+jets production can be mis-tagged as b jets. The SM tZq final
¹⁵⁰⁶ state expects the same signal as FCNC tZq.

¹⁵⁰⁷ The NPL events give a significant background contribution. This background is coming mainly
¹⁵⁰⁸ from Z/ γ^* + jets and t̄t + jets processes (in a less significant way, also WW and tWZ contributes),
¹⁵⁰⁹ which have very high cross sections and causes a large number of NPL background events
¹⁵¹⁰ compared to signal.

¹⁵¹¹ In order to reduce the large uncertainties in backgrounds, five independent regions are used
¹⁵¹² as defined in Table 5.9. In Figure 5.12, the strategy and usage of each region is illustrated.

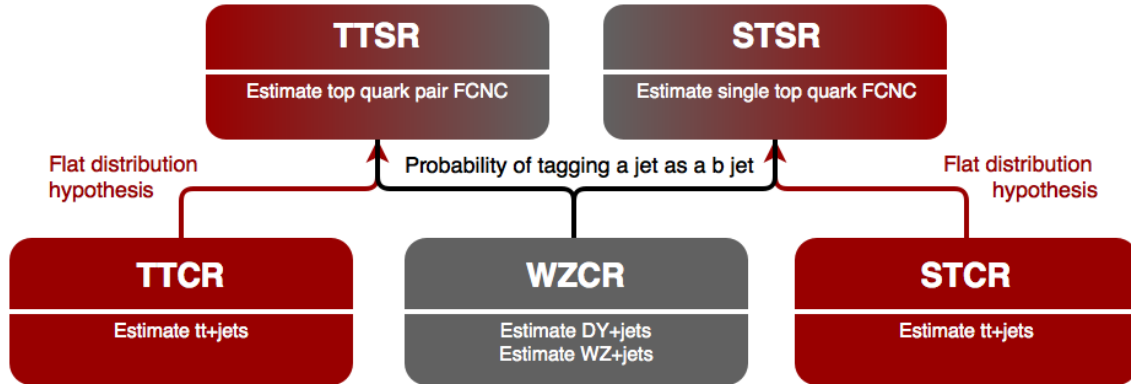


Figure 5.12: The strategy used for this search. The WZCR region is used to estimate the WZ+jets background process as well as the NPL background coming from the $Z/\gamma^* + \text{jets}$ process. The TTCR and STCR regions are used to estimate the contributions of the NPL background coming from the $t\bar{t} + \text{jets}$ process.

1513 5.4.1 WZCR

1514 The WZCR is constructed by vetoing events with jets tagged as being a b-jet, making it statistically
 1515 independent from the signal regions where at least one b-tagged jet is required. In this region,
 1516 a fit is performed on the transverse mass of the W boson, in order to estimate the NPL yield
 1517 coming from $Z/\gamma^* + \text{jets}$ and the WZ+jets backgrounds.

A transfer factor is used to account for going from a region without b-tagged jets to a region with exactly or at least one b-tagged jet. For this the probability of tagging at least one jet with the CSVv2 algorithm at the loose working point is used to calculate the expected number of events, N_b , after b-tagging:

$$N_b = \frac{\sum_{\text{events}} \mathcal{P}_b}{\text{total nb of events}}, \quad (5.8)$$

where \mathcal{P}_b is the probability that an event survives the b-tagging requirement

$$\begin{aligned} \mathcal{P}_b &= 1 - P(\text{event doesn't survive b tag}) \\ &= 1 - \left(\prod_b P(\text{b not tagged}) \prod_c P(\text{c not tagged}) \prod_{uds} P(\text{light not tagged}) \right) \end{aligned} \quad (5.9)$$

1518 with the products going over all b-, c-, and light jets. The jet flavour is determined by means of
 1519 matching the reconstructed jet to the generated quark based on the distance in the $\eta\phi$ plane.
 1520 In order to estimate the probability for exactly one b-tagged jet, the expected number of events
 1521 is corrected by the fraction of events with exactly one jet in the WZCR. The resulting transfer
 1522 factors are given in [Appendix C](#). The yield of WZ+jets events in the signal region estimated
 1523 using the above described transfer factor and the yield calculated with simulated events are in
 1524 agreement.

1525 **5.4.2 TTCR and STCR**

The TTCR and STCR have are constructed with the same selection criteria as TTSR and STSR but are outside the Z mass window (sidebands):

$$7.5 \text{ GeV} < |m_Z^{\text{reco}} - m_Z| < 30 \text{ GeV}. \quad (5.10)$$

where m_Z^{reco} is the reconstructed mass of the Z boson in the event, and m_Z the mass of the Z boson. These regions are dominated by $t\bar{t}$ +jets (see Appendix C) and are used to estimate the NPL coming from $t\bar{t}$ +jets in the STSR and TTSR. Since there aren't enough events entering these regions, no shapes are used in the fit. The distribution of the mass of the Z boson is flat for $t\bar{t}$ +jets events, as shown in Fig. Figure 5.13, and thus the number of expected events, N_s , in the signal regions estimated from the number of expected events, N_c , in the control region is obtained as

$$N_s = \frac{15}{60 - 15} N_c. \quad (5.11)$$

1526 The resulting transfer factors are given in Appendix C. The expected yield in the signal region
1527 estimated from the TTCR (STCR) is in agreement with the yield calculated from simulated events.

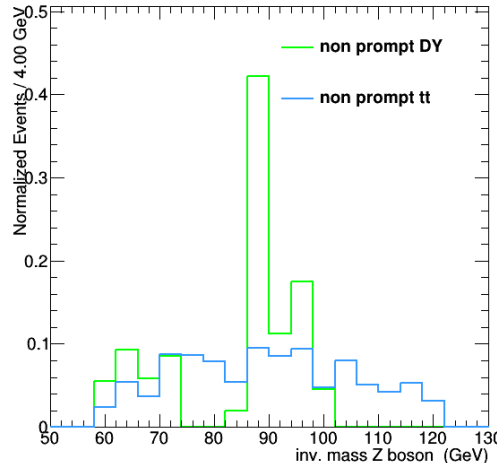


Figure 5.13: The normalized distribution for $Z/\gamma^* + \text{jets}$ and $t\bar{t} + \text{jets}$ events before dividing the events in to regions, after $|m_Z^{\text{reco}} - m_Z| < 30 \text{ GeV}$. All leptonic channels combined.

1528

1529 **5.4.3 TTSR and STSR**

1530 The TTSR is defined to target top quark pair FCNC (tZq), while the STSR focusses on single top
1531 quark FCNC (tZ). They have NPL contributions coming from $Z/\gamma^* + \text{jets}$ and $t\bar{t} + \text{jets}$ events. In
1532 this region, the data driven NPL template is split into two templates based on the presence of the
1533 NPL in the Z boson. The NPL associated with W boson is assigned to $Z/\gamma^* + \text{jets}$ and estimated
1534 in the WZCR, while the NPL associated with Z boson is assigned to $t\bar{t} + \text{jets}$ and estimated in
1535 the TTCR and STCR.

The search for FCNC involving a top quark and a Z boson

6

1536

1537 6.1 Construction of template distributions

1538 There were no selection criteria found to make a clear rejection of the background events without
1539 sacrificing a significant amount of signal. For this reason, a multivariate approach using Boosted
1540 Decision Trees that combines several discriminating variables in the TMVA framework is used.
1541 For the training, the BDTs are trained against all backgrounds, where the NPL background is not
1542 taken into account. The BDT settings avoid over-training and maintain a good discriminating
1543 power against all backgrounds. The background and signal yields follow the relative fractions
1544 predicted by the simulation.

1545 The variables used to construct the BDTs include the angles, distances, masses and transverse
1546 momenta:

- 1547 1. pseudo rapidity of the SM top: TT+ST tZu, ST tZc
- 1548 2. invariant mass of the W lepton and the SM b jet: TT+ST tZu, TT+ST tZc
- 1549 3. $\Delta\Phi$ between the W lepton and the SM b jet: TT+ST tZu, ST tZc
- 1550 4. minimal ΔR between the W lepton and jets: TT tZu
- 1551 5. invariant mass of the Z boson: TT tZu, TT tZc
- 1552 6. $\Delta\Phi$ between the W lepton and the Z boson: TT+ST tZu, TT tZc
- 1553 7. ΔR between the W lepton and the SM b jet: TT+ST tZu, TT tZc
- 1554 8. number of CSVv2 medium WP b jets: TT tZu, TT tZc
- 1555 9. invariant mass of the FCNC top: TT tZu, TT tZc
- 1556 10. ΔR between the Z boson and the FCNC light jet: TT tZu, TT tZc
- 1557 11. ΔR between the FCNC light jet and the SM b jet: TT tZu, TT tZc

- 1558 12. charge of the W lepton times the absolute pseudo rapidity of the W lepton: ST tZu
 1559 13. b discriminant of the highest p_T jet: ST tZu, ST tZc
 1560 14. total Ht of the leptons: ST tZu
 1561 15. the p_T of the W lepton times its charge: ST tZu
 1562 16. total invariant mass of the leptons: ST tZc
 1563 17. ΔR between the W lepton and Z boson: TT+ST tZc
 1564 18. total invariant mass of the event: TT tZc
 1565 19. b discriminant of the FCNC light jet: TT tZc
 1566 20. ΔR between the SM b jet and Z boson: TT tZc

1567 The pre fit distributions of the variables used for creating the multivariate discriminator are
 1568 given in [Section 6.1.1](#). The resulting multivariate discriminator are shown in [Section 6.1.2](#).

1569 **6.1.1 Distributions of the BDT variables**

NOTE: include distributions of the vars

1571 **6.1.2 BDTs**

NOTE: better to do normalised?

Figure 6.1: Distributions of the discriminating variable before the fit, all different leptonic channels together. Upper left: TTSR tZu, upper right: TTSR tZc; lower left: STSR tZu, lower right: STSR tZc.

1572

Figure 6.2: Distributions of the discriminating variable before the fit, 3 μ channel. Upper left: TTSR tZu, upper right: TTSR tZc; lower left: STSR tZu, lower right: STSR tZc.

Figure 6.3: Distributions of the discriminating variable before the fit, 1e2 μ channel. Upper left: TTSR tZu, upper right: TTSR tZc; lower left: STSR tZu, lower right: STSR tZc.

Figure 6.4: Distributions of the discriminating variable before the fit, 2e1 μ channel. Upper left: TTSR tZu, upper right: TTSR tZc; lower left: STSR tZu, lower right: STSR tZc.

1573 **6.1.3 Transverse mass in WZCR**

1574 The WZCR is used to estimate the contribution from WZ+jets and NPL background. In this
 1575 region, a fit is performed on the transverse mass distribution of the W boson. The pre-fit
 1576 templates are given in [Figure 6.6](#).

Figure 6.5: Distributions of the discriminating variable before the fit, 3e channel. Upper left: TTSR tZ_u, upper right: TTSR tZ_c; lower left: STSR tZ_u, lower right: STSR tZ_c.

Figure 6.6: The transverse mass of the W boson in the WZCR, before the fit. All different leptonic channels together. Left: scaled to the data, right: normalized.

1577 6.2 Systematic uncertainties

1578 The systematic uncertainties entering the analysis are coming from different sources. The
 1579 experimental uncertainties arise from the reconstruction of the objects and are discussed in
 1580 [Section ??](#). These influence the number of events passing the selection, so-called normalisation
 1581 uncertainties, or the relative occupancies of the distributions, so-called shape uncertainties. The
 1582 normalisation uncertainties coming from reconstruction include the uncertainty of 2.5% on
 1583 the measured integrated luminosity and the efficiency of the trigger logic used for the analysis
 1584 which has a 1% (5%) uncertainty on the 3 μ and 1e2 μ (2e1 μ and 3e) channels. The pileup
 1585 distribution is calculated via the minimum bias cross section which has a 4.6% uncertainty.
 1586 This uncertainty results in a systematic shift in the pileup distribution and its shape effect is
 1587 estimated by recalculating the pileup distribution for each variation of the minimum bias cross
 1588 section. The effect of the systematic upwards and downwards shift on the pileup distribution is
 1589 demonstrated in [Section ??](#). The shape uncertainties also include the uncertainties coming from
 1590 the applied lepton scale factors. Their systematic uncertainty originates from three sources:
 1591 identification, isolation and tracking. The effect of systematic upwards or downwards shift
 1592 on shapes is demonstrated in [Section ??](#) and [Section ??](#). The uncertainties arising from jet
 1593 energy corrections require a recalculation of all jet related kinematic observables and its effect
 1594 is propagated to the missing transverse energy. The resulting effect of the systematic upwards
 1595 or downwards shift on shapes is demonstrated in [Section ??](#) and [Section ??](#). The reweighting of
 1596 the CSVv2 discriminant is also a source of uncertainty. There are three sources of uncertainty
 1597 contributing to the measurement of the b-tag related scale factors: statistical uncertainties, jet
 1598 energy scale and the purity of the sample. These result in eight uncorrelated contributions for
 1599 which the effects on the shapes are shown in [Section ??](#).

1600 Since the NPL sample is artificially made from data by inverting the isolation of the third
 1601 lepton. Its effect has to be estimated. The shape uncertainty one the NPL processes is obtained
 1602 by varying the isolation inversion with respect to tight working point to the loose working point
 1603 for electrons and muons at the same time. This found to have negligible effect. The uncertainty
 1604 on the normalisation of the overall NPL yield is taken as 50% in accordance the the SM tZq
 1605 search.

NOTE: Add source

1606 The uncertainty on the expected yield of the simulated backgrounds is taken to be 30%
 1607 of the yield such that it covers all uncertainties at next to leading order accuracy. Theory
 1608 uncertainties originating from the modelling of the main backgrounds are estimated to account
 1609 for the effect on the shape of the distributions from the choice of parton density funnctions, and
 1610 renormalization (μ_R) and factorization (μ_F) scales. The effect of the renormalization (μ_R) and
 1611 factorization (μ_F) scales is estimated by varying each independently and correlated up and
 1612 down by a factor of two, where the anti-correlated variations are dropped. The envelope of
 1613 these variations is used as an uncertainty. The uncertainties coming from the parton density

functions used for simulation are estimated using the PDF4LHC recipe [182], which combines the MMHT14, CT14, and NNPDF3.0 PDF sets [182]. The theory uncertainties are considered for the main backgrounds coming from simulation: WZ+jets, ZZ+jets, t̄Z, and tZq. This is found to have a negligible effect.

The way the uncertainties are treated as nuisance parameters is summarized in Table 6.1.

Table 6.1: Uncertainties used in this analysis. The column labelled type represents how the uncertainty is treated for the fit.

Source	Systematic input	Type
nonprompt muon norm.	50%	normalisation
nonprompt electron norm.	50%	normalisation
background t̄Z norm.	30%	normalisation
background WZ norm.	30%	normalisation
background tZq norm.	30%	normalisation
background ZZ norm.	30%	normalisation
background other MC norm.	30%	normalisation
trigger	1% (5%)	normalisation
lepton identification	$\pm\sigma(p_T, \eta)$	shape
JES	$\pm\sigma(p_T, \eta)$	shape
JER	$\pm\sigma(p_T, \eta)$	shape
b-tagging	$\pm\sigma(p_T, \eta)$	shape
pileup	$\pm\sigma$ of min. bias cross section	shape
PDF	PDF4LHC recipe	shape (WZ,tZq, ttZ, ZZ)
luminosity	2.5%	normalisation
renorm. and fact. scales	varying indep. and corr.	shape

6.3 Limit setting procedure validation

The analysis strategy has been established using a blinded strategy. Through the use of a pseudo dataset, the limit setting procedure has been validated. Signal injection tests for which the signal strength from a pseudo dataset with a pre-set signal strength is estimated are performed and shown in Figure 6.7.

Another validation has been done by performing a Maximum Likelihood fit in the WZCR only, considering all lepton channels. A simultaneous fit of the signal strength of the NPe, NPμ and

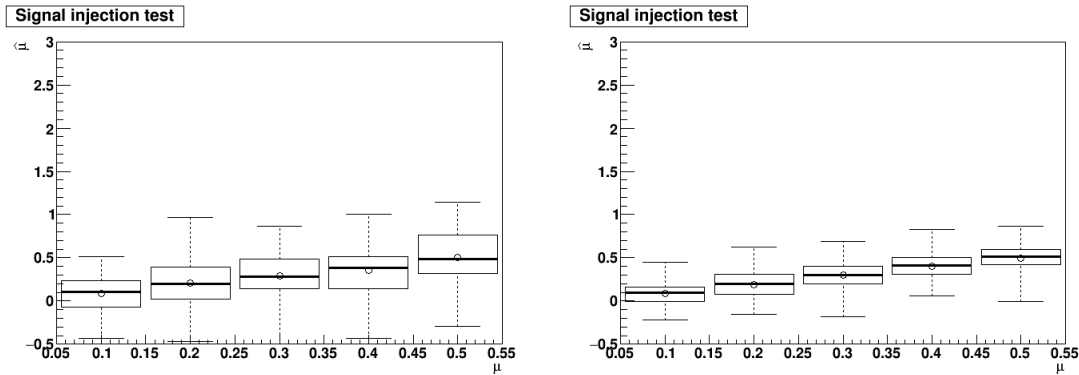


Figure 6.7: The obtained signal strength with the Maximum Likelihood method is in agreement with the signal strength used to generate the Asimov data set for the tZu (left) and tZc (right) couplings.

1626 the WZ+jets backgrounds is done by using the multi-dimensional fit in Higgs Combine Tool.
 1627 The resulting signal strengths can then be applied on the distribution of the transverse mass of
 1628 the W boson to verify data/MC agreement, as can be seen in Fig. 6.9. Furthermore, a goodness
 1629 of fit test is performed, resulting in a p-value of 0.3 (see Fig. 6.8).

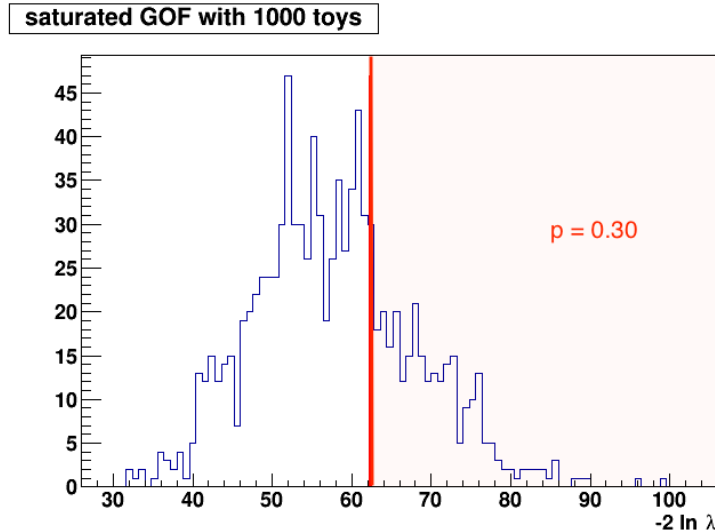


Figure 6.8: Goodness of fit testing in the WZCR with 1000 toys. The likelihood ration is denoted as λ .

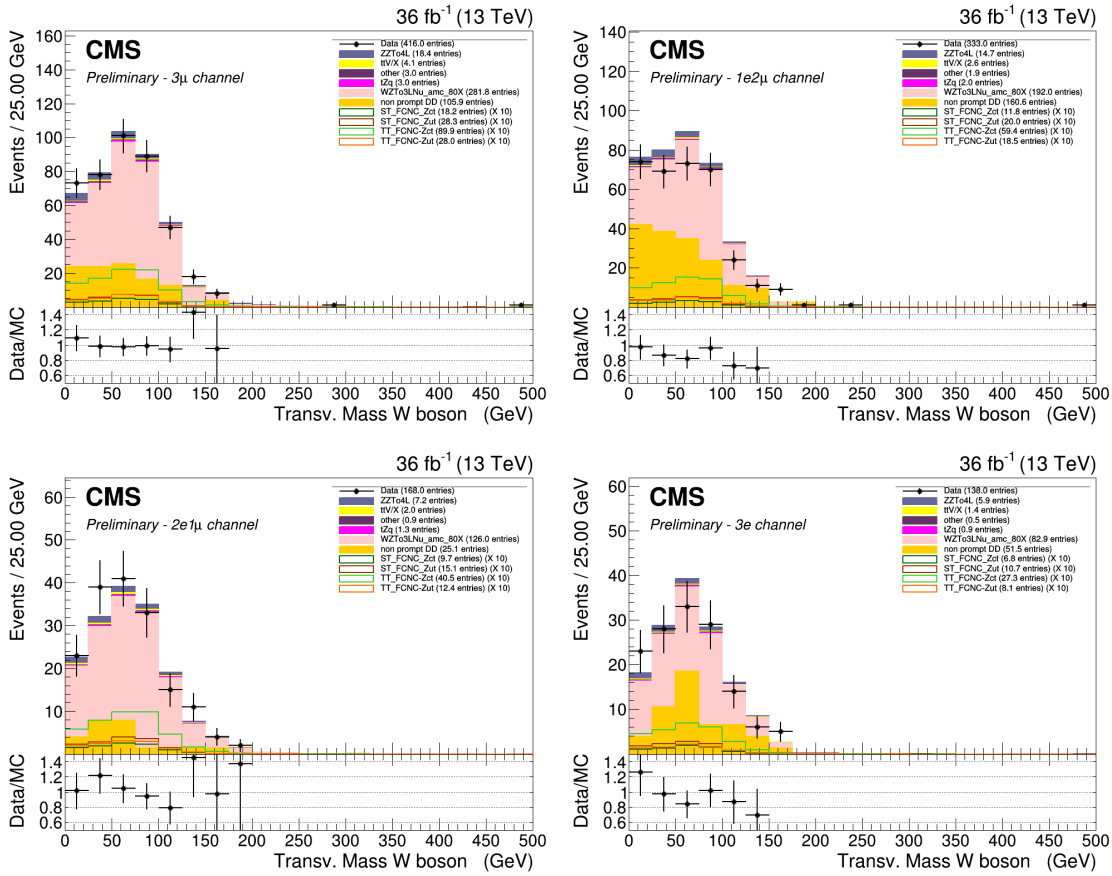


Figure 6.9: The transverse mass of the W boson in the WZCR for the 3μ channel (left, upper), $1e2\mu$ channel (right, upper), $2e1\mu$ channel (left, lower), and 3 electrons channel (right, lower).

Using the normalisations obtained by fitting the WZCR only, one can look at the data/MC agreement in the WZCR for all the variables used to create the BDT variables. These show good agreement as illustrated in Figure ??.

6.4 Result and discussion

The limit setting procedure explained in Section 3.4 is applied and results are obtained for each lepton channel separately as well as the combination. For both the tZu and tZc coupling, the maximum likelihood estimator of their signal strengths $\hat{\mu}$ is compatible with zero. . The maximum likelihood estimators for the nuisance parameters $\hat{\theta}$ are shown in figfig:171102zctmle and figfig:171102zutmle. Their values obtained from the signal plus background or background only fits are in agreement. Furthermore, the pulls on each of the nuisance parameters are shown in Figure 6.12, Figure 6.13, Figure 6.14, and Figure 6.15. Here one can see that the nuisance parameters related to the NPL normalisations are shifted with respect to their initial values. This is to be expected since their initial normalisation is arbitrary. The distributions of multivariate discriminating variables as well as the distribution of

NOTE: 1636
MAKE THIS 1637
plot

¹⁶⁴⁴ the transverse mass of the W boson are recreated with the maximum likelihood estimations
¹⁶⁴⁵ of the nuisance parameters. The resulting distributions are shown in Figure ??, Figure 6.18,
¹⁶⁴⁶ Figure 6.19, and Figure 6.20. The post fit event yields are given in .

NOTE:
MAKE TA-
BLE

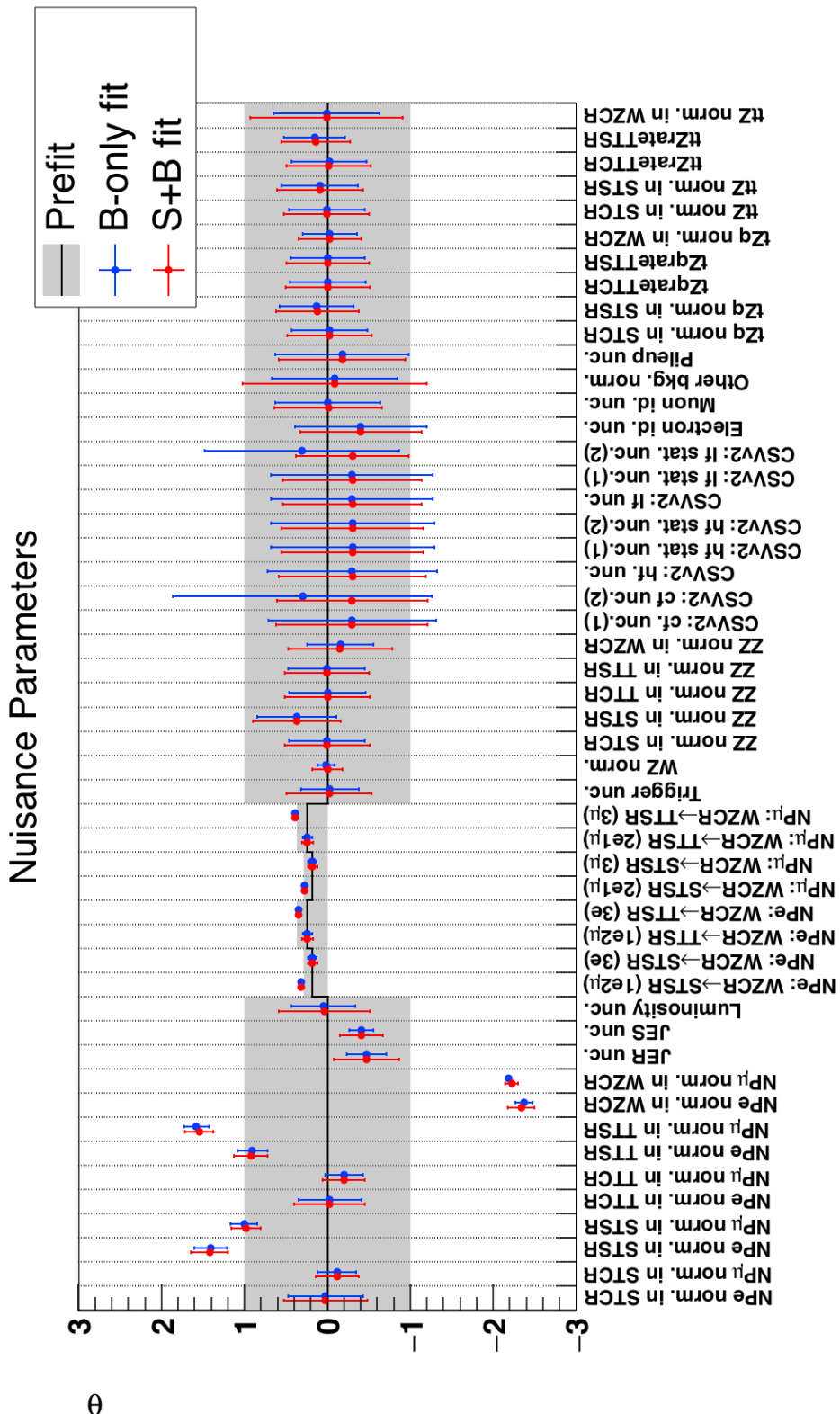


Figure 6.10: Maximum likelihood estimators for the tZc vertex.

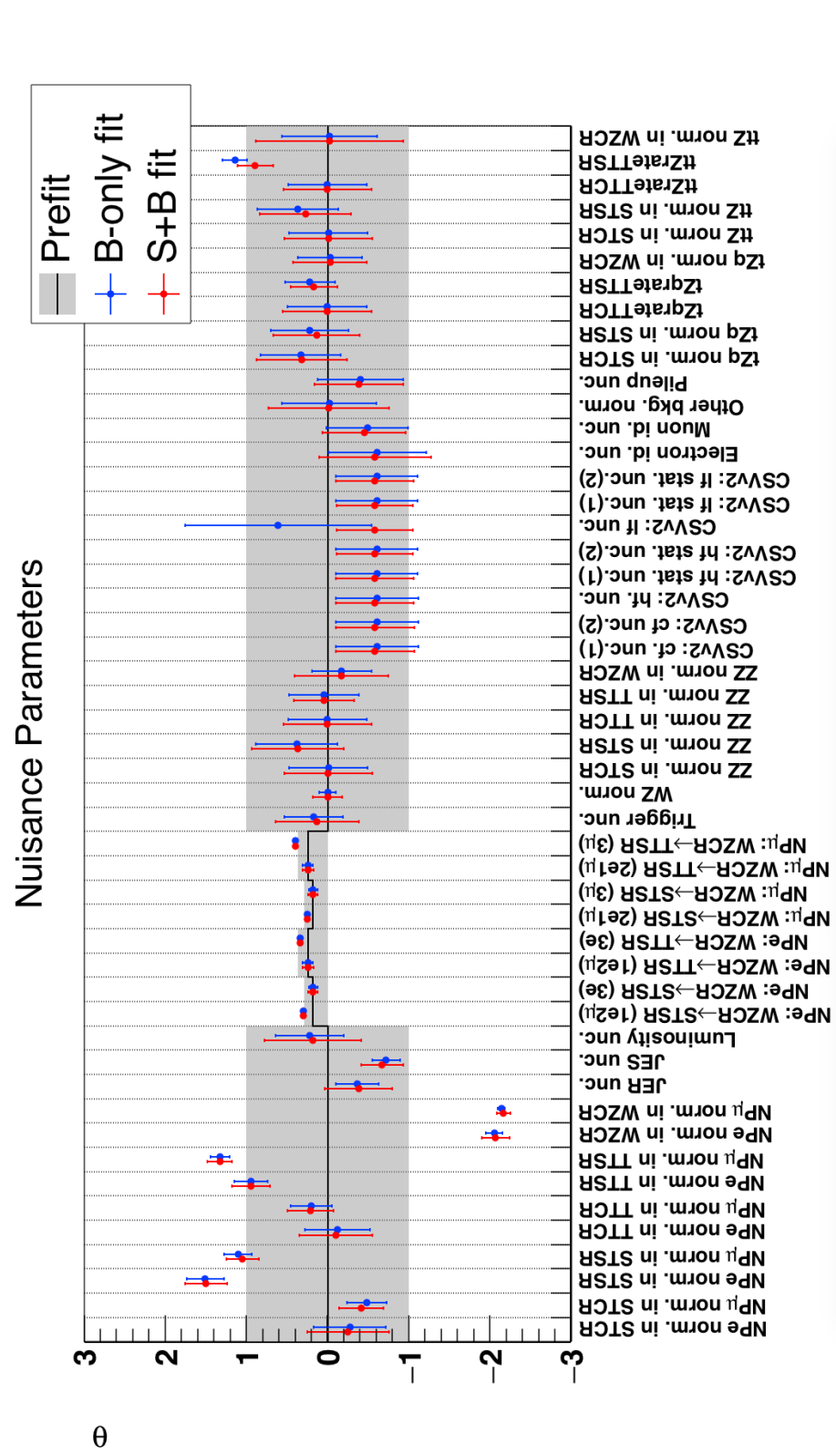


Figure 6.11: Maximum likelihood estimators for the tZu vertex.

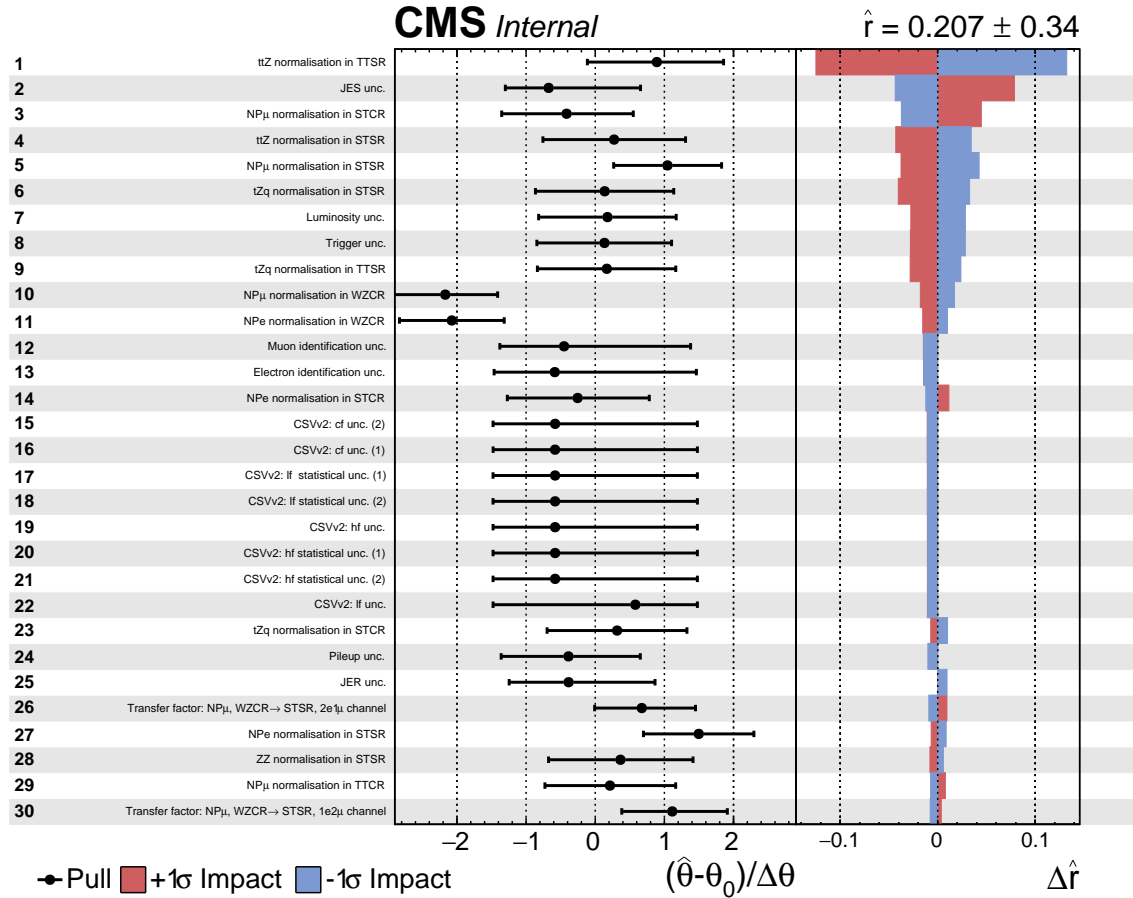


Figure 6.12: The pulls of each nuisance parameter and the influence of their uncertainty on the maximum likelihood estimation of the signal strength \hat{r} for the tZu vertex, part one.

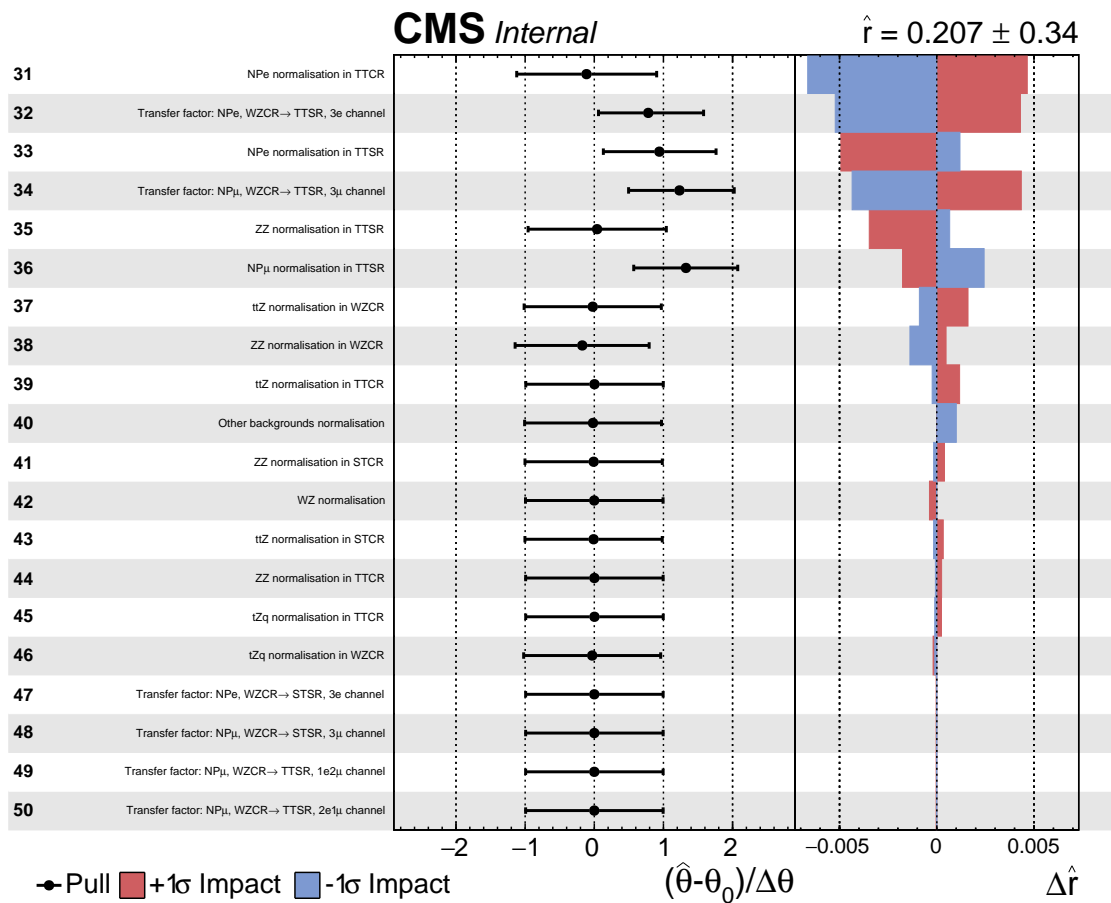


Figure 6.13: The pulls of each nuisance parameter and the influence of their uncertainty on the maximum likelihood estimation of the signal strength \hat{r} for the tZ ν vertex, part two.

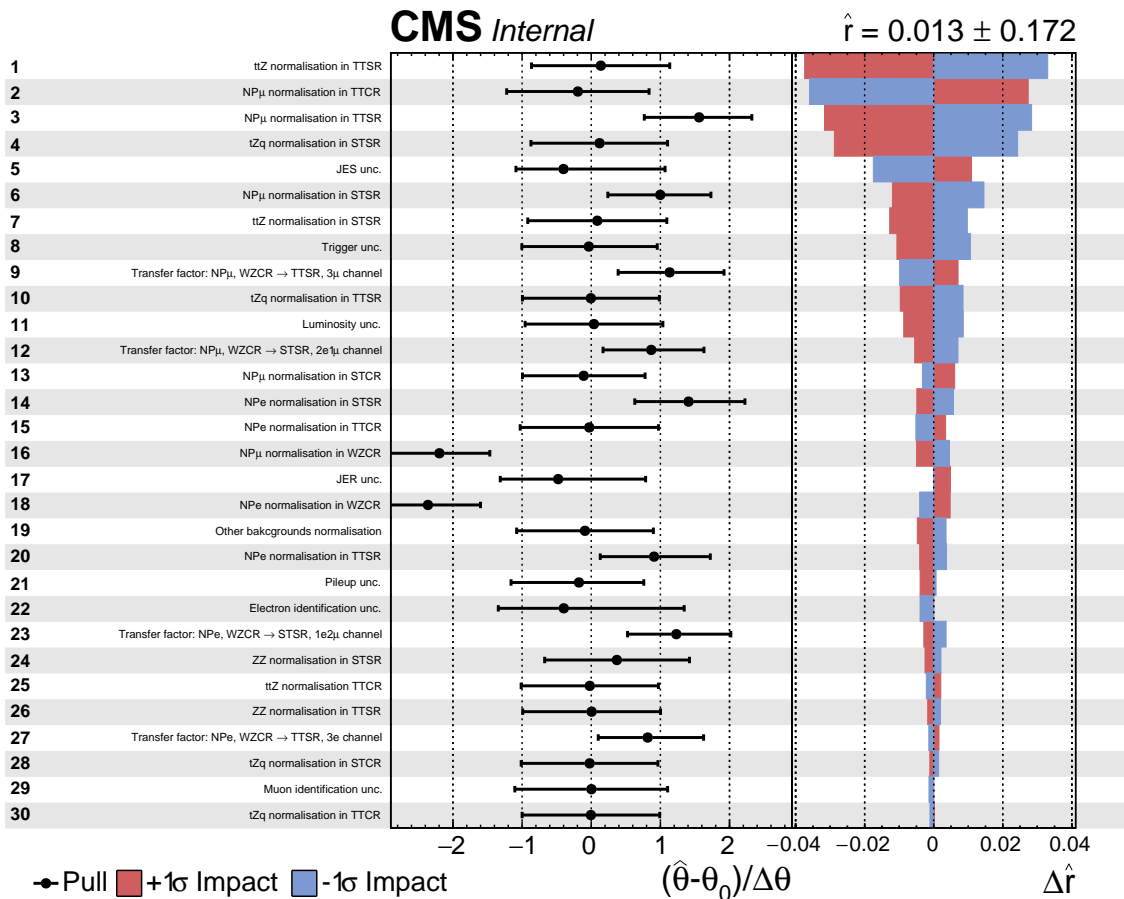


Figure 6.14: The pulls of each nuisance parameter and the influence of their uncertainty on the maximum likelihood estimation of the signal strength \hat{r} for the tZc vertex, part one.

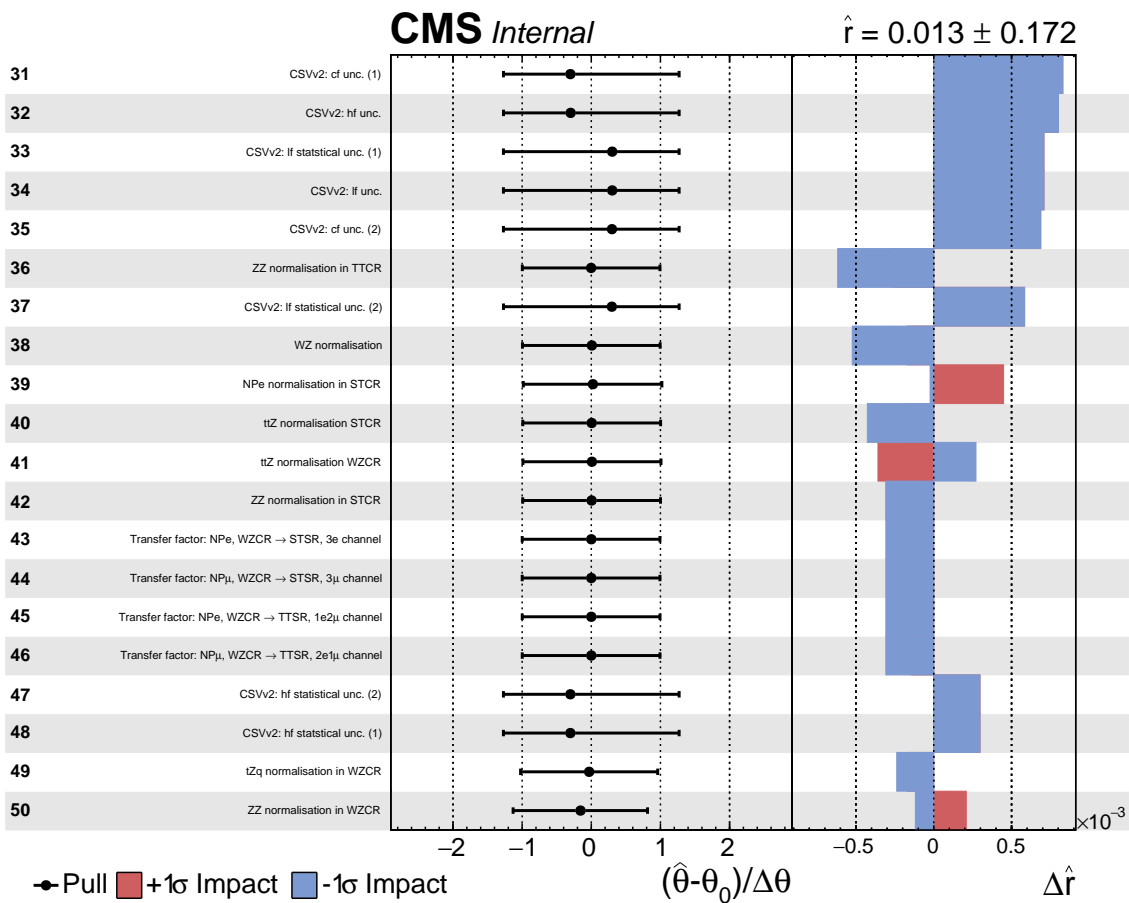


Figure 6.15: The pulls of each nuisance parameter and the influence of their uncertainty on the maximum likelihood estimation of the signal strength \hat{r} for the tZc vertexg, part two.

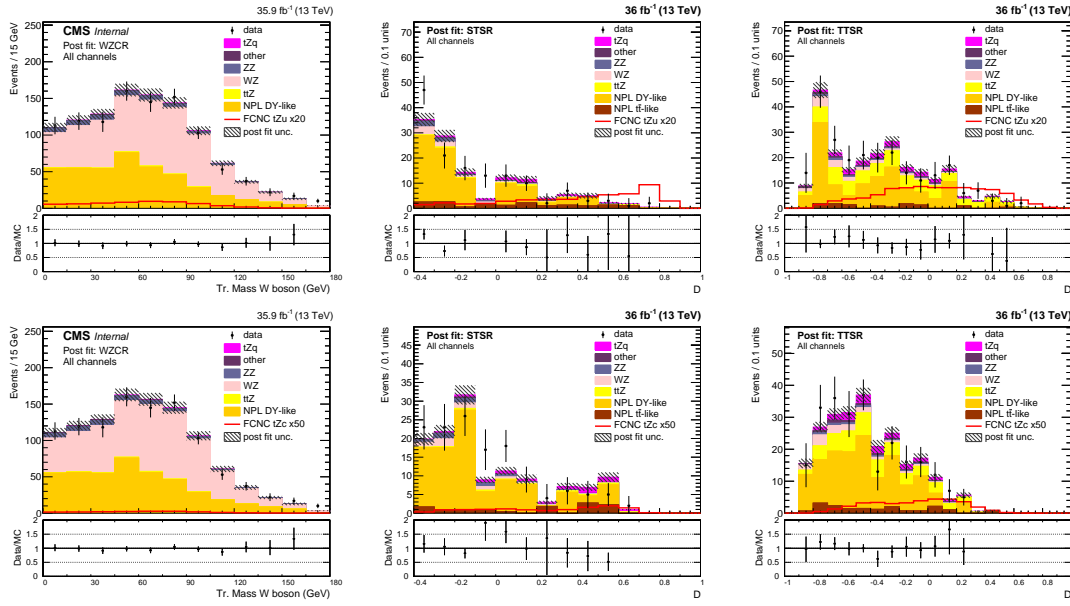


Figure 6.16: Post fit distributions for the all leptonic channels of the transverse mass of the W boson in the WZCR (left), the multivariate discriminating variable in the STSR (middle), and the multivariate discriminating variable in the TTSR (right) for the tZu (top) and tZc (bottom) couplings.

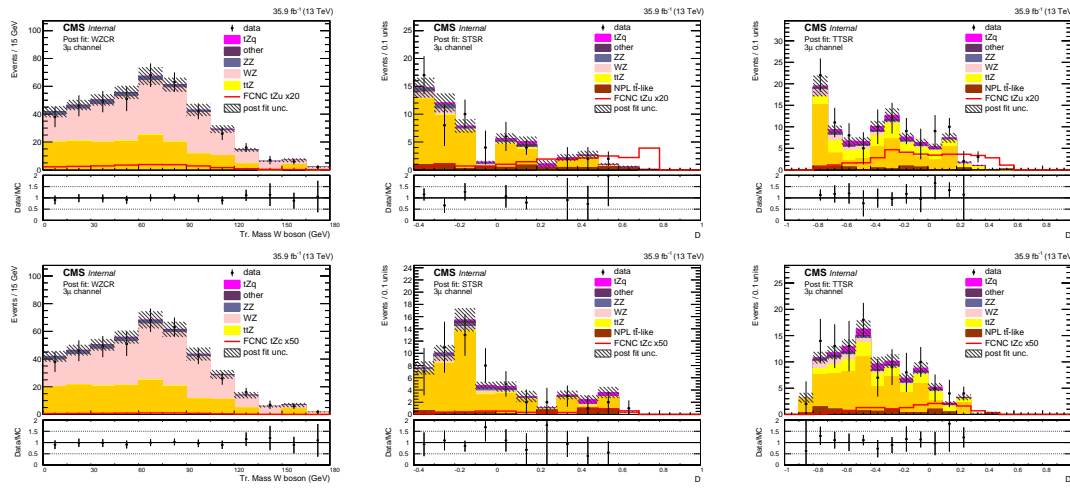


Figure 6.17: Post fit distributions for the 3μ leptonic channel of the transverse mass of the W boson in the WZCR (left), the multivariate discriminating variable in the STSR (middle), and the multivariate discriminating variable in the TTSR (right) for the tZu (top) and tZc (bottom) couplings.

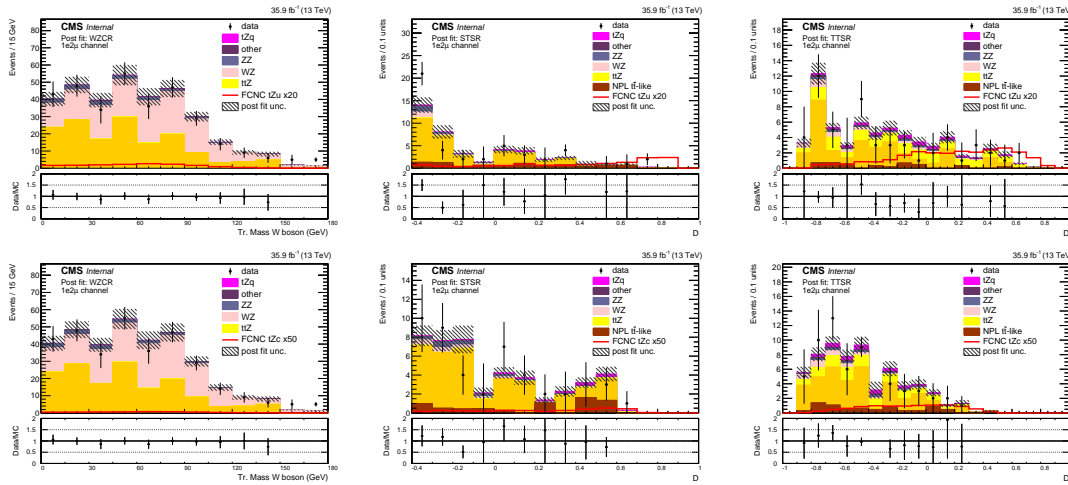


Figure 6.18: Post fit distributions for the $1e2\mu$ leptonic channel of the transverse mass of the W boson in the WZCR (left), the multivariate discriminating variable in the STSR (middle), and the multivariate discriminating variable in the TTSR (right) for the tZu (top) and tZc (bottom) couplings.

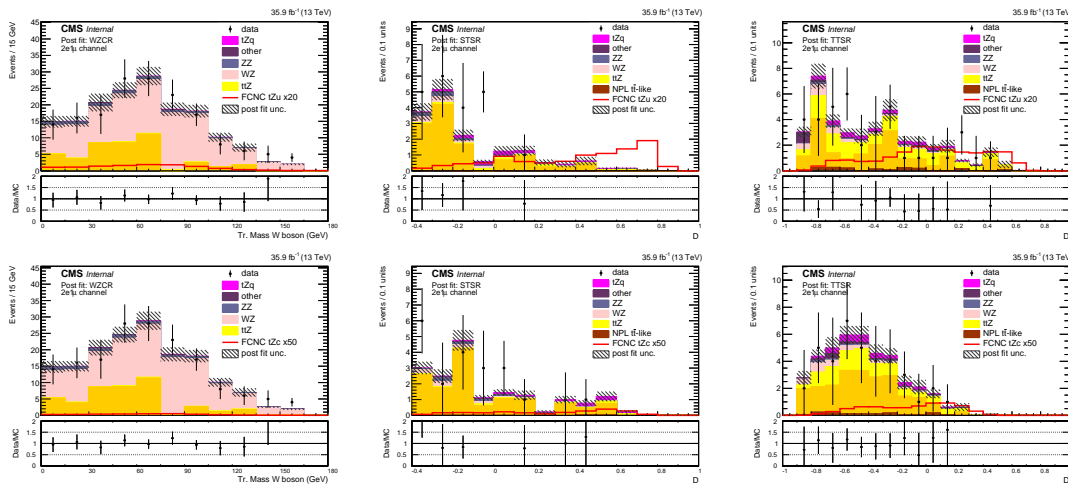


Figure 6.19: Post fit distributions for the $2e1\mu$ leptonic channel of the transverse mass of the W boson in the WZCR (left), the multivariate discriminating variable in the STSR (middle), and the multivariate discriminating variable in the TTSR (right) for the tZu (top) and tZc (bottom) couplings.

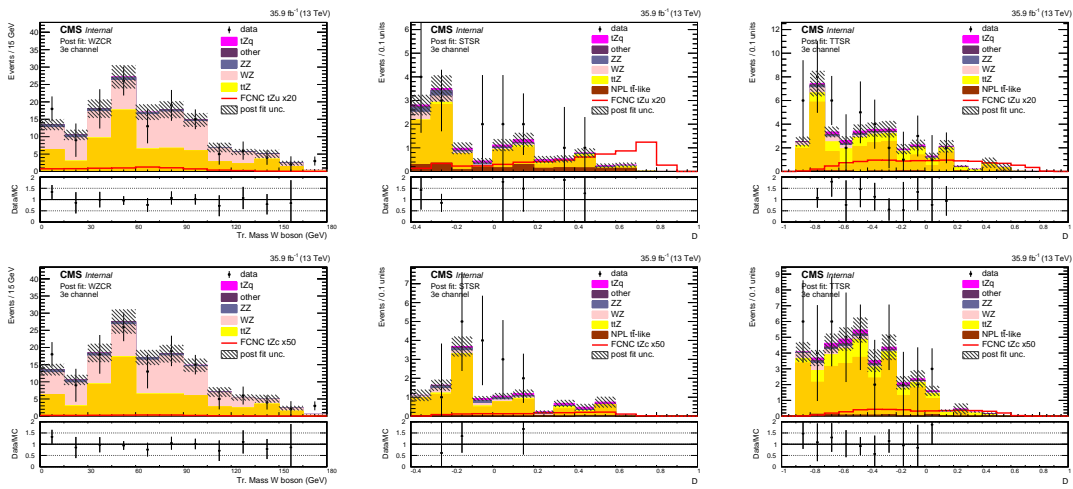


Figure 6.20: Post fit distributions for the 3e leptonic channel of the transverse mass of the W boson in the WZCR (left), the multivariate discriminating variable in the STSR (middle), and the multivariate discriminating variable in the TTSR (right) for the tZu (top) and tZc (bottom) couplings.

6.4.1 One dimensional limits

The limit setting procedure used in this search returns limits on the signal strength modifier which can be translated to signal cross sections. These limits are translated to a limit on the branching fraction using Equation 1.39. Additionally, the limit on the couplings are extracted using the fact that the cross sections are quadratically dependent on the couplings. In Figure 6.21, the resulting limits at 95% CL on the branching fraction and couplings related to the tZu vertex is shown. This observed (expected) limit amounts to $\mathcal{B} < 0.024\%$ (0.015%) when $\kappa_{tZu}/\Lambda \neq 0$ and $\kappa_{tZc}/\Lambda = 0$. The expected limit surpasses the CMS search at a centre-of-mass of 8 TeV expected limits of 0.027% [41]. The observed limit of 0.024% for the tZu interaction doesn't surpass the CMS 8 TeV observed limit of 0.022% [41]. The ATLAS collaboration has set limits 95% CL at a centre-of-mass of 13 TeV [40] with observed (expected) limits of 0.017% (0.024%) for the tZu coupling. The expected limit presented in this analysis surpasses the expected limit for tZu.

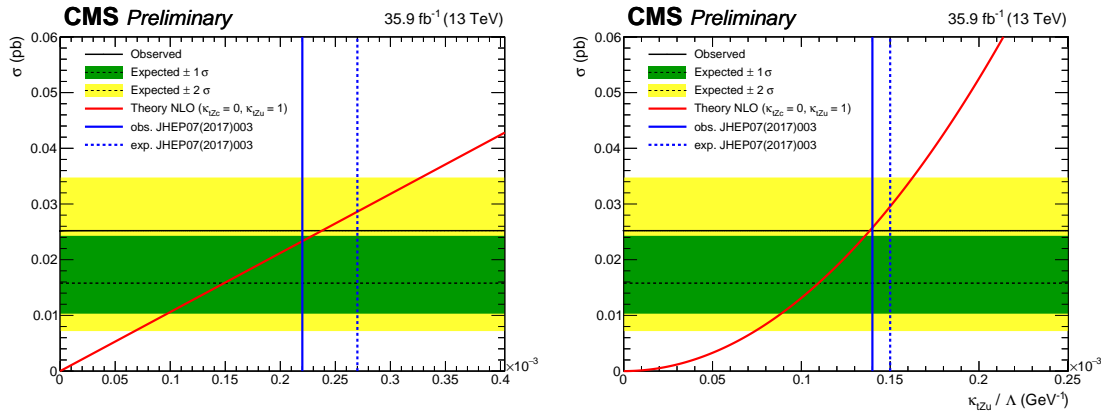


Figure 6.21: Exclusion limits at 95% CL on the FCNC branching fractions (left) and couplings (right) as a function of the cross section of the FCNC process, considering only the tZu vertex. The CMS observed (expected) limit at 95% CL at a centre-of-mass of 8 TeV [41] is given with a blue line (dashed line).

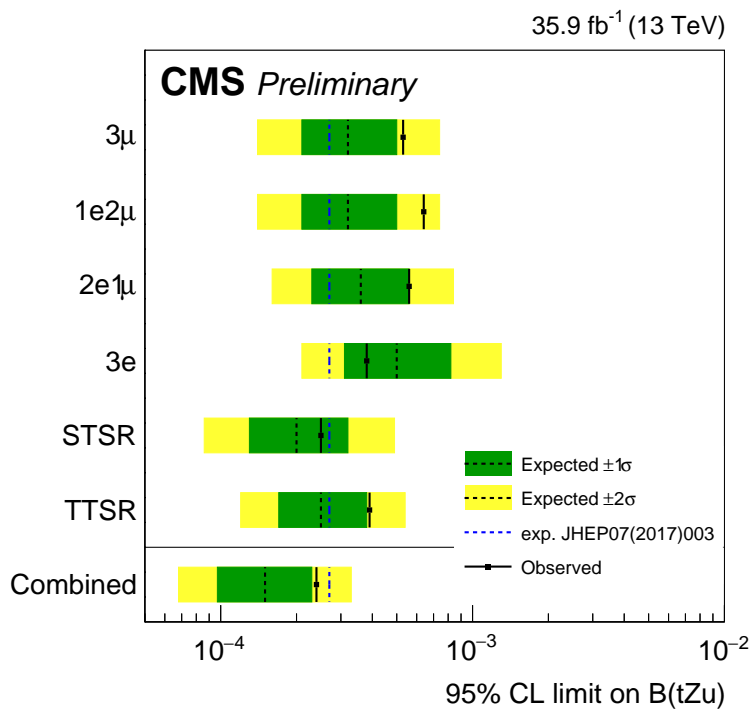
1659

In Figure 6.22 and Table 6.2, the limits for each leptonic channel separate as well as their combined limits are shown for the tZu vertex. The leptonic channels are in agreement with each other, where the presence of a muon helps pushing the limit further. The STSR is the most sensitive region because of the higher presence of the targeted single top quark signal. Further, one can see that by combining signle top quark and top quark pair signals, one gains in sensitivity.

In Figure 6.23, the resulting limits at 95% CL on the branching fraction and couplings related to the tZc vertex is shown. or this coupling, the observed (expected) limit at 95% CL is $\mathcal{B} < 0.045\%$ (0.037%) when $\kappa_{tZc}/\Lambda \neq 0$ and $\kappa_{tZu}/\Lambda = 0$. The expected limit surpasses the CMS search at a centre-of-mass of 8 TeV expected limits of 0.118% [41]. This also the case for the observed limit of 0.045% for the tZc interaction, which surpasses the CMS 8 TeV observed limit of 0.049% [41]. The observed (expected) limits set by the ATLAS collaboration at a centre-of-mass of 13 TeV [40] are 0.023% (0.032%) for the tZc coupling. The expected limit presented in this analysis is in accordance with this limit.

Table 6.2: Expected limits on the branching fractions at 95% CL for the tZu coupling [40, 41].

	expected	+2 σ	+1 σ	-1 σ	-2 σ	observed
3 μ	0.032%	0.074%	0.050%	0.021%	0.014%	0.053%
1e2 μ	0.032%	0.074%	0.050%	0.021%	0.014%	0.064%
2e1 μ	0.036%	0.084%	0.056%	0.023%	0.016%	0.056%
3e	0.050%	0.13%	0.082%	0.031%	0.021%	0.038%
STSR only	0.020%	0.049%	0.032%	0.013%	0.0086%	0.025%
TTSR only	0.025%	0.054%	0.038%	0.025%	0.017%	0.039%
combined	0.015%	0.033%	0.023%	0.0097%	0.0068%	0.024%
8 TeV CMS (19.7 fb^{-1})	0.027%	-%	0.42%	0.018%	-%	0.022%
13 TeV ATLAS (36 fb^{-1})	0.024%	-%	0.35%	0.017%	-%	0.017%

**Figure 6.22:** Exclusion limits at 95% CL for each leptonic channel and signal region on the FCNC tZu branching fractions considering one non-vanishing coupling at a time. The CMS observed (expected) limit at 95% CL at a centre-of-mass of 8 TeV [41] is given with a blue line (dashed line).

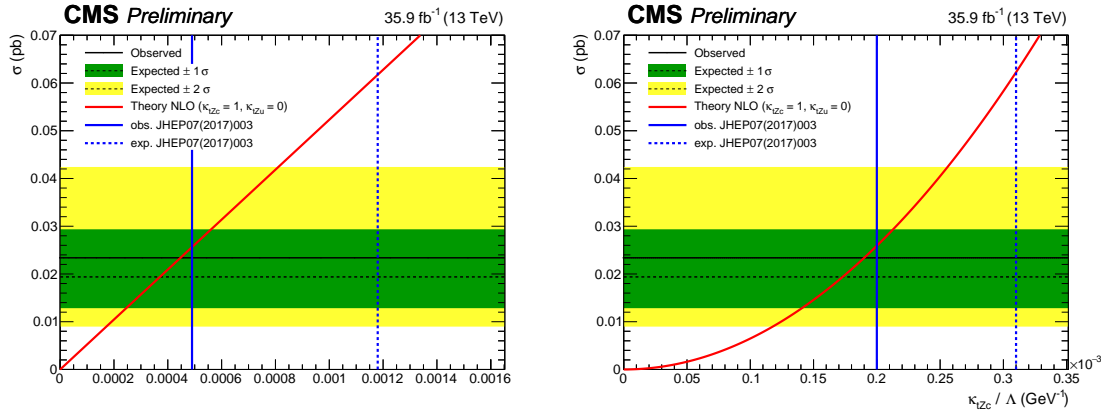


Figure 6.23: Exclusion limits at 95% CL on the FCNC branching fractions (left) and couplings (right) as a function of the cross section of the FCNC process, considering only the tZc vertex. The CMS observed (expected) limit at 95% CL at a centre-of-mass of 8 TeV [41] is given with a blue line (dashed line).

1674 The limits for each leptonic channel separate as well as their combined limits are shown for
 1675 the tZc vertex in [Figure 6.24](#) and [Table 6.3](#). Also here, the leptonic channels are in agreement
 1676 with each other, and the presence of a muon helps the sensitivity. For the tZu vertex, the TTSR
 1677 is the most sensitive region and by combining single top quark and top quark pair signals, one
 1678 also gains in sensitivity.

Table 6.3: Expected limits on the branching fractions at 95% CL for the tZc coupling [40, 41].

	expected	+2σ	+1σ	-1σ	-2σ	observed
3μ	0.070%	0.15%	0.10%	0.046%	0.032%	0.12%
1e2μ	0.079%	0.18%	0.12%	0.052%	0.036%	0.096%
2e1μ	0.089%	0.20%	0.14%	0.058%	0.040%	0.099%
3e	0.12%	0.29%	0.19%	0.075%	0.050%	0.095%
STSR only	0.10%	0.23%	0.16%	0.066%	0.045%	0.17%
TTSR only	0.044%	0.094%	0.066%	0.029%	0.020%	0.043%
combined	0.037%	0.081%	0.056%	0.025%	0.017%	0.045%
8 TeV CMS (19.7 fb^{-1})	0.118%	-%	0.222%	0.071%	-%	0.049%
13 TeV ATLAS (36 fb^{-1})	0.032%	-%	0.046%	0.022%	-%	0.023%

1679 6.4.2 Two-dimensional limits

One can interpolate the one dimensional limits λ_{tZq}^{1D} to a scenario where both couplings are on-vanishing. The interpolation is taken from Ref. , where an experimental extrapolation

NOTE: Add source

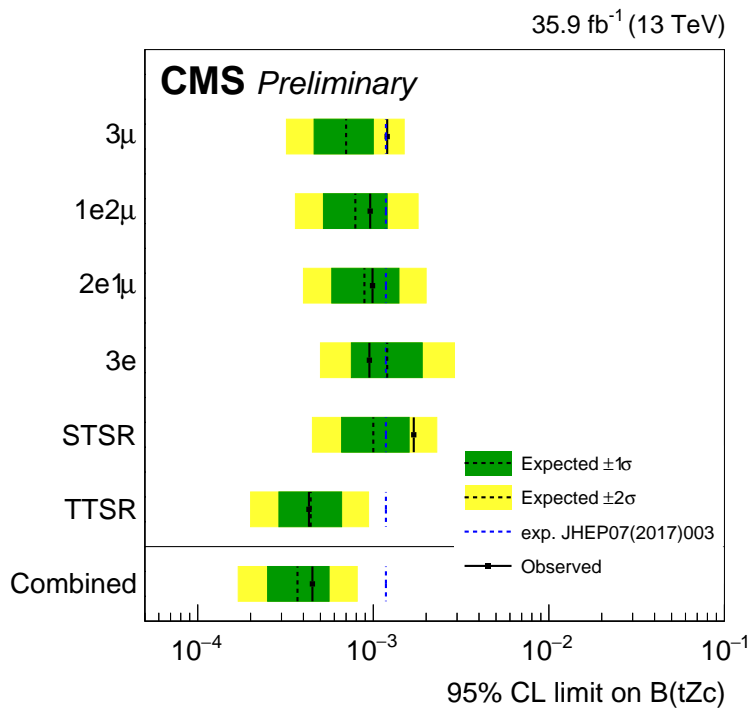


Figure 6.24: Exclusion limits at 95% CL for each leptonic channel and signal region on the FCNC tZ_c branching fractions considering one non-vanishing coupling at a time. The CMS observed (expected) limit at 95% CL at a centre-of-mass of 8 TeV [41] is given with a blue line (dashed line).

formulae

$$\kappa_{tZ_c}/\Lambda = \kappa_{tZ_u}^{1D} \sqrt{1 - \frac{\kappa_{tZ_u}/\Lambda}{\kappa_{tZ_u}^{1D}}}, \quad (6.1)$$

is found from 100 benchmark scenarios. These scenarios are constructed from existing signal samples as

$$\text{Signal yield} = (\kappa_{tZ_u}/\Lambda)^2 (\text{ST Zut yield} + \text{TT Zut yield}) + (\kappa_{tZ_c}/\Lambda)^2 (\text{ST Zct yield} + \text{TT Zct yield}). \quad (6.2)$$

1680 For each scenario a dedicated BDT training is performed and the expected limit at 95% CL are
 1681 calculated. The resulting two-dimensional limits are shown in Figure 6.25.

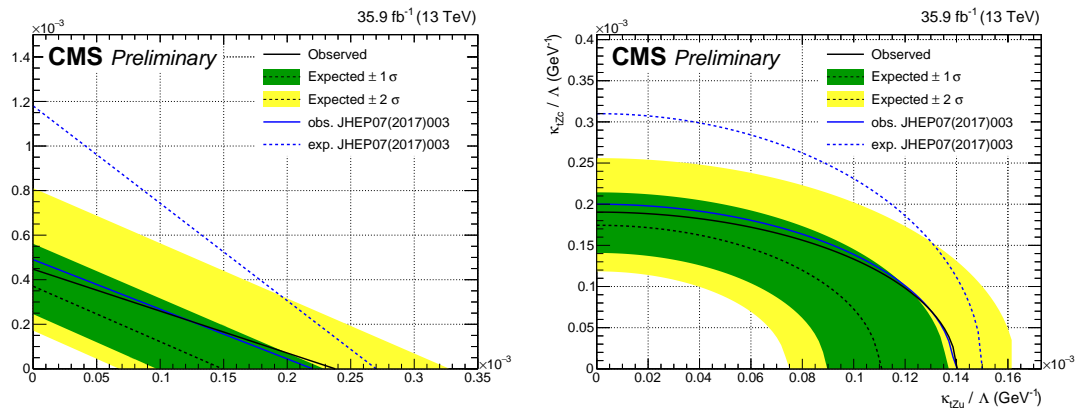


Figure 6.25: Two-dimensional limits on the branching fractions (left) and couplings (right) for FCNC interactions involving a tZq vertex. The CMS observed (expected) limit at 95% CL at a centre-of-mass of 8 TeV [41] is given with a blue line (dashed line).

Denouement of the top-Z FCNC hunt at 13 TeV

1682

7

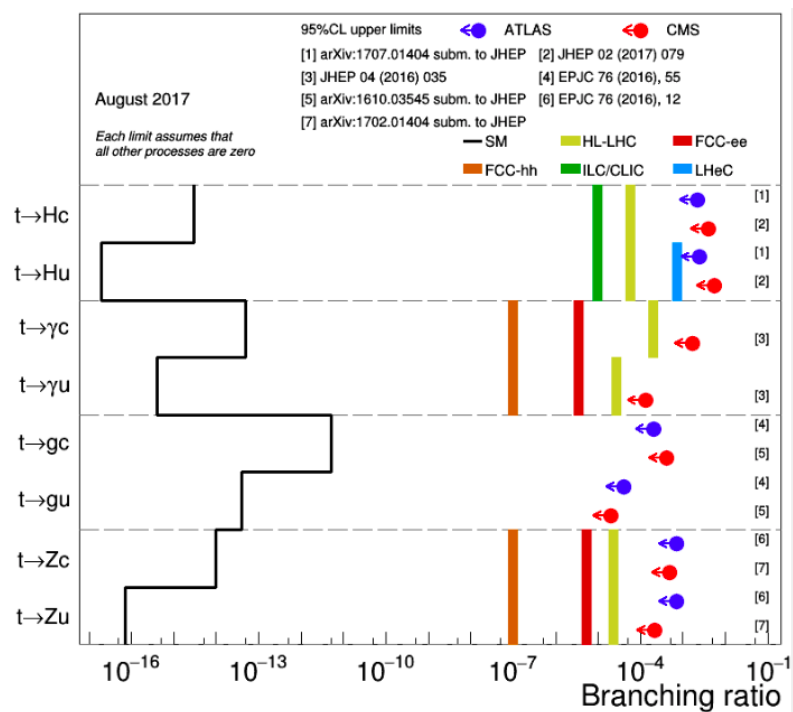


Figure 7.1:

1683

Trigger scale factors



1684 The trigger scale factors measured as a function of lepton p_T , using the dataset collected by
 1685 E_T^{miss} triggers and WZ simulation, after a 3 lepton and jets selection, in the Z mass window. All
 1686 corrections to simulation are applied.

Table A.1: Trigger efficiencies on data events selected with E_T^{miss} triggers and WZ simulation for all leptonic channels together. The unweighed number of events is quoted. When there are no events passing the cuts, it is indicated with N/A. The uncertainties are statistical uncertainties.

ALL CHANNEL	data		WZ simulations	
	Efficiency	unc.	Efficiency	unc.
3 lep, at least one jet	117/118 = 99.15 %	12.94%	18047/18055 = 99.96%	1.05%
STSR	6/6 = 100.00%	57.74%	1541/1541 = 100.00%	3.60%
TTSR	26/27 = 96.30%	26.46%	1791/1792 = 99.94%	3.34%
WZCR	69/69 = 100.00 %	17.03%	14405/14412=99.95%	1.18%

Table A.2: Trigger efficiencies on data events selected with E_T^{miss} triggers and WZ simulation for 3 μ leptonic channel together. The unweighed number of events is quoted. When there are no events passing the cuts, it is indicated with N/A. The uncertainties are statistical uncertainties.

3 μ CHANNEL	data		WZ simulations	
	Efficiency	unc.	Efficiency	unc.
3 lep, at least one jet	40/40 = 100.00 %	22.36 %	7814/7814 = 100.00%	1.60%
STSR	N/A	N/A	687/687 = 100%	5.40%
TTSR	13/13 = 100.00%	39.22%	763/763 = 100.00%	5.12%
WZCR	22/22 = 100.00 %	30.15%	6238/6238=100.00%	1.79%

Table A.3: Trigger efficiencies on data events selected with E_T^{miss} triggers and WZ simulation for 3e leptonic channel together. The unweighted number of events is quoted. When there are no events passing the cuts, it is indicated with N/A. The uncertainties are statistical uncertainties.

3e CHANNEL	data		WZ simulations	
	Efficiency	unc.	Efficiency	unc.
3 lep, at least one jet	20/21 = 95.24%	29.76%	2211/2215 = 99.82 %	3.00%
STS R	4/4 = 100.00%	70.71%	176/176 = 100.00%	10.66%
TTS R	2/3 = 66.67%	60.86%	242/242 = 100.00%	9.09%
WZCR	14/14 = 100.00 %	37.80%	1744/1748=99.77%	3.38%

Table A.4: Trigger efficiencies on data events selected with E_T^{miss} triggers and WZ simulation for 2e1 μ leptonic channel together. The unweighted number of events is quoted. When there are no events passing the cuts, it is indicated with N/A. The uncertainties are statistical uncertainties.

2e1 μ CHANNEL	data		WZ simulations	
	Efficiency	unc.	Efficiency	unc.
3 lep, at least one jet	32/32 = 100.00 %	25.00 %	3116/3118 = 99.94%	2.53%
STS R	1/1 = 100.00%	141.42%	255/255 = 100%	8.86%
TTS R	9/9 = 100.00%	47.14%	291/291 = 100.00%	8.29%
WZCR	14/14 = 100.00 %	37.80%	2529/2531=99.92%	2.81%

Table A.5: Trigger efficiencies on data events selected with E_T^{miss} triggers and WZ simulation for 1e2 μ leptonic channel together. The unweighted number of events is quoted. When there are no events passing the cuts, it is indicated with N/A. The uncertainties are statistical uncertainties.

1e2 μ CHANNEL	data		WZ simulations	
	Efficiency	unc.	Efficiency	unc.
3 lep, at least one jet	25/25 = 100.00%	28.28%	4906/4908 = 99.96 %	2.02%
STS R	1/1 = 100.00%	141.42%	423/423 = 100.00%	6.88%
TTS R	2/2 = 100.00%	100.00%	495/496 = 99.80%	6.34%
WZCR	19/19 = 100.00 %	32.44%	3894/3895 =99.97%	2.27%

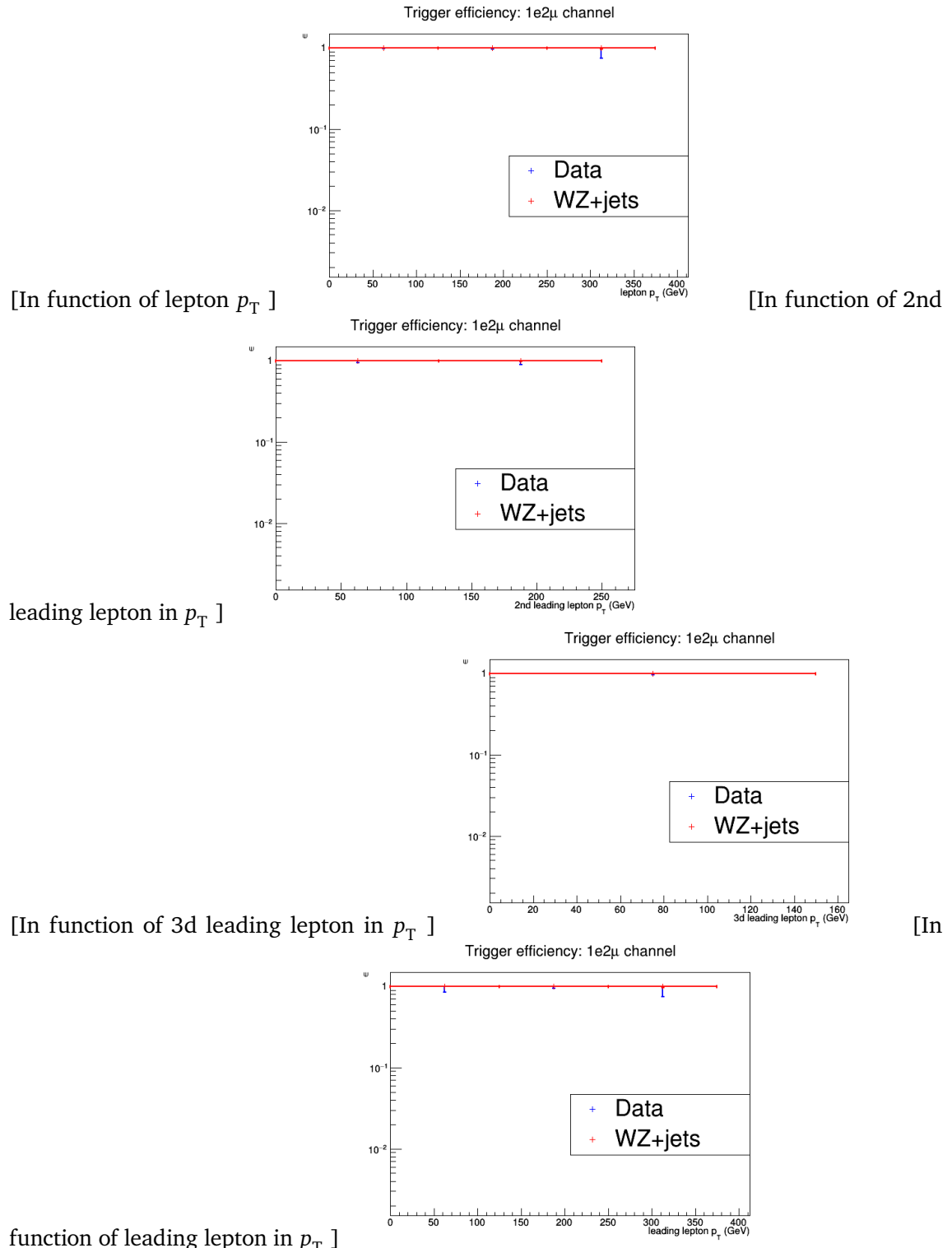


Figure A.1: The trigger efficiencies measured as a function of lepton p_T , using the dataset collected by E_T^{miss} triggers and WZ simulation, after a 3 lepton and jets selection, in the Z mass window. All corrections to simulation are applied. 1e2μ channel.

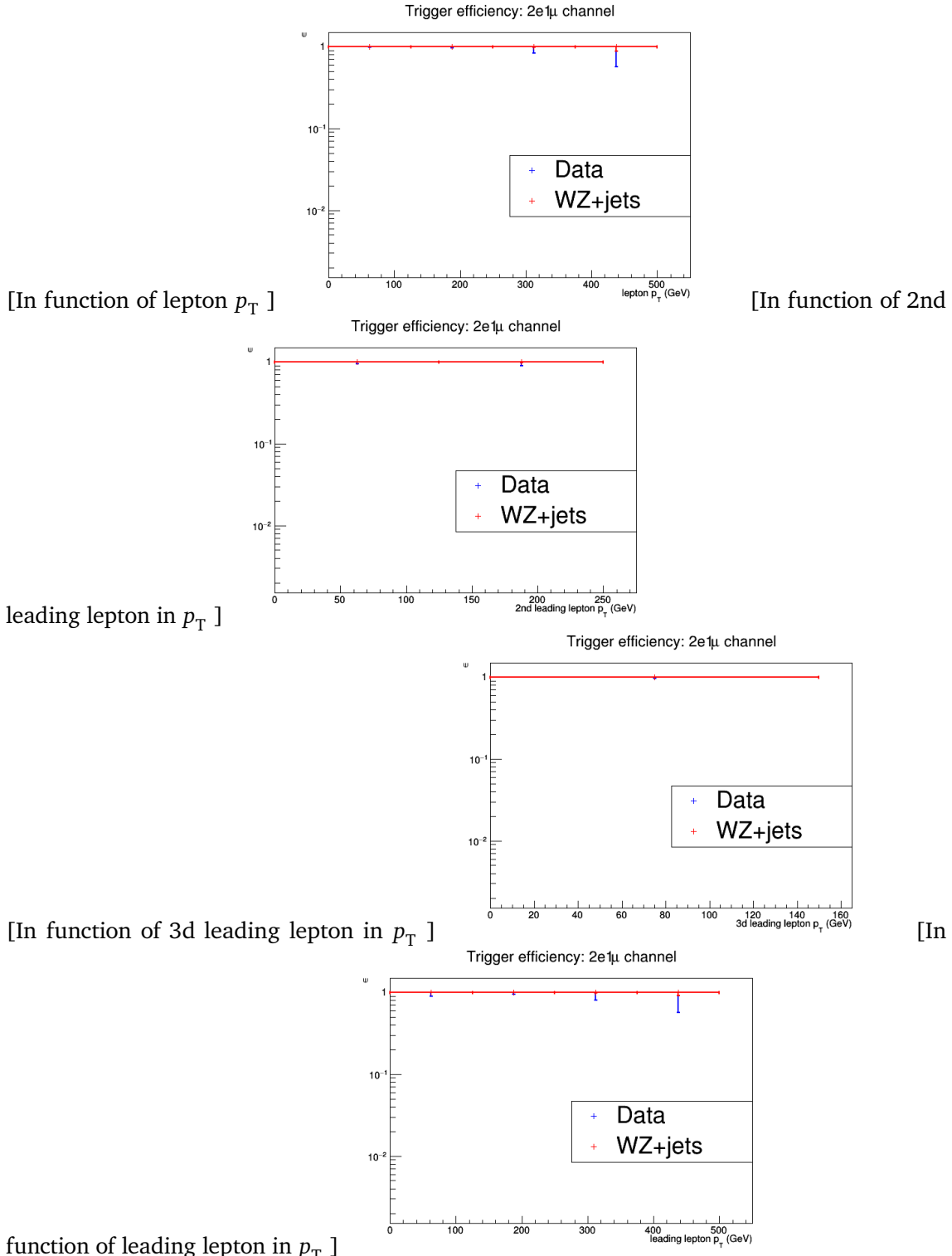


Figure A.2: The trigger efficiencies measured as a function of lepton p_T , using the dataset collected by E_T^{miss} triggers and WZ simulation, after a 3 lepton and jets selection, in the Z mass window. All corrections to simulation are applied. 2e1μ channel.

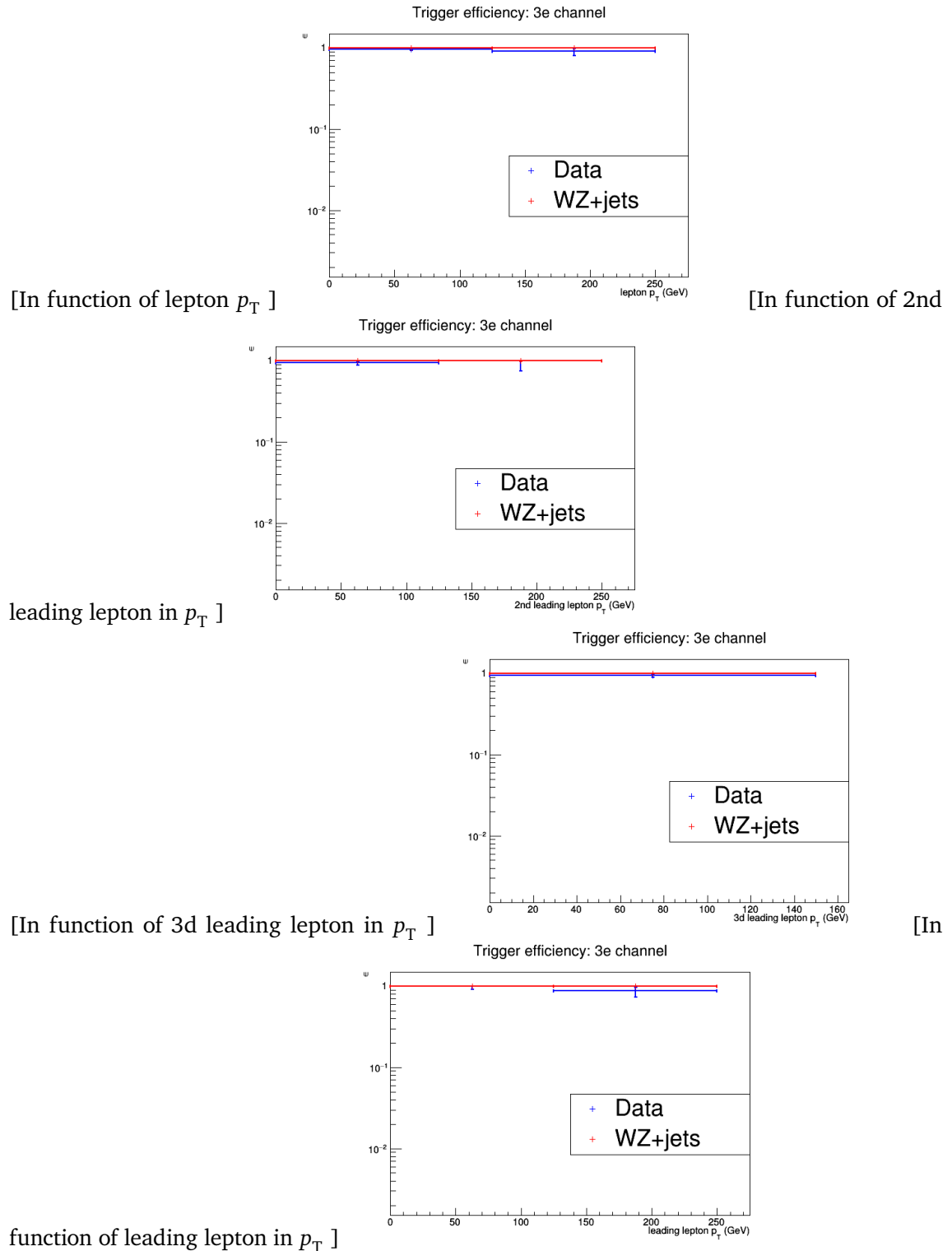


Figure A.3: The trigger efficiencies measured as a function of lepton p_T , using the dataset collected by E_T^{miss} triggers and WZ simulation, after a 3 lepton and jets selection, in the Z mass window. All corrections to simulation are applied. 3e channel.

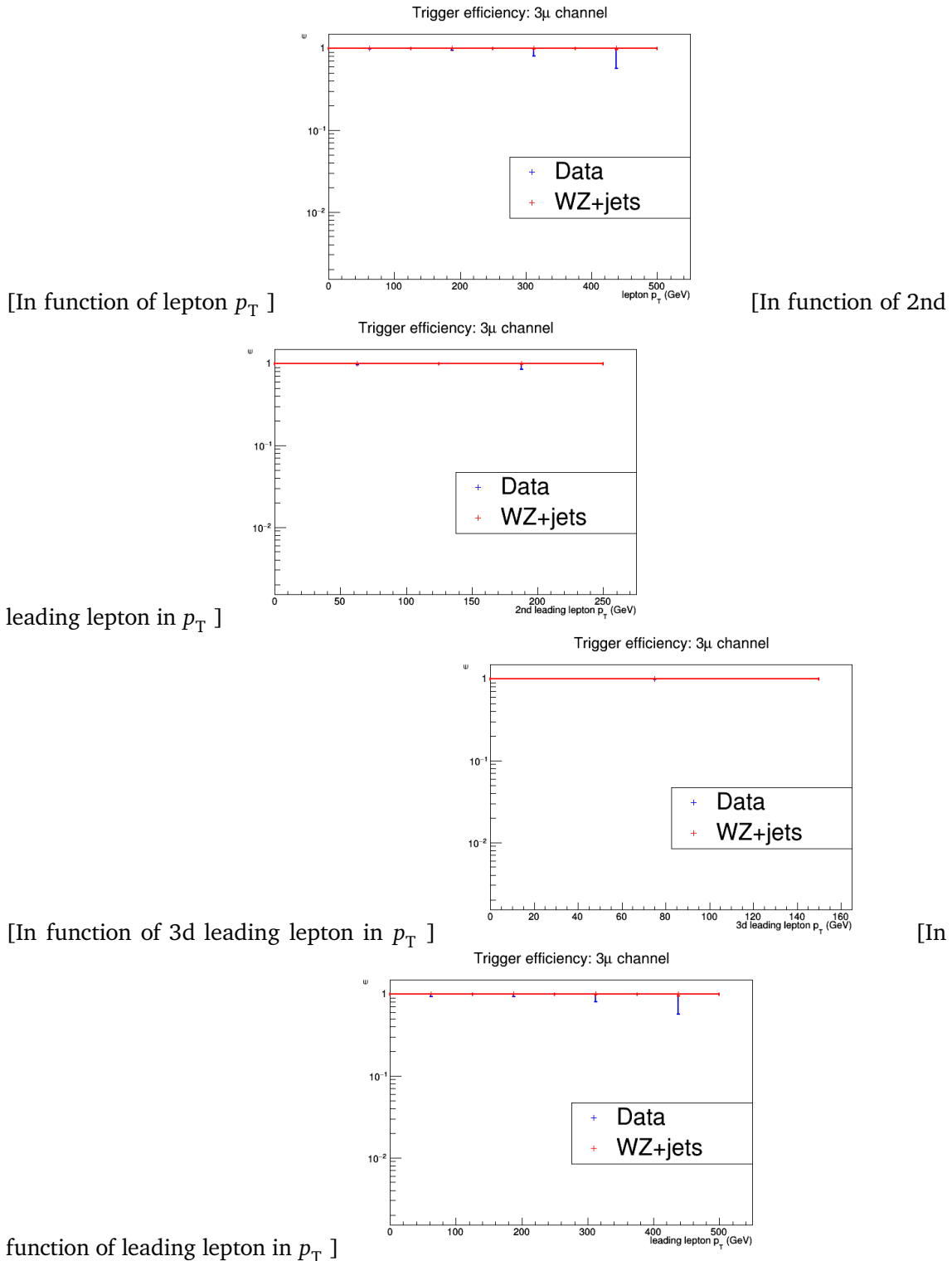


Figure A.4: The trigger efficiencies measured as a function of lepton p_T , using the dataset collected by E_T^{miss} triggers and WZ simulation, after a 3 lepton and jets selection, in the Z mass window. All corrections to simulation are applied. 3μ channel.

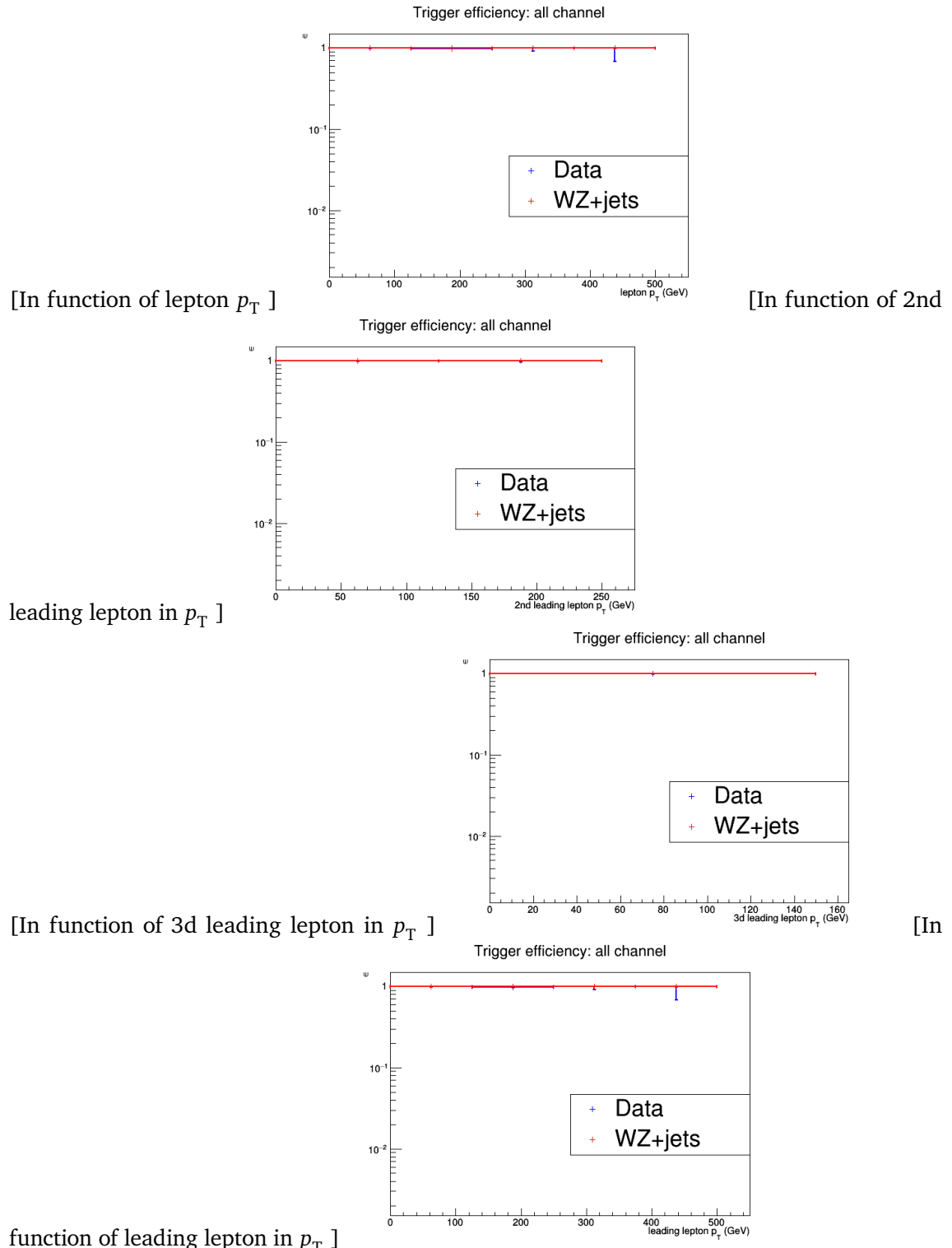


Figure A.5: The trigger efficiencies measured as a function of lepton p_T , using the dataset collected by E_T^{miss} triggers and WZ simulation, after a 3 lepton and jets selection, in the Z mass window. All corrections to simulation are applied. All channel.

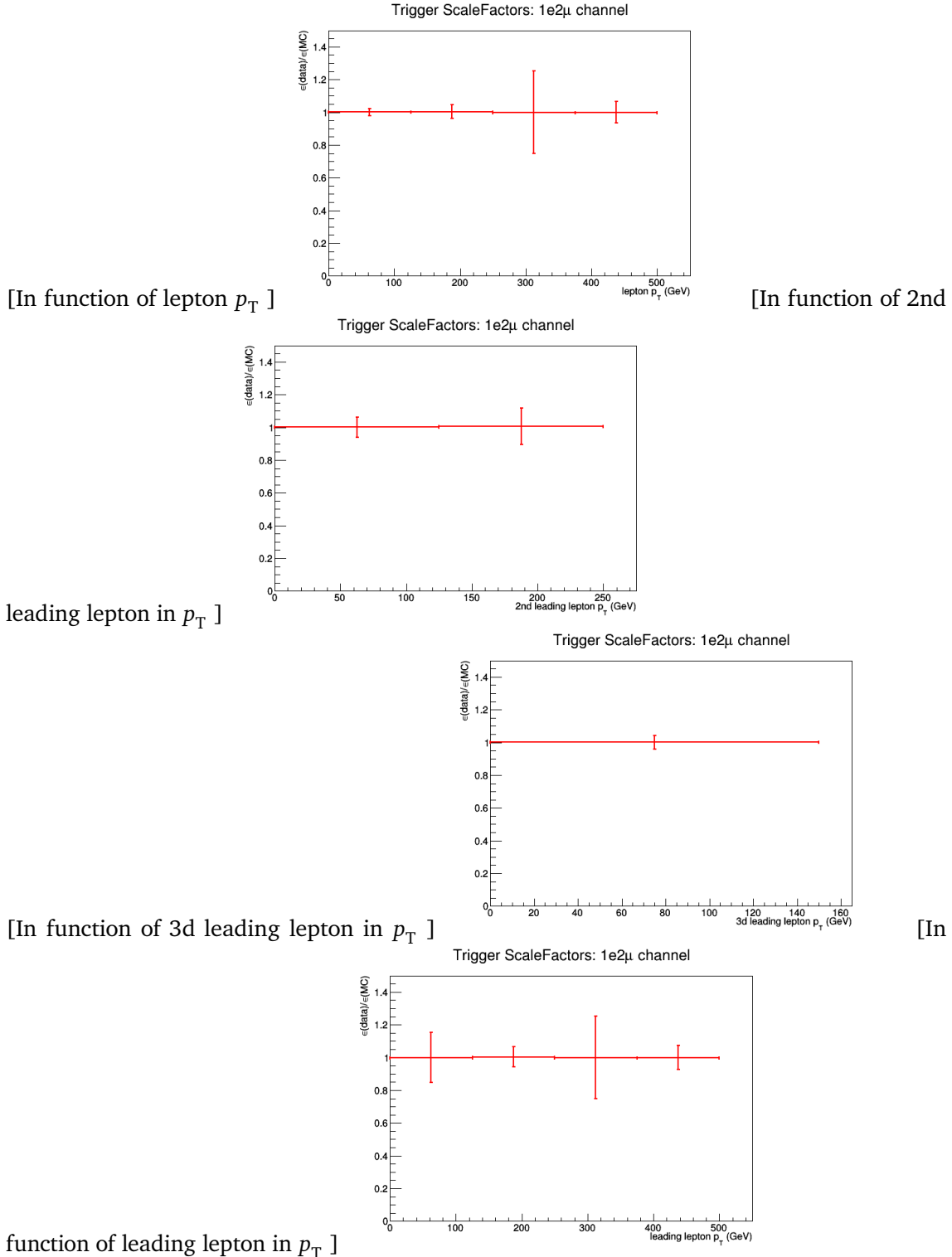


Figure A.6: The trigger scale factors measured as a function of lepton p_T , using the dataset collected by E_T^{miss} triggers and WZ simulation, after a 3 lepton and jets selection, in the Z mass window. All corrections to simulation are applied. 1e2μ channel.

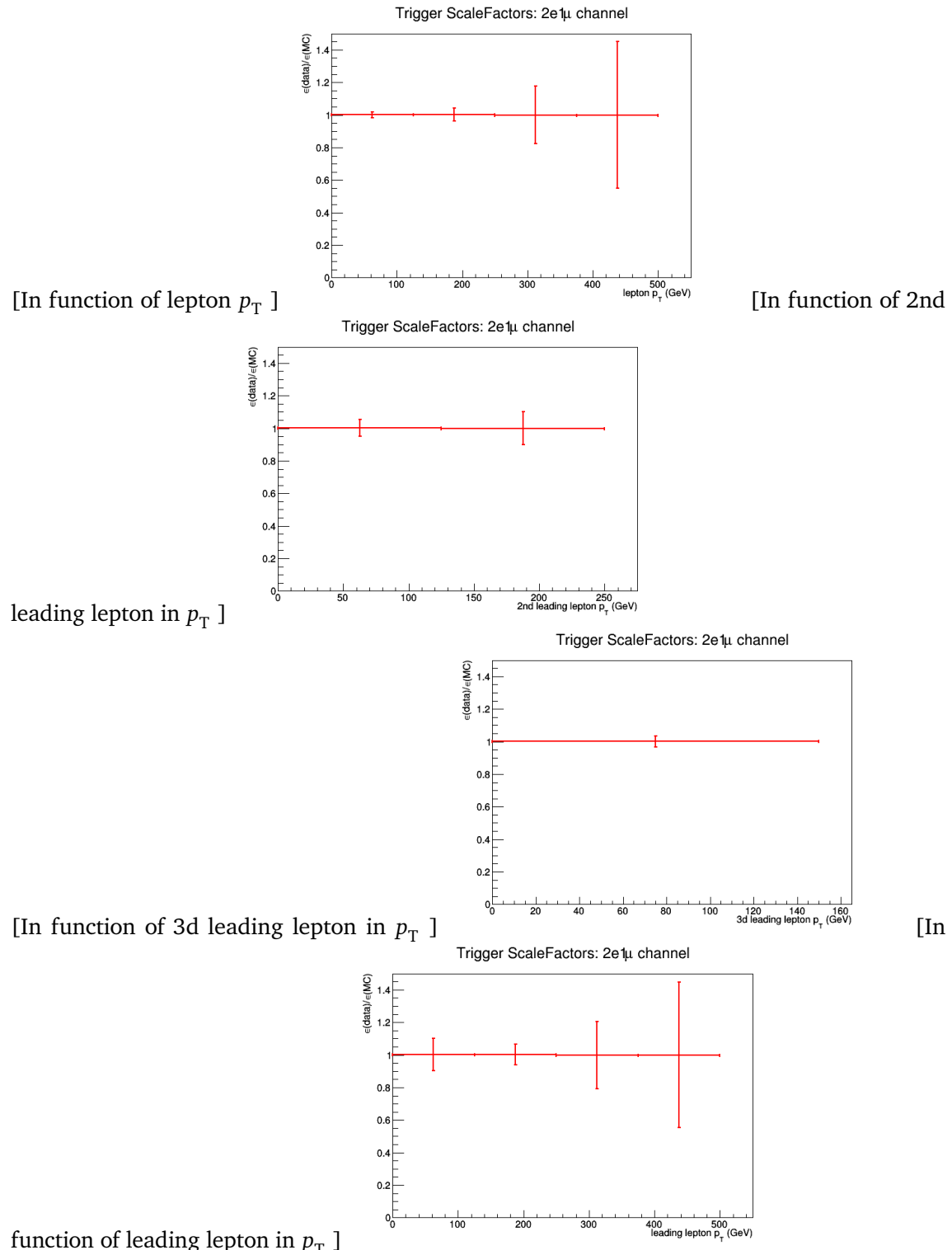


Figure A.7: The trigger scale factors measured as a function of lepton p_T , using the dataset collected by E_T^{miss} triggers and WZ simulation, after a 3 lepton and jets selection, in the Z mass window. All corrections to simulation are applied. 2e1μ channel.

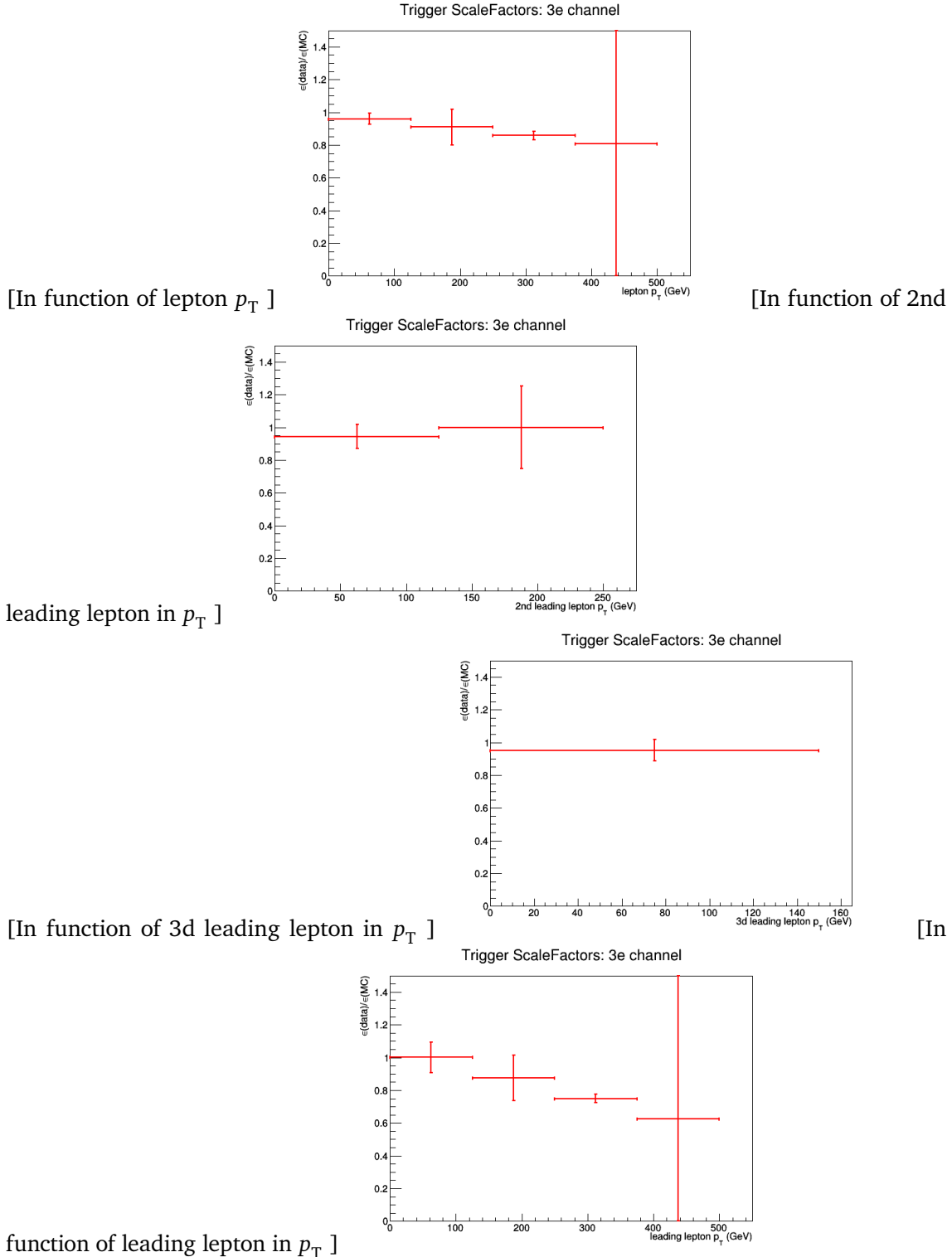


Figure A.8: The trigger scale factors measured as a function of lepton p_T , using the dataset collected by E_T^{miss} triggers and WZ simulation, after a 3 lepton and jets selection, in the Z mass window. All corrections to simulation are applied. 3e channel.

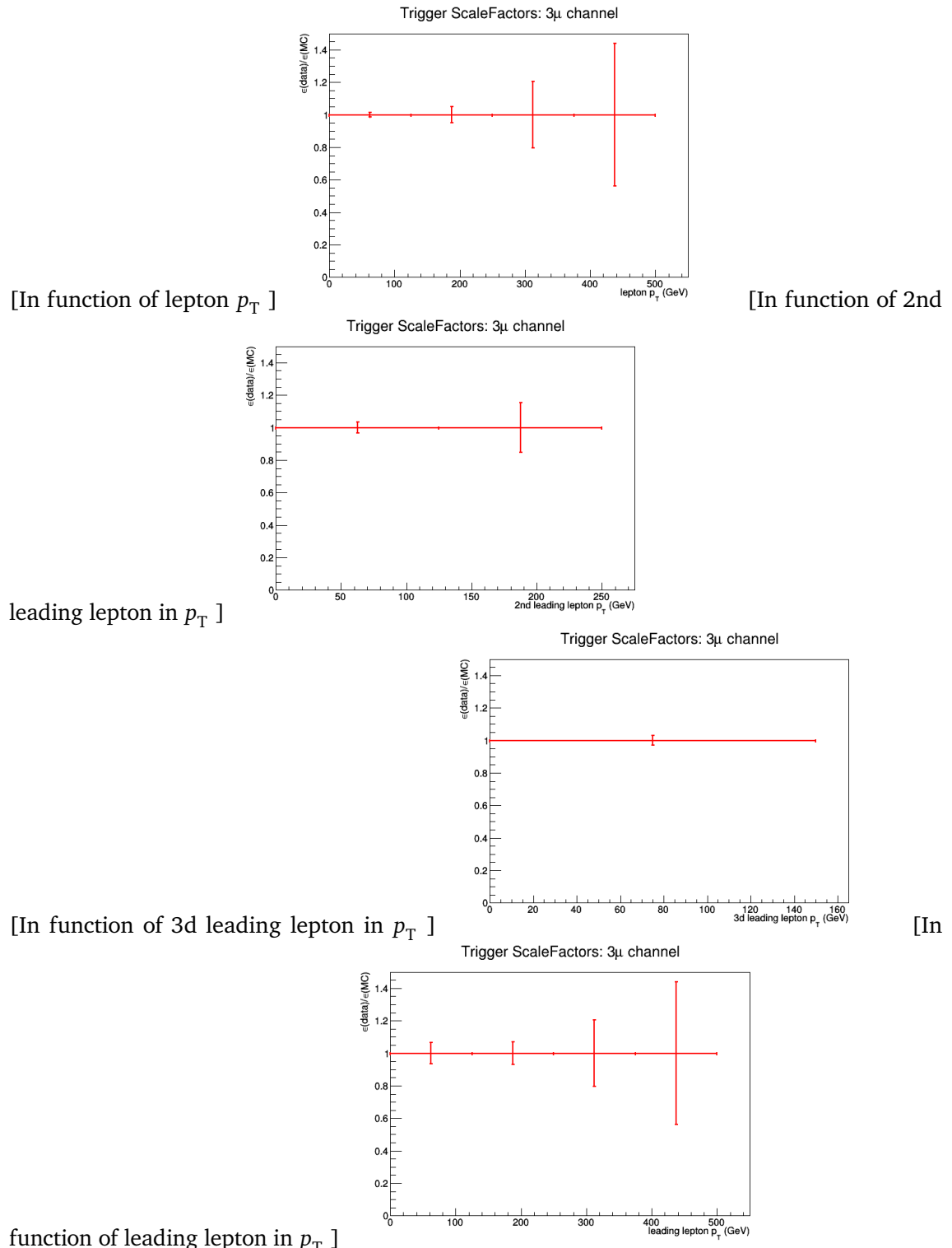


Figure A.9: The trigger scale factors measured as a function of lepton p_T , using the dataset collected by E_T^{miss} triggers and WZ simulation, after a 3 lepton and jets selection, in the Z mass window. All corrections to simulation are applied. 3μ channel.

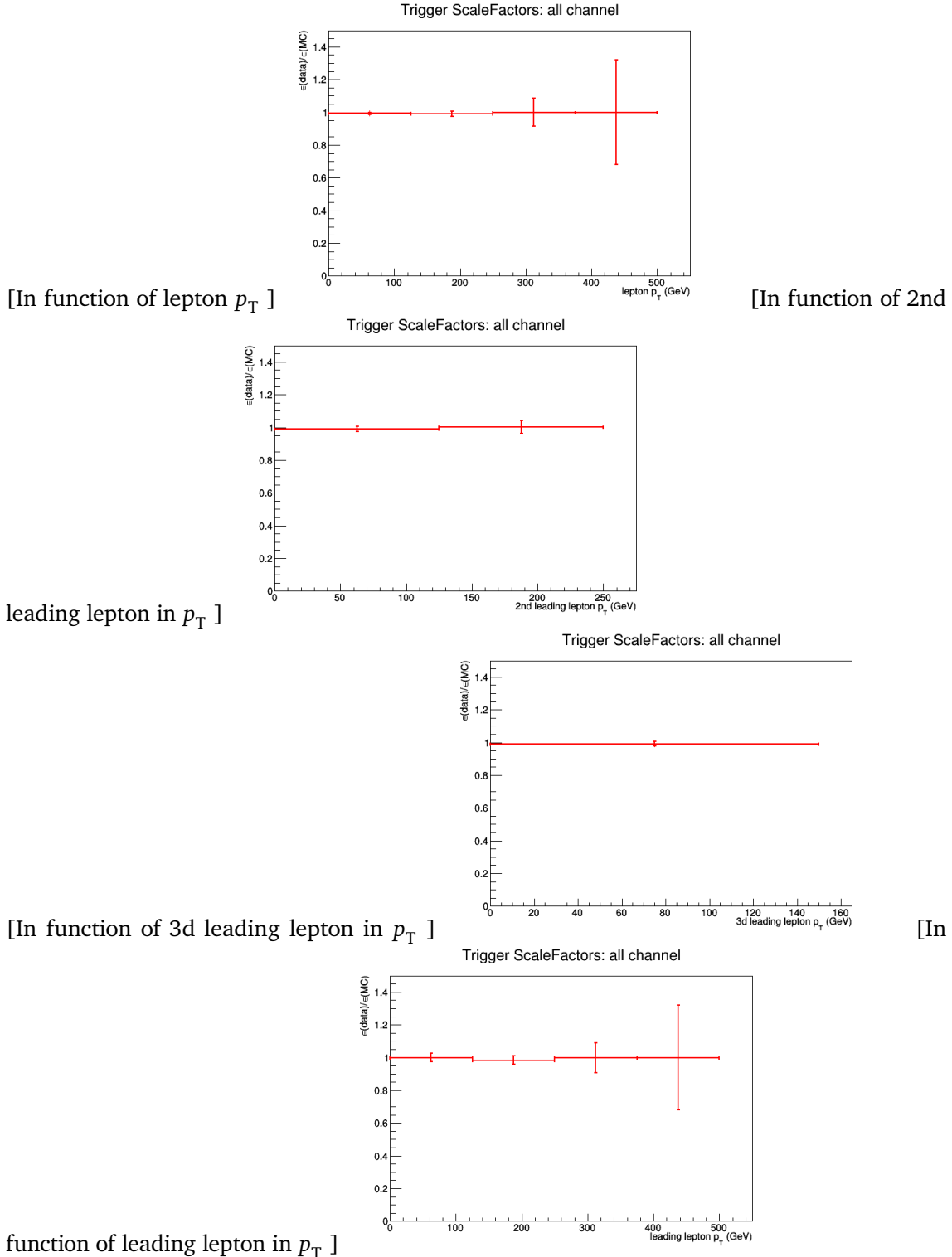


Figure A.10: The trigger scale factors measured as a function of lepton p_T , using the dataset collected by E_T^{miss} triggers and WZ simulation, after a 3 lepton and jets selection, in the Z mass window. All corrections to simulation are applied. All channel.

Dilepton controlplots

B

Statistical independent regions

1688

C

	STS R	TTS R	WZCR	TTCR	STCR	$Tr_{WZCR \rightarrow STSR}$	$Tr_{WZCR \rightarrow TTSR}$	$Tr_{TTCR \rightarrow TTSR}$	$Tr_{STCR \rightarrow STSR}$
FCNC tZu	3.9 ± 0.0	11.2 ± 0.0	7.3 ± 0.0	0.6 ± 0.0	0.3 ± 0.0	0.22 ± 0.00	0.46 ± 0.00	—	—
FCNC tZc	14.1 ± 0.1	30.9 ± 0.1	15.5 ± 0.1	1.7 ± 0.0	1.2 ± 0.0	0.39 ± 0.01	0.76 ± 0.01	—	—
DY	-4.6 ± 21.7	22.3 ± 14.3	136.9 ± 48.5	-14.0 ± 22.2	-15.9 ± 11.3	0.08 ± 0.09	0.10 ± 0.10	—	—
ttbar	13.1 ± 2.5	9.7 ± 2.1	8.5 ± 1.9	22.3 ± 3.1	33.7 ± 3.8	0.54 ± 0.31	0.70 ± 0.31	0.33 ± 0.00	0.33 ± 0.00
DD fake	62.0 ± 7.9	63.0 ± 7.9	204.0 ± 14.3	41.0 ± 6.4	56.0 ± 7.5	—	—	—	—
WZ+jets	60.9 ± 1.6	83.0 ± 1.7	552.7 ± 4.6	11.9 ± 0.6	8.5 ± 0.6	0.10 ± 0.00	0.15 ± 0.00	—	—
tZq	8.0 ± 0.2	16.9 ± 0.2	7.3 ± 0.2	2.2 ± 0.1	1.0 ± 0.1	0.36 ± 0.02	0.67 ± 0.03	—	—
ttZ	3.5 ± 0.3	42.5 ± 0.9	9.6 ± 0.5	6.8 ± 0.4	0.5 ± 0.1	0.14 ± 0.02	0.61 ± 0.05	—	—
ZZ	4.6 ± 0.1	4.8 ± 0.1	46.2 ± 0.3	0.8 ± 0.0	0.6 ± 0.0	0.10 ± 0.00	0.13 ± 0.00	—	—
other	1.2 ± 0.3	5.6 ± 0.3	6.8 ± 0.5	7.5 ± 0.7	2.4 ± 0.5	0.16 ± 0.03	0.30 ± 0.03	—	—

Table C.1: Event yields: All channel. The last three columns represent the transfer factors that have to be applied.

Bibliography

- 1690 [1] MICHAEL E PESKIN and DANIEL V SCHROEDER: **An introduction to quantum field**
 1691 **theory; 1995 ed.** Includes exercises. Boulder, CO: Westview, 1995. URL: <https://cds.cern.ch/record/257493> (see pp. 1, 6, 11, 16).
- 1693 [2] C. P. BURGESS: **Introduction to Effective Field Theory**. In: *Ann. Rev. Nucl. Part. Sci.*, **57**: (2007), pp. 329–362. DOI: [10.1146/annurev.nucl.56.080805.140508](https://doi.org/10.1146/annurev.nucl.56.080805.140508). arXiv: [hep-th/0701053 \[hep-th\]](https://arxiv.org/abs/hep-th/0701053) (see p. 1).
- 1696 [3] NADIA ROBOTTI: **The discovery of the electron: I**. In: *European Journal of Physics*,
 1697 **18**:3 (1997), p. 133. URL: <http://stacks.iop.org/0143-0807/18/i=3/a=002> (see p. 2).
- 1698 [4] Y. FUKUDA et al.: **Evidence for oscillation of atmospheric neutrinos**. In: *Phys. Rev. Lett.*, **81**: (1998), pp. 1562–1567. DOI: [10.1103/PhysRevLett.81.1562](https://doi.org/10.1103/PhysRevLett.81.1562). arXiv: [hep-ex/9807003 \[hep-ex\]](https://arxiv.org/abs/hep-ex/9807003) (see pp. 2, 14).
- 1701 [5] Y. ABE et al.: **Indication of Reactor $\bar{\nu}_e$ Disappearance in the Double Chooz Experiment**. In: *Phys. Rev. Lett.*, **108**: (13 Mar. 2012), p. 131801. DOI: [10.1103/PhysRevLett.108.131801](https://doi.org/10.1103/PhysRevLett.108.131801) (see pp. 2, 14).
- 1704 [6] C. PATRIGNANI et al.: **Review of Particle Physics**. In: *Chin. Phys.*, **C40**:10 (2016),
 1705 p. 100001. DOI: [10.1088/1674-1137/40/10/100001](https://doi.org/10.1088/1674-1137/40/10/100001) (see pp. 2–3, 6–8, 10, 42–43).
- 1706 [7] S. ABACHI et al.: **Observation of the top quark**. In: *Phys. Rev. Lett.*, **74**: (1995),
 1707 pp. 2632–2637. DOI: [10.1103/PhysRevLett.74.2632](https://doi.org/10.1103/PhysRevLett.74.2632). arXiv: [hep-ex/9503003 \[hep-ex\]](https://arxiv.org/abs/hep-ex/9503003)
 1708 (see p. 2).
- 1709 [8] F. ABE et al.: **Observation of top quark production in $\bar{p}p$ collisions**. In: *Phys. Rev. Lett.*, **74**: (1995), pp. 2626–2631. DOI: [10.1103/PhysRevLett.74.2626](https://doi.org/10.1103/PhysRevLett.74.2626). arXiv: [hep-ex/9503002 \[hep-ex\]](https://arxiv.org/abs/hep-ex/9503002) (see p. 2).
- 1712 [9] **First combination of Tevatron and LHC measurements of the top-quark mass**. In:
 1713 (2014). arXiv: [1403.4427 \[hep-ex\]](https://arxiv.org/abs/1403.4427) (see p. 2).
- 1714 [10] SERGUEI CHATRCHYAN et al.: **Observation of a new boson at a mass of 125 GeV**
 1715 **with the CMS experiment at the LHC**. In: *Phys. Lett.*, **B716**: (2012), pp. 30–61. DOI:
 1716 [10.1016/j.physletb.2012.08.021](https://doi.org/10.1016/j.physletb.2012.08.021). arXiv: [1207.7235 \[hep-ex\]](https://arxiv.org/abs/1207.7235) (see pp. 2, 23).
- 1717 [11] GEORGES AAD et al.: **Observation of a new particle in the search for the Standard**
 1718 **Model Higgs boson with the ATLAS detector at the LHC**. In: *Phys. Lett.*, **B716**:
 1719 (2012), pp. 1–29. DOI: [10.1016/j.physletb.2012.08.020](https://doi.org/10.1016/j.physletb.2012.08.020). arXiv: [1207.7214 \[hep-ex\]](https://arxiv.org/abs/1207.7214)
 1720 (see pp. 2, 23).

- [12] NICOLA CABIBBO: **Unitary Symmetry and Leptonic Decays**. In: *Phys. Rev. Lett.*, **10**: (12 June 1963), pp. 531–533. doi: [10.1103/PhysRevLett.10.531](https://doi.org/10.1103/PhysRevLett.10.531) (see p. 5).
- [13] S. L. GLASHOW, J. ILIOPoulos, and L. MAIANI: **Weak Interactions with Lepton-Hadron Symmetry**. In: *Phys. Rev. D*, **2**: (7 Oct. 1970), pp. 1285–1292. doi: [10.1103/PhysRevD.2.1285](https://doi.org/10.1103/PhysRevD.2.1285) (see p. 5).
- [14] B.J. BJØRKEN and S.L. GLASHOW: **Elementary particles and SU(4)**. In: *Physics Letters*, **11**:3 (1964), pp. 255–257. doi: [https://doi.org/10.1016/0031-9163\(64\)90433-0](https://doi.org/10.1016/0031-9163(64)90433-0) (see p. 5).
- [15] LUCIANO MAIANI: **The GIM Mechanism: origin, predictions and recent uses**. In: *Proceedings, 48th Rencontres de Moriond on Electroweak Interactions and Unified Theories: La Thuile, Italy, March 2-9, 2013*. 2013, pp. 3–16. arXiv: [1303.6154 \[hep-ph\]](https://arxiv.org/abs/1303.6154). URL: <https://inspirehep.net/record/1225307/files/arXiv:1303.6154.pdf> (see p. 5).
- [16] PATRICK KOPPENBURG and SEBASTIEN DESCOTES-GENON: **The CKM Parameters**. In: (2017). arXiv: [1702.08834 \[hep-ex\]](https://arxiv.org/abs/1702.08834) (see p. 6).
- [17] J. A. AGUILAR-SAAVEDRA: **Top flavor-changing neutral interactions: Theoretical expectations and experimental detection**. In: *Acta Phys. Polon.*, **B35**: (2004), pp. 2695–2710. arXiv: [hep-ph/0409342 \[hep-ph\]](https://arxiv.org/abs/hep-ph/0409342) (see pp. 6, 15–17).
- [18] S. ABACHI et al.: **Observation of the top quark**. In: *Phys. Rev. Lett.*, **74**: (1995), pp. 2632–2637. doi: [10.1103/PhysRevLett.74.2632](https://doi.org/10.1103/PhysRevLett.74.2632). arXiv: [hep-ex/9503003 \[hep-ex\]](https://arxiv.org/abs/hep-ex/9503003) (see p. 6).
- [19] F. ABE et al.: **Observation of top quark production in $\bar{p}p$ collisions**. In: *Phys. Rev. Lett.*, **74**: (1995), pp. 2626–2631. doi: [10.1103/PhysRevLett.74.2626](https://doi.org/10.1103/PhysRevLett.74.2626). arXiv: [hep-ex/9503002 \[hep-ex\]](https://arxiv.org/abs/hep-ex/9503002) (see p. 6).
- [20] LHCTOP WORKING GROUP: **LHCTopWG Summary plots**. Sept. 2017. URL: <https://twiki.cern.ch/twiki/bin/view/LHCPhysics/LHCTopWGSummaryPlots> (see pp. 9, 21).
- [21] ANDREA GIAMMANCO and JEANNINE WAGNER-KUHR: **Measurement of the t-channel single Top-quark production rates in pp collisions at 7 TeV**. Sept. 2011. URL: <http://cms.web.cern.ch/news/measurement-t-channel-single-top-quark-production-rates-pp-collisions-7-tev> (see p. 9).
- [22] LHCTOP WORKING GROUP: **ATLAS-CMS recommended predictions for single top cross sections using the Hathor v2.1 program**. Sept. 2017. URL: https://twiki.cern.ch/twiki/bin/view/LHCPhysics/SingleTopRefXsec#Predictions_at_7_8_13_and_14_TeV (see p. 10).
- [23] CMS COLLABORATION: **Summaries of CMS cross section measurements**. Oct. 2017. URL: <https://twiki.cern.ch/twiki/bin/view/CMSPublic/PhysicsResultsCombined> (see pp. 10, 20, 22, 50).
- [24] CÉLINE DEGRANDE: **Effective field theories in the Standard Model and beyond**. Thesis. Université Catholique de Louvain, Sept. 2011. URL: <https://cp3.irmp.ucl.ac.be/upload/theses/phd/degrande.pdf> (see p. 11).
- [25] ENRICO FERMI: **Tentativo di una Teoria Dei Raggi β** . In: *Il Nuovo Cimento (1924-1942)*, **11**:1 (Sept. 20, 2008), p. 1. doi: [10.1007/BF02959820](https://doi.org/10.1007/BF02959820) (see p. 11).

- 1762 [26] B. GRZADKOWSKI, M. ISKRZYNSKI, M. MISIAK, and J. ROSIEK: **Dimension-Six Terms**
 1763 **in the Standard Model Lagrangian.** In: *JHEP*, **1010**: (2010), p. 085. doi: [10.1007/JHEP10\(2010\)085](https://doi.org/10.1007/JHEP10(2010)085). arXiv: [1008.4884 \[hep-ph\]](https://arxiv.org/abs/1008.4884) (see pp. 12–13, 16).
- 1765 [27] J.A. AGUILAR SAVVEDRA, C. DEGRANDE, G. DURIEUX, et al.: **Constraining the MSMEFT**
 1766 **in the top sector at the LHC.** Working document for the TOP LHC WG. June 2017.
 1767 URL: http://www.desy.de/~durieux/topbasis/basis_note.pdf (see p. 12).
- 1768 [28] ANDY BUCKLEY, CHRISTOPH ENGLERT, JAMES FERRANDO, et al.: **Constraining top**
 1769 **quark effective theory in the LHC Run II era.** In: *JHEP*, **04**: (2016), p. 015. doi:
 1770 [10.1007/JHEP04\(2016\)015](https://doi.org/10.1007/JHEP04(2016)015). arXiv: [1512.03360 \[hep-ph\]](https://arxiv.org/abs/1512.03360) (see p. 13).
- 1771 [29] YORIKIYO NAGASHIMA: **Beyond the standard model of elementary particle physics.**
 1772 Weinheim, Germany: Wiley-VCH Verlag, 2014. URL: [http://www-spires.fnal.gov/
 1773 spires/find/books/www?cl=QC793.2.N34::2014](http://www-spires.fnal.gov/spires/find/books/www?cl=QC793.2.N34::2014) (see p. 14).
- 1774 [30] P. A. R. ADE et al.: **Planck 2015 results. XIII. Cosmological parameters.** In: *Astron.*
 1775 *Astrophys.*, **594**: (2016), A13. doi: [10.1051/0004-6361/201525830](https://doi.org/10.1051/0004-6361/201525830). arXiv: [1502.01589
 1776 \[astro-ph.CO\]](https://arxiv.org/abs/1502.01589) (see p. 14).
- 1777 [31] P. J. E. PEEBLES and BHARAT RATRA: **The Cosmological constant and dark energy.**
 1778 In: *Rev. Mod. Phys.*, **75**: (2003), pp. 559–606. doi: [10.1103/RevModPhys.75.559](https://doi.org/10.1103/RevModPhys.75.559). arXiv:
 1779 [astro-ph/0207347 \[astro-ph\]](https://arxiv.org/abs/astro-ph/0207347) (see p. 14).
- 1780 [32] A. D. SAKHAROV: **Violation of CP Invariance, c Asymmetry, and Baryon Asym-**
 1781 **metry of the Universe.** In: *Pisma Zh. Eksp. Teor. Fiz.*, **5**: (1967). [*Usp. Fiz.*
 1782 *Nauk* **161**, 61(1991)], pp. 32–35. doi: [10.1070/PU1991v034n05ABEH002497](https://doi.org/10.1070/PU1991v034n05ABEH002497) (see p. 14).
- 1783 [33] GUSTAVO BURDMAN: **New solutions to the hierarchy problem.** In: *Braz. J. Phys.*, **37**:
 1784 (2007), pp. 506–513. doi: [10.1590/S0103-97332007000400006](https://doi.org/10.1590/S0103-97332007000400006). arXiv: [hep-ph/0703194
 1785 \[hep-ph\]](https://arxiv.org/abs/hep-ph/0703194) (see p. 14).
- 1786 [34] T. ET AL. AALTONEN: **Search for the Flavor-Changing Neutral-Current Decay $t \rightarrow Zq$**
 1787 **in $p\bar{p}$ Collisions at $\sqrt{s} = 1.96$ TeV.** In: *Phys. Rev. Lett.*, **101**: (19 Nov. 2008),
 1788 p. 192002. doi: [10.1103/PhysRevLett.101.192002](https://doi.org/10.1103/PhysRevLett.101.192002) (see p. 15).
- 1789 [35] VICTOR MUKHAMEDOVICH ABAZOV et al.: **Search for flavour changing neutral cur-**
 1790 **rents via quark-gluon couplings in single top quark production using 2.3 fb^{-1} of**
 1791 **$p\bar{p}$ collisions.** In: *Phys. Lett.*, **B693**: (2010), pp. 81–87. doi: [10.1016/j.physletb.2010.08.011](https://doi.org/10.1016/j.physletb.2010.08.011). arXiv: [1006.3575 \[hep-ex\]](https://arxiv.org/abs/1006.3575) (see p. 15).
- 1793 [36] GEORGES AAD et al.: **Search for flavour-changing neutral current top-quark decays**
 1794 **to qZ in pp collision data collected with the ATLAS detector at $\sqrt{s} = 8$ TeV.** In: *Eur. Phys. J.*, **C76**:1 (2016), p. 12. doi: [10.1140/epjc/s10052-015-3851-5](https://doi.org/10.1140/epjc/s10052-015-3851-5). arXiv:
 1795 [1508.05796 \[hep-ex\]](https://arxiv.org/abs/1508.05796) (see p. 15).
- 1797 [37] GEORGES AAD et al.: **Search for single top-quark production via flavour-changing**
 1798 **neutral currents at 8 TeV with the ATLAS detector.** In: *Eur. Phys. J.*, **C76**:2 (2016),
 1799 p. 55. doi: [10.1140/epjc/s10052-016-3876-4](https://doi.org/10.1140/epjc/s10052-016-3876-4). arXiv: [1509.00294 \[hep-ex\]](https://arxiv.org/abs/1509.00294) (see pp. 15,
 1800 19).
- 1801 [38] GEORGES AAD et al.: **Search for flavour-changing neutral current top quark decays**
 1802 **$t \rightarrow Hq$ in pp collisions at $\sqrt{s} = 8$ TeV with the ATLAS detector.** In: *JHEP*, **12**:
 1803 (2015), p. 061. doi: [10.1007/JHEP12\(2015\)061](https://doi.org/10.1007/JHEP12(2015)061). arXiv: [1509.06047 \[hep-ex\]](https://arxiv.org/abs/1509.06047) (see
 1804 p. 15).

- 1805 [39] MORAD AABOUD et al.: **Search for top quark decays $t \rightarrow qH$, with $H \rightarrow \gamma\gamma$, in**
- 1806 $\sqrt{s} = 13$ TeV pp collisions using the ATLAS detector. In: (2017). arXiv: [1707.01404](https://arxiv.org/abs/1707.01404) [hep-ex] (see pp. 15, 19).
- 1808 [40] **Search for flavour-changing neutral current top quark decays $t \rightarrow qZ$ in proton-**
- 1809 **proton collisions at $\sqrt{s} = 13$ TeV with the ATLAS Detector.** Tech. rep. ATLAS-CONF-
- 1810 2017-070. Geneva: CERN, Sept. 2017. URL: <https://cds.cern.ch/record/2285808>
- 1811 (see pp. 15, 19, 105–107).
- 1812 [41] ALBERT M SIRUNYAN et al.: **Search for associated production of a Z boson with a**
- 1813 **single top quark and for tZ flavour-changing interactions in pp collisions at \sqrt{s}**
- 1814 **= 8 TeV.** In: (2017). arXiv: [1702.01404](https://arxiv.org/abs/1702.01404) [hep-ex] (see pp. 15, 19, 105–109).
- 1815 [42] SERGUEI CHATRCHYAN et al.: **Search for Flavor-Changing Neutral Currents in Top-**
- 1816 **Quark Decays $t \rightarrow Zq$ in pp Collisions at $\sqrt{s} = 8$ TeV.** In: *Phys. Rev. Lett.*, **112**:17
- 1817 (2014), p. 171802. doi: [10.1103/PhysRevLett.112.171802](https://doi.org/10.1103/PhysRevLett.112.171802). arXiv: [1312.4194](https://arxiv.org/abs/1312.4194) [hep-ex]
- 1818 (see p. 15).
- 1819 [43] VARDAN KHACHATRYAN et al.: **Search for anomalous single top quark production in**
- 1820 **association with a photon in pp collisions at $\sqrt{s} = 8$ TeV.** In: *JHEP*, **04**: (2016),
- 1821 p. 035. doi: [10.1007/JHEP04\(2016\)035](https://doi.org/10.1007/JHEP04(2016)035). arXiv: [1511.03951](https://arxiv.org/abs/1511.03951) [hep-ex] (see pp. 15, 19).
- 1822 [44] VARDAN KHACHATRYAN et al.: **Search for top quark decays via Higgs-boson-mediated**
- 1823 **flavor-changing neutral currents in pp collisions at $\sqrt{s} = 8$ TeV.** In: *JHEP*, **02**:
- 1824 (2017), p. 079. doi: [10.1007/JHEP02\(2017\)079](https://doi.org/10.1007/JHEP02(2017)079). arXiv: [1610.04857](https://arxiv.org/abs/1610.04857) [hep-ex] (see
- 1825 p. 15).
- 1826 [45] **Search for the flavor-changing interactions of the top quark with the Higgs boson**
- 1827 **in $H \rightarrow b\bar{b}$ channel at $\sqrt{s} = 13$ TeV.** Tech. rep. CMS-PAS-TOP-17-003. Geneva:
- 1828 CERN, 2017. URL: <https://cds.cern.ch/record/2284743> (see p. 15).
- 1829 [46] M. BENEKE et al.: **Top quark physics.** In: *1999 CERN Workshop on standard model*
- 1830 *physics (and more) at the LHC, CERN, Geneva, Switzerland, 25-26 May: Proceedings.*
- 1831 2000, pp. 419–529. arXiv: [hep-ph/0003033](https://arxiv.org/abs/hep-ph/0003033) [hep-ph]. URL: <http://weblib.cern.ch/abstract?CERN-TH-2000-100> (see p. 17).
- 1833 [47] JUN GAO, CHONG SHENG LI, and HUA XING ZHU: **Top Quark Decay at Next-to-Next-**
- 1834 **to Leading Order in QCD.** In: *Phys. Rev. Lett.*, **110**:4 (2013), p. 042001. doi:
- 1835 [10.1103/PhysRevLett.110.042001](https://doi.org/10.1103/PhysRevLett.110.042001). arXiv: [1210.2808](https://arxiv.org/abs/1210.2808) [hep-ph] (see pp. 18, 47).
- 1836 [48] STEPHEN MYERS: **The LEP Collider, from design to approval and commissioning.**
- 1837 John Adams' Lecture. Delivered at CERN, 26 Nov 1990. Geneva: CERN, 1991. URL:
- 1838 [http://cds.cern.ch/record/226776](https://cds.cern.ch/record/226776) (see p. 23).
- 1839 [49] STEPHEN HOLMES, RONALD S MOORE, and VLADIMIR SHILTSEV: **Overview of the**
- 1840 **Tevatron collider complex: goals, operations and performance.** In: *Journal of In-*
- 1841 *strumentation*, **6**:08 (2011), T08001. URL: <http://stacks.iop.org/1748-0221/6/i=08/a=T08001> (see p. 23).
- 1843 [50] R. BARATE et al.: **Search for the standard model Higgs boson at LEP.** In: *Phys.*
- 1844 *Lett.*, **B565**: (2003), pp. 61–75. doi: [10.1016/S0370-2693\(03\)00614-2](https://doi.org/10.1016/S0370-2693(03)00614-2). arXiv: [hep-ex/0306033](https://arxiv.org/abs/hep-ex/0306033) [hep-ex] (see p. 23).

- 1846 [51] KENNETH HERNER: **Higgs Boson Studies at the Tevatron**. In: *Nucl. Part. Phys. Proc.*,
1847 273-275: (2016), pp. 852–856. doi: [10.1016/j.nuclphysbps.2015.09.131](https://doi.org/10.1016/j.nuclphysbps.2015.09.131) (see p. 23).
- 1848 [52] ABDELHAK DJOUADI: **The Anatomy of electro-weak symmetry breaking. I: The**
1849 **Higgs boson in the standard model**. In: *Phys. Rept.*, 457: (2008), pp. 1–216. doi:
1850 [10.1016/j.physrep.2007.10.004](https://doi.org/10.1016/j.physrep.2007.10.004). arXiv: [hep-ph/0503172 \[hep-ph\]](https://arxiv.org/abs/hep-ph/0503172) (see p. 23).
- 1851 [53] LYNDON EVANS and PHILIP BRYANT: **LHC Machine**. In: *Journal of Instrumentation*,
1852 3:08 (2008), S08001. url: <http://stacks.iop.org/1748-0221/3/i=08/a=S08001> (see
1853 p. 23).
- 1854 [54] THOMAS SVEN PETTERSSON and P LEFÈVRE: **The Large Hadron Collider: conceptual**
1855 **design**. Tech. rep. CERN-AC-95-05-LHC. Oct. 1995, p. 20 and 22. URL: <https://cds.cern.ch/record/291782> (see p. 23).
- 1857 [55] JORG WENNINGER and EZIO TODESCO: **Large Hadron Collider momentum calibration**
1858 **and accuracy**. Tech. rep. CERN-ACC-2017-0007. Geneva: CERN, Feb. 2017. URL:
1859 <https://cds.cern.ch/record/2254678> (see p. 24).
- 1860 [56] CINZIA DE MELIS: **The CERN accelerator complex. Complexe des accélérateurs du**
1861 **CERN**. In: (July 2016). General Photo. URL: <https://cds.cern.ch/record/2197559>
1862 (see p. 24).
- 1863 [57] ANTONELLA DEL ROSSO: **HL-LHC updates in Japan. Projet HL-LHC : une réunion**
1864 **fait le point au Japon**. In: BUL-NA-2014-272. 51/2014 (Dec. 2014), p. 4. URL:
1865 <https://cds.cern.ch/record/1975962> (see p. 25).
- 1866 [58] OLIVER SIM BRÜNING, PAUL COLLIER, P LEBRUN, et al.: **LHC Design Report**. CERN
1867 Yellow Reports: Monographs. Geneva: CERN, 2004. URL: [https://cds.cern.ch/](https://cds.cern.ch/record/782076)
1868 [record/782076](https://cds.cern.ch/record/782076) (see p. 25).
- 1869 [59] G. AAD et al.: **The ATLAS Experiment at the CERN Large Hadron Collider**. In: *JINST*,
1870 3: (2008), S08003. doi: [10.1088/1748-0221/3/08/S08003](https://doi.org/10.1088/1748-0221/3/08/S08003) (see p. 25).
- 1871 [60] S. CHATRHYAN et al.: **The CMS Experiment at the CERN LHC**. In: *JINST*, 3: (2008),
1872 S08004. doi: [10.1088/1748-0221/3/08/S08004](https://doi.org/10.1088/1748-0221/3/08/S08004) (see pp. 25, 33–35).
- 1873 [61] K. AAMODT et al.: **The ALICE experiment at the CERN LHC**. In: *JINST*, 3: (2008),
1874 S08002. doi: [10.1088/1748-0221/3/08/S08002](https://doi.org/10.1088/1748-0221/3/08/S08002) (see p. 25).
- 1875 [62] A. AUGUSTO ALVES JR. et al.: **The LHCb Detector at the LHC**. In: *JINST*, 3: (2008),
1876 S08005. doi: [10.1088/1748-0221/3/08/S08005](https://doi.org/10.1088/1748-0221/3/08/S08005) (see p. 25).
- 1877 [63] M. BONGI et al.: **Astroparticle physics at LHC: The LHCf experiment ready for data**
1878 **taking**. In: *Nucl. Instrum. Meth.*, A612: (2010), pp. 451–454. doi: [10.1016/j.nima.2009.08.039](https://doi.org/10.1016/j.nima.2009.08.039) (see p. 26).
- 1880 [64] G. ANELLI et al.: **The TOTEM experiment at the CERN Large Hadron Collider**. In:
1881 *JINST*, 3: (2008), S08007. doi: [10.1088/1748-0221/3/08/S08007](https://doi.org/10.1088/1748-0221/3/08/S08007) (see p. 26).
- 1882 [65] B. ACHARYA et al.: **The Physics Programme Of The MoEDAL Experiment At The LHC**.
1883 In: *Int. J. Mod. Phys.*, A29: (2014), p. 1430050. doi: [10.1142/S0217751X14300506](https://doi.org/10.1142/S0217751X14300506).
1884 arXiv: [1405.7662 \[hep-ph\]](https://arxiv.org/abs/1405.7662) (see p. 26).
- 1885 [66] BY JAMES GILLIES: **Luminosity? Why don't we just say collision rate?** In: (Mar.
1886 2011). URL: [http://cds.cern.ch/record/1997001](https://cds.cern.ch/record/1997001) (see p. 26).

- 1887 [67] BY HARRIET JARLETT and HARRIET KIM JARLETT: **LHC pushes limits of performance.**
 1888 In: (Aug. 2016). URL: <http://cds.cern.ch/record/2212301> (see p. 26).
- 1889 [68] CMS COLLABORATION. Okt 2017. URL: https://twiki.cern.ch/twiki/bin/view/CMSPublic/LumiPublicResults#Online_Luminosity_AN2 (see p. 27).
- 1891 [69] **Technical proposal.** LHC Tech. Proposal. Cover title : CMS, the Compact Muon
 1892 Solenoid : technical proposal. Geneva: CERN, 1994. URL: <https://cds.cern.ch/record/290969> (see p. 27).
- 1894 [70] G. L. BAYATIAN et al.: **CMS physics: Technical design report.** In: (2006) (see p. 27).
- 1895 [71] G L BAYATIAN, S CHATRCHYAN, G HMAYAKYAN, et al.: **CMS Physics: Technical Design**
 1896 **Report Volume 1: Detector Performance and Software.** Technical Design Report
 1897 CMS. There is an error on cover due to a technical problem for some items. Geneva:
 1898 CERN, 2006. URL: <https://cds.cern.ch/record/922757> (see pp. 27, 32, 57).
- 1899 [72] CMS COLLABORATION: **Detector Drawings.** CMS Collection. Mar. 2012. URL: <https://cds.cern.ch/record/1433717> (see p. 28).
- 1901 [73] S CHATRCHYAN, V KHACHATRYAN, A M SIRUNYAN, et al.: **Performance of the CMS**
 1902 **Drift Tube Chambers with Cosmic Rays.** In: *J. Instrum.*, 5:arXiv:0911.4855. CMS-
 1903 CFT-09-012 (Nov. 2009), T03015. URL: <http://cds.cern.ch/record/1223944> (see
 1904 pp. 30–31).
- 1905 [74] TOM DODINGTON: **News from the CMS experimental site: 22 November 2013.** Nov.
 1906 2013. URL: <http://cms.web.cern.ch/news/news-point-5-22-november-2013> (see
 1907 p. 31).
- 1908 [75] INSTITUTE OF RESEARCH INTO THE FUNDAMENTAL LAWS THE UNIVERSE: **The CMS**
 1909 **detector superconducting solenoid.** Jan. 2006. URL: http://irfu.cea.fr/en/Phoebe/Vie_des_labos/Ast/ast_visu.php?id_ast=839 (see p. 33).
- 1911 [76] FERGUS WILSON: **Experimental Particle Physics.** Apr. 2012. URL: <http://slideplayer.com/slide/794631/> (see p. 33).
- 1913 [77] EMRAH TIRAS, BURAK BILKI, and YASAR ONEL: **Commissioning of CMS Forward**
 1914 **Hadron Calorimeters with Upgraded Multi-anode PMTs and μTCA Readout.** In:
 1915 (2016). arXiv: 1611.05232 [physics.ins-det] (see p. 34).
- 1916 [78] LUCAS TAYLOR: **Experimental Particle Physics.** Nov. 2011. URL: <http://cms.web.cern.ch/news/electromagnetic-calorimeter> (see p. 34).
- 1918 [79] **Proceedings, 34th International Conference on High Energy Physics (ICHEP 2008)**
 1919 URL: <http://www.slac.stanford.edu/econf/C080730> (see p. 34).
- 1920 [80] L. BRIANZA: **Precision crystal calorimetry in LHC Run II with the CMS ECAL.** In:
 1921 *Journal of Instrumentation*, 12:01 (2017), p. C01069. URL: <http://stacks.iop.org/1748-0221/12/i=01/a=C01069> (see pp. 35, 38).
- 1923 [81] SERGUEI CHATRCHYAN, KHACHATRYAN, et al.: **Description and performance of track**
 1924 **and primary-vertex reconstruction with the CMS tracker.** In: *J. Instrum.*, 9:arXiv:1405.6569
 1925 CERN-PH-EP-2014-070. CMS-TRK-11-001 (May 2014). Comments: Replaced with
 1926 published version. Added journal reference and DOI, P10009. 80 p. URL: <http://cds.cern.ch/record/1704291> (see pp. 35, 58).

- 1928 [82] BY CHRISTINE SUTTON: **Chronicles of CMS: the saga of LS1**. In: (May 2015). URL: <http://cds.cern.ch/record/2024986> (see p. 36).
- 1929
- 1930 [83] **A beautiful barrel for CMS**. In: (Mar. 2014). URL: <http://cds.cern.ch/record/1998635> (see p. 36).
- 1931
- 1932 [84] VARDAN KHACHATRYAN et al.: **The CMS trigger system**. In: *JINST*, **12**:01 (2017), P01020. DOI: [10.1088/1748-0221/12/01/P01020](https://doi.org/10.1088/1748-0221/12/01/P01020). arXiv: [1609.02366 \[physics.ins-det\]](https://arxiv.org/abs/1609.02366) (see p. 37).
- 1933
- 1934
- 1935 [85] BY CORINNE PRALAVORIO and CORINNE PRALAVORIO: **Major work to ready the LHC experiments for Run 2**. In: (May 2015). URL: <http://cds.cern.ch/record/2024977> (see p. 37).
- 1936
- 1937
- 1938 [86] LUIGI GUIDUCCI: **CMS muon system towards LHC Run 2 and beyond**. Tech. rep. CMS-CR-2014-333. Geneva: CERN, Oct. 2014. URL: <https://cds.cern.ch/record/1966038> (see p. 38).
- 1939
- 1940
- 1941 [87] CARLO BATTILANA: **The CMS muon system status and upgrades for LHC run-2 and performance of muon reconstruction with 13 TeV data**. Tech. rep. CMS-CR-2016-437. Geneva: CERN, Dec. 2016. URL: <http://cds.cern.ch/record/2239185> (see p. 38).
- 1942
- 1943
- 1944
- 1945 [88] SERGUEI CHATRCHYAN et al.: **Energy Calibration and Resolution of the CMS Electromagnetic Calorimeter in pp Collisions at $\sqrt{s} = 7$ TeV**. In: *JINST*, **8**: (2013). [JINST8,9009(2013)], P09009. DOI: [10.1088/1748-0221/8/09/P09009](https://doi.org/10.1088/1748-0221/8/09/P09009). arXiv: [1306.2016 \[hep-ex\]](https://arxiv.org/abs/1306.2016) (see p. 38).
- 1946
- 1947
- 1948
- 1949 [89] **Cool running for CMS tracker**. In: (Mar. 2014). URL: <http://cds.cern.ch/record/1998606> (see p. 38).
- 1950
- 1951 [90] L. CADAMURO: **The CMS Level-1 trigger system for LHC Run II**. In: *Journal of Instrumentation*, **12**:03 (2017), p. C03021. URL: <http://stacks.iop.org/1748-0221/12/i=03/a=C03021> (see p. 38).
- 1952
- 1953
- 1954 [91] DAVID AARON MATZNER DOMINGUEZ, D. ABBANEO, K. ARNDT, et al.: **CMS Technical Design Report for the Pixel Detector Upgrade**. In: (2012) (see p. 39).
- 1955
- 1956 [92] HANNO CHRISTOPHER PERREY: **Plans and Status of the Phase I Upgrade of the CMS Pixel Tracker**. Tech. rep. CMS-CR-2014-005. Geneva: CERN, Jan. 2014. URL: <http://cds.cern.ch/record/1644757> (see p. 39).
- 1957
- 1958
- 1959 [93] CLAUDIO GRANDI, DAVID STICKLAND, LUCAS TAYLOR, ACHILLE PETRILLI, and ALAIN HERVÉ: **CMS Computing Model: The "CMS Computing Model RTAG"**. Tech. rep. CMS-NOTE-2004-031. CERN-LHCC-2004-035. LHCC-G-083. Geneva: CERN, Dec. 2004. URL: <http://cds.cern.ch/record/814248> (see p. 39).
- 1960
- 1961
- 1962
- 1963 [94] CHRISTOPH ECK, J KNOBLOCH, LESLIE ROBERTSON, et al.: **LHC computing Grid: Technical Design Report. Version 1.06 (20 Jun 2005)**. Technical Design Report LCG. Geneva: CERN, 2005. URL: <https://cds.cern.ch/record/840543> (see p. 39).
- 1964
- 1965
- 1966 [95] **WORLDWIDE LHC COMPUTING GRID: WorldWide LHC Computing Gird - 2017**. Oct. 2017. URL: <http://wlcg-public.web.cern.ch> (see p. 40).
- 1967

- 1968 [96] JOHN C. COLLINS, DAVISON E. SOPER, and GEORGE F. STERMAN: **Factorization of Hard
Processes in QCD**. In: *Adv. Ser. Direct. High Energy Phys.*, **5**: (1989), pp. 1–91. doi:
10.1142/9789814503266_0001. arXiv: hep-ph/0409313 [hep-ph] (see p. 41).
- 1971 [97] RINGAILE PLACAKYTE: **Parton Distribution Functions**. In: *Proceedings, 31st International Conference on Physics in collisions (PIC 2011): Vancouver, Canada, August 28-September 1, 2011*. 2011. arXiv: 1111.5452 [hep-ph]. URL: <https://inspirehep.net/record/954990/files/arXiv:1111.5452.pdf> (see p. 41).
- 1975 [98] RICHARD D. BALL, VALERIO BERTONE, STEFANO CARRAZZA, et al.: **Parton distributions
for the LHC run II**. In: *Journal of High Energy Physics*, **2015**:4 (2015), p. 40. doi:
10.1007/JHEP04(2015)040 (see p. 41).
- 1978 [99] JON BUTTERWORTH et al.: **PDF4LHC recommendations for LHC Run II**. In: *J. Phys.*,
G43: (2016), p. 023001. doi: 10.1088/0954-3899/43/2/023001. arXiv: 1510.03865
[hep-ph] (see pp. 41–42).
- 1981 [100] H. ABRAMOWICZ and A. CALDWELL: **HERA collider physics**. In: *Rev. Mod. Phys.*, **71**:
(1999), pp. 1275–1410. doi: 10.1103/RevModPhys.71.1275. arXiv: hep-ex/9903037
[hep-ex] (see p. 42).
- 1984 [101] STEPHEN HOLMES, RONALD S. MOORE, and VLADIMIR SHILTSEV: **Overview of the Teva-
tron Collider Complex: Goals, Operations and Performance**. In: *JINST*, **6**: (2011),
T08001. doi: 10.1088/1748-0221/6/08/T08001. arXiv: 1106.0909 [physics.acc-ph]
(see p. 42).
- 1988 [102] JUAN ROJO et al.: **The PDF4LHC report on PDFs and LHC data: Results from Run I
and preparation for Run II**. In: *J. Phys.*, **G42**: (2015), p. 103103. doi: 10.1088/0954-
3899/42/10/103103. arXiv: 1507.00556 [hep-ph] (see p. 42).
- 1991 [103] ALAN D. MARTIN: **Proton structure, Partons, QCD, DGLAP and beyond**. In: *Acta
Phys. Polon.*, **B39**: (2008), pp. 2025–2062. arXiv: 0802.0161 [hep-ph] (see p. 42).
- 1993 [104] J. PUMPLIN, D. STUMP, R. BROCK, et al.: **Uncertainties of predictions from parton dis-
tribution functions. 2. The Hessian method**. In: *Phys. Rev.*, **D65**: (2001), p. 014013.
doi: 10.1103/PhysRevD.65.014013. arXiv: hep-ph/0101032 [hep-ph] (see p. 42).
- 1996 [105] FRANZ MANDL and GRAHAM G SHAW: **Quantum field theory; 2nd ed.** New York, NY:
Wiley, 2010. URL: <https://cds.cern.ch/record/1236742> (see p. 44).
- 1998 [106] S BANERJEE: **CMS Simulation Software**. In: *Journal of Physics: Conference Series*,
396:2 (2012), p. 022003. URL: <http://stacks.iop.org/1742-6596/396/i=2/a=022003>
(see p. 44).
- 2001 [107] M HILDRETH, V N IVANCHENKO, D J LANGE, and M J KORTELAINEN: **CMS Full Simu-
lation for Run-2**. In: *Journal of Physics: Conference Series*, **664**:7 (2015), p. 072022.
URL: <http://stacks.iop.org/1742-6596/664/i=7/a=072022> (see p. 44).
- 2004 [108] S. AGOSTINELLI, J. ALLISON, K. AMAKO, et al.: **Geant4-a simulation toolkit**. In: *Nuclear
Instruments and Methods in Physics Research Section A: Accelerators, Spectrometers,
Detectors and Associated Equipment*, **506**:3 (2003), pp. 250–303. doi: [https://doi.org/10.1016/S0168-9002\(03\)01368-8](https://doi.org/10.1016/S0168-9002(03)01368-8) (see pp. 44, 46).

- 2008 [109] MICHAEL H. SEYMOUR and MARILYN MARX: **Monte Carlo Event Generators**. In: *Proceedings, 69th Scottish Universities Summer School in Physics : LHC Phenomenology (SUSSP69): St.Andrews, Scotland, August 19-September 1, 2012.* 2013, pp. 287–319. DOI: [10.1007/978-3-319-05362-2_8](https://doi.org/10.1007/978-3-319-05362-2_8). arXiv: [1304.6677 \[hep-ph\]](https://arxiv.org/abs/1304.6677) (see p. 44).
- 2012 [110] TORBJORN SJÖSTRAND: **Monte Carlo Tools**. In: *Proceedings, 65th Scottish Universities Summer School in Physics: LHC Physics (SUSSP65): St. Andrews, UK, August 16-29, 2009.* 2009, pp. 309–339. DOI: [10.1201/b11865-14](https://doi.org/10.1201/b11865-14). arXiv: [0911.5286 \[hep-ph\]](https://arxiv.org/abs/0911.5286) (see p. 44).
- 2016 [111] STEFAN HÖCHE: **Introduction to parton-shower event generators**. In: *Proceedings, Theoretical Advanced Study Institute in Elementary Particle Physics: Journeys Through the Precision Frontier: Amplitudes for Colliders (TASI 2014): Boulder, Colorado, June 2-27, 2014.* 2015, pp. 235–295. DOI: [10.1142/9789814678766_0005](https://doi.org/10.1142/9789814678766_0005). arXiv: [1411.4085 \[hep-ph\]](https://arxiv.org/abs/1411.4085) (see pp. 44–45).
- 2021 [112] ADAM ALLOUL, NEIL D. CHRISTENSEN, CÉLINE DEGRANDE, CLAUDE DUHR, and BENJAMIN FUKS: **FeynRules 2.0 - A complete toolbox for tree-level phenomenology**. In: *Comput. Phys. Commun.*, **185**: (2014), pp. 2250–2300. DOI: [10.1016/j.cpc.2014.04.012](https://doi.org/10.1016/j.cpc.2014.04.012). arXiv: [1310.1921 \[hep-ph\]](https://arxiv.org/abs/1310.1921) (see p. 44).
- 2025 [113] CELINE DEGRANDE, CLAUDE DUHR, BENJAMIN FUKS, et al.: **UFO - The Universal FeynRules Output**. In: *Comput. Phys. Commun.*, **183**: (2012), pp. 1201–1214. DOI: [10.1016/j.cpc.2012.01.022](https://doi.org/10.1016/j.cpc.2012.01.022). arXiv: [1108.2040 \[hep-ph\]](https://arxiv.org/abs/1108.2040) (see p. 44).
- 2028 [114] JOHAN ALWALL, MICHEL HERQUET, FABIO MALTONI, OLIVIER MATTELAER, and TIM STELZER: **MadGraph 5 : Going Beyond**. In: *JHEP*, **06**: (2011), p. 128. DOI: [10.1007/JHEP06\(2011\)128](https://doi.org/10.1007/JHEP06(2011)128). arXiv: [1106.0522 \[hep-ph\]](https://arxiv.org/abs/1106.0522) (see pp. 45, 48).
- 2031 [115] MICHELANGELO L. MANGANO, MAURO MORETTI, FULVIO PICCININI, and MICHELE TREC-CANI: **Matching matrix elements and shower evolution for top-quark production in hadronic collisions**. In: *JHEP*, **01**: (2007), p. 013. DOI: [10.1088/1126-6708/2007/01/013](https://doi.org/10.1088/1126-6708/2007/01/013). arXiv: [hep-ph/0611129 \[hep-ph\]](https://arxiv.org/abs/hep-ph/0611129) (see p. 45).
- 2035 [116] TORBJORN SJOSTRAND, STEFAN ASK, JESPER R. CHRISTIANSEN, et al.: **An introduction to {PYTHIA} 8.2**. In: *Computer Physics Communications*, **191**: (2015), pp. 159–177. DOI: <http://dx.doi.org/10.1016/j.cpc.2015.01.024> (see pp. 45–46).
- 2038 [117] TORBJORN SJOSTRAND, STEPHEN MRENNA, and PETER Z. SKANDS: **PYTHIA 6.4 Physics and Manual**. In: *JHEP*, **0605**: (2006), p. 026. DOI: [10.1088/1126-6708/2006/05/026](https://doi.org/10.1088/1126-6708/2006/05/026). arXiv: [hep-ph/0603175 \[hep-ph\]](https://arxiv.org/abs/hep-ph/0603175) (see pp. 45–46).
- 2041 [118] TORBJORN SJOSTRAND, STEFAN ASK, JESPER R. CHRISTIANSEN, et al.: **An Introduction to PYTHIA 8.2**. In: *Comput. Phys. Commun.*, **191**: (2015), pp. 159–177. DOI: [10.1016/j.cpc.2015.01.024](https://doi.org/10.1016/j.cpc.2015.01.024). arXiv: [1410.3012 \[hep-ph\]](https://arxiv.org/abs/1410.3012) (see pp. 45–46, 48–49).
- 2044 [119] JOHAN ALWALL et al.: **Comparative study of various algorithms for the merging of parton showers and matrix elements in hadronic collisions**. In: *Eur. Phys. J.*, **C53**: (2008), pp. 473–500. DOI: [10.1140/epjc/s10052-007-0490-5](https://doi.org/10.1140/epjc/s10052-007-0490-5). arXiv: [0706.2569 \[hep-ph\]](https://arxiv.org/abs/0706.2569) (see p. 45).

- 2048 [120] J. ALWALL, R. FREDERIX, S. FRIXIONE, et al.: **The automated computation of tree-level**
 2049 **and next-to-leading order differential cross sections, and their matching to parton**
 2050 **shower simulations.** In: *JHEP*, **07:** (2014), p. 079. doi: [10.1007/JHEP07\(2014\)079](https://doi.org/10.1007/JHEP07(2014)079).
 2051 arXiv: [1405.0301](https://arxiv.org/abs/1405.0301) [hep-ph] (see p. 45).
- 2052 [121] STEFANO FRIXIONE and BRYAN R. WEBBER: **Matching NLO QCD computations and**
 2053 **parton shower simulations.** In: *JHEP*, **06:** (2002), p. 029. doi: [10.1088/1126-6708/2002/06/029](https://doi.org/10.1088/1126-6708/2002/06/029). arXiv: [hep-ph/0204244](https://arxiv.org/abs/hep-ph/0204244) [hep-ph] (see pp. 45, 48).
- 2055 [122] RIKKERT FREDERIX and STEFANO FRIXIONE: **Merging meets matching in MC@NLO.**
 2056 In: *JHEP*, **12:** (2012), p. 061. doi: [10.1007/JHEP12\(2012\)061](https://doi.org/10.1007/JHEP12(2012)061). arXiv: [1209.6215](https://arxiv.org/abs/1209.6215)
 2057 [hep-ph] (see p. 45).
- 2058 [123] SIMONE ALIOLI, PAOLO NASON, CARLO OLEARI, and EMANUELE RE: **A general frame-**
 2059 **work for implementing NLO calculations in shower Monte Carlo programs: the**
 2060 **POWHEG BOX.** In: *Journal of High Energy Physics*, **2010**:6 (2010), p. 43. doi: [10.1007/JHEP06\(2010\)043](https://doi.org/10.1007/JHEP06(2010)043) (see pp. 45, 48).
- 2062 [124] SIMONE ALIOLI, PAOLO NASON, CARLO OLEARI, and EMANUELE RE: **NLO single-top**
 2063 **production matched with shower in POWHEG: s - and t -channel contributions.**
 2064 In: *Journal of High Energy Physics*, **2009**:09 (2009), p. 111. URL: <http://stacks.iop.org/1126-6708/2009/i=09/a=111> (see pp. 45, 48).
- 2066 [125] STEFANO FRIXIONE, PAOLO NASON, and CARLO OLEARI: **Matching NLO QCD com-**
 2067 **putations with parton shower simulations: the POWHEG method.** In: *Journal of*
 2068 *High Energy Physics*, **2007**:11 (2007), p. 070. URL: <http://stacks.iop.org/1126-6708/2007/i=11/a=070> (see pp. 45, 48).
- 2070 [126] SIMONE ALIOLI, PAOLO NASON, CARLO OLEARI, and EMANUELE RE: **A general frame-**
 2071 **work for implementing NLO calculations in shower Monte Carlo programs: the**
 2072 **POWHEG BOX.** In: *JHEP*, **06:** (2010), p. 043. doi: [10.1007/JHEP06\(2010\)043](https://doi.org/10.1007/JHEP06(2010)043). arXiv:
 2073 [1002.2581](https://arxiv.org/abs/1002.2581) [hep-ph] (see pp. 45, 48).
- 2074 [127] STEFANO FRIXIONE, PAOLO NASON, and CARLO OLEARI: **Matching NLO QCD com-**
 2075 **putations with Parton Shower simulations: the POWHEG method.** In: *JHEP*, **11:**
 2076 (2007), p. 070. doi: [10.1088/1126-6708/2007/11/070](https://doi.org/10.1088/1126-6708/2007/11/070). arXiv: [0709.2092](https://arxiv.org/abs/0709.2092) [hep-ph] (see
 2077 pp. 45, 48).
- 2078 [128] PAOLO NASON: **A New method for combining NLO QCD with shower Monte Carlo**
 2079 **algorithms.** In: *JHEP*, **11:** (2004), p. 040. doi: [10.1088/1126-6708/2004/11/040](https://doi.org/10.1088/1126-6708/2004/11/040).
 2080 arXiv: [hep-ph/0409146](https://arxiv.org/abs/hep-ph/0409146) [hep-ph] (see pp. 45, 48).
- 2081 [129] ANDREI V. GRITSAN, RAOUL RÖNTSCH, MARKUS SCHULZE, and MENG XIAO: **Constraining**
 2082 **anomalous Higgs boson couplings to the heavy flavor fermions using matrix**
 2083 **element techniques.** In: *Phys. Rev.*, **D94**:5 (2016), p. 055023. doi: [10.1103/PhysRevD.94.055023](https://doi.org/10.1103/PhysRevD.94.055023). arXiv: [1606.03107](https://arxiv.org/abs/1606.03107) [hep-ph] (see pp. 45, 48).
- 2085 [130] IAN ANDERSON et al.: **Constraining anomalous HVV interactions at proton and**
 2086 **lepton colliders.** In: *Phys. Rev.*, **D89**:3 (2014), p. 035007. doi: [10.1103/PhysRevD.89.035007](https://doi.org/10.1103/PhysRevD.89.035007). arXiv: [1309.4819](https://arxiv.org/abs/1309.4819) [hep-ph] (see pp. 45, 48).
- 2088 [131] SARA BOLOGNESI, YANYAN GAO, ANDREI V. GRITSAN, et al.: **On the spin and parity of**
 2089 **a single-produced resonance at the LHC.** In: *Phys. Rev.*, **D86:** (2012), p. 095031.
 2090 doi: [10.1103/PhysRevD.86.095031](https://doi.org/10.1103/PhysRevD.86.095031). arXiv: [1208.4018](https://arxiv.org/abs/1208.4018) [hep-ph] (see pp. 45, 48).

- 2091 [132] YANYAN GAO, ANDREI V. GRITSAN, ZIJIN GUO, et al.: **Spin determination of single-produced resonances at hadron colliders.** In: *Phys. Rev.*, **D81**: (2010), p. 075022. doi: [10.1103/PhysRevD.81.075022](https://doi.org/10.1103/PhysRevD.81.075022). arXiv: [1001.3396 \[hep-ph\]](https://arxiv.org/abs/1001.3396) (see pp. 45, 48).
- 2092
- 2093
- 2094 [133] PIERRE ARTOISENET, RIKKERT FREDERIX, OLIVIER MATTELAER, and ROBBERT RIETKERK: **Automatic spin-entangled decays of heavy resonances in Monte Carlo simulations.** In: *JHEP*, **03**: (2013), p. 015. doi: [10.1007/JHEP03\(2013\)015](https://doi.org/10.1007/JHEP03(2013)015). arXiv: [1212.3460 \[hep-ph\]](https://arxiv.org/abs/1212.3460) (see p. 46).
- 2095
- 2096
- 2097
- 2098 [134] V. KHACHATRYAN and ETAL: **Event generator tunes obtained from underlying event and multiparton scattering measurements.** In: *The European Physical Journal C*, **76**:3 (Mar. 17, 2016), p. 155. doi: [10.1140/epjc/s10052-016-3988-x](https://doi.org/10.1140/epjc/s10052-016-3988-x) (see p. 46).
- 2099
- 2100
- 2101 [135] RICHARD D. BALL et al.: **Parton distributions with LHC data.** In: *Nucl. Phys.*, **B867**: (2013), pp. 244–289. doi: [10.1016/j.nuclphysb.2012.10.003](https://doi.org/10.1016/j.nuclphysb.2012.10.003). arXiv: [1207.1303 \[hep-ph\]](https://arxiv.org/abs/1207.1303) (see p. 46).
- 2102
- 2103
- 2104 [136] YUE ZHANG, BO HUA LI, CHONG SHENG LI, JUN GAO, and HUA XING ZHU: **Next-to-leading order QCD corrections to the top quark associated with γ production via model-independent flavor-changing neutral-current couplings at hadron colliders.** In: *Phys. Rev.*, **D83**: (2011), p. 094003. doi: [10.1103/PhysRevD.83.094003](https://doi.org/10.1103/PhysRevD.83.094003). arXiv: [1101.5346 \[hep-ph\]](https://arxiv.org/abs/1101.5346) (see p. 47).
- 2105
- 2106
- 2107
- 2108
- 2109 [137] J ALWALL, R FREDERIX, S FRIXIONE, et al.: **The automated computation of tree-level and next-to-leading order differential cross sections, and their matching to parton shower simulations.** In: *JHEP*, **07**:arXiv:1405.0301. CERN-PH-TH-2014-064. CP3-14-18. LPN14-066. MCNET-14-09. ZU-TH 14-14 (May 2014), 079. 158 p. URL: <http://cds.cern.ch/record/1699128> (see p. 48).
- 2110
- 2111
- 2112
- 2113
- 2114 [138] RIKKERT FREDERIX and STEFANO FRIXIONE: **Merging meets matching in MC@NLO.** In: *JHEP*, **12**:arXiv:1209.6215. CERN-PH-TH-2012-247. ZU-TH 21-12 (Sept. 2012). Comments: 40 pages, 14 figures, 061. 40 p. URL: <http://cds.cern.ch/record/1481985> (see p. 48).
- 2115
- 2116
- 2117
- 2118 [139] **CMS Monte Carlo Generator Group** (see pp. 48–49).
- 2119 [140] T. GEHRMANN, M. GRAZZINI, S. KALLWEIT, et al.: **W^+W^- Production at Hadron Colliders in Next to Next to Leading Order QCD.** In: *Phys. Rev. Lett.*, **113**:21 (2014), p. 212001. doi: [10.1103/PhysRevLett.113.212001](https://doi.org/10.1103/PhysRevLett.113.212001). arXiv: [1408.5243 \[hep-ph\]](https://arxiv.org/abs/1408.5243) (see p. 49).
- 2120
- 2121
- 2122
- 2123 [141] A. HOECKER, P. SPECKMAYER, J. STELZER, et al.: **TMVA - Toolkit for Multivariate Data Analysis.** In: *ArXiv Physics e-prints*, (Mar. 2007). eprint: [physics/0703039](https://arxiv.org/abs/physics/0703039) (see p. 50).
- 2124
- 2125 [142] R. BRUN and F. RADEMAKERS: **ROOT: An object oriented data analysis framework.** In: *Nucl. Instrum. Meth.*, **A389**: (1997), pp. 81–86. doi: [10.1016/S0168-9002\(97\)00048-X](https://doi.org/10.1016/S0168-9002(97)00048-X) (see p. 50).
- 2126
- 2127
- 2128 [143] A. MAYR, H. BINDER, O. GEFELLER, and M. SCHMID: **The Evolution of Boosting Algorithms - From Machine Learning to Statistical Modelling.** In: *ArXiv e-prints*, (Mar. 2014). arXiv: [1403.1452 \[stat.ME\]](https://arxiv.org/abs/1403.1452) (see p. 51).
- 2129
- 2130
- 2131 [144] OLAF BEHNKE, KEVIN KRONINGER, GREGORY SCHOTT, and THOMAS SCHORNER-SADENIUS: **Data Analysis in High Energy Physics: A Practical Guide to Statistical Methods.** 1st. Wiley-VCH, 2013 (see p. 51).
- 2132
- 2133

- 2134 [145] CHRISTIAN BÖSER, SIMON FINK, and STEFFEN RÖCKER: **Introduction to Boosted**
 2135 **Decision Trees: A multivariate approach to classification problems.** Presented at
 2136 the 'KSETA Doktoranden' workshop, Lauterbad. July 2014. URL: <https://indico.scc.kit.edu/indico/event/48/session/4/contribution/35/material/slides/0.pdf> (see
 2137 p. 51).
- 2138
- 2139 [146] SERGUEI CHATRCHYAN et al.: **Combined results of searches for the standard model**
 2140 **Higgs boson in pp collisions at $\sqrt{s} = 7$ TeV.** In: *Phys. Lett.*, **B710**: (2012), pp. 26–
 2141 48. DOI: [10.1016/j.physletb.2012.02.064](https://doi.org/10.1016/j.physletb.2012.02.064). arXiv: [1202.1488 \[hep-ex\]](https://arxiv.org/abs/1202.1488) (see p. 52).
- 2142 [147] GLEN COWAN, KYLE CRANMER, EILAM GROSS, and OFER VITELLS: **Asymptotic formulae**
 2143 **for likelihood-based tests of new physics.** In: *Eur. Phys. J.*, **C71**: (2011). [Erratum:
 2144 *Eur. Phys. J.* C73,2501(2013)], p. 1554. DOI: [10.1140/epjc/s10052-011-1554-0](https://doi.org/10.1140/epjc/s10052-011-1554-0), [10.1140/epjc/s10052-013-2501-z](https://doi.org/10.1140/epjc/s10052-013-2501-z). arXiv: [1007.1727 \[physics.data-an\]](https://arxiv.org/abs/1007.1727) (see
 2145 pp. 52–53).
- 2146
- 2147 [148] **Observation of a new boson with a mass near 125 GeV.** Tech. rep. CMS-PAS-HIG-
 2148 12-020. Geneva: CERN, 2012. URL: <https://cds.cern.ch/record/1460438> (see
 2149 p. 52).
- 2150 [149] **Procedure for the LHC Higgs boson search combination in Summer 2011.** Tech.
 2151 rep. CMS-NOTE-2011-005. ATL-PHYS-PUB-2011-11. Geneva: CERN, Aug. 2011. URL:
 2152 [http://cds.cern.ch/record/1379837](https://cds.cern.ch/record/1379837) (see p. 52).
- 2153 [150] HIGGS WORKING GROUP: **Documentation of the RooStats based statistics tools for**
 2154 **Higgs PAG.** Aug. 2017. URL: <https://twiki.cern.ch/twiki/bin/viewauth/CMS/SWGuideHiggsAnalysisCombinedLimit> (see p. 52).
- 2155
- 2156 [151] LORENZO MONETA, KEVIN BELASCO, KYLE S. CRANMER, et al.: **The RooStats Project.**
 2157 In: *PoS, ACAT2010*: (2010), p. 057. arXiv: [1009.1003 \[physics.data-an\]](https://arxiv.org/abs/1009.1003) (see p. 52).
- 2158 [152] GLEN COWAN, KYLE CRANMER, EILAM GROSS, and OFER VITELLS: **Asymptotic formulae**
 2159 **for likelihood-based tests of new physics.** In: *The European Physical Journal C*, **71**:2
 2160 (Feb. 2011). DOI: [10.1140/epjc/s10052-011-1554-0](https://doi.org/10.1140/epjc/s10052-011-1554-0). arXiv: [1007.1727 \[hep-ph\]](https://arxiv.org/abs/1007.1727) (see
 2161 p. 52).
- 2162 [153] THOMAS JUNK: **Confidence level computation for combining searches with small**
 2163 **statistics.** In: *Nuclear Instruments and Methods in Physics Research Section A: Accelerators,*
 2164 *Spectrometers, Detectors and Associated Equipment*, **434**:2 (1999), pp. 435–443.
 2165 DOI: [https://doi.org/10.1016/S0168-9002\(99\)00498-2](https://doi.org/10.1016/S0168-9002(99)00498-2) (see p. 52).
- 2166 [154] AL READ: **Presentation of search results: the CL s technique.** In: *Journal of Physics G: Nuclear and Particle Physics*, **28**:10 (2002), p. 2693. URL: <http://stacks.iop.org/0954-3899/28/i=10/a=313> (see p. 52).
- 2167
- 2168
- 2169 [155] A. M. SIRUNYAN et al.: **Particle-flow reconstruction and global event description**
 2170 **with the CMS detector.** In: *JINST*, **12**: (2017), P10003. DOI: [10.1088/1748-0221/12/10/P10003](https://doi.org/10.1088/1748-0221/12/10/P10003). arXiv: [1706.04965 \[physics.ins-det\]](https://arxiv.org/abs/1706.04965) (see pp. 56–60, 62).
- 2171
- 2172 [156] R. FRÜHWIRTH: **Application of Kalman filtering to track and vertex fitting.** In:
 2173 *Nuclear Instruments and Methods in Physics Research Section A: Accelerators, Spectrometers,*
 2174 *Detectors and Associated Equipment*, **262**:2 (1987), pp. 444–450. DOI: [http://dx.doi.org/10.1016/0168-9002\(87\)90887-4](https://doi.org/10.1016/0168-9002(87)90887-4) (see p. 57).
- 2175

- 2176 [157] PIERRE BILLOIR: **Progressive track recognition with a Kalman like fitting proce-**
 2177 **dure.** In: *Comput. Phys. Commun.*, **57**: (1989), pp. 390–394. DOI: [10.1016/0010-4655\(89\)90249-X](https://doi.org/10.1016/0010-4655(89)90249-X) (see p. 57).
- 2179 [158] SERGUEI CHATRCHYAN et al.: **Performance of CMS muon reconstruction in pp col-**
 2180 **lision events at $\sqrt{s} = 7$ TeV.** In: *JINST*, **7**: (2012), P10002. DOI: [10.1088/1748-0221/7/10/P10002](https://doi.org/10.1088/1748-0221/7/10/P10002). arXiv: [1206.4071 \[physics.ins-det\]](https://arxiv.org/abs/1206.4071) (see p. 57).
- 2182 [159] W ADAM, R FRÜHWIRTH, A STRANDLIE, and T TODOROV: **Reconstruction of electrons**
 2183 **with the Gaussian-sum filter in the CMS tracker at the LHC.** In: *Journal of Physics*
 2184 *G: Nuclear and Particle Physics*, **31**:9 (2005), N9. URL: <http://stacks.iop.org/0954-3899/31/i=9/a=N01> (see p. 57).
- 2186 [160] **Performance of electron reconstruction and selection with the CMS detector in**
 2187 **proton-proton collisions at $\sqrt{s} = 8$ TeV.** In: *Journal of Instrumentation*, **10**:06 (2015),
 2188 P06005. URL: <http://stacks.iop.org/1748-0221/10/i=06/a=P06005> (see p. 58).
- 2189 [161] **Electron and photon performance in CMS with the full 2016 data sample.** In: (Mar.
 2190 2017). URL: <http://cds.cern.ch/record/2255497> (see pp. 58, 62, 64).
- 2191 [162] K. ROSE: **Deterministic annealing for clustering, compression, classification, re-**
 2192 **gression, and related optimization problems.** In: *Proceedings of the IEEE*, **86**:11
 2193 (Nov. 1998), pp. 2210–2239. DOI: [10.1109/5.726788](https://doi.org/10.1109/5.726788) (see p. 58).
- 2194 [163] WOLFGANG WALTENBERGER: **Adaptive Vertex Reconstruction.** Tech. rep. CMS-NOTE-
 2195 2008-033. Geneva: CERN, July 2008. URL: <https://cds.cern.ch/record/1166320> (see
 2196 p. 58).
- 2197 [164] ANDREAS KORN Mayer: **The CMS Pixel Luminosity Telescope.** Tech. rep. CMS-CR-
 2198 2015-121. Geneva: CERN, June 2015. URL: <https://cds.cern.ch/record/2039978> (see
 2199 p. 59).
- 2200 [165] **CMS Luminosity Measurements for the 2016 Data Taking Period.** Tech. rep. CMS-
 2201 PAS-LUM-17-001. Geneva: CERN, 2017. URL: <http://cds.cern.ch/record/2257069>
 2202 (see p. 59).
- 2203 [166] **Measurement of the inelastic proton-proton cross section at $\sqrt{s} = 13$ TeV.** Tech.
 2204 rep. CMS-PAS-FSQ-15-005. Geneva: CERN, 2016. URL: <https://cds.cern.ch/record/2145896> (see p. 60).
- 2206 [167] **Muon Identification and Isolation efficiency on full 2016 dataset.** In: (Mar. 2017).
 2207 URL: <http://cds.cern.ch/record/2257968> (see pp. 60–61).
- 2208 [168] **Effective areas used for Summer16 samples.** May 2017. URL: https://indico.cern.ch/event/482673/contributions/2187022/%20attachments/1282446/1905912/talk_electron_ID_spring16.pdf (see p. 63).
- 2211 [169] MATTEO CACCIARI, GAVIN P. SALAM, and GREGORY SOYEZ: **The Anti-k(t) jet clustering**
 2212 **algorithm.** In: *JHEP*, **04**: (2008), p. 063. DOI: [10.1088/1126-6708/2008/04/063](https://doi.org/10.1088/1126-6708/2008/04/063). arXiv:
 2213 [0802.1189 \[hep-ph\]](https://arxiv.org/abs/0802.1189) (see p. 63).
- 2214 [170] **Jet algorithms performance in 13 TeV data.** Tech. rep. CMS-PAS-JME-16-003.
 2215 Geneva: CERN, 2017. URL: <http://cds.cern.ch/record/2256875> (see p. 63).

- 2216 [171] V. KHACHATRYAN et al.: **Jet energy scale and resolution in the CMS experiment in**
 2217 **pp collisions at 8 TeV.** In: *Journal of Instrumentation*, **12**:02 (2017), P02014. URL:
 2218 <http://stacks.iop.org/1748-0221/12/i=02/a=P02014> (see pp. 65–66).
- 2219 [172] **Jet energy scale and resolution performances with 13TeV data.** In: (June 2016).
 2220 URL: <http://cds.cern.ch/record/2160347> (see pp. 65–66).
- 2221 [173] THE CMS COLLABORATION: **Identification of b-quark jets with the CMS experiment.**
 2222 In: *Journal of Instrumentation*, **8**:04 (2013), P04013. URL: <http://stacks.iop.org/1748-0221/8/i=04/a=P04013> (see p. 66).
- 2224 [174] **Identification of b quark jets at the CMS Experiment in the LHC Run 2.** Tech. rep.
 2225 CMS-PAS-BTV-15-001. Geneva: CERN, 2016. URL: <http://cds.cern.ch/record/2138504> (see pp. 66, 68).
- 2227 [175] NAZAR BARTOSIK: **Diagram showing the common principle of identification of jets**
 2228 **initiated by b-hadron decays.** May 2016. URL: http://bartosik.pp.ua/hep_sketches/btagging (see p. 67).
- 2230 [176] **Identification of b quark jets at the CMS Experiment in the LHC Run 2.** Tech. rep.
 2231 CMS-PAS-BTV-16-001. unpublished. Geneva: CERN, 2017 (see pp. 68–69).
- 2232 [177] **Performance of missing energy reconstruction in 13 TeV pp collision data using**
 2233 **the CMS detector.** Tech. rep. CMS-PAS-JME-16-004. Geneva: CERN, 2016. URL:
 2234 <http://cds.cern.ch/record/2205284> (see pp. 69, 74–75).
- 2235 [178] JORDAN DAMGOV: **Missing Et Optional Filters Run 2.** Oct. 2017. URL: <https://twiki.cern.ch/twiki/bin/viewauth/CMS/MissingETOptionalFiltersRun2> (see p. 74).
- 2237 [179] **EGM corrections for Moriond17.** URL: https://indico.cern.ch/event/613162/contributions/2472046/attachments/1410308/2156822/EGMSmearerAndRegression_PPD_022017.pdf (see p. 78).
- 2240 [180] **Misalignment and Muon Scale corrections.** URL: https://www-cdf.fnal.gov/~jyhan/cms_momscl/rochcor_cmsnote.pdf (see p. 79).
- 2242 [181] **Rochestor Correction.** Accessed: 2017-05-20. URL: <https://twiki.cern.ch/twiki/bin/viewauth/CMS/RochcorMuon> (see p. 79).
- 2244 [182] RICHARD D. BALL et al.: **Parton distributions from high-precision collider data.** In:
 2245 *Eur. Phys. J. C*, **77**: (2017), p. 663. DOI: [10.1140/epjc/s10052-017-5199-5](https://doi.org/10.1140/epjc/s10052-017-5199-5). arXiv:
 2246 [1706.00428 \[hep-ph\]](https://arxiv.org/abs/1706.00428) (see p. 92).